Charles University

Faculty of Science

Institute of Petrology and Structural Geology

Study program: Geology

Record of metamorphic and metasomatic processes at the contact of felsic granulites and garnet clinopyroxenites in the Bohemian Massif

Záznam metamorfních a metasomatických procesů na kontaktu felsických granulitů a granátických klinopyroxenitů v Českém masivu

Mgr. Tereza Zelinková

Doctoral dissertation

Supervisor: Mgr. Martin Racek, Ph.D.

Advisor: Prof. Mgr. Vojtěch Janoušek, Ph.D.

Advisor: doc. Mgr. Ondrej Lexa, Ph.D.

Prague, 2024

Acknowledgments

First of all, I would like to thank my supervisor Martin Racek for the opportunity to work on this topic, his patience, help with the measurements in the electron microscopy laboratories, willingness to help in all situations and for the overall supervision of the work, which was carried out in a pleasant and friendly atmosphere all the time. I would also like to thank Vojta Janoušek for the consultations, help with the collecting of the geochemical samples and their processing, introduction to the secrets of GCDkit and geochemistry, careful editing and comments on the written texts and for kind words of support during the finishing of the study. I would also like to thank Rainer Abart for his editing of the manuscripts, consultations and for the pleasant time spent during our field trips. I thank Pavla Štípská for consultations, constructive ideas and thorough editing of the text during the work on the second article. I would like to thank Rene Asenbaum for his collaboration on the second article and for the pleasant time in the field. I thank Julian Portenkirchner for his help with geochemical sampling and a pleasant company during the fieldwork. I thank Ondrej Lexa for his occasional help with Python and Thermocalc, and Vítek Peřestý for the occasional advice with the P–T modelling.

I would also like to thank the management of the Czech Geological Survey (CGS), especially the successive heads of Department 420: Jára Pertoldová, Zita Bukovská and Honza Jelínek, for providing the time and space necessary to the completion of this thesis. I also thank other colleagues and friends from CGS for their important moral support.

Many thanks also go to other students from the Institute of Petrology and Structural Geology for the support and moments of fun during the studies.

There are not enough thanks in the world for my loved ones who have been there for me throughout my studies, even though they often had a hard time with me.

This work was funded by joint grant of the Czech and Austrian funding agencies (GACR: 20-24210L, FWF: I 4580-N).

Poděkování

V prvé řadě velmi děkuji svému školiteli Martinovi Rackovi za možnost pracovat na tomto tématu, za trpělivost, za pomoc při měření v laboratořích elektronové mikroskopie, ochotu pomoci za všech situací a za celkové vedení práce, které se po celou dobu neslo v příjemném přátelském duchu. Dále patří obrovské poděkování Vojtovi Janouškovi za konzultace, pomoc při odběru geochemických vzorků a jejich zpracování, uvedení do tajů GCDkitu a geochemie, pečlivé komentáře a připomínky k psaným textům a za milá slova podpory během dokončování studia. Dále bych ráda poděkovala Rainerovi Abartovi za pečlivou editaci manuskriptů, konzultace a za příjemně strávený čas během společných výjezdů do terénu. Děkuji Pavle Štípské za konzultace, konstruktivní nápady a důkladnou editaci textu během tvorby druhého článku. Renému Asenbaumovi děkuji za spolupráci na druhém článku a za příjemně strávený čas v terénu. Julianovi Portenkirchnerovi děkuji za pomoc při odběru geochemických vzorků a za společný čas během terénních prací. Ondreji Lexovi děkuji za příležitostné rady ohledně Pythonu a Thermocalcu a Vítkovi Peřestému za občasné rady během P–T modelování.

Dále bych chtěla poděkovat vedení České geologické služby (ČGS), především postupným vedoucím odboru 420: Jáře Pertoldové, Zitě Bukovské a Honzovi Jelínkovi, za poskytnutí času a prostoru potřebnému k dokončení této práce. Děkuji i ostatním kolegům a přátelům z ČGS za důležitou morální podporu.

Velké díky patří také spolužákům z fakulty za vzájemnou oporu a chvíle rozptýlení.

Na světě není dostatek díků pro mé nejbližší, kteří tu pro mě byli po celou dobu studia, i když to se mnou často neměli jednoduché.

Tato práce byla podpořená grantovou agenturou České a Rakouské republiky (GACR: 20-24210L, FWF: I 4580-N).

Declaration / Prohlášení

I declare that this thesis is a result of my own work and that I have cited all the resources and literature. Neither this thesis nor its substantial part has been submitted to fulfill requirements for any other academic degree. The results of the thesis are my own work or the product of collaboration with other members of the research team.

Prohlašuji, že jsem závěrečnou práci vypracovala samostatně, a že jsem uvedla všechny použité informační zdroje a literaturu. Tato práce ani její podstatná část nebyla předložena k získání jiného nebo obdobného druhu vysokoškolské kvalifikace. Výsledky práce jsou produktem mé vlastní práce nebo práce ve výzkumném týmu.

In Prague, 13.11.2024

V Praze, 13.11.2024

……..

Mgr. Tereza Zelinková

List of papers and authors contributions

This thesis is a monography, which contains data from two published papers and one manuscript in preparation. The candidate is the first author of all of them. Published papers in their original form are part of the online supplementary material of this thesis.

Published paper in the *American Mineralogist*:

Zelinková, T., Racek, M., and Abart, R. (2023) Compositional trends in Ba-, Ti-, and Cl-rich micas from metasomatized mantle rocks of the Gföhl Unit, Bohemian Massif, Austria. American Mineralogist, 108, 1840–1851.

https://doi.org/10.2138/am-2022-8746

- The data from this paper form the Part I of the thesis. The original published paper is included as an electronic appendix. The candidate was responsible for the petrographic descriptions of the studied samples, and together with the supervisor for collecting of studied samples and the measurement of mineral analyses on an electron microprobe. The candidate prepared the figures, tables, supplementary material and the manuscript text, which were consulted with the co-authors. (Author's contribution 75%).

Published paper in the *Journal of Petrology*:

Zelinková, T., Racek, M., Janoušek, V., Štípská, P., Abart, R., and Asenbaum, R. (2024) Metasomatic interaction of ultramafic mantle xenoliths with their felsic HP–UHT granulite host (Moldanubian Domain, Bohemian Massif in Lower Austria). Journal of Petrology, 65, egae075.

https://doi.org/10.1093/petrology/egae075

- The data from this paper form Part II of the thesis. The original published paper is included as an electronic appendix. The candidate was responsible for the petrographic descriptions of the studied samples, and together with the supervisor for the measurement of mineral analyses on an electron microprobe and the area analysis on an electron microscope. The candidate prepared the tables, supplementary material, the original manuscript text, and most of the figures. The candidate is also responsible for the P–T modelling of studied lithologies. (Author's contribution 75%).

Manuscript in preparation for a submission to the *Journal of Petrology (*the name of the manuscript is preliminary):

Zelinková, T., Janoušek, V., and Racek, M.: Indications for the metasomatic origin of intermediate and mafic granulites at the contact of garnet clinopyroxenites with felsic HP–UHT granulites (Moldanubian Domain, Bohemian Massif in Lower Austria).

- Data from this manuscript form parts III and IV of the thesis. The candidate is responsible for the sample collection, petrological description of the representative samples, and together with the supervisor for the measurement of mineral analyses on an electron microprobe and the area analysis on an electron microscope. The candidate prepared the tables, the manuscript text, and most of the figures and is responsible for the P–T modelling of all lithologies and in cooperation with a consultant for the interpretation of the geochemical data (Author's contribution 70%).

I certify that the above records are an accurate representation of the involvement of the candidate in the aforementioned research papers.

……..

Mgr. Martin Racek, Ph.D.

Project supervisor

ABSTRACT

St. Leonhard and Dunkelsteiner Wald granulite massifs (Bohemian Massif, Lower Austria) are dominantly formed by kyanite-bearing felsic granulites hosting mantle bodies (from a few cm to several km) including garnet clinopyroxenites. Their contact is sometimes accompanied by intermediate and mafic granulites traditionally interpreted as the metamorphic products different to protoliths of kyanite-bearing felsic granulites. According to the detailed petrography, phase-stability modelling, and whole-rock geochemistry and Sr–Nd isotopic data, this research suggests the metasomatic origin of at least some of these transition granulites as the consequences of the metasomatic interaction between kyanite-bearing felsic granulites with garnet clinopyroxenites.

The evidence of metasomatism in garnet clinopyroxenites are Ba- and/or Cl-rich minerals in the matrix or as a part of multiphase solid inclusions (MSI). The presence of Ba-, Ti-, and Cl-rich micas (Ba-rich phlogopite to chloroferrokinoshitalite to oxykinositalite), Cl-apatite, goryainovite, and carbonates indicating high-Cl and -CO_2 activity and low-H_2O activity in metasomatizing fluids/melts. According to the whole-rock geochemistry and Sr–Nd isotopic composition, garnet clinopyroxenites show signs of derivation from mantle peridotites due to metasomatism by fluids derived from the oceanic part of the subducting Saxothuringian plate with variable overprinting by fluids and/or melts coming from the Saxothuringian felsic metaigneous crust (presumed protolith of the felsic granulites), which could have caused the transformation some of the garnet clinopyroxenites to mafic granulites.

The formation of mafic granulites required movement of Mg, Al and, especially, Ca from the garnet clinopyroxenites to the kyanite-bearing felsic granulites and migration of K and Na in the opposite direction, which caused the breakdown of clinopyroxene and formation of symplectite textures (plagioclase ± clinopyroxene ± orthopyroxene ± amphibole). For the formation of intermediate granulites, the addition of Mg, and especially Ca to the kyanite-bearing felsic granulites from garnet clinopyroxenites was required, leading to the breakdown of the Al_2SiO_5 phase and stabilization of orthopyroxene. The migration of K from the felsic host to garnet clinopyroxenites is reflected by K-feldspar-poor haloes around small mantle xenoliths and K-rich net along plagioclase in the matrix of mafic granulites.

The metasomatic interactions associated with the growth of the reaction textures and changes in mineral associations are estimated to ~900–1100 °C and 1.0–1.5 GPa. The duration of coronae growth around mantle xenoliths up to several cm across was 13–532 ka.

Keywords: garnet clinopyroxenite, peridotite, granulite, metasomatism, multiphase solid inclusions, fluids, melts, kinoshitalite

ABSTRAKT

Granulitové masivy St. Leonhard a Dunkelsteiner Wald (Český Masiv, Dolní Rakousko), jsou dominantně tvořeny kyanitonosným felsickým granulitem, ve kterém se vyskytují plášťová tělesa (od několika cm do několika km), mezi které patří i granátické klinopyroxenity. Kontakt těchto plášťových těles s hostitelským granulitem je občas doprovázen výskytem intermediálních a mafických granulitů, jejichž vznik je tradičně vysvětlován metamorfózou protolitu odlišného od převažujících kyanitonosných granulitů. Na základě detailního petrografického studia, modelování stability fází, celohorninové geochemie a Sr-Nd izotopových dat, tento výzkum navrhuje možnost metasomatického vzniku alespoň části těchto přechodných granulitů jako následek metasomatické interakce mezi kyanitonosnými granulity s granátickými klinopyroxenity.

Důkazem metasomatismu v granátických klinopyroxenitech jsou Ba- a/nebo Cl-bohaté minerály, které se vyskytují v matrix nebo jsou součástí multifázových pevných inkluzí (MSI). Přítomnost Ba-, Ti-, a Cl-bohatých slíd (Ba-bohatý flogopit až chloroferrokinoshitalit až oxykinositalit), Cl-apatitu, goryainovitu, a karbonátů indikuje vysokou aktivitu Cl a CO_2 a nízkou aktivitu H_2O v metasomatizujícím fluidu/tavenině. Na základě celohorninové geochemie a Sr–Nd izotopových dat, granátické klinopyroxenity ukazují znaky derivace z plášťových peridotitů díky metasomatóze fluidy z oceánské části subdukující Saxothuringské desky s následným variabilním přetiskem fluidy/taveninou pocházející ze Saxothuringských přeměněných felsických magmatitů (předpokládaný protolit felsických granulitů), který mohl způsobit transformaci některých granátických klinopyroxenitů na mafické granulity.

Vznik mafických granulitů vyžaduje migraci Mg, Al, a především Ca z granátických klinopyroxenitů do felsických granulitů a přísun K a Na opačným směrem, což má za následek rozpad klinopyroxenu a vznik symplektitové textury (plagioklas ± klinopyroxen ± ortopyroxen ± amfibol). Pro vznik intermediálních granulitů je zapotřebí přísun Mg a především Ca z granátických klinopyroxenitů do felsických granulitů, což vede k rozpadu Al_2SiO_5 fáze a stabilizaci ortopyroxenu. Pohyb K z felsických granulitů do granátických klinopyroxenitů je doložen vznikem K-živcem chudých zón kolem malých plášťových xenolitů a K-bohaté sítě podél plagioklasu v matrix mafických granulitů.

Metasomatická interakce spojená s růstem reakčních textur a změn v minerálních asociacích je odhadována do ~900–1100 °C a 1.0–1.5 GPa. Růst koron kolem několik centimetrů velkých plášťových xenolitů trval 13 000–532 000 let.

Klíčová slova: granátický klinopyroxenit, peridotit, granulit, metasomatóza, multifázové pevné inkluze, fluidum, tavenina, kinoshitalit

TABLE OF CONTENTS

PREFACE

1 Introduction and aims of the study

“Metamorphism” is a process, during which the composition and/or structure of a rock is changing by heat, pressure or fluid/melt interaction or their combination. The special type of metamorphic process is "metasomatism“ – the process affecting the chemical composition of a rock due to the supply and/or removal of chemical components as a result of the interaction with aqueous fluids (solutions) (Harlov & Austrheim, 2013). Metasomatism may be a local process that affects only a small area of the rock or a more extensive process affecting rocks in the regional scale (White *et al.,* 2014; Engvik *et al*., 2011).

Variscan felsic (U)HP–(U)HT (garnet–kyanite-bearing) granulite in the Bohemian Massif has been the subject of numerous studies over the last decades (Fiala *et al.,* 1987; Janoušek *et al.,* 2004; Kotková & Harley, 2010; Schulmann *et al.,* 2014) and may contain numerous (ultra-)mafic mantle bodies (Medaris *et al.,* 2006b; Kusbach *et al.,* 2015). Less common orthopyroxene-bearing intermediate to clinopyroxene-bearing mafic granulites occurring occasionally at the interface of mantle bodies with kyanite-bearing felsic granulites have received considerably less attention. They are usually interpreted as a product of metamorphism of a protolith different from that required for the kyanite-bearing felsic granulite (Carswell & O’Brien, 1993; Cooke, 2000; Vrána *et al.*, 2013). However, detailed work by Štípská *et al*. (2014a and b) in the Blanský les granulite massif (southern Bohemia) documented an origin of intermediate granulite from cm-sized mantle-derived eclogite xenoliths by an addition of K_2O and H_2O from the host felsic granulite. Experimental work using rock powders of the same endmembers confirmed that a chemically cryptic diffusion of water and migration of limited amount of melt can trigger major textural and localised chemical changes on grain-scale (Pistone *et al.*, 2020). In general, diffusion of mobile components is caused by the gradients in their chemical potentials at the contact of chemically different mineral phases or assemblages (e.g. Joesten, 1977 and 1986; Abart *et al.,* 2001).

The mentioned research (Štípská *et al*., 2014a and b) is unique as the metasomatic interaction at the contact between the lower crustal and the upper mantle rocks is rarely described. More common studies with similar focus deal with metasomatic interactions of lithologies from different geological environments, for example the interaction of volcanic rocks with peridotite xenoliths derived from the mantle beneath the volcanic front (Ishimaru *et al*., 2007; Arai &

Ishimaru, 2008), and the interaction between hornblendite xenoliths in a marble from a granulite facies terrain (Abart *et al*., 2001; Abart & Sperb, 2001).

The example of metasomatism around large ultramafic bodies is known from the ophiolite complexes, where the Ca metasomatism related to the serpentinization of adjacent ultramafic rocks caused the transformation of gabbros and dolerites to rodingites (e.g. Abuamarah *et al.,* 2023; Tsikouras *et al*., 2009).

The indirect evidence of the crustal-mantle metasomatic interaction are mineral phases rich in crustal-derived chemical components in mantle lithologies including garnet clinopyroxenites described also from the Bohemian Massif (Zaccarini *et al.,* 2004; Faryad *et al.,* 2010; Borghini *et al.,* 2018, 2020; Čopjaková & Kotková, 2018; Naemura *et al.,* 2018; Kotková *et al*., 2021a).

The aims of the thesis are to assess the possibility of the metasomatic interaction between garnet clinopyroxenites with the host felsic granulites in St. Leonhard and Dunkelsteiner Wald granulite massifs (Moldanubian Zone, Lower Austria) in different scales and develop a new genetic hypothesis for the origin of the transition granulite types at their contacts. The research uses textural analysis, thermodynamic modelling, mineral and local bulk-rock compositions, the whole-rock composition, and Sr–Nd isotopic geochemistry.

The results of the thesis allows to develop a new genetic hypothesis for the origin of the intermediate orthopyroxene-bearing granulites by metasomatic transformation of kyanite-bearing felsic granulites and the origin of the mafic granulites by transformation of garnet clinopyroxenites due to the metasomatic interaction between kyanite-bearing felsic granulites and garnet clinopyroxenites.

2 Structure of the thesis

This thesis consist of four parts. Each part deals with possible evidences of metasomatic interactions between garnet clinopyroxenites and Ky-bearing felsic granulites at the different scale and methodology.

Part I brings information about behaviour and composition of metasomatizing fluids or melts, which have been captured in the form of few μm large multiphase solid inclusions and mineral phases from the matrix of garnet clinopyroxenites. The work focuses mainly on the compositional trends in Ba, Ti, Cl-rich micas ranging between Ba-rich phlogopite, chloroferrokinoshitalite, and oxykinoshitalite. The documentation of Cl-rich phases including mica with 10.98 wt. % Cl together with carbonates indicates high-Cl and -CO_2 activity and low-H_2O activity in metasomatizing fluids/melts.

Part II describes the metasomatic interaction between cm-sized mantle xenoliths (garnet clinopyroxenite and peridotite) with host felsic granulite in St. Leonhard granulite massif. This research is based on textural analysis across the contact between the xenoliths and the surrounding granulite, thermodynamic modelling, and mineral and local bulk-rock compositions. Based on the obtained results, a new genetic hypothesis for the origin of the intermediate orthopyroxene-bearing granulite by transformation of kyanite-bearing felsic granulite through metasomatic interaction with the mantle xenoliths has been developed.

Part III is focused on the petrological study of the lithologies from the Dunkelsteiner Wald granulite massif containing mantle bodies up to several km across. At the contact of these mantle bodies, the metasomatic interaction between felsic granulites with garnet clinopyroxenites on decametric scale is to be expected. The obtained results support the possible formation of intermediate and mafic granulites by a metasomatic interaction between felsic granulites and garnet clinopyroxenites even on a scale larger than the metasomatic interaction described in Part II.

Part IV builds on the previous Part III and is devoted to the study of the major- and trace-elements whole-rock compositions and Sr–Nd isotopic ratios of selected samples from the Dunkelsteiner Wald granulite massif (Part III). Based on the results, the metasomatic origin of at least some of the intermediate and mafic granulites should be considered as a relevant genetic model.

3 Geological setting

The studied lithologies occur in the St. Leonhard and Dunkelsteiner Wald granulite massifs in Lower Austria. The granulite massif forms part of the Gföhl Unit of the Moldanubian Domain in the Bohemian Massif – the eastern part of the European Variscides (Figure 0. 1). The area of interest with the all studies localities is shown in the Figure 0. 2.

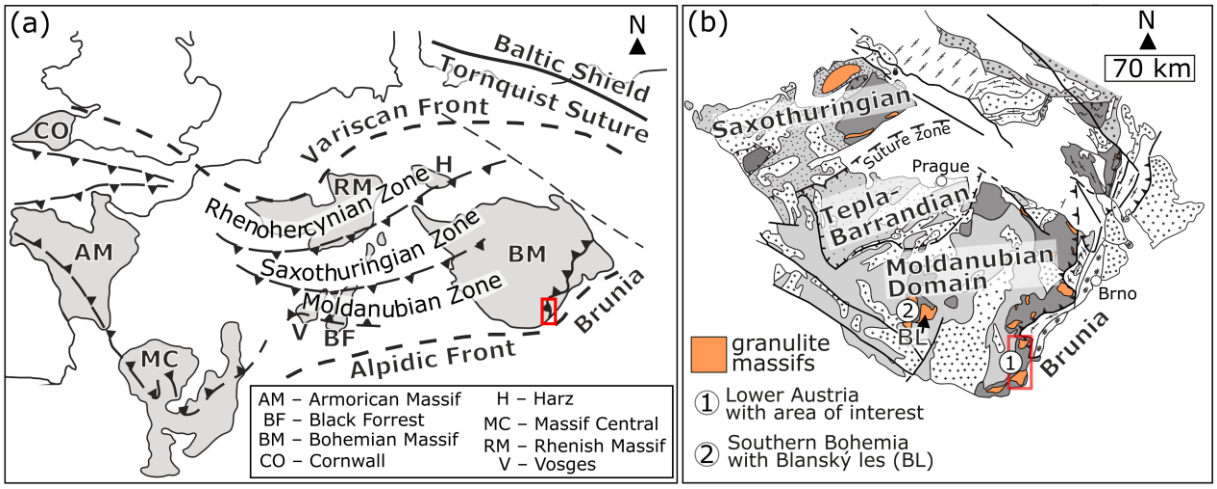

Figure 0. 1: a) European Variscides and b) Bohemian Massif with position of the area of interest: Lower Austria with St. Leonhard and Dunkelsteiner Wald granulite massifs (Figure 0. 2). Modified after Franke (2000) and Schulmann et al. (2014).

3.1 Origin of the Gföhl Unit

The Variscan Bohemian Massif consists, from west to east, of the Saxothuringian, the Moldanubian (high-grade Moldanubian s.s. and generally lower grade to unmetamorphosed Teplá–Barrandian assemblages), and the Brunia domains (Figure 0. 1b; e.g. Schulmann *et al.*, 2009). The spatial arrangement of these domains is interpreted as a consequence of an Andean-type subduction and collision of the Saxothuringian domain with the Teplá–Barrandian (fore-arc) and Moldanubian domains (back-arc), whereas the Brunia domain represented a shortened and thickened region in a back-arc position (Schulmann *et al.*, 2009). The Moldanubian domain consists of the Ostrong Unit (Monotonous Series), the Drosendorf Unit (Variegated Series), and the high-grade metamorphic Gföhl Unit (e.g. Fuchs, 1986).

As first proposed by Janoušek *et al.* (2004) based on the geochemical data, the Moldanubian granulites and Gföhl gneisses developed from the felsic Saxothuringian metaigneous lithologies, deeply subducted under the Moldanubian domain. The crustal material of the lower plate was then partially exhumed and attached to the bottom of the thickened Moldanubian

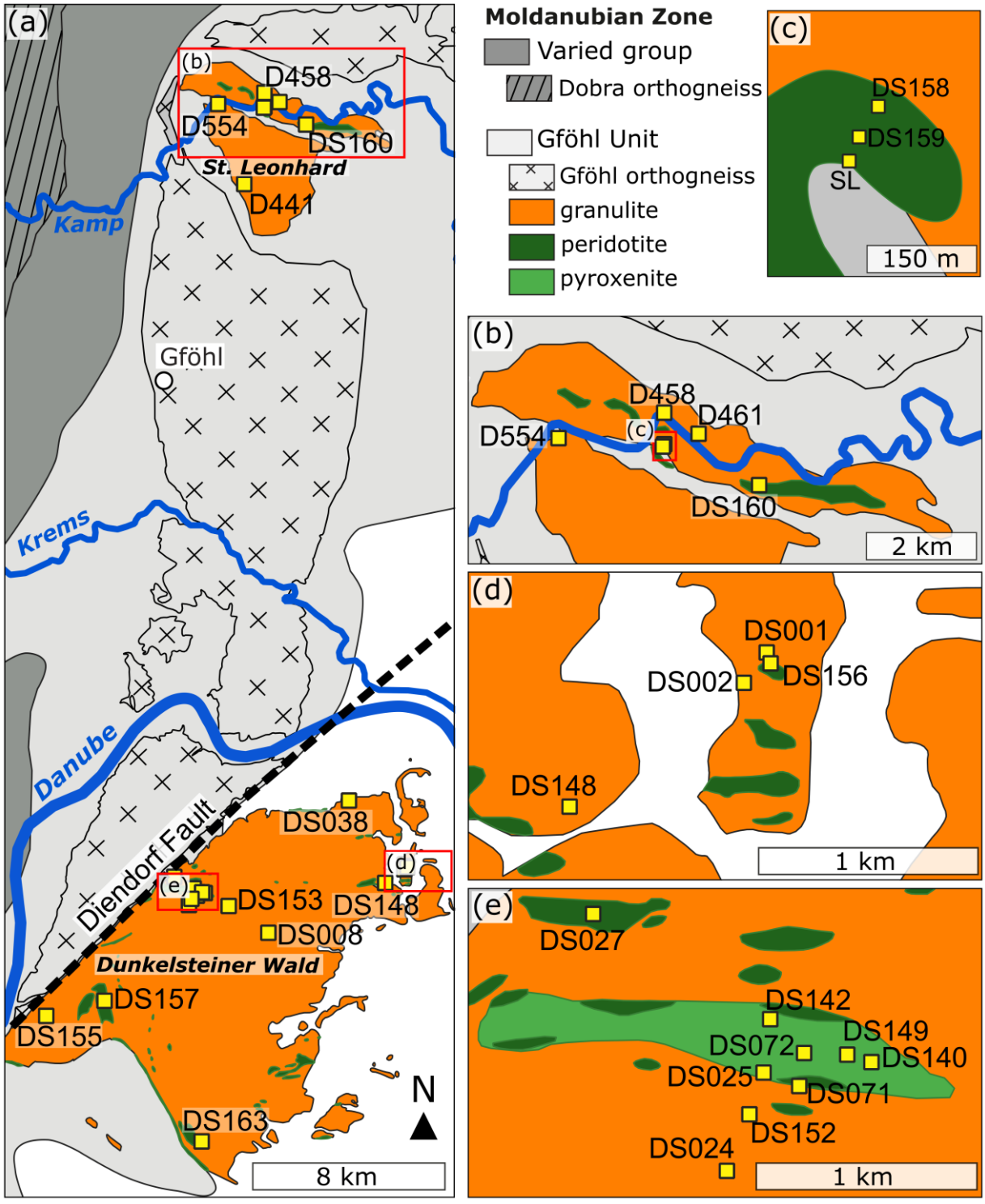

Figure 0. 2: Simplified geological map with the St. Leonhard and Dunkelsteiner Wald granulite massifs with the positions of all studied localities. Modified after Matura (1983); Fuchs & Grill (1984); Fuchs (1984); Schnabel (2002). The position of the studied area within the European Variscides and Bohemian Massif is shown in Figure 0. 1. For the GPS coordinates see Table S. 1.

upper plate (Figure 0. 3; Guy *et al.*, 2011; Schulmann *et al.*, 2014) by a process called relamination (Hacker *et al.*, 2011; Maierová *et al.*, 2018). The transport of the felsic material to the relamination levels at about the Moho depth took place, largely or fully, by return flow through the subduction channel (Lexa *et al*. 2011). The latest theory ascribed an important role to trans-lithospheric diapirs (Maierová *et al.*, 2021). The presence of low-density and partly molten material of Saxothuringian provenance beneath a higher density Moldanubian lower crust caused gravitational instabilities, diapir-like ascent enhanced by the lateral forcing by the Brunia indenter and finally the formation of granulite domes at mid-crustal levels (Franěk *et al.*, 2011; Lexa *et al.*, 2011; Schulmann *et al.*, 2014; Kusbach *et al.*, 2015; Racek *et al.*, 2006).

This relamination model is originally based on the observation that the compositions and ages of the HP–(U)HT granulite and anatectic orthogneiss of the Gföhl Unit resemble Ordovician–Silurian metaigneous rocks preserved in the Saxothuringian Domain (Janoušek *et al.,* 2004; Janoušek & Holub, 2007) and is further supported by independent evidence provided by geophysics (Guy *et al.*, 2011), numerical modelling and petrology (Maierová *et al.*, 2014, 2018; Nahodilová *et al.,* 2020).

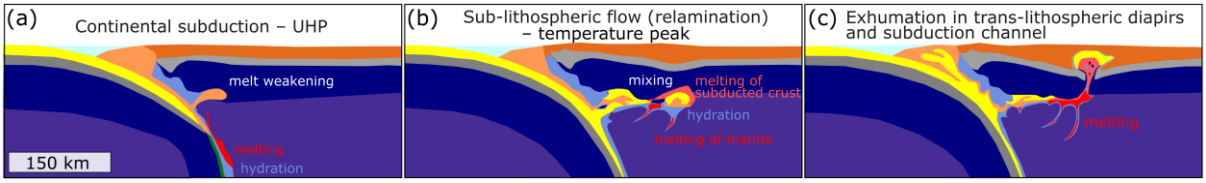

Figure 0. 3: Proposed mechanism of formation of U(HP) felsic rocks (including granulites) connected with the relamination process and diapir ascent adapted after Maierová et al. (2021). a) Continental subduction. b) Sub-lithospheric flow and subduction of mixed crust- and mantle-derived magma. c) Growth of trans-lithospheric diapir and exhumation along the plate interface.

3.2 Granulite massifs of the Gföhl Unit

The granulite massifs of the Gföhl Unit consist predominantly of felsic granulite with the HP–(U)HT mineral assemblage garnet + kyanite + quartz + mesoperthite, where the latter has, partially or fully, been transformed to a K-feldspar + plagioclase mosaic. The granulite massifs are commonly surrounded by Gföhl gneiss – a polydeformed granitic gneiss with transitions to migmatite, which usually contains the mineral assemblage garnet + kyanite + sillimanite + biotite + K-feldspar + plagioclase + quartz + rutile + ilmenite (Petrakakis, 1997; Cooke, 2000; Cooke & O'Brien, 2001; Hasalová *et al.*, 2008; Kusbach *et al.*, 2015). Based on SHRIMP U–Pb dating of inherited zircon from the felsic granulite, the formation of their igneous protoliths

was date at 470–400 Ma and their subsequent high-grade Variscan metamorphism at ~340 Ma (Kröner *et al.*, 2000; Friedl *et al.*, 2011; Kusbach *et al.*, 2015).

The felsic granulite is interpreted as metamorphosed and partly anatectic derivative of felsic metaigneous rocks of Saxothuringian origin subducted beneath the continental root during the Variscan collision (Janoušek *et al.*, 2004, 2007; Janoušek & Holub, 2007; Kotková & Harley, 2010).

3.3 Mantle bodies within granulite massifs

Within the felsic granulite and the Gföhl gneiss occur occasionally garnet- or spinel-bearing, up to several km large peridotite bodies associated with layers or lenses of garnet clinopyroxenite and eclogite (Medaris *et al.*, 1995, 2005; Becker, 1996a, b). These are interpreted as mantle fragments tectonically incorporated during Variscan collision into the Moldanubian crust (Medaris *et al.*, 2006a; Racek *et al.*, 2008; Štípská *et al.*, 2014a; Kusbach *et al.*, 2015; Svojtka *et al.*, 2016). The origin of the garnet clinopyroxenite and eclogite in association with mantle peridotite bodies has been interpreted by: 1) HP–HT crystallization from silicate melts with components of the oceanic crust (Medaris *et al*., 1995, 2013), 2) HP crystal accumulation from transient asthenospheric mantle melts (Becker, 1997; Schmädicke *et al.*, 2010) and/or 3) metasomatism of peridotite by melts derived from a phengite-bearing protolith already present in the peridotite or, more likely, contained in a deeply subducted continental crust.

The latter (metasomatic) hypothesis is corroborated by melt inclusions ("nanogranites") enriched in typical lithophile elements (Borghini *et al.*, 2018, 2020, 2023; Zelinková *et al.*, 2023). Metasomatism of peridotite is also indicated by the occurrence of veins formed by nearly monomineralic, phlogopite-rich rock – glimmerite, whose chemical composition suggests that they were formed by the reaction of granulite-derived ultrapotassic fluids with mantle peridotite (Becker *et al.,* 1999). Further, albeit indirect, evidence of mantle metasomatism is the presence of (ultra-) potassic magmatic rocks spatially and temporally associated with the Moldanubian HP–(U)HT granulite. These (ultra-) potassic magmas were presumably derived from anomalous mantle sources contaminated by Saxothuringian mature crustal material (Janoušek & Holub, 2007; Janoušek *et al.*, 2022).

3.4 Intermediate and mafic granulites

The contact of felsic granulite with mantle fragments is sometimes accompanied by the intermediate and mafic granulite with the mineral assemblage garnet + clinopyroxene +

plagioclase + K-feldspar + orthopyroxene (+ quartz), whereby the width of the transition zone between these lithologies can range from centimetres to tens of meters (Cooke, 2000; Racek *et al*. 2008; Štípská *et al*. 2014a, b). However, this transitional granulite also occurs in places where mantle bodies are unknown. The lithological contacts between mantle bodies and felsic granulite, in places accompanied by the intermediate–mafic granulite, are rarely preserved. This is probably due to intense polyphase deformation (Racek *et al.*, 2006), causing detachment of the intermediate and mafic granulite lithologies from their original positions.

3.5 P–T conditions

The presence of coesite and microdiamond in felsic granulite from the Moldanubian and Saxothuringian domains suggests that at least some of the granulite was subducted to UHP conditions of 850–1100 °C and ~4.5 GPa (Kotková *et al.*, 2011, 2021b; Perraki & Faryad, 2014). Based on thermodynamic modelling and conventional thermobarometry the maximum P–T conditions in the Moldanubian domain were estimated to 1.4–2.3 GPa and 800–1000 °C for felsic granulite, 1.4–1.6 GPa and 800–1050 °C for intermediate granulite, and 1.4–2.3 GPa and 760–1050 °C for mafic granulite, and the decompression conditions for various granulite types were estimated to 0.4–1.3 GPa and 500–910 °C (Carswell & O'Brien, 1993; Cooke, 2000; Kröner et al., 2000; Cooke & O'Brien, 2001; O'Brien & Rötzler, 2003; Medaris *et al.*, 2006b; Racek *et al.*, 2006, 2008; Vrána *et al.*, 2013; Petrakakis *et al.*, 2018). The interaction of felsic granulite with mantle xenoliths in the Blanský les granulite massif was constrained to 950 °C and 1.2 GPa (Štípská *et al.*, 2014a, b).

The peak metamorphic conditions for garnet peridotite were estimated at 2.0–6.0 GPa and 840–1340 °C (Carswell, 1991; Medaris *et al.*, 2005). The equilibration of peridotite from Lower Austria took place at *c.* 3.0–3.5 GPa and 1050–1200 °C (Carswell, 1991; Becker, 1997). Equilibration conditions for garnet pyroxenite associated with peridotite were calculated to ~900 °C and 2.2–3.7 GPa (Faryad *et al*., 2009; Medaris *et al*., 2013). The conditions of the low-P overprint of eclogite was estimated to 1.8–2.0 GPa and 835–935 °C (Medaris *et al*., 2006b).

4 Methodology

This research started with a field-trips which were devoted to systematic sampling and field observations at localities in the vicinity of presumed contacts of felsic granulite with garnet clinopyroxenite bodies. Due to the poor field exposure and the lack of direct contacts of felsic granulites with these bodies (except one locality in St. Leonhard granulite massif, see Part 2),

the research is focused on the petrological and geochemical study of the felsic, intermediate, and mafic granulites and garnet clinopyroxenites present close to these presumed contacts of garnet clinopyroxenite bodies with the host granulite.

A total of 77 localities in Dunkelsteiner Wald and 5 localities in the St. Leonhard granulite massifs were documented, from which approximately 250 rock pieces were sampled for the following research. After a careful study of the thin-sections under an optical microscope, the representative samples were selected for further detailed study of the mineral assemblages, mineral analyses, and local bulk-rock compositions under electron microscope and electron microprobe in the laboratories at the Institute of Petrology and Structural Geology at the Faculty of Science, Charles University. A Tescan Vega Scanning Electron Microscope (SEM) with Oxford Instruments X-Max 50 Energy-Dispersive Spectroscope (EDS) and a Jeol JXA-8530F Field-Emission Gun Electron Probe Micro Analyser (FEG–EPMA) were used for a detailed study of the mineral assemblages and for the acquisition of mineral chemical analyses.

The specific analytical settings and methodology for each Part of this thesis are in the particular Part.

Mineral abbreviations are used according to Whitney & Evans (2010).

$XFe^{2+} = Fe^{2+}/(Fe^{2+} + Mg)$, $XFe^{tot} = Fe^{tot}/(Fe^{tot}+Mg)$, $Alm = Fe^{2+}/(Fe^{2+} + Mg + Ca + Mn) \times 100$, $Prp = Mg/(Mg + Fe^{2+} + Ca + Mn) \times 100$, $Grs = Ca/(Ca + Fe^{2+} + Mg + Mn) \times 100$, $Sps = Mn/(Mn + Fe^{2+} + Mg + Ca) \times 100$, $An = Ca/(Ca + Na + K) \times 100$, $Ab = Na/(Na + Ca + K) \times 100$, $Or = K/(Ca + Na + K) \times 100$, $Jd = Na/(Na + Ca) \times 100$, $CaTs = AlT \times CaM2/(Mg + Fe + Mn + Ca)M2$, p.f.u. = (atoms) per formula unit.

Part I: Ba-Cl rich mineral phases in studied garnet clinopyroxenites – an evidence of metasomatizing fluid/melt

1 Introduction

This Part is focused on the Ba and Cl rich phases that are present in the matrix and in the multiphase solid inclusions (MSI) in garnet and clinopyroxene in garnet clinopyroxenites in Dunkelsteiner Wald and St. Leonhard ganulite massifs. These Ba and Cl- rich mineral phases are exotic for such mantle lithologies, because Ba and Cl are typical crustal components. The research is focused on the origin of these exotic mineral phases and deals with the composition trends in Ba-Ti-Cl rich trioctahedral micas.

1.1 Occurrence and origin of Ba- (Cl-) bearing micas

Ba- and Cl-rich mineral assemblages including Ba-rich micas have been documented from a wide range of crustal lithologies including ore deposits (Pattiaratchi *et al.,* 1967; Jiang *et al.,* 1996; Gnos & Armbruster, 2000), banded iron-formations (Henry & Daigle, 2018; Kullerud, 1995), metacherts (Grapes, 1993), metaexhalites (Oen & Lustenhouwer, 1992), magnetite bearing gneisses (Léger *et al.,* 1996), skarns and marbles (Bol *et al.,* 1989; Tracy, 1991), charnockites and related rocks (Kamineni *et al.,* 1982; Sharygin *et al.,* 2014), olivine nephelinite (Kogarko *et al.,* 2005; Manuella *et al.,* 2012) and MORB derived amphibolite and associated lithologies (Blanco-Quintero *et al.,* 2011). Their formation is mainly related to infiltration of metasomatizing fluid or melt, which may be derived from barite-bearing sediments (e.g. Grapes, 1993; Tracy, 1991), or to hydrothermal alteration of the rocks by fluids or melts associated with ore formation (e.g. Jiang *et al.,* 1996; Henry & Daige, 2018). In magmatic rocks, they may originate from melting of enriched/metasomatized mantle (Kogarko *et al.,* 2005, 2007; Manuella *et al.,* 2012; Lopes & Ulbrich, 2015) or from subducted MORB infiltrated by Ba(-Cl) fluids or melts (Blanco-Quintero *et al.,* 2011).

In mantle lithologies, Ba(-Cl)-rich micas and other Ba(-Cl)-rich phases are rare, but they are known from the matrix of garnet peridotite (Tumiati *et al.,* 2007). These phases specifically occur within multiphase solid inclusions, henceforth referred to as MSI, in garnet or spinel from (U)HP garnet pyroxenites, eclogites, peridotites, and chromitites (Zaccarini *et al.,* 2004; Faryad *et al.,* 2010; Borghini *et al.,* 2018, 2020; Čopjaková & Kotková, 2018; Naemura *et al.,* 2018; Kotková *et al.,* 2021a).

In general, MSI are a type of inclusion up to 100 μm in size interpreted as fluid or melt trapped in crystals during their initial growth or during healing of cracks in preexisting crystals. In

crustal lithologies, MSI may occur as so called nanogranites (Cesare *et al.,* 2011; Ferrero *et al.,* 2015a, 2015b). MSI occur mostly in peak mineral assemblages of (U)HP and (U)HT rocks and are comprised of hydrous aluminosilicate minerals including micas, anhydrous silicates and carbonates, whereas sulphates, sulphides, phosphates, and oxides are less common. Very rarely MSI contain diamond and/or graphite (Frezzotti & Ferrando, 2015 and references therein).

In mantle rocks, Ba(-Cl)-bearing micas are often associated with other silicate, carbonate, and phosphate minerals and are usually interpreted as a result of interaction with metasomatizing LILE and Cl-rich, sometimes potassic carbonatitic fluids or melts derived from a subducting crustal slab (Faryad *et al.,* 2013, Naemura *et al.,* 2018). Furthermore, the metasomatizing agent may be enriched in Mg, Fe, Al, and Cr derived from rocks in the mantle wedge (Tumiati *et al.,* 2007; Naemura *et al.,* 2009, 2018; Borghini *et al.,* 2018, 2020; Čopjaková & Kotková, 2018; Kotková *et al.,* 2021a).

1.2 Trioctahedral Ba(-Cl) bearing micas

The basic building blocks of the crystal structure of mica are represented by layers comprised of one central sheet of octahedrally coordinated cations sandwiched between two sheets of tetrahedrally coordinated cations. The three-sheet layers have a net negative charge and are held together by interlayer cations. A simplified formula of mica can be written as I $M^{VI}_{2–3}$ $□_{1–0}$ T^{IV}_4 O_{10} A_2, where I represents interlayer cations (Cs^{1+}, K^{1+}, Na^{1+}, NH_4^{1+}, Rb^{1+}, Ba^{2+}, Ca^{2+}); M represents octahedrally coordinated cations (Li^{1+}, Fe^{2+}, Fe^{3+}, Mg^{2+}, Mn^{2+}, Mn^{3+}, Zn^{2+}, Al^{3+}, Cr^{3+}, V^{2+}, V^{3+}, Ti^{4+}); □ represents a vacancy; T represents tetrahedrally coordinated cations (Be^{2+}, Al^{3+}, B^{3+}, Fe^{3+}, Si^{4+}); A represents anions (Cl^{1-}, F^{1-}, OH^{1-}, O^{2-}, S^{2-}) (Rieder *et al.,* 1999). Of the octahedrally coordinated lattice sites, two thirds may be filled with trivalent cations or all octahedrally coordinated lattice sites may be filled with divalent cations, giving rise to dioctahedral and trioctahedral micas, respectively.

In trioctahedral micas, K–Ba substitution at the interlayer I position connects the phlogopite-annite series with Ba-micas and is coupled with Al–Si substitution at the T position: $Ba^{2+}+Al^{3+}\leftrightarrow(K^{1+},Na^{1+})+Si^{4+}$ (Tischendorf *et al.,* 2007). If the Ba content exceeds 0.5 atoms per formula unit (p.f.u.), the mica is classified as kinoshitalite (Mg-rich end-member) or ferrokinoshitalite, where Mg is replaced by Fe in the M position (Guggenheim & Frimmel, 1999). In oxykinoshitalite, the K–Ba substitution is accompanied by the exchange $Ti^{4+}+2O^{2-}\leftrightarrow Mg^{2+}+2(OH,F)^{1-}$ (Kogarko *et al.,* 2005). With increasing Cl content on the A position, the transition from ferrokinoshitalite to chloroferrokinoshitalite occurs. Mica with a composition

of chloroferrokinoshitalite with Cl occupying more than 0.5 of the A position was previously described (Tracy, 1991), although it was misidentified as anandite – Ba-bearing mica that contains predominantly S on the A position (Filut *et al.,* 1985; Pattiaratchi *et al.,* 1967). Another Ba-rich dioctahedral brittle micas is chernykhite, where the M position is rich in V (Ankinovich *et al.,* 1973). The composition of the micas mentioned above and the assignments to structural positions are shown in Table I. 1.

The following text documents the occurrence of Ba(-Cl)-rich trioctahedral micas and related exotic phases including Cl-rich phosphates with carbonates and other silicate phases in MSI hosted by garnet and clinopyroxene as well as in the matrix of mantle-derived garnet clinopyroxenites. Detailed evaluation of a large set of mica analyses involving compositions so far not described from natural samples allows identification of the main substitution mechanisms and compositional correlations that help to better constrain the factors controlling such uncommon mica compositions. The study of mineral assemblages extremely enriched in Ba, Cl, and CO_2 can shed light on the character of metasomatic agents that affect mantle rocks during orogenic processes.

Table I. 1: Structural formulae of mica end-members that can be used for defining the substitutions related to the transition between phlogopite/annite and Ba-micas.

Position:	***I***	***M^{VI}***	***T^{IV}***	***O***	***A***
Phlogopite	K	Mg_3	$AlSi_3$	O_{10}	$(OH)_2$
Annite	K	$Fe^{2+}{}_3$	$AlSi_3$	O_{10}	$(OH)_2$
Kinoshitalite	Ba	Mg_3	Al_2Si_2	O_{10}	$(OH)_2$
Fluorokinoshitalite	Ba	Mg_3	Al_2Si_2	O_{10}	F_2
Ferrokinoshitalite	Ba	$Fe^{2+}{}_3$	Al_2Si_2	O_{10}	$(OH)_2$
Oxykinoshitalite	Ba	Mg_2Ti^{4+}	Al_2Si_2	O_{10}	O_2
Chloroferrokinoshitalite	Ba	$Fe^{2+}{}_3$	Al_2Si_2	O_{10}	Cl_2
Anandite	Ba	$Fe^{2+}{}_3$	$Fe^{3+}Si_3$	O_{10}	S(OH)
Chernykhite	Ba	$V^{3+}{}_2$	Al_2Si_2	O_{10}	$(OH)_2$

2 Methods

Mineral assemblages involving Ba- and Cl- rich phases were documented in 10 polished thin sections of garnet clinopyroxenites collected from five localities (DS025, DS072, DS142,

DS148, SL; for the locations see Figure 0. 2 and Table S. 1 in Supplementary Material). Representative chemical analyses of Ba-, Ti-, and Cl- rich micas are given in Table I. 2 and representative chemical analyses of phosphates are given in Table I. 3. All analyses of Ba-, Ti-, and Cl-rich micas (Table S. 2); and silicates, and carbonates in MSI (Table S. 3). A total of 100 mica analyses were taken, 22 from micas in the matrix, 73 from micas hosted by garnet, and 5 from MSIs hosted by clinopyroxene. The recalculation of cations/anions in the structural positions of the micas (Table S. 2): TAl = Al – (Al + Si – 4), IAl = (Si + Al – 4; values less than 0 → 0), O = Ti × 2, and OH = 2 – Cl – F – O.

Micas were analysed with an accelerating voltage of 15 kV and a probe current of 12 nA with the electron beam defocused to 2–5 μm (depending on crystal size); phosphates and carbonates were analysed at 15 kV and 10 nA with the electron beam defocused to 2–5 μm; garnet was analysed at 15 kV and 40 nA with a focused 1 μm electron beam spot; other minerals were analysed at 15 kV and 20 nA with the electron beam defocused to 2–5 μm for scapolite and plagioclase and focused for other phases. The following standards consisting of natural or synthetic phases with certified compositions were used for quantitative analyses: topaz (F), albite (Na), periclase (Mg), corundum (Al), quartz (Si), apatite (P), anhydrite (S), tugtupite (Cl), sanidine (K), diopside (Ca), rutile (Ti), vanadium (V), chromium oxide (Cr), rhodonite (Mn), magnetite (Fe), willemite (Zn), celestite (Sr), baryte (Ba), LaP_5O_{14} (La), and CeP_5O_{14} (Ce). Kα lines of the characteristic X-rays were used for detection and quantification of all elements, except for Ba, Sr, La, and Ce where Lα lines were used. The ZAF method was applied for matrix correction. Due to the interference of the TiKα and BaLα peaks, correction of the peak intensities was performed based on the coefficients defined by the analysis of the Ti and Ba standards (rutile and baryte). Chemical analyses of garnet were calculated to 12 O atoms/8 cations, pyroxenes on 6 O atoms/4 cations, feldspar on 8 O atoms/5 cations, spinel on 4 O atoms/3 cations, apatite on 12.5 O atoms/8 cations, goryainovite on 4.5 O atoms/3 cations, cordierite on 18 O atoms/11 cations, sapphirine on 20 O atoms/14 cations and margarite on 11 O atoms/7cations. Amphiboles were calculated on 23 O atoms with the methodology of Locock (2014) modified by the addition of BaO to oxides. Scapolite was normalized to (Si + Al) = 12 apfu after Teertstra and Sherriff (1997). Micas that form solid solutions between phlogopite/annite and Ba-bearing trioctahedral micas contain 8 cations, but their charge is not constant. While most end-members have charge 22, oxykinoshitalite has charge 24 due to the $OH^- \leftrightarrow O^{2-}$ substitution. Therefore, all Ba-bearing mica analyses were recalculated to 8 cations.

3 Results

3.1 Sample description

Although the garnet clinopyroxenites studied come from different localities, they generally show a common feature in the form of remnants of the primary mineral assemblage comprising garnet porphyroblasts with rare inclusions of clinopyroxene and kyanite, and preserved clinopyroxene grains in a fine to medium-grained matrix. Summary petrographic description of garnet clinopyroxenites is given in the chapter 1.1.4 in the Part III (Detailed description of each sample from which the Ba-Cl phases are described in Zelinková et al., 2023, the original paper; also available in the online materials of this thesis).

Ba- and Cl-rich silicates including micas and phosphate minerals, are present in the matrix as single grains most often in fine-grained symplectites at the contact with garnet, or they occur in small garnet-hosted MSI together with carbonates. More rarely, they can also be found in MSI hosted by clinopyroxene that typically also show orthopyroxene exsolution lamellae.

3.2 Ba-Cl-rich mineral phases in the matrix

Ba-rich mica associated with celsian and Cl-rich apatite is present in the matrix, where it is mostly in contact with garnet (Figure I. 1a–c) and forms relatively large crystals, up to 0.3 mm in size. In some cases, this mica shows compositional zoning, which can be inferred from relatively bright BSE contrast at the rims and brightness variations across the cleavage (Figure I. 1a, b).

The compositional range of Ba-rich micas in the matrix is XFe^{tot} = 0.07–0.21; K = 0.5–0.7, Ba = 0.1–0.3, Mg = 1.9–2.4, Fe^{tot} = 0.2–0.5, Ti = 0.2–0.4, Si = 2.5–2.8, Al = 1.5–1.7, Cl = 0.0–0.1 (p.f.u) (Table I. 2, Table S. 2). Domains with relatively bright BSE contrast are relatively rich in Fe^{tot}, Ba, and Cl with representative compositions of XFe^{tot} = 0.21; K = 0.5, Ba = 0.3, Mg = 1.9, Fe^{tot} = 0.5, Ti = 0.4, Si = 2.6, Al = 1.6, Cl = 0.0 (p.f.u) compared to domains with comparatively dark BSE contrast, where compositions are XFe^{tot} = 0.15; K = 0.7, Ba = 0.1, Mg = 2.1, Fe^{tot} = 0.4, Ti = 0.3, Si = 2.7, Al = 1.5, Cl = 0.0 (p.f.u). Apatite with compositions in the range of Ca = 4.8–4.9, Sr = 0.0–0.1, P = 3.0–3.0, Cl = 0.5–0.7, F = 0.1–0.2 (p.f.u) corresponds to a solid solution between hydroxyapatite and Cl-apatite with low F content (Table I. 3). Celsian has compositions of Ba = 0.7–0.9, K ~0.1, Ca = 0.0–0.1, Na = 0.0–0.1, Al ~1.8, Si ~2.1 (p.f.u).

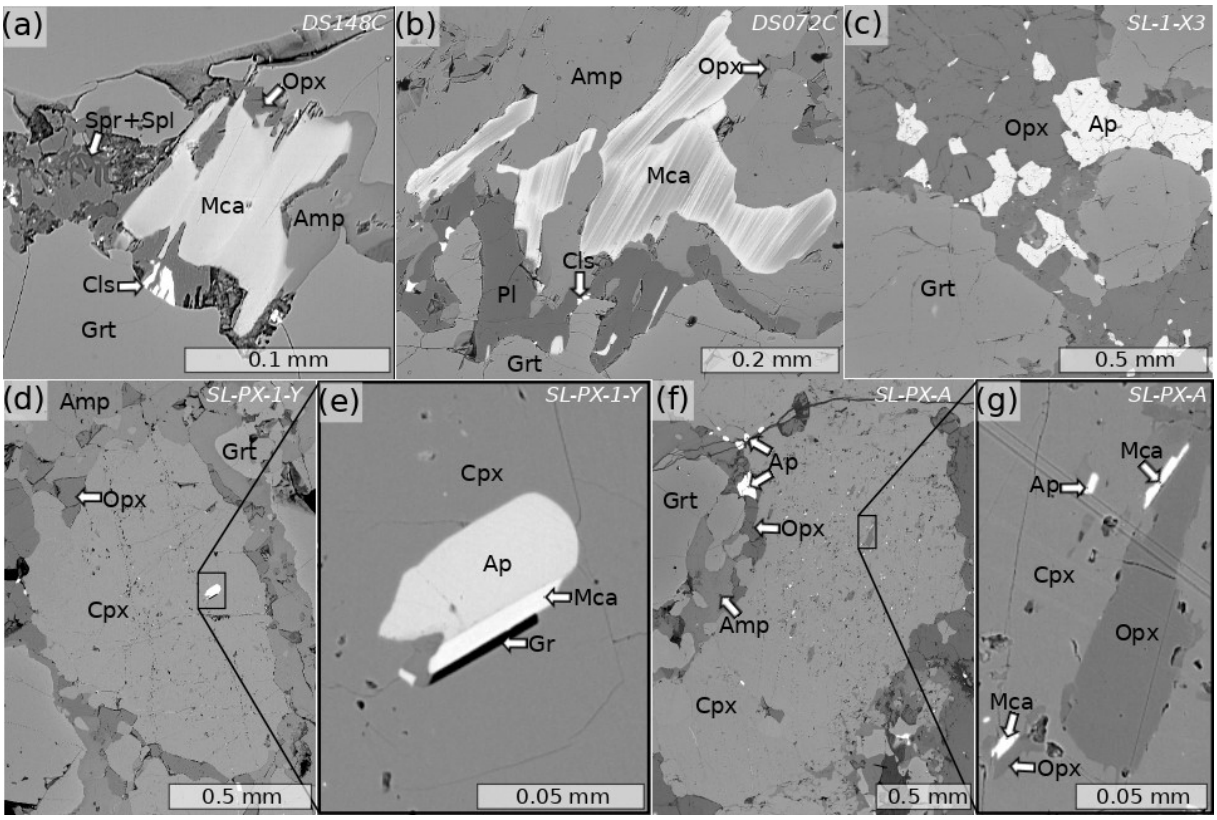

Figure I. 1: Ba(-Cl)-rich mineral phases in the matrix and in clinopyroxene. a) Mica with celsian in fine-grained symplectite of sapphirine, spinel, orthopyroxene, and amphibole between garnet grains. b) Zoned mica with celsian, plagioclase and amphibole close to garnet. c) Apatite in the matrix with orthopyroxene and garnet. d) Clinopyroxene containing MSI. e) Detail of MSI comprising apatite, graphite, and mica. f) Clinopyroxene with large amounts of MSI and orthopyroxene lamellae. g) Detail of orthopyroxene lamella associated with mica and apatite.

3.3 Ba-Cl-rich mineral phases in clinopyroxene

Ba-mica and Cl-apatite are present as inclusions in clinopyroxene or are found in association with orthopyroxene exsolution lamellae (Figure I. 1d–g). In some cases, graphite is also present in these multiphase inclusions (Figure I. 1e).

The micas have compositions of XFe^{tot} = 0.21–0.30; K ~0.4, Ba = 0.4–0.5, Mg = 1.8–2.0, Fe^{tot} = 0.5–0.8, Ti = 0.3–0.4, Si = 2.5–2.6, Al = 1.5–1.6, Cl = 0.2–0.3 (p.f.u) (Table I. 2, Table S. 2). Apatite with compositions of Ca = 4.7–4.8, Sr ~0.1, P = 2.9–3.0, Cl = 0.9–1.0, F~0.0 (p.f.u) corresponds to Cl-apatite with a minor hydroxyapatite component and a negligible F content (Table I. 3). Orthopyroxene exsolution lamellae associated with mica have compositions of

XFe^{2+} ~0.14. Amphibole associated with mica in MSI has a pargasitic composition with XFe^{2+} ~ 0.15; Ba ~0.0, Ti ~0.2, Cl ~0.5, Si ~6.3 (p.f.u) (Table S. 3).

3.4 Garnet-hosted polyphase inclusions containing Ba-Cl-rich minerals

Inclusions rich in carbonate minerals such as dolomite, calcite, and magnesite often form narrow chains crosscutting garnet crystals (Figure I. 2). Carbonate-rich inclusions are up to 15 µm in size and often have a hexagonal shape, indicating that they have a negative crystal shape controlled by the host garnet. They are sometimes accompanied by 3–60 µm sized MSIs, which are dispersed across all parts of the garnet. They do not form clusters (Figure 4a) or show any kind of systematic relation to the garnet zones (core or rim) nor do they correlate with the compositional zoning of garnet. Common mineral phases in these inclusions are Cl-rich apatite, monazite, dolomite, magnesite, amphibole, orthopyroxene, clinopyroxene, spinel, and Ba- (Ti-, Cl-) rich mica. Rarely, scapolite, aspidolite, cordierite, muscovite, goryainovite, celsian, norsethite, scheelite, epidote, and SiO_2 and Al_2SiO_5 polymorphs occur in these MSIs. All these phases can occur in various combinations and form intergrows with each other (Figure I. 2b–j).

Orthopyroxene is rich in enstatite with XFe^{2+} = 0.07–0.09. Clinopyroxene is highly variable in composition and can locally contain considerably elevated amounts of Na and Al. Its composition mostly corresponds to the range from augite to diopside to omphacite: $CaTs_{3.9–20.5}Jd_{3.2–25.3}$; XFe^{2+} = 0.08–0.10. In spinel, Al-end-members prevail with XFe^{2+} = 0.20–0.44; Al = 0.9–2.0, Cr ~0.0 (p.f.u). The compositional range of amphibole varies from sadanagait to tschermakite to pargasite: XFe^{tot} = 0.09–0.30; Ba = 0.0–0.2, Ti = 0.1–0.3, Cl = 0.1–0.8, Si = 5.4–6.1 (p.f.u). The other phases have the following compositions: cordierite: XFe^{2+} ~0.29, scapolite: K ~0.0, Na ~0.7, Ca ~3.0, Cl ~0.2, Al ~5.2, Si ~6.8 (p.f.u), margarite: Ca ~0.7, Na ~0.2, K ~0.0 (p.f.u.), celsian: Ba = 0.7–0.9, K = 0.0–0.1, Ca ~0.0, Na = 0.0–0.1, Si = 2.0–2.2, Al = 1.8–1.9 (p.f.u). Their representative chemical compositions are given in Online Materials (Table S. 3).

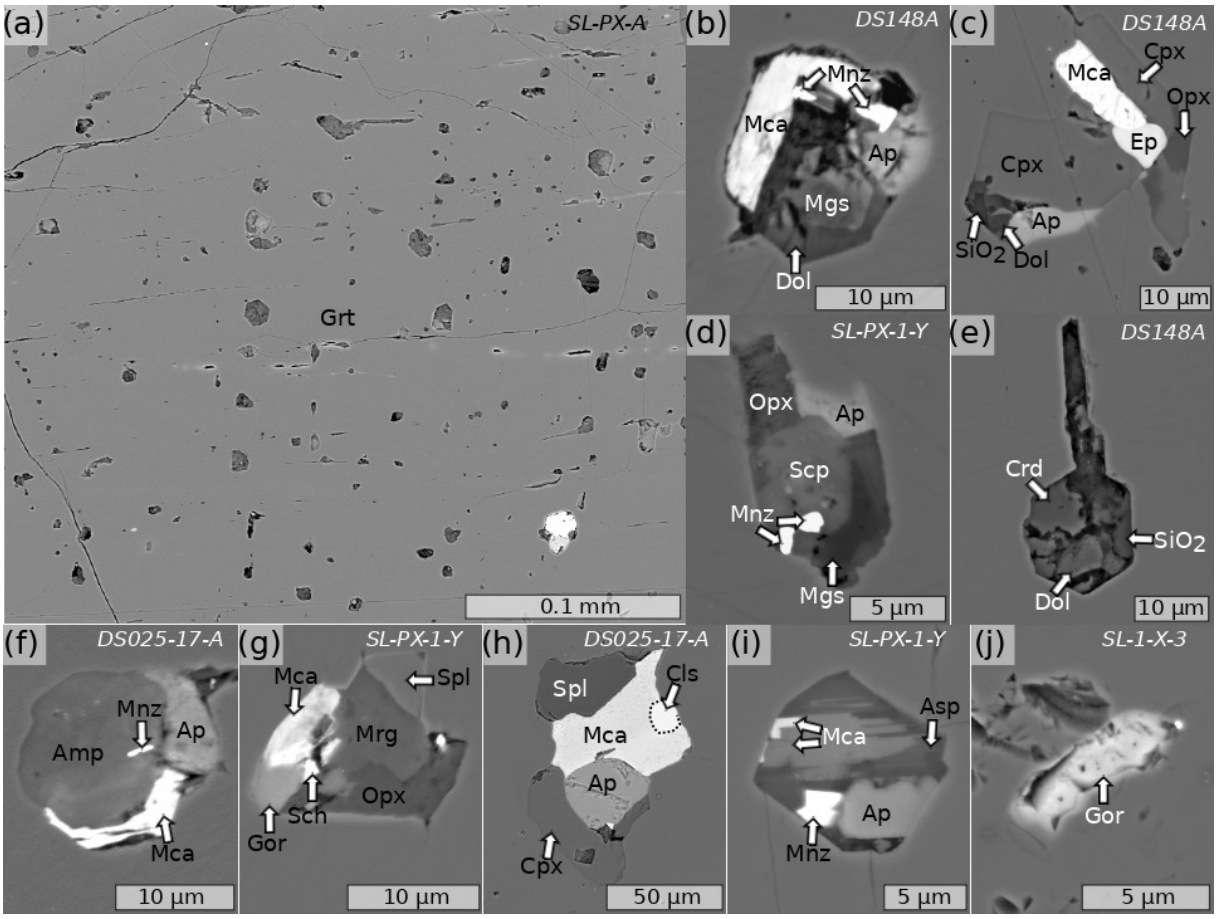

Figure I. 2: Multiphase solid inclusions (MSI) in garnet. a) Part of a garnet porphyroblast with chains of carbonate-rich inclusions accompanied by MSI. b) MSI containing dolomite, magnesite, apatite, mica, and monazite. c) MSI containing undefined SiO_2 polymorph, dolomite, apatite, clinopyroxene, epidote, and orthopyroxene. d) MSI containing orthopyroxene, scapolite, apatite, monazite, and magnesite. e) MSI containing cordierite, dolomite, and undefined SiO_2 polymorph. f) MSI containing amphibole, monazite, apatite, and mica. g) MSI with mica, margharite, apatite, clinopyroxene, spinel, scheelite and celsian. i) MSI of mica, apatite, monazite, and aspidolite. j) Inclusion of goryainovite.

Table I. 2: Representative chemical analyses in wt. % of Ba-, Cl- and Ti-rich micas.

Mineral	Mica											
Position		matrix		MSI in Cpx					MSI in Grt			
Sample	DS072C	DS072C	DS148C	SL-PX-A	SL-PX-A	SL-PX-1-Y	DS025	DS148A	DS148A	DS025-17A	SL-PX-1-Y	SL-PX-1-Y
Analysis	Mca-12	Mca-11	Mca-03	Mca-13	Mca-11	Mca-12	Mca-29	Mca-M05	Mca-M40	Mca-21	Mca-60	Mca-65
SiO_2	36.58	32.04	34.66	29.81	30.37	30.05	38.65	25.25	23.53	21.99	20.70	18.93
TiO_2	4.82	7.10	3.80	5.96	5.76	5.28	1.76	10.01	12.55	8.37	0.05	0.07
P_2O_5	b.d.	b.d.	b.d.	b.d.	b.d.	0.04	b.d.	b.d.	b.d.	b.d.	0.11	0.11
Al_2O_3	17.09	17.52	18.38	16.53	15.29	16.28	21.37	17.05	18.93	17.16	15.43	15.20
Cr_2O_3	0.15	0.25	0.43	0.77	0.56	0.34	b.d.	0.08	0.06	0.21	0.02	0.02
V_2O_3	0.04	b.d.	0.10	b.d.	0.06	b.d.	0.13	b.d.	b.d.	b.d.	b.d.	b.d.
FeO	5.92	7.28	2.76	9.27	10.79	8.16	3.31	9.44	8.25	12.70	24.99	30.15
MnO	b.d.	b.d.	b.d.	0.02	b.d.	b.d.	b.d.	b.d.	b.d.	b.d.	b.d.	0.03
MgO	19.15	15.79	21.15	14.43	13.95	16.10	22.42	12.21	9.16	9.47	5.98	2.34
BaO	3.17	10.35	6.59	13.35	12.85	13.87	2.95	19.20	22.27	24.48	21.57	22.76
SrO	0.19	0.15	0.12	0.14	0.19	0.16	–	0.20	0.19	0.16	0.83	0.00
CaO	0.04	0.09	0.05	0.21	0.34	0.39	0.10	0.26	0.24	0.30	0.75	0.17
K_2O	7.74	5.37	7.28	3.71	3.91	3.79	4.65	1.89	1.16	0.05	0.61	0.19
Na_2O	0.94	0.64	0.42	0.70	0.45	0.66	0.69	0.40	0.28	0.39	0.13	0.05
F	b.d.	b.d.	b.d.	b.d.	b.d.	b.d.	b.d.	b.d.	b.d.	b.d.	b.d.	b.d.
Cl	0.14	0.23	0.36	1.67	2.05	1.33	0.26	0.14	0.69	3.13	10.04	10.98
Total	95.83	96.57	95.75	94.89	94.51	95.12	96.01	95.98	96.61	95.27	91.17	90.02
	Calculated on 8 cations											
Si	2.73	2.56	2.61	2.50	2.57	2.49	2.81	2.24	2.16	2.09	2.08	2.01
Ti	0.27	0.43	0.21	0.38	0.37	0.33	0.10	0.67	0.87	0.60	0.00	0.01
P	0.00	0.00	0.00	0.00	0.00	0.00	0.00	0.00	0.00	0.00	0.01	0.01
Al	1.50	1.65	1.63	1.63	1.53	1.59	1.83	1.78	2.05	1.92	1.83	1.91
Cr	0.01	0.02	0.03	0.05	0.04	0.02	0.00	0.01	0.00	0.02	0.00	0.00
V	0.00	0.00	0.01	0.00	0.00	0.00	0.01	0.00	0.00	0.00	0.00	0.00
Fe^{tot}	0.37	0.49	0.17	0.65	0.77	0.57	0.20	0.70	0.63	1.01	2.10	2.68
Mn	0.00	0.00	0.00	0.00	0.00	0.00	0.00	0.00	0.00	0.00	0.00	0.00
Mg	2.13	1.88	2.37	1.81	1.76	1.99	2.43	1.62	1.26	1.34	0.90	0.37
Ba	0.09	0.32	0.19	0.44	0.43	0.45	0.08	0.67	0.80	0.91	0.85	0.95
Sr	0.01	0.01	0.01	0.01	0.01	0.01	–	0.01	0.01	0.01	0.05	0.00
Ca	0.00	0.01	0.00	0.02	0.03	0.03	0.01	0.03	0.02	0.03	0.08	0.02
K	0.74	0.55	0.70	0.40	0.42	0.40	0.43	0.21	0.14	0.01	0.08	0.03
Na	0.14	0.10	0.06	0.11	0.07	0.11	0.10	0.07	0.05	0.07	0.02	0.01
F	0.00	0.00	0.00	0.00	0.00	0.00	0.00	0.00	0.00	0.00	0.00	0.00
Cl	0.02	0.03	0.05	0.24	0.29	0.19	0.03	0.02	0.11	0.50	1.71	1.98
XFe^{tot}	0.15	0.21	0.07	0.26	0.30	0.22	0.08	0.30	0.34	0.43	0.70	0.88

– not measured, b.d. below detection limit

Table I. 3: Representative chemical analyses in wt. % of apatite and goryainovite.

Mineral					**Apatite**						**Goryainovite**	
Position	matrix				MSI in Cpx		MSI in Grt					
Sample	DS148C	SL-1-X-3	SL-PX-1-Y	DS148C	SL-1-X-3	SL-PX-1-Y	SL-1-X-3	SL-PX-1-Y	DS142C	SL-PX-1-Y	SL-1B-I	SL-1-X-3
Analysis	Ap-08	Ap-05	Ap-20	Ap-09	Ap-03	Ap-18	Ap-02	Ap-07	Ap-35	Ap-23	Gor-02	Gor-04
SiO_2	0.18	0.46	0.30	0.27	1.10	0.36	0.55	0.71	0.24	0.87	0.55	0.58
P_2O_5	41.91	40.73	40.57	41.36	40.28	39.91	40.99	38.02	39.22	39.06	33.11	32.41
FeO	0.26	0.21	0.29	0.11	0.20	0.13	0.31	0.58	0.38	0.49	0.54	0.69
MnO	b.d.	b.d.	b.d.	b.d.	b.d.	b.d.	b.d.	b.d.	b.d.	b.d.	b.d.	b.d.
MgO	0.10	0.15	0.21	0.08	0.77	0.03	0.22	0.15	0.07	0.05	0.28	0.18
SrO	b.d.	0.93	0.60	0.30	2.20	1.56	2.14	3.35	8.75	2.90	0.44	2.54
CaO	53.91	52.57	52.47	53.17	50.97	51.11	52.79	47.54	46.96	50.64	55.22	50.59
La_2O_3	–	–	0.41	–	–	0.53	0.20	1.78	0.47	0.58	b.d.	b.d.
Ce_2O_3	–	–	0.54	–	–	0.62	0.34	1.96	0.44	1.08	b.d.	b.d.
Na_2O	0.06	0.28	0.20	0.10	0.09	0.16	b.d.	0.24	0.12	b.d.	b.d.	0.06
F	0.91	0.54	0.57	0.27	0.03	b.d.	0.98	0.15	b.d.	b.d.	b.d.	b.d.
Cl	3.28	3.44	3.60	4.85	6.22	6.50	1.09	5.68	6.54	7.25	12.32	13.38
total	96.41	95.33	95.59	95.38	95.62	94.40	97.54	94.32	96.64	95.68	90.14	87.05
					Calculated on 12.5 oxygens						**Calculated on 4.5 O**	
Si	0.02	0.04	0.03	0.02	0.09	0.03	0.05	0.06	0.02	0.08	0.02	0.02
P	3.01	2.98	2.98	3.01	2.94	2.98	2.96	2.92	2.97	2.92	0.97	0.95
Fe^{tot}	0.02	0.02	0.02	0.01	0.01	0.01	0.02	0.04	0.03	0.04	0.02	0.02
Mn	0.00	0.00	0.00	0.00	0.00	0.00	0.00	0.00	0.00	0.00	0.00	0.00
Mg	0.01	0.02	0.03	0.01	0.10	0.00	0.03	0.02	0.01	0.01	0.01	0.01
Sr	0.00	0.05	0.03	0.01	0.11	0.08	0.11	0.18	0.45	0.15	0.01	0.05
Ca	4.90	4.87	4.87	4.89	4.72	4.83	4.82	4.62	4.50	4.78	2.05	1.88
La	–	–	0.01	–	–	0.02	0.01	0.06	0.02	0.02	0.00	0.00
Ce	–	–	0.02	–	–	0.02	0.01	0.07	0.01	0.03	0.00	0.00
Na	0.01	0.05	0.03	0.02	0.02	0.03	0.00	0.04	0.02	0.00	0.00	0.00
F	0.24	0.15	0.16	0.07	0.01	0.00	0.26	0.04	0.00	0.00	0.00	0.00
Cl	0.47	0.50	0.53	0.71	0.91	0.97	0.16	0.87	0.99	1.08	0.73	0.79
XFe^{tot}	0.61	0.44	0.43	0.44	0.13	0.68	0.44	0.68	0.75	0.83	0.52	0.68

– not measured, b.d. below detection limit

Apatite has a composition of Ca = 4.5–5.0, Sr = 0.0–0.5, P = 2.8–3.0, Cl = 0.2–1.1, F = 0.0–0.3 (p.f.u). With an average content of Cl = 0.8 p.f.u., apatite classified as chlorapatite prevails. The composition range of goryainovite is Ca = 1.9–2.0, Sr = 0.0–0.1, P ~1.0, Cl = 0.7–0.8 (p.f.u). The highest Sr content in goryainovite is 2.5 wt. % (Table I. 3).

Micas from MSI have compositions in the range XFe^{tot} = 0.08–0.94; K = 0.0–0.6, Ba = 0.1–0.9, Mg = 0.2–2.4, Fe^{tot} = 0.2–2.7, Ti = 0.0–0.9, Si = 2.0–2.9, Al = 1.5–2.1, Cl = 0.0–2.0 (p.f.u) (Table I. 2, Table S. 2), where Ba predominates over K and are enriched in Cl or Ti. Further details on the compositional correlations in mica are presented in the discussion.

Chemical analyses for the norsethite, scheelite, aspidolite, muscovite, epidote and Al_2SiO_5 polymorph are not given, because they were too small for quantitative analysis, although they were identified based on energy dispersive spectra (EDS).

4 Discussion

4.1 Substitution mechanisms and compositional correlations in micas

The chemical compositions of all micas analysed (Table S. 2) are plotted in element covariation diagrams, where various substitution trends and correlations are visible with regard to XFe^{tot} and microstructural position (Figure I. 3).

$Ba^{2+}Al^{3+}\leftrightarrow K^{1+}Si^{4+}$ substitution. This substitution is inferred from the negative correlation of Ba with Si and K and from the positive correlation of Ba with Al (Figure I. 4). A coupled substitution is required to maintain charge balance. This substitution links Ba-free end-members such as phlogopite to micas bearing Ba such as kinoshitalite, ferrokinoshitalite, chloroferrokinoshitalite, or oxykinoshitalite. The structural formulae of all mica end-members are shown in Table I. 1. The $Ba^{2+}Al^{3+}\leftrightarrow K^{1+}Si^{4+}$ substitution has already been described in previous works (e.g. Čopjaková & Kotková, 2018; Grapes, 1993; Kogarko *et al.,* 2005).

$Ti^{4+}2O^{2-}\leftrightarrow(Fe,Mg)^{2+}2(OH,Cl)^{1-}$substitution. This substitution is inferred from the fact that some mica analyses show variably elevated Ti contents of up to 12.55 wt. % TiO_2 corresponding to 0.87 p.f.u. Ti (Table I. 2). The Ti content is negatively correlated with the total of Mg + Fe, while there is no correlation of Ti with Si and Al. The slope of the correlation between Ti and Mg + Fe is close to -1 over almost the entire range of observed Ti contents. Only at the lowest Ti content below 0.1 p.f.u. the slope changes abruptly to about –4 (see Figure I. 3).

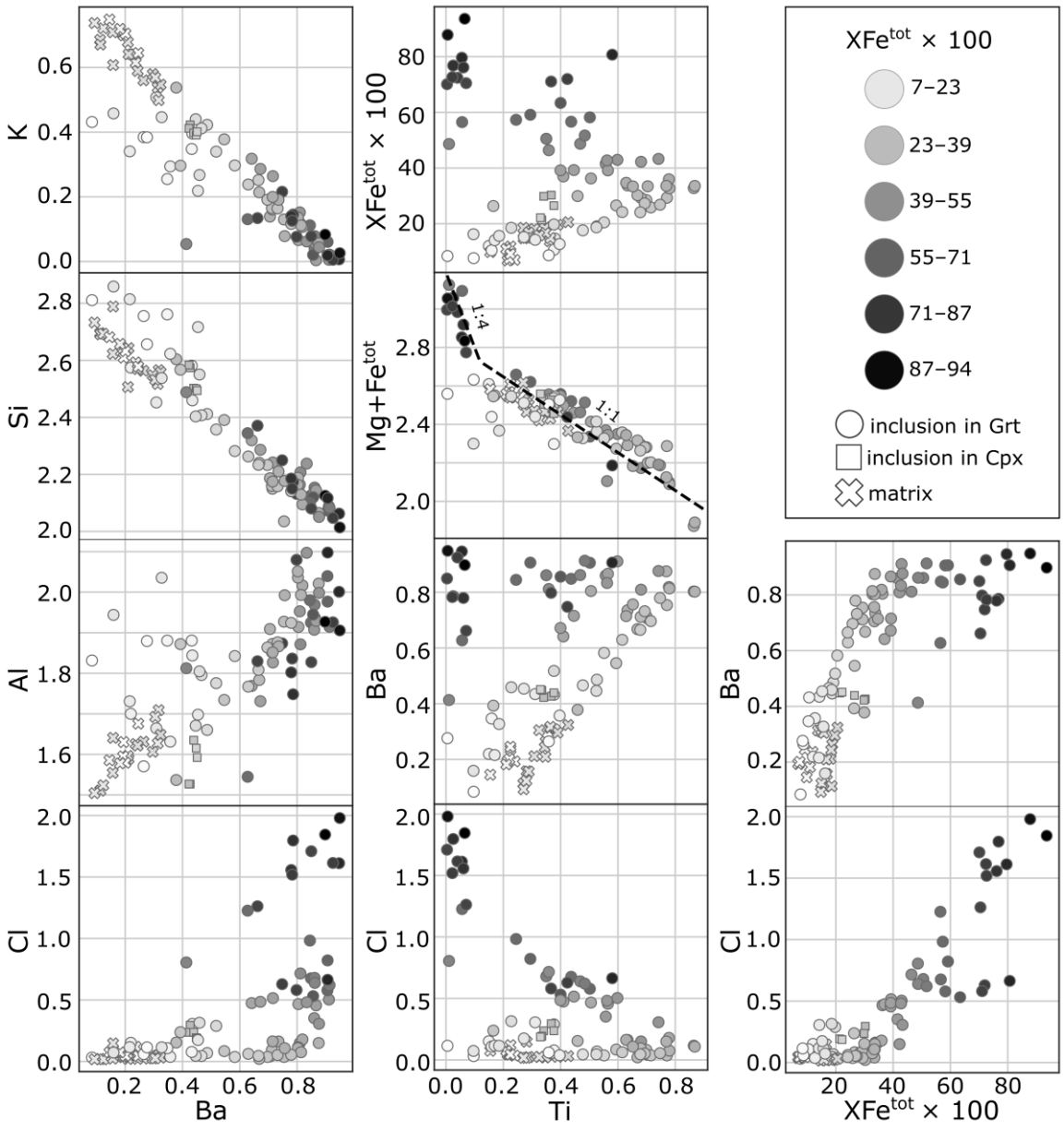

Figure I. 3: Main compositional trends of Ba(-Cl) rich micas from garnet clinopyroxenites with respect to the XFe^{tot} and textural position.

Several substitution schemes may explain the incorporation of Ti into phlogopite (Dymek, 1983; Henry & Guidotti, 2002; Kogarko *et al.*, 2005):

1) Ti-Tschermak's: $(M^{2+})^{VI}+2(Si^{4+})^{IV}\leftrightarrow(Ti^{4+})^{VI}+2(Al^{3+})^{IV}$
2) Ti-vacancy: $2(M^{2+})^{VI}\leftrightarrow(Ti^{4+})^{VI}+\square^{VI}$
3) Ti-oxy: $(M^{2+})^{VI}+2OH^{-}\leftrightarrow(Ti^{4+})^{VI}+2O^{2-}$
4) Ti-M^{2+} $2(Al^{3+})^{VI}\leftrightarrow(Ti^{4+})^{VI}+(M^{2+})^{VI}$

Based on the negative correlation between Ti and Mg + Fe^{tot} with a slope indicating a 1:1 substitution, we suggest that the Ti-oxy substitution predominates in the analysed micas. By

contrast, a correlation with Al or Si is absent, excluding the Ti-Tschermak substitution. Consequently, this substitution allows to calculate the O content of the mica (Ti in p.f.u. multiplied by 2), which is equal to 1.74 p.f.u. in the most Ti-rich mica from the studied samples.

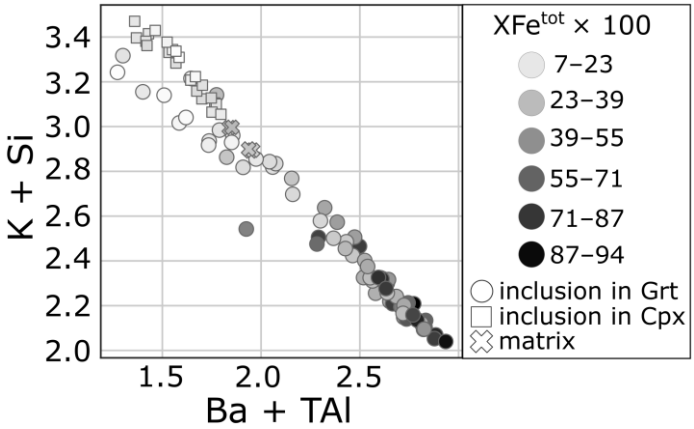

Figure I. 4: Compositional trend corresponding to substitution $Ba^{2+}Al^{3+}\leftrightarrow K^{1+}Si^{4+}$ of Ba(-Cl) rich micas from garnet clinopyroxenites with respect to the XFe^{tot} and textural position. TAl is amount of Al in the tetrahedron structural position.

The Ti-tschermak substitution is known to prevail in Mg-rich biotites (XMg>0.65), which is ascribed to misfit of the octahedral and tetrahedral layers (Henry *et al.*, 2005). The Ti-oxy coupled substitution ensures charge balance and it often accompanies the $Ba^{2+}Al^{3+}\leftrightarrow K^{1+}Si^{4+}$ substitution (Figure I. 4). In the studied micas two variants of the Ti-oxy substitution occur, where the substitution $Ti^{4+}2O^{2-}\leftrightarrow Fe^{2+}2Cl^{1-}$ links chloroferrokinoshitalite with oxykinoshitalite, and the substitution $Ti^{4+}2O^{2-}\leftrightarrow Mg^{2+}2OH^{1-}$ links phlogopite with oxykinoshitalite. The Ti-oxy substitution is also known from amphiboles (Oberti *et al.,* 1992; Hawthorne *et al.,* 1998).

The Ti-oxy substitution implies incorporation of Ti in the octahedrally coordinated position. This is explained by strong electrostatic repulsion between Ba^{2+} and Ti^{4+}, which makes the octahedral position more favourable for Ti than the tetrahedral position, which is closer to the Ba^{2+} ions in the interlayer sites, which ultimately leads to the vacancy-or oxy-substitution (Bol *et al.,* 1989).

Substitutions and correlations related to XFe^{tot}. The covariance diagrams (Figure I. 3) show a positive correlations of XFe^{tot} with Ba, Al, and Cl, and a negative correlations of XFe^{tot} with K, and Si. The positive correlation of XFe^{tot} with Cl together with the coupled substitution $Ba^{2+}Al^{3+}\leftrightarrow K^{1+}Si^{4+}$ (Figure I. 4) leads to the formation of almost pure Cl end-member mica, XFe^{tot} = 0.88; Ba = 0.95, K = 0.03, Fe^{tot} = 2.68, Mg = 0.37, Al = 1.91, Si = 2.01, Cl = 1.98 (p.f.u) with 10.98 wt. % Cl, which is close to chloroferrokinoshitalite with the theoretical formula $BaFe_3Al_2Si_2O_{10}Cl_2$ (Table I. 2). This is possibly the most Cl-rich mica documented so far from natural samples. The highest Cl content reported to date in micas were 7.3 wt. % Cl (Sharygin *et al.,* 2014) and 4.6 wt. % Cl (Léger *et al., 1996)*.

The positive correlation of XFe^{tot} with Cl has also been documented from other mica occurrences as well as from amphiboles. This is mainly ascribed to the effect that the incorporation of Cl is stimulated by the enlargement of the anion site of both minerals with increasing contents of Fe^{2+}, Al (and K in the case of amphibole), resulting in a positive correlation of Cl with these elements (Henry & Daigle, 2018; Oberti *et al.,* 1993; Siron *et al.,* 2018).

The relationship between XFe^{tot} and Ti is more complicated. While micas with relatively low XFe^{tot} show positive correlation between XFe^{tot} and Ti, the trend turns to negative slope when XFe^{tot} exceeds about 0.4. In addition, micas with low XFe^{tot} show a positive correlation of Ti with Ba and no correlation of Ti with Cl, while no Ti vs Ba and negative Ti vs Cl correlations are observed in micas with relatively high XFe^{tot}. These observations are consistent with the fact that for low XFe^{tot}, the compositional trend phlogopite-oxykinoshitalite is observed, which is characterized by an increase of Ba and Ti and by OH^{1-} to O^{2-} exchange. On the other hand, high XFe^{tot} compositions cover the compositional range from chloroferrokinoshitalite to oxykinoshitalite with a decrease in Cl, an increase in Ti and fairly constant, invariably high Ba contents.

In conclusion, the observed compositional trends indicate that XFe^{tot} exerts an important control on the incorporation of Cl or Ti + O in the crystal structure of mica.

4.2 Comparison of micas from the matrix and from the MSI

Micas in the matrix are on average enriched in Mg, Si, and K and depleted in Fe^{tot}, Ba, Cl, and Al compared to micas from MSI. One possible explanation could be that the micas in the matrix were created from different metasomatic agents with different composition compared to the micas from MSI, which possibly formed during different evolutionary stages. This is consistent with the fact that fluid heterogeneities may have occurred on a millimetre- to centimetre-scale in subduction environment (Selverstone *et al.,* 1992). In addition, the matrix behaved as an open system, where Cl could be more easily removed during subsequent processes, as compared to the environment in which the MSI formed, which supposedly had more closed system character. The variability of metasomatizing agents is matched by the high variability of mineral assemblages and the wide range of mica compositions in the MSI. The covariance diagrams (Figure I. 3) show that some micas in the MSI with lower XFe^{tot} superpose with the compositional range of the micas from the matrix. If the micas from the matrix and from the MSI were formed from the same fluids/melts, the overlap in the covariation diagrams can be

explained by a progressive interaction of the metasomatizing fluid/melt with the rock. It is conceivable that some portion of the fluid/melt formed MSI with high Cl content and XFe^{tot} ratio during the initial stage. The fractions that remained in the matrix for longer time reacted with the host rock more intensively allowing for progressive escape of Cl and the related decrease of XFe^{tot} before they were trapped in garnet and formed MSI in the later stage. Another factor that can potentially explain the observed variability of mica composition are small scale compositional heterogeneities of the rocks. This may lead to the formation of local equilibration domains with variable effective bulk rock composition and induce compositional variation in the fluid/melt during interaction with the surrounding rock.

4.3 Possible immiscibility between chloroferrokinoshitalite and oxykinoshitalite

In several cases, two micas with contrasting composition characterized by predominance of chloroferrokinoshitalite or of oxykinoshitalite coexist within one MSI (Figure I. 2i), which is evident from different contents of XFe^{tot}, Ti, and Cl (for example: XFe^{tot} 0.20:0.77; $Ba_{0.48:0.63}$, $Ti_{0.35:0.02}$, $Cl_{0.27:1.45}$ (p.f.u)). This observation suggests the existence of a miscibility gap between chloroferrokinoshitalite and oxykinoshitalite. Distinct compositional trends for Ba, Cl, Ti and XFe^{tot} can be observed for the mica pairs in the covariation diagrams (Figure I. 5).

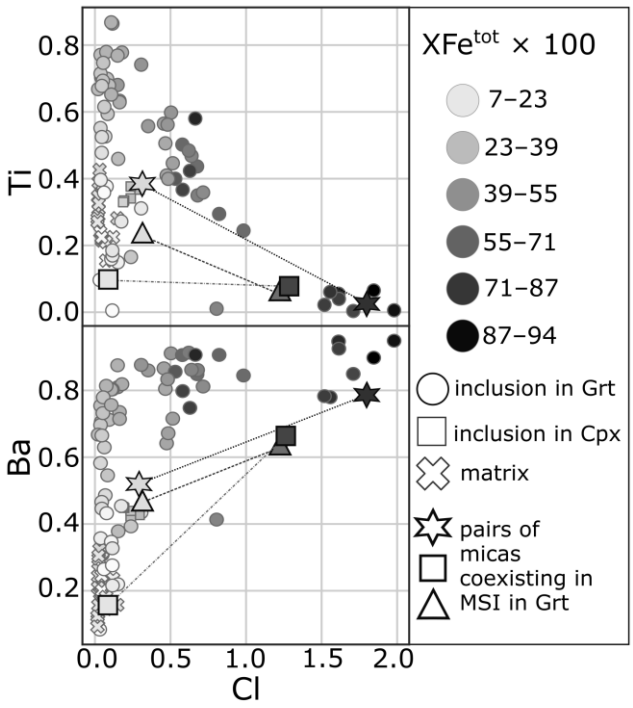

Figure I. 5: Compositional trends of Cl versus Ba and Ti. Analyses highlighted by the same symbols represent pairs of micas coexisting in one garnet hosted polyphase inclusion potentially indicating the existence of a miscibility gap between oxykinoshitalite and chloroferrokinoshitalite.

However, the coexistence of these micas may also be due to local resetting of the original micas along microcracks. Such microcracks have, however, not been observed and this hypothesis cannot be decided unambiguously.

4.4 Formation of MSI and the origin of Ba-, Cl-, and CO_2-rich fluids/melts

It is supposed that the MSI were formed by interaction of mafic lithologies with metasomatic fluid or melt of crustal origin, possibly during interaction with subducting crustal material. The fluid or melt combined with Mg, Fe, Al, Cr, extracted from pyroxenite during metasomatism similarly to genetically related rocks from the Saxothuringian and Moldanubian Domains (Faryad *et al.,* 2013, Borghini *et al.,* 2018, 2020; Čopjaková & Kotková, 2018; Naemura *et al.,* 2018). The fact that the MSI form chains crosscutting garnet crystals and are not correlated with the compositional zoning of garnet indicates that the interaction of the rocks with fluid/melt postdates garnet growth. Fluid or melt probably infiltrated the garnet and clinopyroxene grains along cracks, which were later healed, and the resulting inclusions became isolated. Healing of the cracks indicates that the fluids infiltrated at conditions that were still in the garnet stability field. This led to a closed system behavior and to the effective entrapment of the otherwise mobile Cl. The composition of mica in MSI was controlled by the activities of the species dissolved in the metasomatizing fluid or melt, as described in earlier research (Bol *et al.,* 1989). A different relation between MSI and garnet growth zones than observed in our study was reported by (Čopjaková & Kotková, 2018), who showed MSI to be systematically concentrated in particular garnet growth zones.

Carbonates from inclusions in ultramafic mantle xenoliths often are interpreted as remnants of solid or melt phases of metasomatic origin. Carbonatitic or alkaline-carbonatitic fluids or melts generated in the mantle may react with mantle minerals to trigger release of CO_2-rich fluids/melts, which may contain a brine component. Therefore it is not strictly necessary to invoke crustal material for the formation of these metasomatizing fluids/melts (Zaccarini *et al.,* 2004; Frezzotti & Touret, 2014). This study shows that Ba in the MSI is systematically associated with phases rich in Cl and CO_2, and therefore Ba, like Cl and CO_2, most likely originated from metasomatizing fluids/melts. Given the average Ba content of the upper continental crust (~630 ppm, Rudnick and Gao 2014) as compared to the mantle (~7.0 ppm, Sun & McDonough, 1989), Ba most likely was derived from subducting crustal material.

The presence of nearly pure end-member Cl mica (chloroferrokinoshitalite), Cl-apatite and locally goryainovite together with carbonates suggests high Cl and CO_2 activity in the

metasomatizing fluid or melt. The chemical composition of the micas from the MSI shows that OH is replaced by Cl in the A position in the case of the Fe-rich members and by O in the case of Mg-rich members (XFe^{tot} > 0.5: $OH_{0.01–0.69}Cl_{0.53–1.98}O_{0.01–1.16}$, XFe<0.5: $OH_{0.16–1.87}Cl_{0.02–0.81}O_{0.01–1.74}$; Table S. 2). The micas with compositions close to chlorofferokinoshitalite and oxykinoshitalite are therefore effectively anhydrous and the A position is completely occupied with Cl or O. This indicates low H_2O activity in the metasomatizing fluid or melt, the composition of which may be regarded as silicocarbonatite.

4.5 Composition and stability of goryainovite

The crystallization of this rare phosphate with a very high Cl content in the MSI indicates exceptionally high Cl activity in the fluid or melt. Subsequent decrease of the Cl-activity may have led to its transformation into Cl-apatite or furthermore to Cl-rich hydroxylapatite, which can often be observed in the matrix.

The composition of goryainovite ($Ca_{1.9–2.0}Sr_{0.0–0.1}(P_{\sim1.0}O_{4.0})Cl_{0.7–0.8}$) shows that Ca is partially substituted by Sr. A similar substitution has been described for apatite (Chakhmouradian *et al.,* 2002; Hughes *et al.,* 1991), but due to the rare occurrence of goryainovite (this work describes its second occurrence so far) the Ca-Sr substitution has not yet been reported for this mineral (Ivanyuk *et al.,* 2017). The low Cl content that does not correspond to the theoretical Cl content of the ideal goryainovite formula of ($Ca_2(PO_4)Cl$), may suggest that Cl was partially replaced by OH^{-1}.

5 Conclusions

This study on Ba-, Ti-, and Cl-rich micas has revealed an extremely high compositional variability of the micas ranging between Ba-rich phlogopite, chloroferrokinoshitalite, and oxykinoshitalite. It allowed the principal ionic substitution mechanisms to be discerned and shed light on the influence of XFe^{tot} on the compositional trends. The positive correlation of XFe^{tot} with Cl led to the formation of possibly the most Cl-rich mica so far described, a chloroferrokinoshitalite with 10.98 wt. % Cl. The coexistence of two micas with distinct compositions close to chloroferrokinoshitalite and oxykinoshitalite indicates that these micas can be partially immiscible. The occurrence of exceptionally Ba-, Ti-, and Cl-rich micas associated with other Ba- and/or Cl-rich minerals, including celsian, Cl-apatite, and rare goryainovite in the matrix, as well as in garnet and clinopyroxene-hosted MSI provides

important constraints on the composition of melt or fluid involved in syn-orogenic mantle metasomatism. The prevalence of micas with a low OH content with substantial amounts of Cl or O in the A position together with carbonates indicates high activity of Cl and CO_2 and low H_2O activity in the metasomatizing agent, which can be classified as Ba-Cl-rich silicocarbonatitic. The similarity of the MSI documented in this study with other findings in mantle rocks from the Gföhl and the Saxothuringian Domain of the Bohemian Massif may prove their common origin and further support an extended regional occurrence related to subduction processes during the Variscan orogeny.

Part II: Metasomatic interaction of ultramafic mantle xenoliths with their felsic HP–UHT granulite host in St. Leonhard granulite massif

1 Introduction

This Part describe the metasomatic interaction between only few-centimetre large mantle xenoliths – garnet clinopyroxenites and peridotites, with host granulite in the St. Leonhard granulite massif in Lower Austria (Figure II. 1). Based on textural analysis across the contact between the xenoliths and the surrounding granulite, thermodynamic modelling, mineral and local bulk-rock compositions, is assessed the petrological and chemical consequences of mutual interaction between the xenoliths and the surrounding felsic granulite. In addition, this research allows to develop a new genetic hypothesis for the origin of the intermediate orthopyroxene-bearing granulite by transformation of its kyanite-bearing felsic counterpart through metasomatic interaction with the mantle xenoliths.

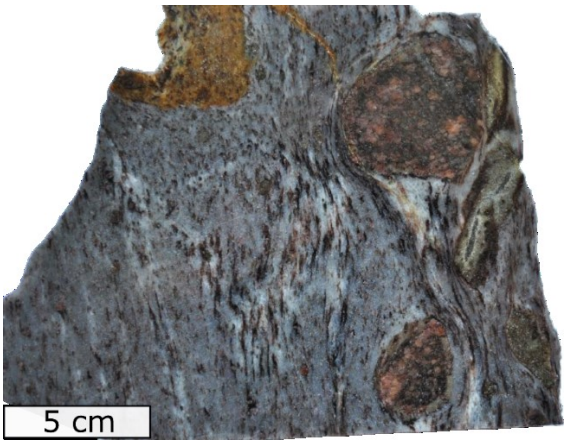

Figure II. 1: Polished slab of intermediate granulite enclosing several rounded garnet clinopyroxenite xenoliths.

2 Samples and analytical methods

Representative samples of intermediate granulite with mantle xenoliths of garnet clinopyroxenite and peridotite, up to 5 cm in size, were prepared as polished thin sections in which the direct contact with mantle xenoliths can be observed. A total of 40 thin-sections were made, including 49 garnet clinopyroxenite and 3 peridotite xenoliths. For further detailed petrographic study, one sample of each type with the best preserved mineral assemblage was selected (garnet clinopyroxenite: sample A3, peridotite: sample D554x11Ol). All analytical studies were performed in the laboratories at the Institute of Petrology and Structural Geology at the Faculty of Science, Charles University, Prague. A Tescan Vega Scanning Electron Microscope (SEM) with Oxford Instruments X-Max 50 Energy-Dispersive Spectroscope (EDS) and a Jeol JXA-8530F Field-Emission Gun Electron Probe Micro Analyser (FEG–EPMA) were

used for a detailed study of the mineral assemblages and for the acquisition of mineral chemical analyses.

An accelerating voltage of 15 kV and a beam current of 20 nA were used for mineral chemical analysis. A defocussed beam with a diameter of 3–10 μm was utilized for analyses of feldspars and micas, while all the other mineral phases were analysed with a focussed beam.

In order to evaluate and quantify chemical changes of the studied lithologies that appear on a thin-section scale, the bulk-rock chemical compositions of individual lithologies/domains were acquired using SEM–EDS with an accelerating voltage of 15 kV, a beam current of 1.5 nA and 50× magnification. Energy dispersive spectra were acquired in scanning mode over areas of interest for 300 s of live time. The acquired spectra represent contributions from all phases present in the respective area of interest in appropriate proportions and thus represent the bulk rock composition of the analysed area. The spectra were quantified with the INCA software (Oxford Instruments), the following standards were used for quantification: apatite (P), albite (Na), MgO (Mg), corundum (Al), quartz (Si), sanidine (K), calcite (Ca), rutile (Ti), Cr_2O_3 (Cr), rhodonite (Mn), and magnetite (Fe). Kα lines were used for the detection of all elements, and the XPP method (Pouchou & Pichoir, 1985) was used for matrix correction. For determining the compositions of individual lithologies/domains, analyses of several areas were averaged for each lithology/domain. In the calculation of the local bulk-rock compositions the densities were not considered.

Element distribution maps were acquired using an accelerating voltage 20 kV and a beam current of 80 nA. Kα lines were used for detection of all elements except for Ba (Lα). The following standards were employed for quantification of concentrations of individual elements: apatite (F, P), albite (Na), MgO (Mg), corundum (Al), quartz (Si), tugtupite (Cl), sanidine (K), calcite (Ca), rutile (Ti), Cr_2O_3 (Cr), rhodonite (Mn), magnetite (Fe), sphalerite (Zn) and barite (Ba).

Chemical analyses of garnet were calculated to 12 oxygens/8 cations, pyroxenes to 6 oxygens/4 cations, feldspar to 5 cations, spinel to 4 oxygens/3 cations, biotite to 11 oxygens, olivine to 4 oxygens/3 cations. Amphiboles were calculated on the basis of 23 oxygen equivalents using the Excel spreadsheet of Locock (2014) based on the recent amphibole classification (Hawthorne et al., 2012).

3 RESULTS

3.1 Petrographical characteristics and mineral compositions

3.1.1 Kyanite-bearing felsic granulite

The St. Leonhard granulite massif is dominated by Ky-granulite characterized by a fine-grained quartzofeldspathic matrix with perthitic K-feldspar, which hosts porphyroblasts of kyanite with thin plagioclase coronae (Figure II. 2a) and porphyroblasts of garnet (Figure II. 2b). Part of the matrix is also biotite, which often occurs at the contacts with garnet. Common accessories are rutile, apatite, monazite, and zircon.

Plagioclase (oligoclase) in the matrix has compositions in the range of $An_{17.4–18.6}Ab_{80.2–81.4}Or_{\sim 1.2}$ (see Table II. 1). Plagioclase forming coronae around kyanite is characterized by a slight decrease of Ca towards the surrounding matrix ($An_{19.8\rightarrow 18.3}Ab_{79.1\rightarrow 80.2}Or_{1.2\rightarrow 1.5}$). The albite component in the K-feldspar varies from 13.6 to 15.4 %. Garnet is rich in almandine component and characterized by a rim-ward increase of Fe and Mg and decrease of Ca: $Prp_{22.6\rightarrow 26.4}Alm_{63.8\rightarrow 69.3}Grs_{12.6\rightarrow 3.2}Sps_{1.0\rightarrow 1.1}$; $XFe^{2+} = 0.74\rightarrow 0.72$ (Fig. 2c). Biotite has $XFe^{tot} =$ 0.32–0.31 and Ti = 0.23–0.25 p.f.u.

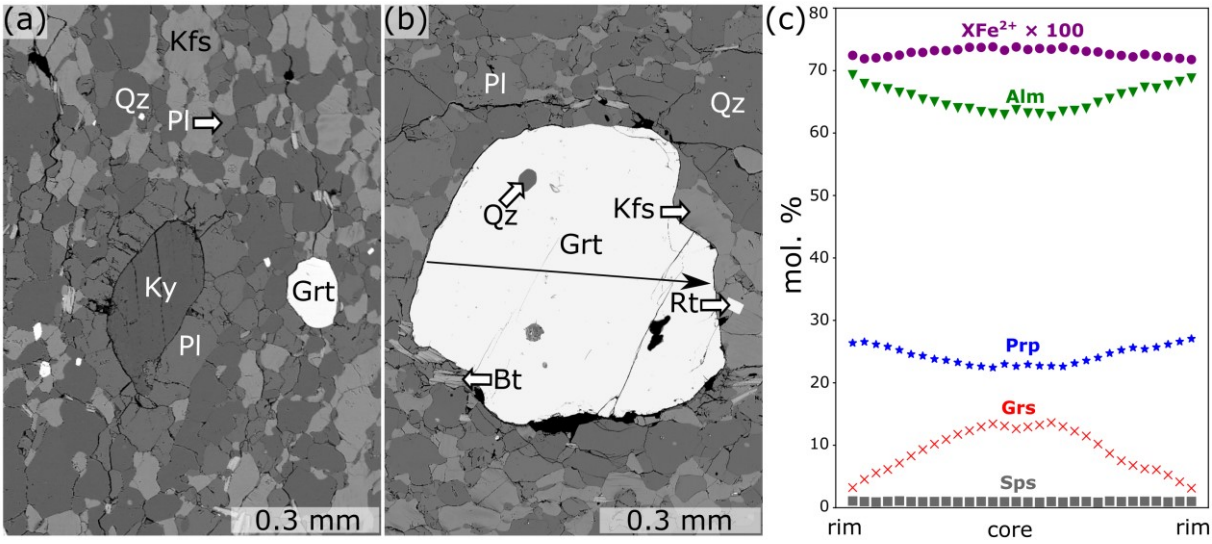

Figure II. 2: Back-scattered electron images of Ky-bearing felsic granulite (sample D441-X) with compositional profile across garnet. Mineral assemblage is Grt–Ky–Kfs–Pl–Qz–Rt. a) Kyanite with corona formed by plagioclase. b) Garnet porphyroblast. c) Compositional profile across the garnet porphyroblast from Figure II. 1b.

Table II. 1: Representative mineral analyses of Ky-bearing felsic granulite in wt. %.

Lithology	Ky-bearing felsic granulite									
Thin-section	D441	D441	D441	D441	D441	D441	D441	D441	D441	D441
Mineral	Grt	Grt	Bt	Bt	Pl	Pl	Pl	Pl	Kfs	Kfs
Analysis	Grt-line 15	Grt-line 01	Bt-13	Bt-14	Pl-03	Pl-04	Pl-19	Pl-21	Kfs-01	Kfs-11
Position	Grt core	Grt rim	Matrix	Matrix	Pl core	Pl rim	Pl rim around Ky, closer to Ky	Pl rim around Ky, further away from Ky	Matrix	Matrix
SiO_2	38.14	38.18	37.84	37.95	63.28	63.59	62.85	63.75	64.73	65.68
P_2O_5	0.08	0.06	b.d.	0.03	0.16	0.17	0.19	0.19	0.19	0.20
TiO_2	0.08	0.02	4.47	4.06	0.02	b.d.	b.d.	b.d.	0.04	0.02
Cr_2O_3	b.d.	0.04	0.03	0.02	b.d.	b.d.	b.d.	b.d.	b.d.	b.d.
Al_2O_3	21.32	21.36	16.66	16.25	23.08	22.61	23.20	23.10	18.62	18.97
FeO	29.13	31.53	12.14	11.95	0.05	0.02	b.d.	b.d.	b.d.	b.d.
MnO	0.44	0.48	b.d.	0.02	b.d.	b.d.	b.d.	b.d.	b.d.	b.d.
MgO	5.81	6.73	14.20	14.79	b.d.	b.d.	b.d.	b.d.	b.d.	b.d.
CaO	4.50	1.14	0.03	0.03	3.85	3.65	4.13	3.84	0.11	0.09
Na_2O	b.d.	0.04	0.09	0.10	9.19	9.44	9.14	9.27	1.49	1.69
K_2O	b.d.	b.d.	9.72	9.44	0.21	0.21	0.21	0.27	14.30	14.06
NiO	b.d.	b.d.	b.d.	0.03	b.d.	b.d.	b.d.	b.d.	b.d.	b.d.
ZnO	b.d.	b.d.	0.10	b.d.	b.d.	0.05	b.d.	0.07	0.02	0.03
Cl	b.d.	b.d.	0.10	0.09	b.d.	b.d.	b.d.	b.d.	b.d.	b.d.
F	b.d.	b.d.	1.79	1.98	b.d.	b.d.	b.d.	b.d.	b.d.	b.d.
Total	99.49	99.58	95.26	94.68	99.83	99.73	99.72	99.50	99.50	100.74
Cations/Charges	8/24	8/24	8/22	8/22	5/16	5/16	5/16	5/16	5/16	5/16
Si	3.00	3.01	2.78	2.80	2.80	2.82	2.79	2.80	2.99	3.00
P	0.01	0.00	–	0.00	0.01	0.01	0.01	0.01	0.01	0.01
Ti	0.00	0.00	0.25	0.23	0.00	–	–	–	0.00	0.00
Cr	–	0.00	0.00	0.00	0.00	–	–	–	–	–
Al	1.98	1.98	1.44	1.41	1.20	1.18	1.21	1.20	1.01	1.02
Fe^{2+}	1.92	2.08	0.75*	0.74*	0.00	0.00	–	–	–	–
Fe^{3+}	0.00	0.00	–	–	0.00	0.00	0.00	0.00	0.00	0.00
Mn	0.03	0.03	–	0.00	–	–	–	–	–	–
Mg	0.68	0.79	1.56	1.63	–	–	–	–	–	–
Ca	0.38	0.10	0.00	0.00	0.18	0.17	0.20	0.18	0.01	0.00
Na	–	0.01	0.01	0.01	0.79	0.81	0.79	0.79	0.13	0.15
K	–	–	0.91	0.89	0.01	0.01	0.01	0.01	0.84	0.82
Ni	–	–	–	0.00	–	–	–	–	–	–
Zn	–	–	0.01	–	–	0.00	–	0.00	0.00	0.00
Cl	–	–	0.01	0.01	–	–	–	–	–	–
F	–	–	0.42	0.46	–	–	–	–	–	–
XFe^{2+}	0.74	0.72	$XFe^{tot} = 0.32$	$XFe^{tot} = 0.31$						

b.d. below detection limit. * – Fe^{tot}

3.1.2 Intermediate granulite

This granulite type is a fine-grained rock characterized by the assemblage Grt–Opx–Bt–Kfs–Pl–Qz. It hosts mantle xenoliths of garnet clinopyroxenite and peridotite up to five centimetres in size. The transition of Ky-bearing to intermediate granulite is concealed in the field due to poor exposure. The matrix is quartzofeldspathic with porphyroblasts of orthopyroxene and garnet, and with biotite often localized at the garnet rims. K-feldspar is perthitic with irregular boundaries at the contacts to plagioclase (Figure II. 3a). Common accessories are pyrite, pyrrhotite, apatite, monazite, rutile, and ilmenite, which occurs at the rims of rutile or forms thin lamellae within rutile.

In the matrix, slightly elongated aggregates ~0.8–1.3 mm long composed of small garnet grains (~0.1 mm in diameter) are surrounded by plagioclase coronae. In the central parts of the aggregates, tiny inclusions of corundum and spinel are commonly concentrated (Figure II. 3b, c), and the aggregates can also contain rutile, apatite, and monazite inclusions.

While K-feldspar is relatively abundant in the typical intermediate granulite, it is almost completely absent in a narrow (up to 2 mm wide) zone in the immediate vicinity of the mantle xenoliths (Figure II. 3d, e).

Plagioclase is oligoclase to andesine: $An_{28.7–32.1}Ab_{65.3–69.8}Or_{1.5–2.6}$ (Table II. 2); the albite component in K-feldspar is $Ab_{3.5–9.5}$. In the Kfs-poor zones around the xenoliths, the anorthite content in plagioclase decreases from the contact with the xenolith towards the host granulite (from clinopyroxenite towards granulite: $An_{34.1→28.9}Ab_{62.4→69.4}Or_{3.5→1.7}$, and from peridotite towards granulite: $An_{29.5→27.2}Ab_{69.5→71.2}Or_{1.0→1.6}$). The orthopyroxene is characterized by slightly higher Ca-content in the cores compared to the rims: 0.02→0.01 p.f.u.; the Al content is in the range of 0.10–0.14 p.f.u. The XFe^{2+} values in the orthopyroxene do not show significant systematic zoning and range from 0.32 to 0.35. Compositional profiles across garnet are mostly flat, with Ca decreasing and Fe increasing only at the rim: XFe^{2+} = 0.58→0.60; $Py_{37.6→37.0}Alm_{51.2→54.9}Grs_{9.8→6.4}Sps_{1.5→1.6}$ (Figure II. 4a). Biotite shows XFe^{2+} = 0.27–0.31 and Ti ~0.36 p.f.u. The garnet grains in the centre of the clusters and close to the Al-rich inclusions have slightly higher Ca and lower Mg ($Py_{40.1}Alm_{51.8}Grs_{7.0}Sps_{1.2}$; XFe^{2+} = 0.56) than the other garnets in the cluster. The latter display weak compositional zoning characterized by Ca-depleted and Fe–Mg-enriched rims ($Py_{41.2→42.1}Alm_{51.0→52.1}Grs_{6.6→4.5}Sps_{1.2→1.2}$; XFe^{2+} = 0.55→0.55). The distinct Ca enrichment in the cores of the clusters is well visible in the compositional map (Figure II. 3c). The An content of plagioclase within the coronae around

garnet aggregates is in the range: $An_{27.9–27.1}Ab_{70.9–72.1}Or_{1.2–0.8}$. Spinel forming tiny inclusions is rich in Al-endmembers: XFe^{2+} ~0.45, Al ~2.00 p.f.u., Cr ~0.02 p.f.u.

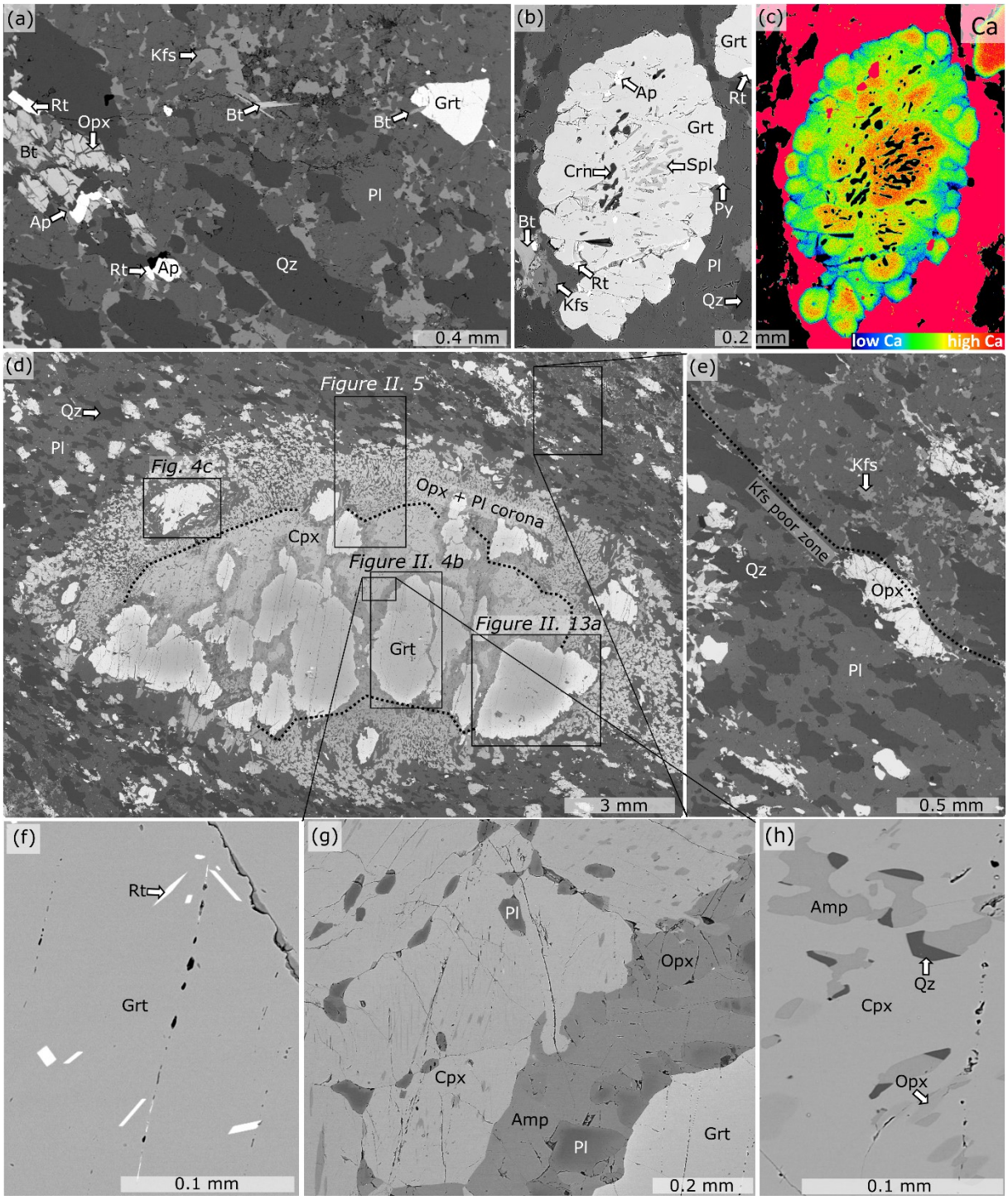

Figure II. 3: Back-scattered electron images of the intermediate granulite enclosing garnet clinopyroxenite xenolith (sample A3) and Ca compositional map of garnet aggregates in the granulite matrix. a) Granulite formed by quartz, plagioclase, K-feldspar, garnet, orthopyroxene and biotite. b) Garnet aggregates in the granulite matrix have tiny inclusions of spinel and

corundum. c) Calcium compositional map of the garnet aggregate from Figure II. 3b showing individual garnet grains and their zoning. d) Garnet clinopyroxenite xenolith in intermediate granulite with orthopyroxene and plagioclase corona at the contact. e) K-feldspar-poor zone developed around the corona along its contact with the intermediate granulite further away. f) Rutile inclusions in garnet from garnet clinopyroxenite. g) Symplectite developed around garnet porphyroblast in the garnet clinopyroxenite xenolith and exsolutions of orthopyroxene associated with inclusions of amphibole, plagioclase, and quartz in clinopyroxene grains. h) A detail of the exsolutions and inclusions.

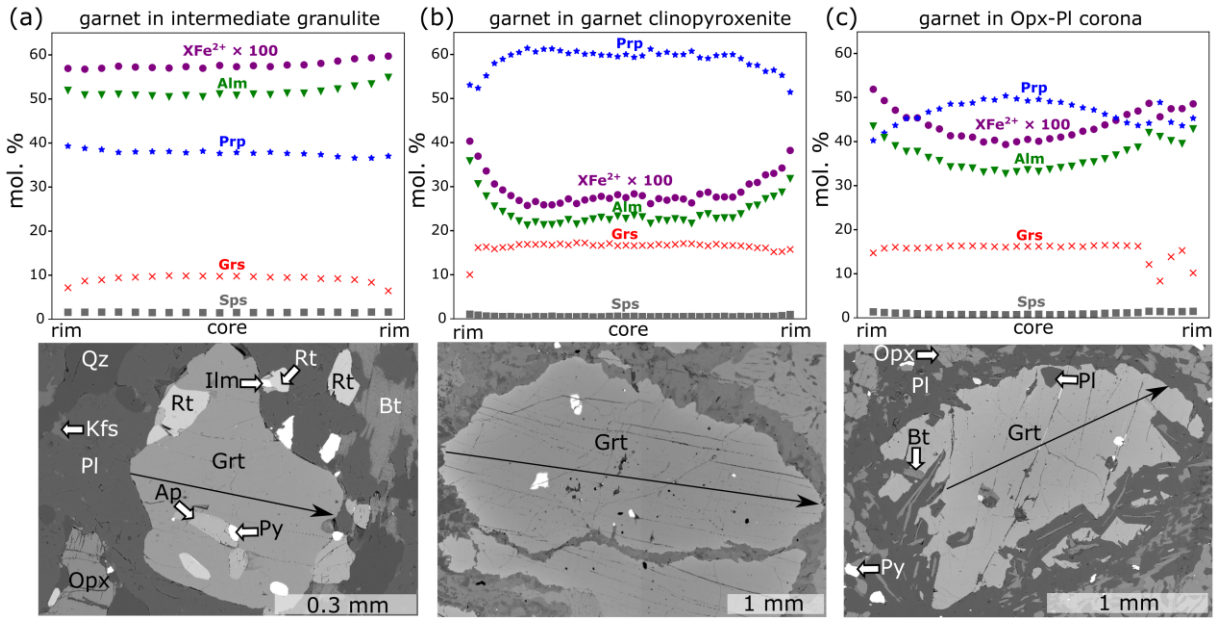

Figure II. 4: Composition profiles across garnets and their BSE images from a) intermediate granulite, b) garnet clinopyroxenite (for location, see Figure II. 3d), and c) Opx–Pl corona around garnet clinopyroxenite (position is also marked in Figure II. 3d).

Table II. 2: Representative mineral analyses of intermediate granulite and Ksp poor zone in wt. %.

Lithology	intermediate granulite							
Thin-section	A3	A3	D554x5-Ky-B	D554x5-Ky-B	A3	A3	A3	A3
Mineral	Grt	Grt	Grt	Grt	Bt	Opx	Opx	Pl
Analysis	Grt-line 10	Grt-line 20	Grt-04	Grt-07	Bt-78	Opx-line 09	Opx-line 02	Pl-67
Position	Matrix, core	Matrix, rim	Grt cluster, Ca rich core near Spl	Grt cluster, Ca depleted rim	Matrix	Matrix, core	Matrix, rim	Matrix
SiO_2	38.64	38.45	38.28	38.44	36.65	51.28	51.46	59.71
P_2O_5	0.05	0.05	0.06	b.d.	b.d.	b.d.	b.d.	0.05
TiO_2	0.09	b.d.	0.03	b.d.	6.36	0.05	0.13	b.d.
Cr_2O_3	0.11	0.21	b.d.	0.02	0.17	0.14	0.10	b.d.
Al_2O_3	21.77	21.64	22.26	22.03	14.50	2.19	3.01	24.86
FeO	25.26	26.09	24.84	24.75	11.93	21.21	21.17	b.d.
MnO	0.67	0.74	0.53	0.55	b.d.	0.20	0.23	b.d.
MgO	9.78	9.54	10.27	10.86	14.69	22.76	22.40	b.d.
BaO	0.02	0.03	0.03	b.d.	0.19	b.d.	b.d.	b.d.
CaO	3.52	2.31	2.48	1.63	0.06	0.47	0.21	6.55
Na_2O	b.d.	b.d.	b.d.	b.d.	0.04	b.d.	b.d.	7.37
K_2O	b.d.	b.d.	b.d.	b.d.	9.81	b.d.	0.02	0.45
NiO	0.02	0.02	0.02	0.02	0.02	0.04	b.d.	b.d.
ZnO	0.04	0.04	0.04	b.d.	0.05	0.12	0.05	0.03
Cl	b.d.	b.d.	b.d.	b.d.	0.09	b.d.	b.d.	b.d.
F	b.d.	b.d.	b.d.	b.d.	0.50	0.04	b.d.	b.d.
Total	99.95	99.11	98.83	98.29	94.47	98.47	98.78	99.02
Cations/Charges	8/24	8/24	8/24	8/24	8/22	4/12	4/12	5/16
Si	2.96	2.98	2.95	2.97	2.74	1.93	1.93	2.69
P	0.00	0.00	0.00	–	–	–	–	0.00
Ti	0.01	–	0.00	–	0.36	0.00	0.00	–
Cr	0.01	0.01	–	0.00	0.01	0.00	0.00	–
Al	1.96	1.97	2.02	2.01	1.28	0.10	0.13	1.32
Fe^{2+}	1.52	1.63	1.53	1.55	0.75*	0.62	0.66	–
Fe^{3+}	0.10	0.06	0.07	0.05	–	0.04	0.00	–
Mn	0.04	0.05	0.03	0.04	–	0.01	0.01	–
Mg	1.11	1.10	1.18	1.25	1.64	1.27	1.25	–
Ba	0.00	0.00	0.00	–	0.01	–	–	–
Ca	0.29	0.19	0.20	0.13	0.00	0.02	0.01	0.32
Na	–	–	–	–	0.01	–	–	0.64
K	–	–	–	–	0.94	–	0.00	0.03
Ni	0.00	0.00	0.00	0.00	0.00	0.00	–	–
Zn	0.00	0.00	0.00	–	0.00	0.00	0.00	0.00
Cl	–	–	–	–	0.01	–	–	–
F	–	–	–	–	0.12	0.00	–	–
XFe^{2+}	0.58	0.60	0.56	0.55	$XFe^{tot} = 0.31$	0.33	0.35	

b.d. below detection limit. * – Fe^{tot}

Table II. 2 (continued): Representative mineral analyses of intermediate granulite and Kfs poor zone in wt. %.

Lithology	intermediate granulite				Kfs poor zone in intermediate granulite next to mantle xenoliths			
Thin-section	A3	D554x5 Ky-B	A3	A5	A3	A3	D554x11Ol	D554x11Ol
Mineral	Pl	Pl	Kfs	Spl	Pl	Pl	Pl	Pl
Analysis	Pl-72	Pl-line 01	Kfs-64	Spl-02	Pl-49	Pl-117	Pl-line 06	line 01
Position	Matrix	Pl rim around garnet cluster	Matrix	Inclusion in Grt cluster	Near garnet clinopyroxenite	Near intermediate granulite	Near peridotite xenolith	Near intermediate granulite
SiO_2	60.43	61.17	67.32	0.04	60.08	62.08	62.52	62.39
P_2O_5	0.04	0.07	0.02	b.d.	0.07	0.04	0.05	0.06
TiO_2	0.02	b.d.	0.05	b.d.	b.d.	0.02	b.d.	0.02
Cr_2O_3	b.d.	b.d.	b.d.	0.85	0.03	b.d.	b.d.	b.d.
Al_2O_3	24.06	23.81	19.40	62.23	25.22	24.54	24.39	24.01
FeO	0.08	0.39	0.05	18.90	0.09	0.03	0.31	0.26
MnO	b.d.	b.d.	b.d.	0.03	b.d.	0.02	b.d.	b.d.
MgO	b.d.	b.d.	b.d.	13.03	b.d.	b.d.	0.02	0.27
BaO	b.d.	0.06	0.95	b.d.	0.02	b.d.	b.d.	b.d.
CaO	5.92	5.78	0.10	0.03	6.96	5.88	5.94	5.54
Na_2O	7.95	8.12	0.27	0.08	7.04	7.79	7.74	8.00
K_2O	0.26	0.21	11.36	b.d.	0.60	0.29	0.17	0.27
NiO	b.d.	b.d.	b.d.	0.08	b.d.	b.d.	0.02	0.04
ZnO	b.d.	0.04	b.d.	3.46	b.d.	b.d.	0.06	b.d.
Cl	b.d.	b.d.	b.d.	b.d.	b.d.	b.d.	b.d.	b.d.
F	b.d.	b.d.	b.d.	b.d.	b.d.	b.d.	b.d.	b.d.
Total	98.77	99.66	99.53	98.73	100.11	100.70	101.20	100.86
Cations/Charges	5/16	5/16	5/16	3/8	5/16	5/16	5/16	5/16
Si	2.72	2.73	3.18	0.00	2.69	2.75	2.76	2.76
P	0.00	0.00	0.00	–	0.00	0.00	0.00	0.00
Ti	0.00	–	0.00	–	–	0.00	–	0.00
Cr	–	–	–	0.02	0.00	–	–	–
Al	1.28	1.25	1.08	1.96	1.33	1.28	1.25	1.27
Fe^{2+}	0.00	0.00	0.00	0.40	0.00	0.00	0.01	0.01
Fe^{3+}	0.00	0.01	–	0.02	0.00	0.00	–	–
Mn	–	–	–	0.00	–	0.00	–	–
Mg	–	–	–	0.52	–	–	0.02	0.00
Ba	–	0.00	0.02	–	0.00	–	–	–
Ca	0.29	0.28	0.01	0.00	0.33	0.28	0.26	0.28
Na	0.69	0.70	0.02	0.00	0.61	0.67	0.69	0.66
K	0.02	0.01	0.68	–	0.03	0.02	0.02	0.01
Ni	–	–	–	0.00	–	–	0.00	0.00
Zn	–	0.00	–	0.07	–	–	0.00	–
Cl	–	–	–	–	–	–	–	–
F	–	–	–	–	–	–	–	–
XFe^{2+}				0.44				

b.d. below detection limit. * – Fe^{tot}

3.1.3 Garnet clinopyroxenite xenolith and orthopyroxene-plagioclase coronae

This xenolith type in the intermediate granulite reaches sizes of up to 5 cm and is surrounded by a fine-grained, several millimetres thick Opx–Pl symplectitic coronae (Figure II. 3d). In most of these xenoliths, extensive growth of secondary biotite obscures the original mineral assemblage. Only sample A3 from locality D554 is exceptionally well preserved and therefore was selected for petrological study.

The preserved part of this xenolith is formed by clinopyroxene up to ~0.7 mm and garnet porphyroblasts up to 4 mm in size, the latter often sticking out into the corona or touching it by at least one rim. These porphyroblasts contain inclusions of rutile (Figure II. 3h), pyrite, and pyrrhotite and are surrounded by a ~0.3 mm wide fine-grained Opx–Amp–Pl ± Spl symplectite (Figure II. 3f). Clinopyroxene is partially replaced by plagioclase, and contains orthopyroxene exsolutions associated with amphibole, plagioclase, spinel and quartz (Figure II. 3g,h). Plagioclase has features documenting crystallization from melt, e.g. elongated shape and position in Cpx triple junctions and at grain boundaries (Hasalová *et al.,* 2008; Stuart *et al*., 2018).

Garnet not protruding into the corona shows weak compositional zoning characterized by rimward decrease in Mg and Ca and increase in Fe: $Prp_{59.7\rightarrow51.5}Alm_{23.1\rightarrow31.8}Grs_{16.6\rightarrow15.7}Sps_{0.52\rightarrow0.98}$; $XFe^{2+} = 0.28\rightarrow0.38$ (see Table II. 3). Rims that are in contact with the Opx–Pl corona show qualitatively similar composition trends but with a more pronounced decrease in Mg and increase in Fe, while the Ca content remains almost constant ($Grs_{\sim16.7}$). The outermost rim is further characterized by an abrupt drop in the Ca content and a concomitant increase in Fe and Mg from the rim toward the outermost rim ($Prp_{52.3\rightarrow53.0}Alm_{30.7\rightarrow35.9}Grs_{16.1\rightarrow10.0}Sps_{0.8\rightarrow1.0}$; $XFe^{2+} = 0.37\rightarrow0.40$). The composition profile across a garnet, where one rim is in contact with the Opx–Pl corona, is shown in Figure II. 4b. Clinopyroxene grains are characterized by a slight outward decrease of Na and Al and increase of Ca: $CaTs_{9.9\rightarrow8.6}Jd_{4.7\rightarrow4.3}$; $XFe^{2+} = 0.13\rightarrow0.12$. Orthopyroxene is Fe-poor ($XFe^{2+} = 0.16–0.19$). Amphibole corresponds to pargasite or magnesio-hornblende: $XFe^{2+} = 0.07–0.15$; Ti = 0.11–0.30, Si = 6.25–6.55 p.f.u. Plagioclase is rich in Ca component: $An_{54.0–75.9}Ab_{23.7–43.9}Or_{0.4–2.1}$.

The Opx–Pl symplectitic corona around the garnet clinopyroxenite xenolith (Figure II. 5a) is ~2 mm wide and mainly consists of Opx–Pl symplectite with a grain size of ~0.1–0.2 mm. Both contacts of the corona, i.e. those with the xenolith as well as with the intermediate granulite,

are relatively sharp. Garnets sticking into this corona are partially replaced by biotite along their rims and are surrounded by plagioclase.

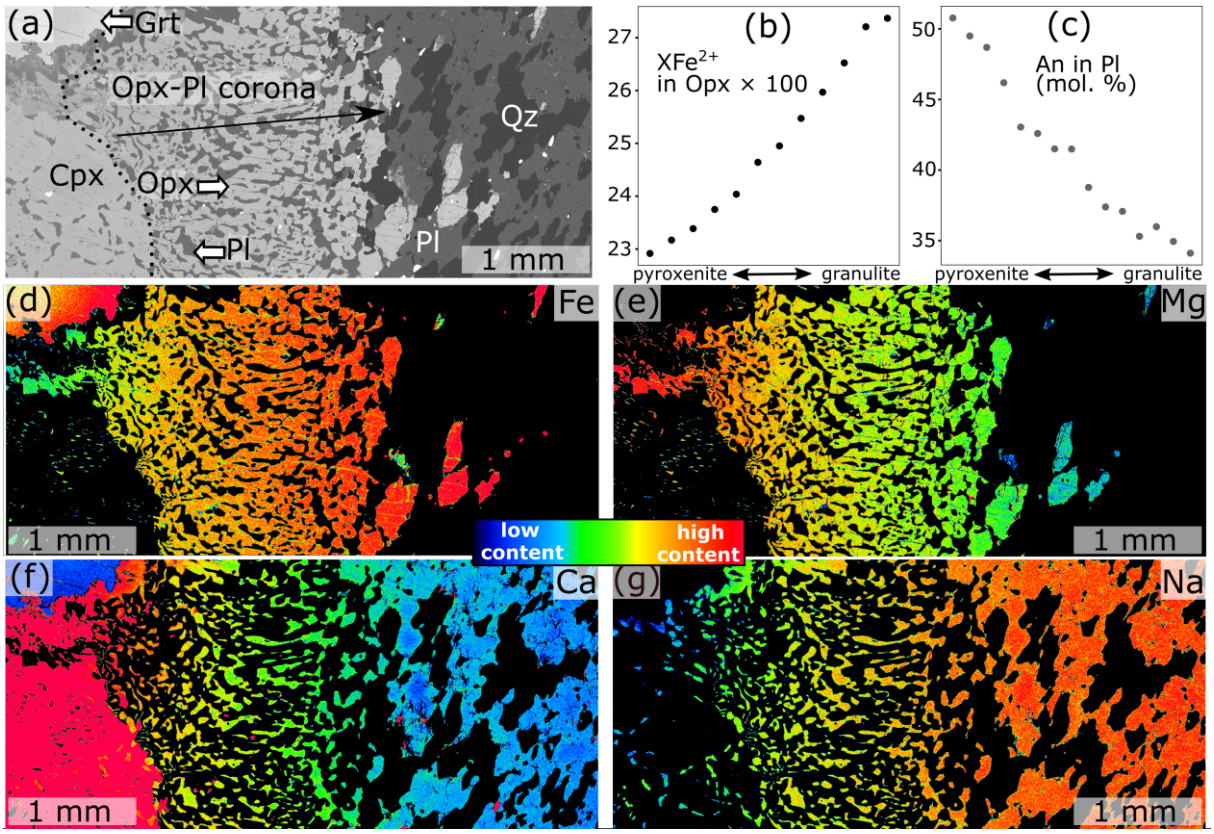

Figure II. 5: Orthopyroxene–plagioclase corona at the contact of garnet clinopyroxenite xenolith with intermediate granulite (see Figure II. 3 for location). a) Back-scattered electron image. b) Diagram of XFe^{2+} in Opx showing an increasing trend within the corona towards the host granulite. c) Diagram showing a decreasing trend of An in plagioclase towards the host granulite. d–g) Compositional maps of the Opx–Pl corona showing Fe increase and Mg decrease in orthopyroxene, and Ca decrease and Na increase in plagioclase from the xenolith to the host granulite.

The chemical zoning of the corona is illustrated in compositional maps of Fe, Mg, Ca, and Na as well as plots of XFe^{2+} in orthopyroxene and An in plagioclase (Figure II. 5b–g). The XFe^{2+} in the orthopyroxene increases while the Al content shows only a slight increase from the contact with the xenolith to the intermediate granulite (XFe^{2+} = 0.23→0.26; Al = 0.08→0.11 p.f.u). At the same time the anorthite content of plagioclase decreases from the contact with the xenolith to the intermediate granulite ($An_{50.8→35.0}Ab_{47.5→62.0}Or_{1.7→3.1}$). The compositional zoning of garnet is characterized mainly by a rimward decrease in Mg and increase in Fe, while Ca remains almost constant, and Mn slightly increases

($Prp_{49.2\rightarrow40.3}Alm_{33.9\rightarrow43.6}Grs_{16.2\rightarrow14.7}Sps_{0.8\rightarrow1.4}$, XFe^{2+} = 0.41→0.52; Fig. 4c). The outermost rim of the garnet (~40 μm) is characterised by a significant drop in the Ca content accompanied by an increase in Mg and Fe ($Prp_{45.3}Alm_{43.0}Grs_{10.2}Sps_{1.5}$, XFe^{2+} = 0.49). Biotite is Fe-poor: XFe^{2+} = 0.17–0.20; Ti = 0.22–0.25 p.f.u.

3.1.4 Peridotite xenolith and orthopyroxene-bearing corona

This type of xenolith is very rare; moreover, the majority of these samples are highly serpentinized. For petrological description, the best preserved sample D554x11Ol from locality D554 was selected.

Sample D554x11Ol is formed by a few partially serpentinized olivine and spinel grains surrounded by an up to 4 millimetres wide, almost monomineralic orthopyroxene corona. Tiny olivine forms inclusions in orthopyroxene near the preserved olivine core. A small amount of biotite also occurs in the corona (Figure II. 6a–c).

Olivine is close to the forsterite endmember: XFe^{2+} = 0.11–0.12 (Table II. 4). The composition of spinel is variable: XFe^{2+} = 0.35–0.44, Al = 1.32–1.51 p.f.u., Cr = 0.47–0.68 p.f.u. The orthopyroxene corona is zoned, showing an increase in XFe^{2+} and Al towards the host granulite: XFe^{2+} = 0.12→0.24, Al = 0.08→0.13 p.f.u. (Figure II. 6d–g). Biotite is phlogopite with Fe content gradually increasing towards the contact with the granulite: XFe^{tot} = 0.06→0.19; Ti = 0.07→0.26 p.f.u.

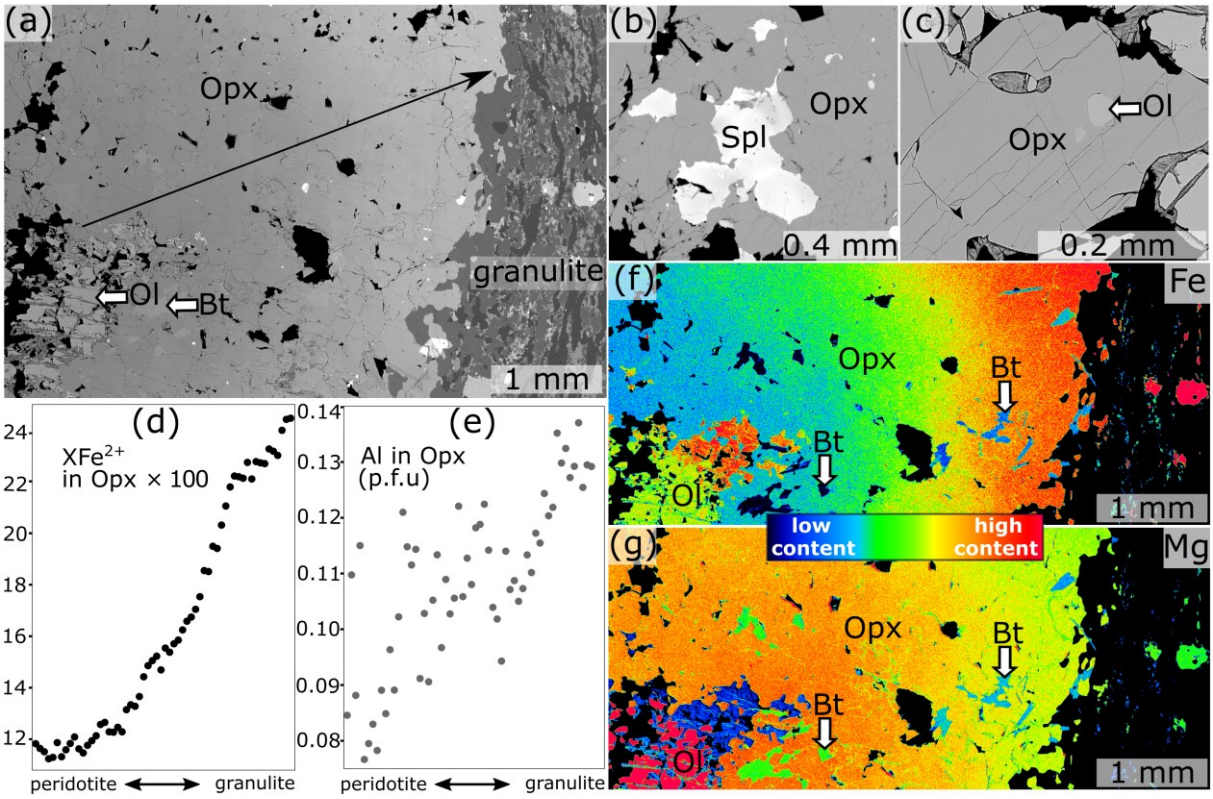

Figure II. 6: Back-scattered electron images (a–c), compositional diagrams (d–e) and maps (f–g) of peridotite xenolith and orthopyroxene corona at the contact with intermediate granulite. a) Corona at the contact of the mantle xenolith and host granulite. b) Spinel in orthopyroxene. c) Olivine inclusions in orthopyroxene. d–e) Diagrams showing increase of XFe^{2+} and Al in orthopyroxene towards the granulite. f–g) Compositional maps of Fe and Mg.

Table II. 3: Representative mineral analyses of garnet clinopyroxenite and its Opx–Pl corona in wt. %.

Lithology	Garnet clinopyroxenite xenolith											
Thin-section	A3	A3	A3	A3	A3	A3	A3	A3	A3	A3	A3	A3
Mineral	Grt	Grt	Grt	Grt	Cpx	Cpx	Pl	Pl	Pl	Opx	Opx	Opx
Analysis	line 20	line 40	line-02	line 01	A3-Cpx-12	A3-Cpx-11	Pl-08	Pl-104	Pl-06	Opx-101	Opx-14	Opx-09
Position	Grt core	Grt rim	Grt outermost rim extending into the Opx–Pl corona	Grt rim extending into the Opx–Pl corona	Cpx core	Cpx rim	symplectite around Grt	inclusion in Cpx	between Cpx grains	symplectite around Grt	symplectite around Grt	Opx lamella in Cpx
SiO_2	40.96	40.32	40.06	39.99	51.64	52.23	48.85	54.38	53.06	53.91	53.83	53.42
P_2O_5	0.12	0.05	0.06	0.03	0.14	0.14	0.09	0.14	0.10	b.d.	b.d.	b.d.
TiO_2	0.21	0.16	0.21	0.03	0.39	0.32	b.d.	b.d.	b.d.	0.07	0.06	0.07
Cr_2O_3	0.07	0.17	0.17	0.38	0.17	0.11	b.d.	0.02	0.03	0.11	0.12	0.07
Al_2O_3	23.51	22.59	22.61	22.92	5.83	4.76	32.40	28.08	29.67	4.35	3.81	3.28
FeO	11.60	15.33	15.63	17.97	4.21	3.65	0.21	0.16	0.06	10.10	11.30	12.60
MnO	0.25	0.47	0.40	0.49	0.10	0.07	b.d.	b.d.	b.d.	0.10	0.10	0.12
MgO	16.55	13.91	14.10	14.21	15.33	14.93	b.d.	b.d.	b.d.	30.17	29.80	28.92
BaO	b.d.	b.d.	b.d.	b.d.	0.03	b.d.	0.02	b.d.	b.d.	b.d.	b.d.	b.d.
CaO	6.40	5.92	6.05	3.74	21.41	23.13	15.40	11.03	12.39	0.27	0.39	0.34
Na_2O	b.d.	b.d.	0.02	0.02	0.59	0.57	2.66	4.96	4.27	b.d.	0.02	b.d.
K_2O	b.d.	b.d.	b.d.	b.d.	b.d.	b.d.	0.07	0.36	0.23	b.d.	b.d.	b.d.
NiO	b.d.	b.d.	b.d.	b.d.	0.02	0.03	b.d.	b.d.	b.d.	0.05	0.02	b.d.
ZnO	b.d.	b.d.	0.03	b.d.	b.d.	b.d.	b.d.	b.d.	0.05	0.02	b.d.	0.06
Cl	b.d.	b.d.	b.d.	b.d.	b.d.	b.d.	b.d.	b.d.	b.d.	b.d.	b.d.	b.d.
F	b.d.	b.d.	b.d.	b.d.	b.d.	b.d.	b.d.	b.d.	b.d.	b.d.	b.d.	b.d.
Total	99.68	98.90	99.34	99.78	99.87	99.93	99.70	99.12	99.87	99.14	99.45	98.89
Cations⁄Charges	8⁄24	8⁄24	8⁄24	8⁄24	4⁄12	4⁄12	5⁄16	5⁄16	5⁄16	4⁄12	4⁄12	4⁄12
Si	2.97	3.00	2.97	2.96	1.88	1.91	2.24	2.48	2.41	1.91	1.91	1.92
P	0.01	0.00	0.00	0.00	0.00	0.00	0.00	0.01	0.00	–	–	–
Ti	0.01	0.01	0.01	0.00	0.01	0.01	–	–	–	0.00	0.00	0.00
Cr	0.00	0.01	0.01	0.02	0.00	0.00	–	0.00	0.00	0.00	0.00	0.00
Al	2.01	1.98	1.97	2.00	0.25	0.20	1.75	1.51	1.59	0.18	0.16	0.14
Fe^{2+}	0.69	0.95	0.92	1.06	0.13	0.11	0.01	0.01	0.00	0.30	0.31	0.35
Fe^{3+}	0.01	0.00	0.05	0.05	0.00	0.00	0.00	0.00	0.00	0.00	0.02	0.03
Mn	0.02	0.03	0.02	0.03	0.00	0.00	–	–	–	0.00	0.00	0.00
Mg	1.79	1.54	1.56	1.57	0.83	0.81	–	–	–	1.59	1.57	1.55
Ba	–	–	–	–	0.00	–	0.00	–	–	–	–	–
Ca	0.50	0.47	0.48	0.30	0.84	0.90	0.76	0.54	0.60	0.01	0.01	0.01
Na	–	–	0.00	0.00	0.04	0.04	0.24	0.44	0.38	–	0.00	–
K	–	–	–	–	–	–	0.00	0.02	0.01	–	–	–
Ni	–	–	–	–	0.00	0.00	–	–	–	0.00	0.00	–
Zn	–	–	0.00	–	–	–	–	–	0.00	0.00	–	0.00
Cl	–	–	–	–	–	–	–	–	–	–	–	–
F	–	–	–	–	–	–	–	–	–	–	–	–
XFe^{2+}	0.28	0.38	0.37	0.40	0.13	0.12				0.16	0.17	0.19

b.d. below detection limit. * – Fe^{tot}

Table II. 3 (continued): Representative mineral analyses of garnet clinopyroxenite and its Opx–Pl corona in wt. %.

Lithology	Garnet clinopyroxenite xenolith				Opx–Pl corona around Grt-clinopyroxenite xenolith							
Thin-section	A3	A3	A3	A3	A3	A3	A4	A3	A3	A3	A3	A3
Mineral	Opx	Amp	Amp	Amp	Grt	Grt	Grt	Pl	Pl	Opx	Opx	Bt
Analysis	Opx-88	Amp-02	Amp-90	Amp-10	line 15	line 01	line 30	Pl-15	Pl-47	Opx-16	Opx-50	Bt-57
Position	Opx lamella in Cpx	inclusion in Grt	lamella in Cpx	symplectite around Grt	Grt core	Grt rim	Grt outermost rim	near Grt-clinopyroxenite xenolith	near intermediate granulite	near Grt-clinopyroxenite xenolith	near intermediate granulite	at Grt rim
SiO_2	52.31	43.64	44.31	43.88	39.61	39.49	38.61	56.10	60.01	54.31	53.16	38.51
P_2O_5	b.d.	0.11	0.13	0.09	0.07	0.06	0.05	0.07	0.02	b.d.	b.d.	b.d.
TiO_2	0.05	1.92	1.03	1.43	0.26	0.17	b.d.	b.d.	b.d.	0.12	0.06	4.13
Cr_2O_3	0.08	0.07	0.20	0.25	0.16	0.35	0.85	b.d.	b.d.	0.17	0.21	1.22
Al_2O_3	4.83	14.17	14.10	13.48	22.34	21.96	21.91	27.94	25.48	1.90	2.60	15.89
FeO	12.19	2.99	4.60	5.54	17.23	20.60	20.80	0.23	0.17	14.60	16.19	7.60
MnO	0.11	0.02	0.03	0.06	0.37	0.63	0.67	0.02	b.d.	0.16	0.21	b.d.
MgO	28.36	17.83	16.98	16.27	13.16	10.69	11.73	0.02	0.02	27.55	25.50	18.18
BaO	b.d.	b.d.	b.d.	b.d.	b.d.	b.d.	b.d.	0.02	b.d.	b.d.	0.02	0.14
CaO	0.42	12.27	12.38	12.20	6.02	5.44	3.67	10.33	7.13	0.43	0.17	0.07
Na_2O	b.d.	2.37	1.73	1.44	b.d.	b.d.	b.d.	5.35	6.99	0.02	b.d.	0.07
K_2O	0.02	0.66	1.23	1.53	b.d.	b.d.	b.d.	0.29	0.53	b.d.	b.d.	8.40
NiO	0.07	0.06	0.05	b.d.	b.d.	0.02	b.d.	0.02	0.05	0.02	b.d.	0.02
ZnO	0.07	b.d.	0.02	0.03	b.d.	b.d.	0.05	b.d.	b.d.	0.03	b.d.	b.d.
Cl	b.d.	0.04	b.d.	0.10	b.d.	b.d.	b.d.	b.d.	b.d.	b.d.	b.d.	0.07
F	b.d.	0.43	0.26	0.39	b.d.	b.d.	b.d.	b.d.	b.d.	b.d.	b.d.	0.54
Total	98.51	96.11	96.80	96.19	99.23	99.41	98.33	100.37	100.38	99.30	98.12	94.23
Cations⁄Charges	4⁄12	23 O eq.	23 O eq.	23 O eq.	8⁄24	8⁄24	8⁄24	5⁄16	5⁄16	4⁄12	4⁄12	8⁄22
Si	1.88	6.25	6.34	6.36	2.96	3.00	2.95	2.52	2.68	1.96	1.96	2.79
P	–	0.01	0.01	0.01	0.00	0.00	0.00	0.00	0.00	–	–	–
Ti	0.00	0.21	0.11	0.16	0.01	0.01	–	–	–	0.00	0.00	0.23
Cr	0.00	0.01	0.02	0.03	0.01	0.02	0.05	–	–	0.00	0.01	0.07
Al	0.20	2.39	2.38	2.30	1.97	1.96	1.97	1.48	1.34	0.08	0.11	1.36
Fe^{2+}	0.34	0.30	0.47	0.60	1.01	1.31	1.27	0.01	0.01	0.44	0.50	0.46*
Fe^{3+}	0.03	0.06	0.08	0.07	0.07	0.00	0.06	0.00	0.00	0.00	0.00	–
Mn	0.00	0.00	0.00	0.01	0.02	0.04	0.04	0.00	–	0.00	0.01	–
Mg	1.52	3.81	3.62	3.51	1.46	1.21	1.34	0.00	0.00	1.48	1.40	1.96
Ba	–	–	–	–	–	–	–	0.00	–	–	0.00	0.00
Ca	0.02	1.88	1.90	1.89	0.48	0.44	0.30	0.50	0.34	0.02	0.01	0.01
Na	–	0.66	0.48	0.40	–	–	–	0.47	0.60	0.00	–	0.01
K	0.00	0.12	0.23	0.28	–	–	–	0.02	0.03	–	–	0.78
Ni	0.00	0.01	0.01	–	–	0.00	–	0.00	0.00	0.00	–	0.00
Zn	0.00	–	0.00	0.00	–	–	0.00	–	–	0.00	–	–
Cl	–	0.01	–	0.02	–	–	–	–	–	–	–	0.01
F	–	0.19	0.26	0.18	–	–	–	–	–	–	–	0.12
XFe^{2+}	0.18	0.07	0.12	0.15	0.41	0.52	0.49			0.23	0.26	$XFe^{tot} = 0.19$

b.d. below detection limit. * – Fe^{tot}

Table II. 4: Representative mineral analyses of peridotite xenolith and its Opx corona in wt. %.

Lithology	Peridotite xenolith				Orthopyroxene corona around peridotite xenolith			
Thin-section	D554x11-Ol	D554x11-Ol	D554x11-Ol	D554x11-Ol	D554x11-Ol	D554x11-Ol	D554x11-Ol	D554x11-Ol
Mineral	Ol	Ol	Spl	Spl	Opx	Opx	Bt	Bt
Analysis	Ol-18	Ol-19	Spl-31	Spl-34	line-01	line-60	Bt-03	Bt-40
Position	Preserved grain in Opx corona	Preserved grain in Opx corona	Preserved grain in Opx corona	Preserved grain in Opx corona	Opx corona near Ol	Opx corona near intermediate granulite	Opx corona near intermediate granulite	Opx corona near Ol
SiO_2	42.27	41.03	0.03	0.03	56.25	53.16	39.06	40.40
P_2O_5	0.05	b.d.	b.d.	b.d.	b.d.	0.02	b.d.	b.d.
TiO_2	b.d.	b.d.	0.03	0.07	0.05	0.07	4.82	1.32
Cr_2O_3	0.04	b.d.	29.43	23.50	0.15	0.14	0.50	1.04
Al_2O_3	0.25	b.d.	38.54	44.15	2.04	2.98	15.87	16.25
FeO	10.75	10.82	17.40	14.96	7.70	15.13	7.49	2.77
MnO	0.09	0.10	0.09	0.09	0.13	0.16	b.d.	0.03
MgO	46.17	47.18	12.71	15.19	32.21	26.20	18.08	23.48
BaO	b.d.	b.d.	b.d.	b.d.	0.02	0.02	0.11	b.d.
CaO	0.03	0.02	b.d.	b.d.	0.10	0.15	0.05	0.04
Na_2O	b.d.	b.d.	0.02	0.02	b.d.	b.d.	0.10	0.16
K_2O	b.d.	b.d.	b.d.	b.d.	b.d.	b.d.	8.33	9.57
NiO	1.01	1.15	0.29	0.57	0.25	0.05	0.17	0.47
ZnO	0.08	0.07	0.71	0.57	0.02	b.d.	b.d.	0.00
Cl	b.d.	b.d.	b.d.	b.d.	b.d.	b.d.	0.08	0.09
F	b.d.	b.d.	b.d.	b.d.	b.d.	b.d.	0.52	0.90
Total	100.74	100.37	99.26	99.13	98.93	98.07	94.59	95.53
Cations⁄Charges	3⁄8	3⁄8	3⁄8	3⁄8	4⁄12	4⁄12	8⁄11	8⁄11
Si	1.04	1.01	0.00	0.00	1.98	1.95	2.81	2.84
P	0.00	–	–	–	–	0.00	–	–
Ti	–	–	0.00	0.00	0.00	0.00	0.26	0.07
Cr	0.00	–	0.68	0.52	0.00	0.00	0.03	0.06
Al	0.01	–	1.32	1.46	0.08	0.13	1.35	1.35
Fe^{2+}	0.22	0.22	0.42	0.34	0.23	0.46	0.5*	0.16*
Fe^{3+}	0.00	0.00	0.00	0.01	0.00	0.00	–	–
Mn	0.00	0.00	0.00	0.00	0.00	0.00	–	0.00
Mg	1.70	1.74	0.55	0.64	1.69	1.43	1.94	2.46
Ba	–	–	–	–	0.00	0.00	0.00	–
Ca	0.00	0.00	–	–	0.00	0.01	0.00	0.00
Na	–	–	0.00	0.00	–	–	0.01	0.02
K	–	–	–	–	–	–	0.77	0.86
Ni	0.02	0.02	0.01	0.01	0.01	0.00	0.01	0.03
Zn	0.00	0.00	0.02	0.01	0.00	–	–	0.00
Cl	–	–	–	–	–	–	0.01	0.01
F	–	–	–	–	–	–	0.12	0.20
XFe^{2+}	0.12	0.11	0.43	0.35	0.12	0.24	$XFe^{tot} = 0.19$	$XFe^{tot} = 0.06$

b.d. below detection limit. * – Fe^{tot}

4 Phase stability modelling

P–T pseudosection modelling was applied to estimate the pressure–temperature (P–T) conditions during metamorphism of the intermediate granulite, its garnet clinopyroxenite xenolith, and the corona developed at their contacts (all from the sample A3). The current mineral assemblage of the intermediate granulite (Grt, Opx, Qz, Pl, Kfs) is well equilibrated and without any pronounced compositional zoning of the phases, and therefore it can be safely assumed that this mineral assemblage and that of the coronae around the mantle xenoliths, evolved simultaneously under the same P–T conditions. Therefore, the matrix mineral assemblage and the chemical compositions of the granulite minerals were used to estimate the P–T conditions of the coronae formation.

No P–T pseudosection was constructed for the peridotite xenolith, because of the difficulty in estimating its composition and mineral assemblage prior to interaction with the host granulite, due to the small amount of preserved grains surrounded by an Opx-corona.

4.1 Methodology of pseudosection modelling

The P–T pseudosection modelling was carried out with the software THERMOCALC 3.50 with the internally consistent thermodynamic dataset (Holland & Powell, 2011, dataset version 6.2). The pseudosections were plotted by the *pypsbuilder* software (Lexa, 2020). The chemical compositions of the modelled lithologies were estimated by averaging representative area analyses in sample A3 acquired by SEM–EDS in a scanning mode. The bulk-rock chemical analyses of intermediate granulite and garnet clinopyroxenite are given in Table II. 5.

For the intermediate granulite, the area analyses were measured around a garnet clinopyroxenite xenolith (away from the Kfs-poor reaction halo), and for the garnet clinopyroxenite, they were obtained from a preserved part of the xenolith (except the Opx–Pl corona). In order to use the Ti-bearing system, the O content for both lithologies was set to very low value of 0.01 mol. % based on the observed mineral assemblage lacking any Fe^{3+}-rich phase and very low Fe^{3+} contents estimated in the analysed minerals (Table II. 2, Table II. 3).

The P–T pseudosection modelling for the intermediate granulite was undertaken in the system $MnO–Na_2O–CaO–K_2O–FeO–MgO–Al_2O_3–SiO_2–H_2O–TiO_2–O_2$ (MnNCKFMASHTO). The following mixing models were used: clinopyroxene for metabasic rocks (Green *et al.*, 2016), garnet, orthopyroxene, biotite, cordierite, ilmenite, muscovite and melt models for metapelites (White *et al.*, 2014) and ternary plagioclase/K-feldspar were calculated with models for ternary

feldspar (model C1 for Pl; Holland & Powell, 2003). The amount of H_2O was set to 1 mol. %, a value estimated from phase equilibria calculations of granulites from Lower Austria (e.g. Racek *et al*., 2006, 2008).

Calculations for garnet clinopyroxenite was undertaken in the system Na_2O–CaO–K_2O–FeO–MgO–Al_2O_3–SiO_2–H_2O–TiO_2–O_2 (NCKFMASHTO). The following mixing models were used: olivine (Holland & Powell, 2011), clinopyroxene, amphibole, and melt for metabasic rocks (Green *et al.*, 2016), garnet, orthopyroxene, and ilmenite models for metapelites (White *et al.*, 2014), and plagioclase was calculated with the model for ternary feldspar (model I1; Holland & Powell, 2003). The amount of H_2O was set to 0.8 mol. % according to the whole-rock chemical analyses of garnet clinopyroxenites from the St. Leonhard granulite massif (Becker, 1996a). We assume that the potassium content was increased due to the interaction with the surrounding granulite, and therefore K_2O was set to 0.001 mol. % for modelling purposes.

4.2 P–T pseudosection modelling for intermediate granulite hosting mantle xenoliths

The mineral assemblage presumably preserved from peak metamorphic conditions is garnet, orthopyroxene, K-feldspar, quartz, and rutile, which corresponds to the compatibility field Grt–Kfs–Pl–Opx–Qz–Rt–Liq, where composition isopleths of the garnet core $Prp_{37.6}Alm_{51.2}Grs_{9.8}Sps_{1.5}$; $XFe^{2+} = 0.58$ intersect in a P–T range of 1.0–1.2 GPa and 900–1000 °C (Figure II. 7). This field is closely adjacent to the compatibility field of biotite (towards lower T) and of ilmenite (towards lower P). The common presence of biotite in the matrix in the vicinity of orthopyroxene and garnet, as well as the occurrence of ilmenite in the matrix, are probably a result of further cooling and decompression, which caused the formation of biotite at the expense of orthopyroxene and garnet, and transformation of rutile to ilmenite. This is also consistent with the observed diffusional modification of the garnet rims characterized mainly by the increase of Fe and decrease of Ca contents to the composition $Prp_{37.0}Alm_{54.9}Grs_{6.4}Sps_{1.6}$; $XFe^{2+} = 0.60$. The compositional isopleths of the garnet rim intersect

at 0.7–0.9 GPa and 800–880 °C. This field can be considered as cooling conditions associated with the formation of biotite and ilmenite.

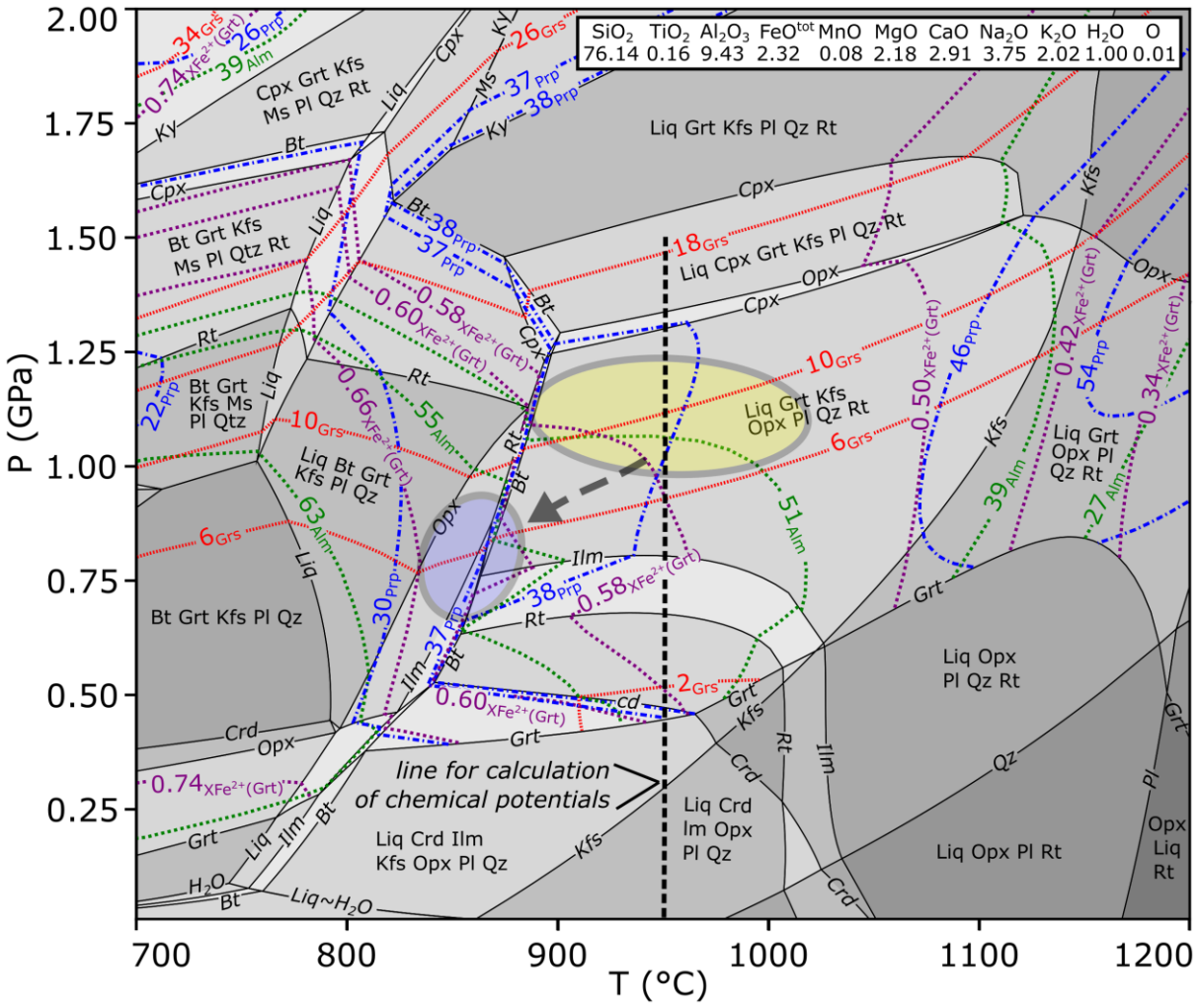

Figure II. 7: P–T pseudosection for the intermediate granulite with composition isopleths of garnet. The conditions of formation of the matrix assemblage (compatibility field of Liq–Grt–Kfs–Opx–Pl–Qz–Rt) were estimated at 1.0–1.2 GPa and 900–1000 °C (large yellow ellipse). Subsequent cooling took place at 0.7–0.9 GPa and 800–880 °C (small blue ellipse).

4.3 P–T pseudosection modelling for garnet clinopyroxenite xenolith in intermediate granulite

The calculated P–T pseudosection for the garnet clinopyroxenite xenolith is shown in the Figure II. 8. The mineral assemblage in the preserved part of the xenolith is dominated by garnet and clinopyroxene, with subordinate orthopyroxene, amphibole, and plagioclase. This corresponds to the boundary between the compatibility fields Liq–Cpx–Grt–Rt, Liq–Cpx–Grt–Pl–Rt, and Liq–Cpx–Grt–Pl–Rt–Opx, where composition isopleths of garnet core

$Prp_{59.7}Alm_{23.1}Grs_{16.6}Sps_{0.5}$; XFe^{2+} = 0.28 intersect in a P–T range of 1.1–1.4 GPa and 1150–1190 °C. Since the sample probably has already re-equilibrated and interacted with the surrounding granulite to some extent during decompression, these conditions seem not completely accurate, and therefore the compatibility field was extended considering the mineral association to 960–1220 °C. The compositions of the garnet cores may be better preserved than the compositions of its rims, which extend into the Opx–Pl corona, and therefore intersection of the garnet isopleths of the rim compositions are considered to have no physical meaning.

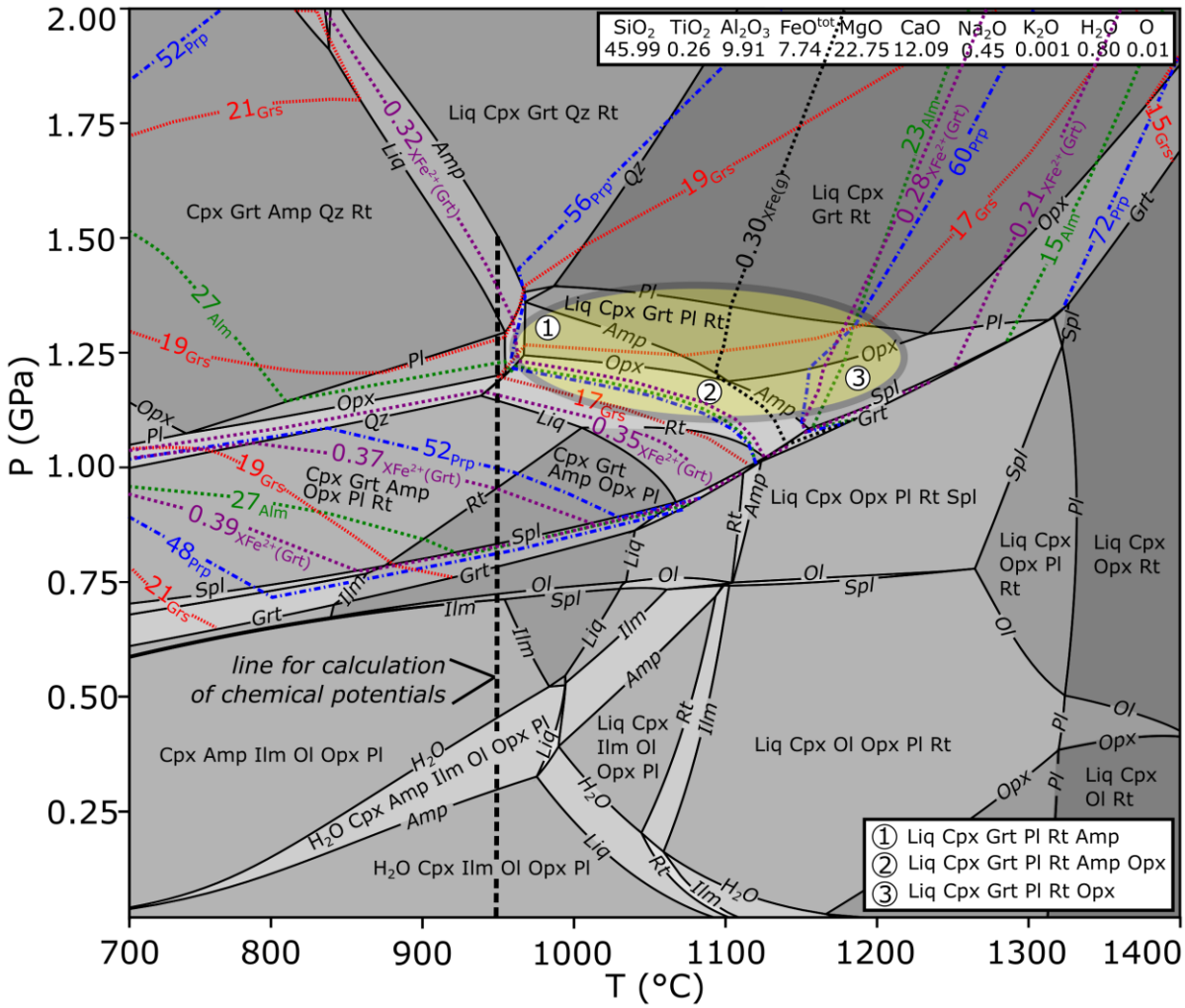

Figure II. 8: P–T pseudosection of garnet clinopyroxenite xenolith with composition isopleths of garnet. The formation of the preserved assemblage was constrained to 1.1–1.4 GPa and 960–1220 °C (yellow ellipse) at the transition between the compatibility fields Liq–Cpx–Grt–Rt, Liq–Cpx–Grt–Pl–Rt, and Liq–Cpx–Grt–Pl–Rt–Opx.

Table II. 5: Bulk-rock chemical analyses from SEM-EDS (in wt. %)

Lithology	Ky-bearing felsic granulite	Ky-bearing felsic granulite	Ky-bearing felsic granulite	intermediate granulite*	Kfs-depleted zone in intermediate granulite – spectrum 1	Kfs-depleted zone in intermediate granulite – spectrum 2	Opx–Pl corona in garnet clinopyroxenite xenolith – spectrum 1	Opx–Pl corona in garnet clinopyroxenite xenolith – spectrum 2	Opx–Pl corona around garnet clinopyroxenite xenolith – spectrum 3	Garnet clinopyroxenite xenolith*
Thin-section	D441	D485B	D461	A3	A3	A3	A3	A3	A3	A3
Abbreviation in Fig. 10	Ky-Gr	Ky-Gr	Ky-Gr	Opx-Gr	GrI	GrII	CorI	CorII	CorIII	UB
SiO_2	72.50	73.05	69.50	71.54	75.54	72.61	57.08	52.57	49.64	45.45
TiO_2	0.25	0.23	0.57	0.21	0.13	0.18	0.51	0.28	0.30	0.34
Al_2O_3	13.08	13.45	15.50	15.03	14.91	15.28	13.56	13.89	16.11	16.61
Cr_2O_3	b.d.	b.d.	b.d.	b.d.	b.d.	b.d.	0.14	0.22	0.18	0.14
FeO^{tot}	1.35	1.92	3.06	2.61	0.75	0.76	9.40	11.15	10.50	9.15
MnO	0.03	0.04	0.04	0.08	b.d.	b.d.	0.12	0.16	0.16	0.15
MgO	0.34	0.53	0.98	1.37	0.62	0.73	12.10	14.18	13.88	15.08
CaO	1.10	1.24	2.09	2.55	3.85	4.25	3.40	3.68	5.20	11.15
Na_2O	3.09	3.46	3.42	3.63	4.60	4.59	2.91	2.17	1.71	0.46
K_2O	5.34	4.54	4.62	2.98	0.67	0.47	0.62	0.38	0.40	0.26
Total	97.08	98.45	99.78	100.00	101.07	98.86	99.69	98.45	97.90	98.66

* Samples to which phase stability modelling was applied. b.d. below detection limit.

4.4 Chemical potentials (μ) across P–T pseudosections of intermediate granulite and garnet clinopyroxenite

Formation of the Opx–Pl coronae around the garnet clinopyroxenite requires chemical mass transport between the garnet clinopyroxenite and the surrounding granulite. Such a chemical mass transport can occur either by advection, which requires movement of melt or fluid through the pore spaces of a rock, or by diffusion along the grain boundaries or through their interiors. As the Opx–Pl coronae form a concentric structure enveloping the entire garnet clinopyroxenite, chemical mass transfer by advection can be excluded, as it would require a fluid source or sink within the garnet clinopyroxenite, which is hardly conceivable due to the generally low H_2O contents in standard mantle rocks (e.g. Li *et al., 2019*; Bell & Rossman, 1992). Even though the appearance of plagioclase among clinopyroxene grains in the garnet clinopyroxenite implies crystallization from melt (Figure II. 3 f; Hasalová *et al.,* 2008; Stuart *et al*., 2018), the melt had to be probably largely stagnant. The presence of such a melt, however, would greatly enhance diffusion mediated chemical mass transfer between the garnet clinopyroxenite and the host granulite.

In any case, diffusion of chemical components would be driven by gradients in the respective chemical potentials. We therefore calculated the chemical potentials of the system components in the two lithologies in order to assess the driving force for the exchange of chemical components across the interface between the garnet clinopyroxenite and the host granulite. The rationale is that, during chemical mass transport by diffusion, the chemical components migrate "downhill" with respect to their chemical potentials (e.g. White *et al.,* 2008; Štípská *et al*., 2014b; Gaidies *et al.*, 2017; Schorn & Diener, 2017; Schorn, 2022), i.e., from locations where their chemical potential (μ) is high towards those, where their chemical potential is low (Figure II. 9).

Chemical potentials were calculated in P–T pseudosections of intermediate granulite and the enclosed garnet clinopyroxenite xenolith (sample A3) along the 950 °C isotherm with

decreasing pressure, starting at 1.5 GPa, where equilibration P–T conditions for intermediate granulite were inferred from the assemblage and garnet core composition (Figure II. 7 and Figure II. 8).

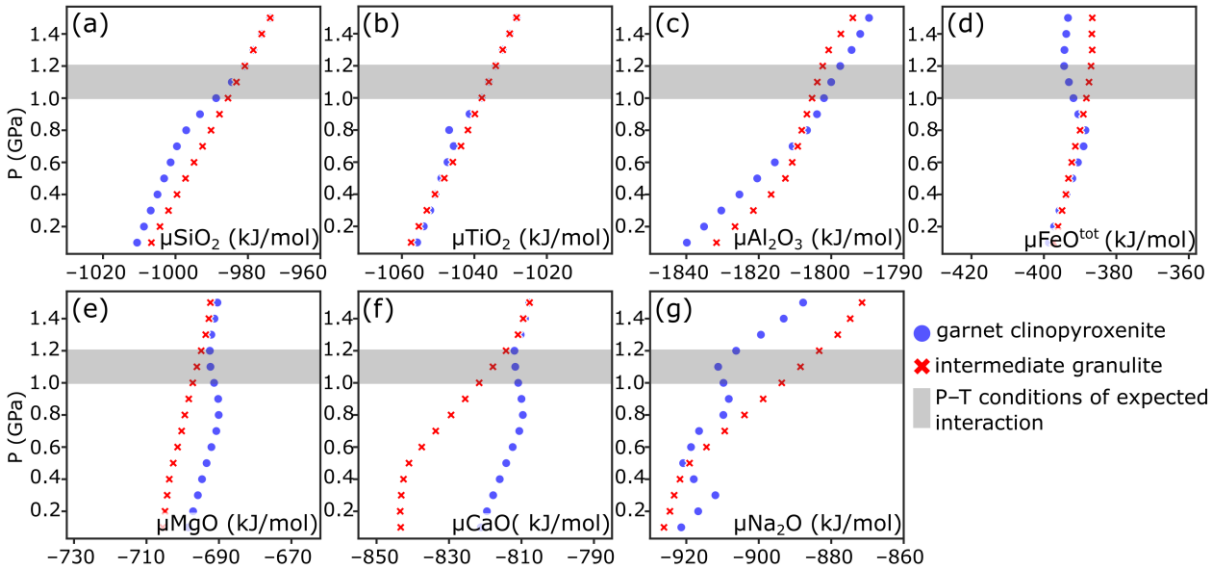

Figure II. 9: a–g) Comparison of chemical potentials for garnet clinopyroxenite xenolith and host intermediate granulite calculated from both P–T pseudosections at 950 °C. Grey shaded area at 1.0–1.2 GPa corresponds to conditions of their expected interaction (see Figure II. 7 and Figure II. 8).

For both lithologies μSiO2 is identical from 1.5 to 1.0 GPa. Only at pressures below about 1.0 GPa, μSiO_2 is higher in the felsic granulite than in the garnet clinopyroxenite (Figure II. 9a). Furthermore, μTiO_2 is almost identical for both lithologies, except at 0.8 GPa, where it is slightly lower in the garnet clinopyroxenite than in the felsic granulite (Figure II. 9b). From 1.5 GPa to 0.65 GPa, μAl_2O_3 is lower for the felsic granulite than for the clinopyroxenite, this is reversed below 0.65 GPa (Figure II. 9c). Intermediate granulite shows higher μFeO^{tot} compared to the clinopyroxenite between 1.5 and 0.8 GPa, with further decreasing pressure μFeO^{tot} is very similar in both lithologies (Figure II. 9d). Both lithologies show almost identical μMgO and μCaO evolutions between 1.5 and 1.25 GPa, below 1.2 GPa they diverge and μMgO and μCaO of the intermediate granulite are lower compared to the garnet clinopyroxenite (Figure

II. 9e, f). With decreasing pressure, μNa_2O of the intermediate granulite decreases, but is higher than for the garnet clinopyroxenite down to 0.4 GPa, where the two curves swap (Figure II. 9g).

Summarizing, in the P–T window determined for the assumed interaction between the mantle xenoliths and the felsic granulite (900–1000 °C, 1.0–1.2 GPa), the only components for which there is no chemical driving force for diffusion from one lithology into the other are Si and Ti.

5 LOCAL BULK COMPOSITION OF THE GARNET CLINOPYROXENITE XENOLITH A3, ITS INTERMEDIATE GRANULITE HOST AND THEIR CONTACT ZONE

5.1 Conventional assessment of chemical changes across the intermediate granulite–garnet clinopyroxenite interface

This section summarizes the results from SEM–EDS area analyses taken from 'profiles' across the contact zone between the intermediate granulite and its garnet clinopyroxenite xenolith (Table II. 5). For convenience, the analysed area was divided into five contiguous concentric bands that include, if going inward, two for the Kfs-poor zone in the intermediate granulite (GrI → GrII), and three for the Opx–Pl corona rimming the xenolith (CorI → CorIII) (Figure II. 10).

These compositions were also compared with averaged SEM–EDS area analyses of the intermediate granulite (Opx-Gr) and three of the felsic Ky-granulite (Ky-Gr) from the St. Leonhard massif. Lastly, the ultrabasic (garnet clinopyroxenite) xenolith itself is represented by a set of area analyses labelled 'UB'.

Examining Figure II. 10, there is no apparent change in SiO_2 between both granulite types and the Kfs-poor zone, followed by a sharp drop towards the xenolith and its Opx–Pl corona followed by a linear decrease of SiO_2 towards the preserved part of the xenolith (Figure II. 10a). The TiO_2 shows a peak at the outer edge of the corona, but the overall TiO_2 concentrations remain below 0.7 wt. % (Figure II. 10b). The Al_2O_3 content increases slightly from the Ky-granulites to the Kfs-poor zone; in the corona it is highly and unsystematically scattered (Figure II. 10c). From the granulite towards the Kfs-poor zone, there is a slight decrease in FeO^{tot}, but this oxide is strongly enriched in the corona and the xenolith (Figure II. 10d). In detail, FeO^{tot} enrichment can be seen in the internal parts of the corona compared to the xenolith itself and the external margins. The MgO content remains very low in the granulites and in the Kfs-poor zone. Within the xenolith, MgO gradually increases from corona margins towards the preserved

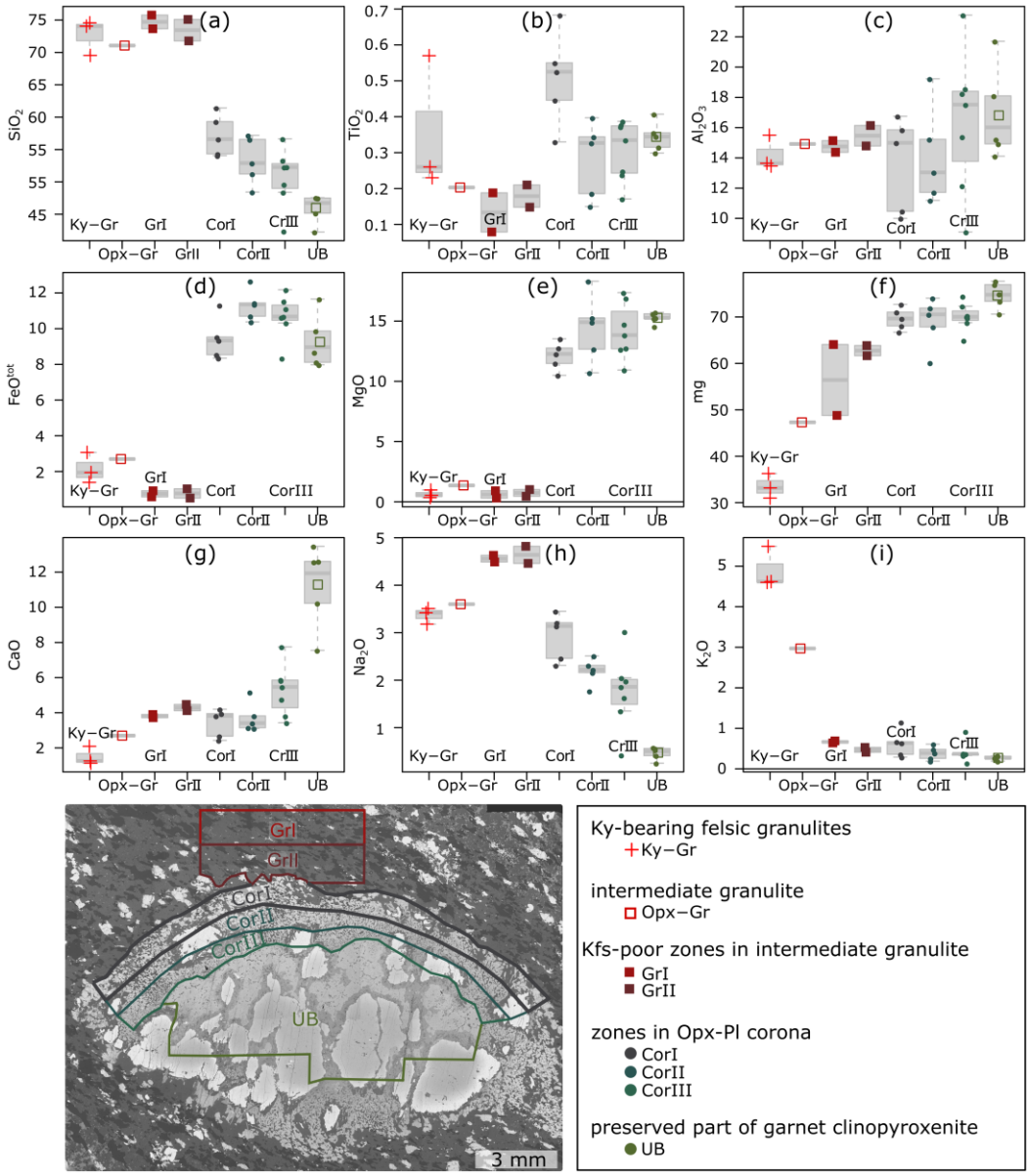

Figure II. 10: a–i) Boxplots of oxide concentrations (wt. %) from area SEM–EDS analyses of three typical Ky-granulites from St. Leonhard granulite massif (Ky–Gr) and a 'profile' from the sample A3 including the Opx granulite (Opx–Gr), its Kfs-poor zones (GrI → GrII), the corona (CorI → CorII → CorIII), and the garnet clinopyroxenite xenolith (UB). The sampled domains are outlined in the BSE image below.

internal part (Figure II. 10e). As a consequence, the mg number [MgO/(MgO + FeO^{tot}) in mol. %] increases gradually from the Ky-bearing granulite towards the xenolith (Figure II. 10f). The CaO content gradually increases from the Ky-bearing granulite to the Kfs-poor zone, drops slightly at the outer edge of the corona, and then increases sharply towards the xenolith (Figure II. 10g). The Kfs-poor zone is enriched in Na_2O compared to the Ky- and Opx-bearing granulite

and the corona, and contents of this oxide drop quickly across the corona towards the xenolith (Figure II. 10h). The K_2O decreases sharply from the Ky-bearing granulite (~5 wt. %) through the intermediate granulite (~3 wt. %) towards the Kfs-poor zone. Further inwards through the Opx–Pl corona, a further gentle decrease can be seen in K_2O (Figure II. 10i).

6 Discussion

In the studied intermediate granulite centimetre-sized mantle xenoliths occur surrounded by coronae, which formed at the expense of the xenoliths. The predominant xenolith type is represented by garnet clinopyroxenite, which is separated from the granulite by Opx–Pl coronae. Peridotite xenoliths formed by a few preserved grains of olivine surrounded by an almost monomineralic Opx-coronae are comparatively rare.

The modification of the xenoliths and of the host felsic granulite took place due to a mutual exchange of chemical components driven by the compositional contrast between the two lithologies of mantle and crustal origin. The exchange took place at least on a centimetre to decimetre scale and was likely mediated by diffusion along the grain- and phase boundaries or through the grains' interiors.

6.1 Net chemical changes associated with the garnet clinopyroxenite → Opx–Pl corona transformation

The observed continuity of garnet crystals projecting from the preserved garnet clinopyroxenite xenolith into the Opx–Pl corona indicates that the latter formed at the expense of the mantle xenolith rather than of the surrounding granulite. From the chemical compositions shown in Figure II. 10 we infer that the outer parts of the original garnet clinopyroxenite xenolith behaved as an open-system during interaction with the felsic granulite and progressive replacement of the clinopyroxenite by the Opx–Pl corona. The assessment of open-/closed-system character always depends on the scale of equilibration (e.g. Carmichael, 1969).

Comparing the chemical compositions of the preserved part of the mantle xenolith with its corona can give information on possible chemical component gains or losses during corona formation, which can be also extrapolated further into the felsic host. Considering that there is no *a priori* reason why the overall mass of the original garnet clinopyroxenite should be preserved after corona formation, the compositional 'trends' shown in Figure II. 10 would be simplistic, if not misleading.

For a quantitative assessment of the gains/losses of individual chemical species during open-system alteration, one needs to find an immobile chemical component that can be used as a framework to constrain the possible change in the overall mass of the whole system and thus also in the mass concentrations of the remaining chemical species (Ague, 1994, 2003; Ague & Van Haren, 1996). Assuming that the corona was derived from the garnet clinopyroxenite, comparison of the area-averaged analyses of the preserved xenolith and its Opx–Pl corona (Table II. 5) can provide insight into possible component gains/losses. For this purpose, an average of the area analyses of the xenolith A3 served as the "fresh" rock (UB in Figure II. 10); the average composition of the Opx–Pl corona (CorI to CorIII) was taken as the "altered" rock. At the P–T conditions prevailing during the interaction between the garnet clinopyroxenite xenoliths and the felsic granulites, most components are likely to be mobile and would possibly move along suitable chemical potential gradients.

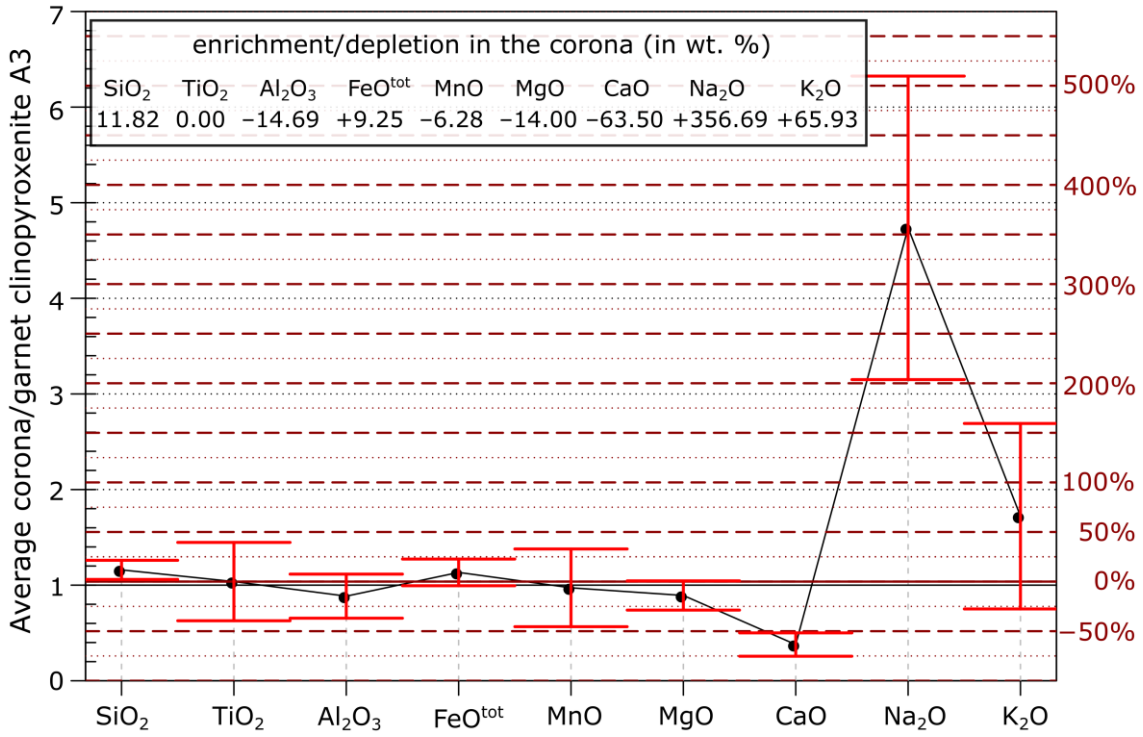

Figure II. 11: Quantification of the major-element mobility in the course of Opx–Pl corona formation around the garnet clinopyroxenite xenolith by means of the concentration ratio diagram (Ague, 2003). An average of the area analyses of the xenolith A3 was taken as the "fresh" rock; the "altered rock" is represented by averaged analyses from all the three bands distinguished in the corona. Error bars are ± 1 sigma. Titanium was selected as the immobile component based on the chemical potential diagrams (Figure II. 9).

From the chemical potential trends shown in Figure II. 9 over the likely pressure interval determined for the interaction between the two lithologies, TiO_2 was chosen as the immobile component. Based on the concentration ratio diagrams (Ague, 2003), implemented in our R package *GCDkit* (Janoušek *et al.*, 2006), the most mobile components seem alkalies (Figure II. 11): Na_2O shows more than threefold and K_2O 66% enrichment in the corona if compared with the preserved part of the xenolith A3.

On the other hand, the corona lost about two-thirds of the CaO and approximately 15% of the Al_2O_3 and MgO. The increase in FeO^{tot} and SiO_2 and the decrease in MnO are negligible, if any.

For comparison, results with SiO_2 chosen as immobile component are available in the Supplementary Material (Figure S. 2).

6.2 Elemental transfers during the coronae-forming reaction

Based on the differences in chemical potentials (Figure II. 9), it seems that in the P–T window determined for the assumed interaction of granulite with the xenoliths (900–1000 °C, 1.0–1.2 GPa) Ca would have the greatest tendency to migrate from garnet clinopyroxenite to the granulite followed by Mg. Aluminium would also tend to migrate from garnet clinopyroxenite to the granulite, but the difference in the chemical potentials is smaller. Finally, Fe and Na should migrate in the opposite direction, i.e., from the granulite to the garnet clinopyroxenite, while Si and Ti should remain in place.

This notion is in good agreement with the concentration ratio diagram, which compares the relative enrichment or depletion of Opx–Pl coronae with respect to the garnet clinopyroxenite xenolith (Figure II. 11). Based on this diagram, it can be concluded that the most significant change in the preserved xenolith is enrichment by alkalis and depletion by CaO. The mechanism of alkalis enrichment cannot be determined with certainty because their mobility is generally very high. But clearly the alkalis were sourced from the surrounding granulite generally rich in these elements (Table II. 5; Janoušek *et al.,* 2004; Vrána *et al.,* 2013) and/or can be related to an earlier mantle metasomatism (Borghini *et al.*, 2018, 2020, 2023; Zelinková *et al.*, 2023).

6.3 Potential modification of the host granulite by interaction with chemical components derived from the mantle xenoliths

The only readily observable modification of the host intermediate granulite is the presence of the narrow K-feldspar depleted zone around the xenoliths caused probably by the migration of

potassium into the latter (Figure II. 3e). However, the presence of garnet clusters with spinel and corundum inclusions (Figure II. 3b, c) scattered throughout the intermediate granulite indicates that probably an Al_2SiO_5 phase was formerly present. We assume that it may have been kyanite, because of the abundance of Ky-bearing felsic granulite samples typical of the St. Leonhard and other Moldanubian granulite massifs (e.g. Cooke, 2000), and findings of similar pseudomorphs after kyanite in comparable lithologies (Owen & Dostal, 1996; O'Brien & Rötzler, 2003; Tajčmanová *et al.*, 2007; Štípská *et al.*, 2010; Vrána *et al.*, 2013; Baldwin *et al.*, 2014). The destabilization of the Al_2SiO_5 phase could be caused either by decompression or by a change in the bulk-rock composition.

In the following, we test whether the intermediate granulite with pseudomorphs after an Al_2SiO_5 phase originally could have represented the common Ky-bearing granulite, which was modified due to interaction with the mantle-derived, ultramafic material. The possible influence of the mantle xenoliths on bulk-rock composition and, consequently, the mineral assemblage of the host granulite was evaluated using a pressure–composition (P–X) diagram (Figure II. 12). In this diagram, X1 represents the actual composition of the Grt–Opx–Kfs–Pl–Qz granulite hosting the mantle xenoliths; the vector of change towards a hypothetical composition X0 is deduced from the chemical differences between the mantle xenolith and its corona (Figure II. 11). The procedure of X0 composition calculation is summarised in Table I. 2; finally, it had to be recalculated to mol. % (Figure II. 12a), as required by the THERMOCALC software.

The P–X diagram (Figure II. 12a) was constructed at 950 °C, i.e. the temperature estimated for the intermediate granulite equilibration. The most important feature is the fact that the Al_2SiO_5 phase becomes unstable (at X ~0.58); orthopyroxene appears soon thereafter (beyond X ~0.7, Figure II. 12a, d), if we follow the compositional change from X0 to X1 at the estimated pressure range of 1.0–1.2 GPa (close to Ky–Sil transition). The increase of plagioclase content towards X1 is probably due to the influx of CaO, which increases the An component in Pl requiring the consumption of Al from the immediate surroundings (Figure II. 12b). The Al decrease in the rest of the system causes the decay of Al-rich phases such as Al_2SiO_5 polymorphs and/or garnet. The reduction of garnet content leads to the formation of the Al-poor phase – orthopyroxene. These changes in mineral proportions are shown in Figure II. 12c, d. Moreover, the increase in modal plagioclase towards X1 is at the expense of K-feldspar (Figure II. 12c), which is consistent with petrographic observations of intermediate granulite, where K-feldspar appears to be replaced by plagioclase (Figure II. 3a).

In addition, the dotted line (X = 0.48) denotes the average CaO content in typical Ky-bearing felsic granulites from the St. Leonhard massif (in samples from this study CaO = 1.72 mol. %), which – for the pressure range of interest – falls into the compatibility field of Al_2SiO_5 (Sil). To sum up, the greatest influence on the mineral assemblage of the granulite next to the mantle xenoliths and their coronae seems to be the influx of Ca. This apparently caused an increase in the modal abundance of An-rich plagioclase, which needed extra Al for its stabilization. This resulted in decomposition of the Al-rich mineral phases like garnet and Al_2SiO_5 polymorph, whereby the garnet decomposition caused the stabilization of orthopyroxene. It can be assumed that MgO enrichment affected the chemical composition of the mineral phases in the granulite matrix as well, but this effect was probably minor and cannot be confirmed with certainty. Based solely on petrologic evidence, the change of other elements were negligible.

The important control of CaO on the mineral assemblage is supported by the P–X diagrams available in the Supplementary material. The first one invokes only a change in CaO (Figure S. 1); in the second the composition X0 was calculated using the composition vector with SiO_2 as the immobile component (Table S. 4 and Figure S. 2, Figure S. 3). These diagrams have a very similar topology with the P–X diagram already discussed (Figure II. 12), i.e. showing the decomposition of the Al_2SiO_5 phase and subsequent Opx formation towards the X1 composition.

Table II. 6: Restoring the hypothetical composition X0 of the Ky-bearing granulite before its interaction with the garnet clinopyroxenite with TiO_2 as an immobile component

	[1] garnet clinopyroxenite (wt. %)	×	[2] wt. % change in corona	/100 =	[3] compositional change vector for garnet clinopyroxenite	[4] compositional change vector for intermediate granulite	+	[5] intermediate granulite (wt. %)	=	[6] hypothetical composition X0 of pristine Ky-granulite (wt. %)
SiO_2	45.91		11.82		0.00	0.00		71.54		71.54
TiO_2	0.34		0.00*		–0.04	–0.01		0.21		0.20
Al_2O_3	16.78		–14.69		–3.98	–1.07		15.03		13.95
FeO^{tot}	9.24		9.25		–0.21	–0.06		2.61		2.55
MnO	0.15		–6.28		–0.02	–0.01		0.08		0.08
MgO	15.24		–14.00		–3.52	–0.95		1.37		0.42
CaO	11.27		–63.50		–7.59	–2.05*		2.55		0.50*
Na_2O	0.47		356.69		1.44	0.39		3.63		4.02
K_2O	0.27		65.93		0.13	0.03		2.98		3.02

* assumed. As a basis served the compositional change vector [3] obtained by multiplying the garnet clinopyroxenite composition [1] with wt. % change in its corona [2] (inferred from the concentration ratio diagram; Figure II. 11) and dividing by 100. These elemental losses/gains had to be compensated by the intermediate granulite host. Considering that the degree of the change is limited by the availability of CaO (a component with the most dramatic depletion that would be exhausted first), the CaO content in composition X0 [6] was set to an arbitrarily low value of 0.5 wt. %. This means that the CaO value changes by –2.05 [4]. The remaining items of the compositional change vector [4] were obtained from [3] multiplied by the factor of 2.05/7.15. Applying the vector [4] to the actual intermediate granulite composition [5], we obtained the hypothetical pristine felsic granulite composition X0 [6].

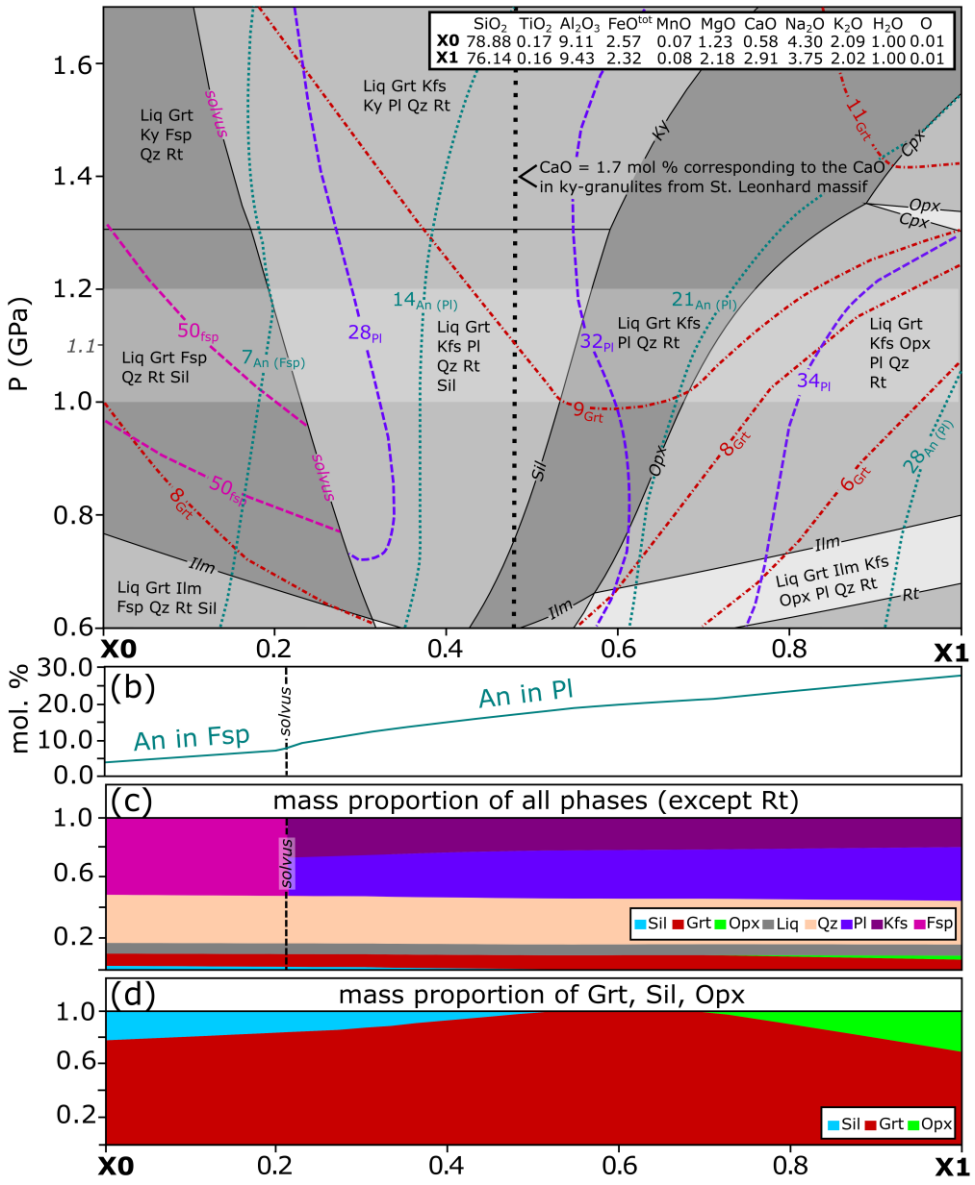

Figure II. 12: P–X diagram showing phase relations along the transition between the Opx- and Ky-bearing felsic granulites calculated at 950 °C (a) with sections at 1.1 GPa portraying An in ternary feldspar/plagioclase (b), and mass proportions of individual phases (c, d). The X1 is the measured chemical composition of the intermediate granulite; towards X0 the composition approaches the estimated hypothetical chemistry of a pristine Ky-granulite prior to the interaction with garnet clinopyroxenite. a) The highlighted area at 1.0–1.2 GPa corresponds to the pressure interval estimated for corona formation using the P–T pseudosection (Figure II. 7). The most significant change is the disappearance of Opx and stabilization of an Al_2SiO_5 phase (sillimanite in the diagram) towards the X0. Dotted line at X ~0.46 indicates where the CaO content corresponds to the average of typical Ky-bearing felsic granulite samples from the St. Leonhard massif. b). Molar percentages of anorthite component in plagioclase (or in ternary feldspar if above solvus). c) Mass proportions of all phases, except rutile. d) Mass proportions of garnet, sillimanite, and orthopyroxene.

6.4 Formation of coronae around mantle xenoliths

6.4.1 Orthopyroxene–plagioclase corona around the garnet clinopyroxenite

Based on the concentration ratio diagram (Figure II. 11), the depletion by mainly CaO >> MgO and Al_2O_3 are the most significant compositional changes in the Opx–Pl corona around the garnet clinopyroxenite xenolith. Furthermore, there is a conspicuous enrichment in Na_2O >> K_2O.

Transfer of Ca and possibly small amounts of Mg and Al from the garnet clinopyroxenite to granulite, together with migration of alkalis in the opposite direction, led to the breakdown of clinopyroxene and to the formation of the Opx–Pl symplectite corona. Symplectite growth is facilitated by the presence of a fluid or melt (Spruzeniece *et al.*, 2016; Pistone *et al.*, 2020) which made the diffusion more efficient. As alkalis are mobilized very efficiently in fluid/melt, their movement could have affected pervasively the entire volume of the xenolith. The influx of K could have caused the formation of biotite and amphibole not only in the coronae, but also in the better preserved central parts of the garnet clinopyroxenite xenoliths.

Nevertheless, an earlier presence of these K-bearing phases cannot be excluded. Indeed, there is an overwhelming evidence that the mantle beneath the orogenic root (Moldanubian Domain) was extensively metasomatized, both direct, as preserved melt inclusions (Borghini *et al.*, 2018, 2023; Ferrero *et al.*, 2018; Naemura *et al.*, 2018; Kotková *et al.*, 2021a; Zelinková *et al.*, 2023) and indirect, in the form of spatially associated ultrapotassic magmatism in the region (Janoušek & Holub 2007; Janoušek *et al.* 2022 and references therein; Krmíček *et al*., 2020).

6.4.2 Orthopyroxene coronae around the peridotite

Given the generally similar chemical composition of orthopyroxene [$(Mg,Fe)_2Si_2O_6$] with olivine [$(Mg,Fe)_2SiO_4$], the orthopyroxene coronae around preserved olivine grains in the peridotite xenolith probably formed at the expense of the peridotite itself.

We assume that the coronae mainly reflect Si movement from the surrounding granulite, which caused the transformation from olivine to orthopyroxene similar to mantle xenoliths that interacted with their host magma/fluids in volcanic environment (Ishimaru *et al.*, 2007; Arai & Ishimaru, 2008). The stabilization of orthopyroxene at the expense of peridotite by a Si-enriched liquid has also been described in subduction zones (Malaspina *el al.*, 2006) and in oceanic mantle (Piccardo *et al.*, 2004; Suhr *et al.*, 2003). Opx-coronae were also produced by experiments showing the growth of orthopyroxene at the contact of olivine and quartz (Milke *et al.*, 2009).

As in the case of the studied garnet clinopyroxenite xenolith, the significant increase of Fe and decrease of Mg in peridotite has an effect only on the chemical zoning of the Opx-coronae; the supply of K from the felsic granulite probably caused the formation of biotite in the Opx-coronae. Also, a weak enrichment of Al towards the felsic granulite, may be taken as an indication for supply of this component from the latter, but its content is very low.

6.5 Thermal history of crust-mantle interaction from Fe–Mg diffusion chronometry

At this point we attempt to constrain the time scales related to crust–mantle interaction. To this end, diffusion chronometry was applied to the secondary compositional zoning of garnet from a garnet clinopyroxenite xenolith at its contact to Opx–Pl corona (Figure II. 13a).

The compositional profile measured along a transect from the garnet interior towards the contact with the Opx–Pl corona displays a gradual outwards increase of the almandine and a concomitant decrease of the pyrope content while the grossular content remains essentially constant (Figure II. 13a, b). Based on the notion that such a compositional trend is present all along the perimeter of the garnet also following complex geometries of the garnet rim, as indicated by a bright BSE contrast along the garnet rim (Figure II. 3d, Figure II. 13a), this is interpreted as secondary compositional zoning.

Very likely the enrichment of garnet in almandine component was first acquired during its partial replacement by the Opx–Pl symplectic corona. As symplectite reaction fronts tend to propagate with constant velocity (Gaidies *et al.,* 2017), a steady-state diffusion profile that can be described by a simple exponential function is expected to have developed during that stage. The shape of the observed concentration profile does, however, not correspond to an exponential function. It is better fit by an error function, indicating that the profile relaxed and acquired its final shape after corona formation had already ceased. Accordingly, fixed geometry was assumed for inverse modelling of the Fe/Mg concentration profile. Taking $D_{Fe–Mg}$ from experimental calibrations, the time needed for the secondary compositional zoning of garnet to from or the corresponding cooling rate can be estimated.

Over large portions the compositional profile (~1500 μm) in garnet (Figure II. 13a) shows an outwards increase of the almandine content counterbalanced by a decrease of the pyrope content, while the grossular content remains constant. Only in the outermost 200 μm the grossular and pyrope contents decrease while the almandine content increases indicating ternary

interdiffusion of Mg, Fe and Ca. Noting that the by far largest portion of the profile can be described in terms of binary Fe-Mg interdiffusion, the garnet profile was cut 200 µm inside from the contact to the Opx–Pl corona, and an Fe-Mg interdiffusion model was fitted to the data (Figure II. 13b, c). To account for the uncertainties in the temperature determination and in the experimental calibration of $D_{Fe–Mg}$, conditions of 900 °C/1.2 GPa were combined with the slowest experimental calibration of $D_{Fe–Mg}$ (Borinski *et al.,* 2012) and conditions of 1000 °C/1.0 GPa were combined with the fastest experimental calibration of $D_{Fe–Mg}$ (Elphick *et al.,* 1985). Fitting of the model curves to the measured concentration profile yield time estimates of 13–532 ka, if diffusion is regarded as isothermal, and cooling rates of 4.7–0.1 °C/ka, if diffusion is regarded as having become successively more sluggish and to have eventually stopped during continuous cooling (see Supplementary Material for details). Similar diffusion-mediated secondary compositional zoning of garnet has been obtained from modelling of the HP–HT evolution of garnet (Chu & Ague 2015) and has also been reported from other regions (e.g. Piccoli *et al.,* 2022).

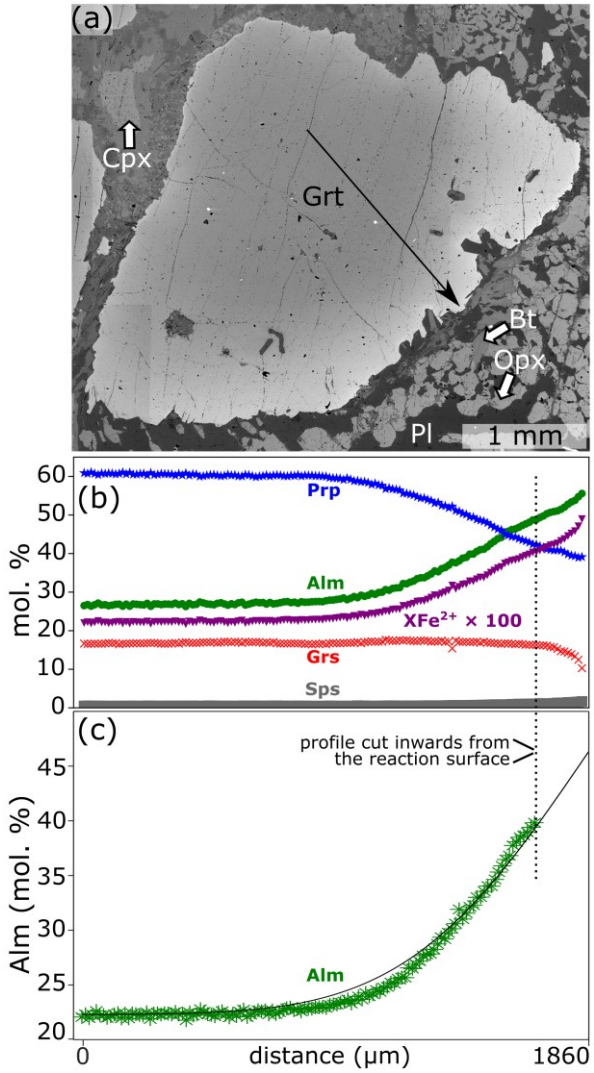

Figure II. 13: Fe–Mg diffusion chronometry. a) Back-scattered electron image of a garnet from the garnet clinopyroxenite (Figure II. 3d) with secondary compositional zoning as indicated by the bright BSE contrast towards its rims that are in contact with the Opx–Pl corona, black arrow shows the position of an EPMA measurement profile. b) Compositional profile obtained from EPMA point analyses. c) Concentration profile of Alm component (mol. %), the solid black line corresponds to the results from binary Fe–Mg diffusion modeling (see text for explanation).

Compared to the supposed metamorphic evolution, the estimated times and cooling rates correspond to an ephemeral episode. It has been argued by Remmert *et al.* (2017) that symplectite formation requires the presence of minute amounts of an aqueous fluid or melt. It is well conceivable that presence of small melt fractions during the juxtaposition of mafic/ultramafic and felsic lithologies in the deep crust beneath the Variscan Orogen may have fostered corona formation and development of the secondary compositional zoning in garnet. Relaxation of the initially acquired Fe-enrichment in the residual garnet in contact with the symplectite started immediately after corona formation had ceased. Preservation of the secondary compositional zoning indicates relatively fast cooling immediately after corona formation and thus after crust–mantle interaction.

The calculated cooling rates concur well with the extremely fast exhumation rates proposed throughout the Central Variscides (e.g. Gayk & Kleinschrodt, 2000; Štípská *et al.,* 2004; Willner *et al.,* 2002; Müller *et al.,* 2015).

6.6 Comparison with eclogite–granulite interaction in Blanský les massif (southern Bohemia)

An analogous example of interaction between mantle-derived eclogite xenoliths and their felsic granulite host was described from the Blanský les granulite massif (southern Bohemia) (Štípská *et al.*, 2014a, b). According to these authors, the transformation of the eclogite into an intermediate granulite was caused primarily by the supply of K_2O and H_2O from the felsic granulite and its partial melt. It is characterized by the replacement of the interior of some garnets by ternary feldspar, the formation of plagioclase coronae around garnet, recrystallization of clinopyroxene into large poikiloblasts with inclusions of ternary feldspar, and the transformation of low-K plagioclase in the matrix into ternary feldspar during isothermal decompression from 1.8–2.0 GPa to 1.2 GPa at 950 °C (Štípská *et al.*, 2014a, b).

In contrast, the mantle xenoliths investigated in the current study are devoid of ternary feldspar. This indicates that supply of K_2O to our samples was significantly lower and is manifested only by the formation of biotite and amphibole throughout the xenoliths, but mostly in the coronae. Our estimated P–T conditions of the interaction between the felsic granulite and the mantle xenoliths (1.0–1.2 GPa and 900–1000 °C) are similar to those reported for crust–mantle interaction in the Blanský les Massif. Therefore, it can be assumed that at least some interactions between mantle and crustal rocks took place at comparable crustal levels and temperatures.

6.7 Possible genetic link between felsic Ky- and felsic–intermediate Opx-bearing Moldanubian granulites?

A question that merits discussion at this point is whether the results of our study focussed on relatively small-scale interaction between ultramafic (mantle) xenoliths and their felsic granulite hosts could be extrapolated to larger masses (up to tens of metres) of intermediate–felsic ('transitional') Opx-bearing granulites, which are common throughout the Gföhl Unit, and elsewhere. This problem is tackled by the comparison of major-element compositions of both granulite groups.

Wedge plots (Ague, 1994) are particularly well suited for the qualitative assessment of component losses/gains in the course of open-system processes such as metasomatism, alteration or partial melting. They have an advantage over the isocon plots (Grant, 1986) or concentration ratio diagrams (Ague, 2003) in that they account for the overall compositional variability of both the putative protolith and the altered product. Wedge plots are simple binary

diagrams of a potentially mobile versus a reference (presumably immobile) element/oxide. The compositionally heterogeneous protolith samples yield a cloud of points, the outer edges of which define a wedge-shaped region that converges towards the origin. As shown by Bucholz & Ague (2010), the altered samples that plot above and to the left of this wedge must have gained the mobile components, whereas those falling below and to the right experienced a loss. The samples that remain in the wedge but moved away from the origin are thought to record residual enrichment, and those shifted towards the origin to have undergone residual dilution.

In our case, analyses of typical felsic Ky-granulites should represent the 'protolith', while the felsic–intermediate Opx-bearing types are taken as the 'altered samples'. Due to its low concentration in the granulites, TiO_2 cannot be chosen as a reference element (Vellmer, 1992; Janoušek *et al.,* 2004; Vrána *et al.,* 2013). However, both Al_2O_3 and SiO_2 are major components in the granulites, and based on the results from the concentration ratio diagram of garnet clinopyroxenite xenolith and its corona, show only negligible gains/losses (Figure II. 11). It has been shown that both Al and Si are characterized by low mobilities during symplectite formation (Mongkoltip & Ashworth, 1983). We have chosen Al_2O_3 as the reference component, because its low mobility has been verified by numerical modelling of corona growth around garnet (Carlson, 2002). In case SiO_2 would be selected as the reference component, very similar results would be obtained (Figure S. 4).

According to the wedge plots (Figure II. 14), the intermediate granulites are characterized by a strong enrichment in CaO (Figure II. 14d), as well as less elevated FeOtot and MgO (Figure II. 14b, c), at practically unchanged alkalis (Figure II. 14e, f).

In case SiO_2 would be selected as the reference component, very similar results would be obtained (Figure S. 4).

The observed increase in CaO > MgO in the 'transitional' granulites is compatible with possible supply of these components from ultramafic bodies into pristine felsic Ky-granulites. This complies with our model formulated based on small-scale observations (see Table II. 6). The conservative behaviour of alkalis does not seem to contradict our hypothesis either, as the movement of these elements would be in the opposite direction (i.e. into the ultramafic xenoliths) and the large volume of Ky-granulite would provide an essentially infinite reservoir for any elements migrating this way. Also, the A/CNK value (molar ratio of Al_2O_3 to CaO + Na_2O + K_2O) is largely preserved as is the mg number (Figure II. 14g, h).

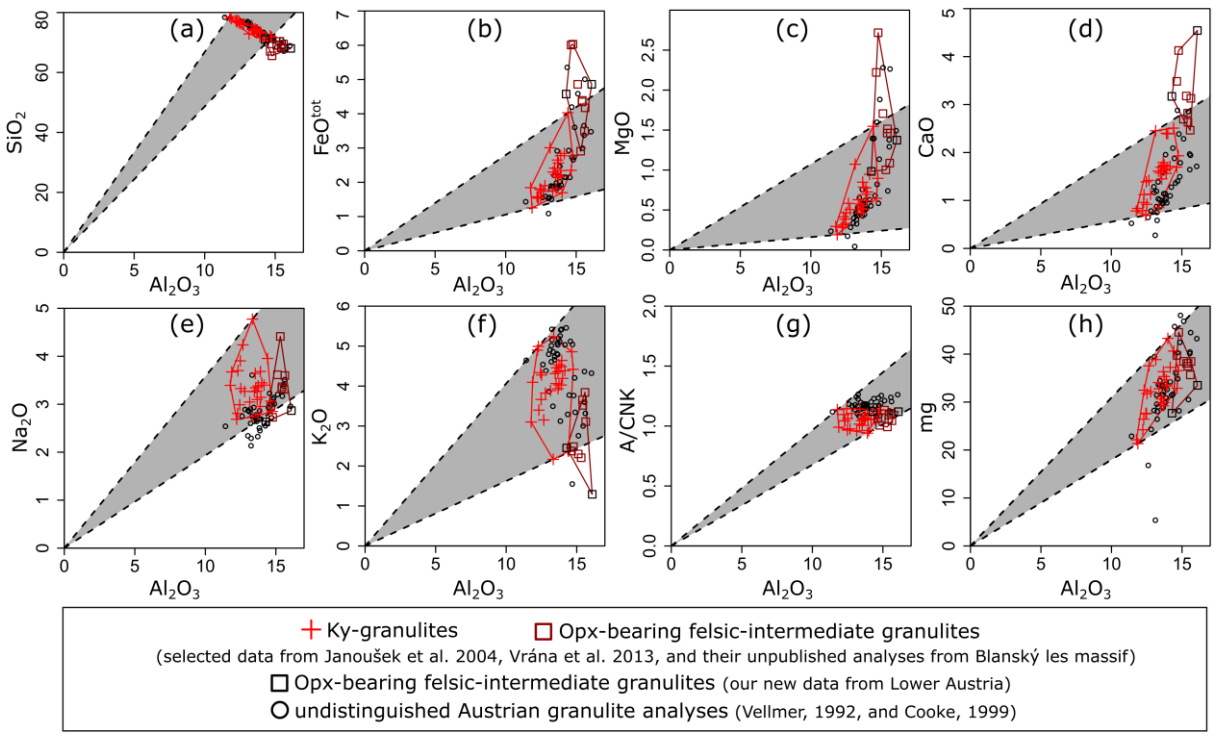

Figure II. 14: a–h) Wedge plots (Ague, 1994; Bucholz & Ague, 2010) comparing analyses of pristine felsic Ky-granulites with 'transitional' Opx-bearing–intermediate types (Janoušek et al., 2004; Vrána et al., 2013) and undistinguished analyses from Ph.D. theses (Vellmer, 1992; Cooke, 1999). The grey fields ("wedges") denote the protolith variability (and no perceptible gain/loss of components in the altered samples). All data were recalculated to 100 % anhydrous basis.

The only oxide whose behaviour does not fully comply with the model is FeO^{tot} that seems enriched in most of the 'transitional' granulites. There is no easy explanation at hand; perhaps the composition of our ultrabasic xenolith A3 was not truly representative, and/or some of the intermediate granulites originated from different, intermediate protoliths uncontaminated by the mantle material. Also one can speculate that the mobility of iron was likely influenced by fO2.

6.8 Significance of the lower crustal interactions between mantle xenoliths and felsic HP–UHT granulites

Any future work concerned with the genesis of the still enigmatic Moldanubian Opx-bearing granulites should focus on broader-scale petrological, mineral- and whole-rock geochemical variation, potentially reflecting interactions of the ultramafic mantle-derived bodies with their felsic Ky-granulite host. These interactions could have taken place at lower to mid crustal levels. Besides major elements, such a research should target also traces as well as radiogenic and stable (both mantle-incompatible and compatible) isotopic systems (Janoušek *et al.,* 2022).

If proven by such follow-up studies in the Variscan Moldanubian Zone, and perhaps elsewhere, the deep crustal chemical exchange between mantle- and crust-derived lithologies should be considered in multidisciplinary studies of composition, thermal structure and geodynamic evolution of orogenic lower crust as well as of crustal growth. The proposed mechanism may be potentially important in hot collisional orogens, in which a deeply subducted felsic crust of the lower plate was relaminated to the base of the overriding plate (Hacker *et al.,* 2011; Lexa *et al.,* 2011; Schulmann *et al.,* 2014). The deeply subducted crustal material does not necessarily need to be exhumed solely via the subduction channel. Instead it also may detach from the slab and ascend as trans-lithospheric diapirs (Cruz-Uribe *et al.,* 2018; Maierová *et al.,* 2018, 2021). Irrespective of the exhumation pathway, deeply subducted felsic material will likely incorporate mantle fragments from the cold subduction channel. If exhumation occurs in the form of a trans-lithospheric diapir, there is a high chance that also material from the relatively hot mantle wedge and very hot orogenic lithosphere is incorporated. Such mélanges offer ample opportunity for chemical interaction between compositionally contrasting crustal and mantle-derived lithologies at various depths.

7 Conclusions

Metasomatic interaction between mantle xenoliths and their host felsic granulite caused the formation of coronae at their mutual contacts and subsequent mineralogical and chemical changes in both the xenoliths and the adjacent felsic granulite. The conditions of this interaction were estimated to 1.0–1.2 GPa and 900–1000 °C. Corona formation was followed by very rapid cooling (4.7–0.1 °C/ka) due to unusually rapid exhumation rates that are characteristic for the entire mid-European Variscides.

The principal change in the mineral assemblage of the host granulite was the decay of the Al_2SiO_5 polymorph accompanied by the formation of orthopyroxene. The Al_2SiO_5 breakdown was probably driven by addition of components derived from the garnet clinopyroxenite xenoliths, especially CaO. Moreover, a Kfs-poor zone developed in the intermediate granulites next to the coronae due to the uptake of potassium from the felsic host by the mantle xenoliths.

Coronae surrounding the garnet clinopyroxenite xenoliths were formed at the expense of the xenoliths. Potassium enrichment in the xenoliths as evident from growth of biotite and amphibole is ascribed to the diffusion-mediated transfer of potassium from the felsic granulite into the xenoliths, which was accompanied by diffusion of CaO, and less so, MgO and Al_2O_3 in the opposite direction. As a result, fine-grained symplectitic Opx–Pl coronae formed at the

interfaces between the garnet clinopyroxenite xenoliths and the felsic granulites. Less abundant peridotite xenoliths were primarily affected by diffusion-mediated supply of SiO_2 from the host granulite, which caused partial replacement of olivine by monomineralic orthopyroxene coronae.

The current study documents a rather rare case of small-scale interaction at the direct contact between ultramafic mantle xenoliths and their felsic HP–UHT granulite host lithology of crustal origin at 1.0–1.2 GPa and 900–1000 °C. The results can be helpful for the interpretation of the origin of similar lithologies on comparable, and larger scales. As such they contribute to a better understanding of the processes of crust–mantle interaction in the roots of hot collisional orogens and the vigorously debated problem of the balance between the crustal recycling and the crustal growth.

Part III: Indications for the possible metasomatic origin of intermediate and mafic granulites at the contact of garnet clinopyroxenites with felsic HP–HT felsic granulites (Dunkelsteiner Wald granulite massif)

The aim of this chapter is to use the petrographic study to find clues that would support the hypothesis of a possible metasomatic formation of intermediate and mafic granulites on a larger scale than described in the previous chapter (Part II). An ideal example is the environment of the Dunkelsteiner Wald granulite massif, which contains bodies of garnet peridotites and clinopyroxenites up to several km in size, and where mafic and intermediate granulites often occur near the presumed contacts of garnet clinopyroxenites with Ky-bearing felsic granulites.

The following text deals with the petrographic characterization including phase-equilibria modelling of the studied lithologies – Ky-bearing felsic granulites and garnet clinopyroxenites as an assumed end-members, and intermediate and mafic granulites as the product of their assumed metasomatic interaction. This chapter also contains a petrographic characterization of garnet peridotites (accompanied by one sample DS159/20A from St. Leonhard) that often occur in the association with garnet clinopyroxenite.

Figure 0. 2 shows the simplified geological map with the locations of the studied lithologies.

1 Petrology

1.1 Petrological description and mineral composition of the lithologies

1.1.1 Kyanite-bearing felsic granulites

This granulite type is formed by fine-grained quartzofeldspathic matrix with perthite, and contains porphyroblasts of garnet and often kyanite. In some cases, around kyanite occurs up to several tens of micrometres wide plagioclase rim accompanied by garnet. Biotite is also present in the matrix and its amount depends on the degree of retrogression. Garnet hosts inclusions of rutile, quartz, plagioclase, and more rarely encloses perthitic K-feldspar. Common accessories besides rutile, are zircon, and apatite. Rutile is often partly replaced to ilmenite.

Representative mineral analysis of Ky-bearing felsic granulites are available in Table III. 1. Perthite analyses are available in Table S. 5

Sample DS024 (Figure III. 1) contains up to 2 mm garnet and up to 0.6 mm kyanite porphyroblasts with plagioclase rim with small garnet (Figure III. 1a, b). Sample is fresh with only small amount of biotite.

Plagioclase (oligoclase) in the matrix shows no systematic zoning ($An_{16.7–17.6}Ab_{82.5–81.1}Or_{0.8–1.3}$) except plagioclase rim around Ky, which is characterized by the high Ca content at the contact with Ky and gradually decrease from Ky towards the surrounding matrix: $An_{19.5→16.9}Ab_{79.3→81.7}Or_{1.2→1.4}$. The albite component in the K-feldspar is $Ab_{7.7–26.1}$. Integrated analysis of perthite has composition range $An_{2.6–8.8}Ab_{20.6–49.7}Or_{41.5–76.8}$.

Garnet is rich in almandine component. Smaller Grt grains are defined by the Ca decrease towards the rim, whereby other components show only small changes in the composition $Prp_{28.9→31.9}Alm_{62.1→64.7}Grs_{7.5→1.9}Sps_{~1.5}$; XFe^{2+} = 0.68→0.67. The larger preserved Grt porphyroblasts have a higher Ca content and are characterized by a rim-ward increase of Fe and Mg and decrease of Ca: $Prp_{25.0→31.0}Alm_{56.0→64.7}Grs_{17.7→2.8}Sps_{1.5→1.4}$; XFe^{2+} = 0.69→0.68 (Figure III. 1c). Biotite has XFe^{tot} = 0.30–0.34 and Ti = 0.13–0.16 p.f.u.

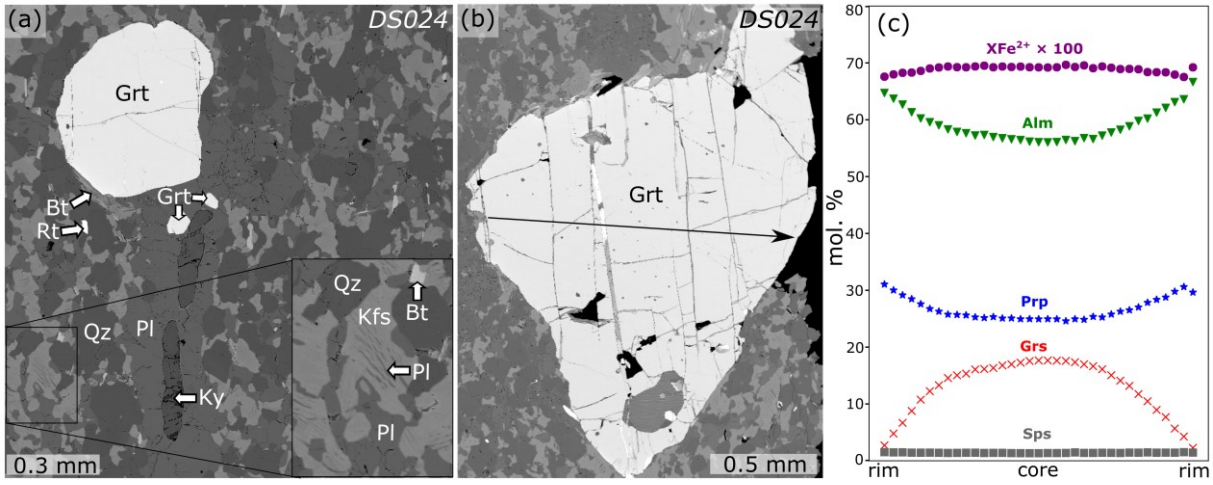

Figure III. 1: a–b) Backscattered electron images of Ky-bearing felsic granulite DS024. c) Composition profile across garnet from the subfigure b.

Sample DS152/20A contains small garnet grains up to 0.6 mm and no observed kyanite. Sample is very fresh with almost no biotite (Figure III. 2). Ilmenite is common accessory phase in the matrix whereas rutile was not observed.

Plagioclase (oligoclase) shows no systematic zoning ($An_{18.6–20.2}Ab_{78.5–79.2}Or_{1.1–2.2}$; see Table III. 1). The albite component in the K-feldspar is $Ab_{9.1–13.0}$.

Garnet is rich in almandine component and its zonality is characterized by a rim-ward increase of Fe and Mg and decrease of Ca: $Prp_{20.6→23.5}Alm_{64.2→68.7}Grs_{13.7→6.4}Sps_{1.5→1.4}$; XFe^{2+} = 0.76→0.75 (Figure III. 2b).

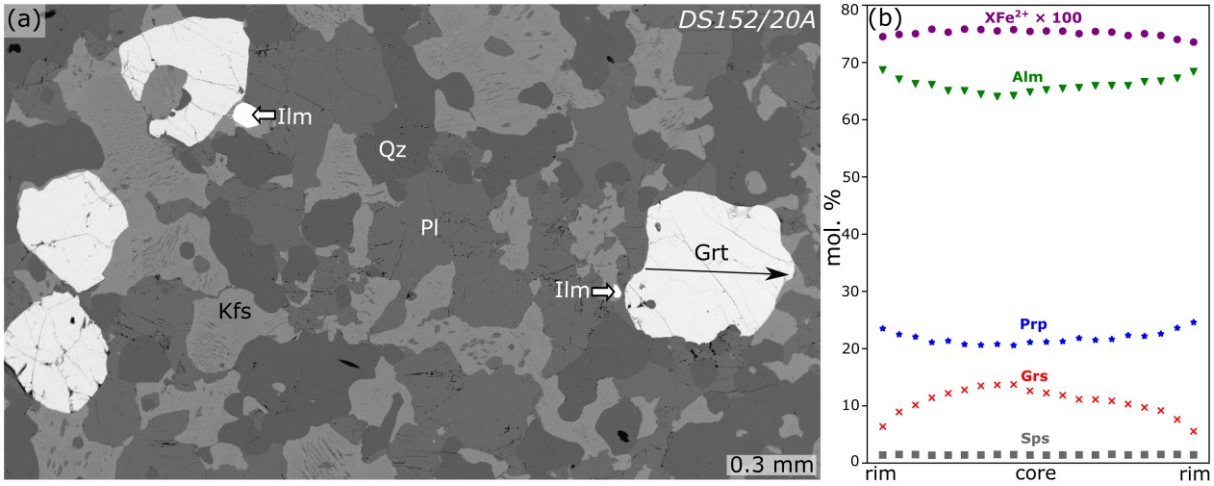

Figure III. 2: a) Backscattered electron image of felsic granulite DS152/20A with b) Composition profile across garnet from the subfigure a.

Table III. 1: Representative mineral analyses of Ky-bearing felsic granulites in wt. %.

Lithology	Ky-bearing felsic granulite										
Thin-section	DS024	DS024	DS152/20A	DS152/20A	DS024	DS024	DS024	DS024	DS152/20A	DS024	DS152/20A
Mineral	Grt	Grt	Grt	Grt	Bt	Bt	Pl	Pl	Pl	Kfs	Kfs
Analysis	Grt-line 01	Grt-line 19	Grt-line 09	Grt-line 01	Bt-01	Bt-03	Pl-02	Pl-06	Pl-02	Kfs-02	Kfs-06
Position	Grt core	Grt rim	Grt core	Grt rim	Matrix	Matrix	Matrix	Pl rim around Ky	Matrix	Matrix	Matrix
SiO_2	37.63	37.48	38.15	38.18	38.36	38.69	64.47	64.17	63.64	66.05	64.88
P_2O_5	0.15	0.06	b.d.	b.d.	b.d.	b.d.	b.d.	b.d.	b.d.	b.d.	b.d.
TiO_2	0.13	0.03	0.24	0.07	2.16	2.50	0.02	0.01	0.03	b.d.	0.01
Cr_2O_3	0.02	0.02	b.d.	b.d.	0.04	0.06	b.d.	b.d.	0.01	b.d.	0.05
Al_2O_3	21.61	21.90	21.25	21.61	17.22	17.00	22.60	22.87	22.96	19.36	18.99
FeO	27.13	30.51	28.89	30.72	11.02	11.80	0.01	0.01	0.03	0.19	0.01
MnO	0.61	0.67	0.66	0.62	0.02	0.04	b.d.	b.d.	b.d.	b.d.	b.d.
MgO	6.35	7.83	5.19	5.90	14.22	12.87	b.d.	b.d.	b.d.	0.01	b.d.
BaO	b.d.	b.d.	b.d.	b.d.	b.d.	b.d.	b.d.	b.d.	b.d.	b.d.	b.d.
CaO	6.25	0.95	4.82	2.23	b.d.	0.02	3.48	3.70	4.07	0.03	0.08
Na_2O	0.02	0.01	0.02	0.02	0.07	0.05	9.53	9.42	8.84	0.97	1.42
K_2O	b.d.	b.d.	b.d.	0.01	9.89	9.12	0.14	0.23	0.21	14.95	14.32
Cl	b.d.	b.d.	b.d.	b.d.	0.09	0.11	b.d.	b.d.	b.d.	b.d.	b.d.
F	b.d.	b.d.	b.d.	b.d.	0.67	0.49	b.d.	b.d.	b.d.	b.d.	b.d.
Total	99.89	99.44	99.21	99.34	93.00	92.15	100.25	100.41	99.80	101.56	99.76
Cations/Charges	8/24	8/24	8/24	8/24	8/22	8/22	5/16	5/16	5/16	5/16	5/16
Si	2.93	2.93	3.02	3.02	2.97	3.05	2.84	2.82	2.83	3.00	2.99
P	0.01	0.00	–	–	–	–	–	–	–	–	–
Ti	0.01	0.00	0.01	0.00	0.13	0.15	0.00	0.00	0.00	–	0.00
Cr	0.00	0.00	–	–	0.00	0.00	–	0.00	0.00	–	0.00
Al	1.98	2.02	1.98	2.02	1.57	1.58	1.17	1.19	1.20	1.04	1.03
Fe^{2+}	1.65	1.90	1.91	2.03	0.71*	0.78*	0.00	0.00	0.00	0.00	0.00
Fe^{3+}	0.11	0.09	0.00	0.00	–	–	–	–	–	–	–
Mn	0.04	0.04	0.04	0.04	0.00	0.00	–	–	–	–	–
Mg	0.74	0.91	0.61	0.70	1.64	1.51	–	–	–	0.00	–
BaO	–	–	–	–	–	–	–	–	–	–	–
Ca	0.52	0.08	0.41	0.19	–	0.00	0.16	0.17	0.19	0.00	0.00
Na	0.00	0.00	0.00	0.00	0.01	0.01	0.81	0.80	0.76	0.09	0.13
K	–	–	–	0.00	0.98	0.92	0.01	0.01	0.01	0.87	0.84
Cl	–	–	–	–	0.01	0.01	–	–	–	–	–
F	–	–	–	–	0.16	0.12	–	–	–	–	–
XFe^{2+}	0.68	0.69	0.68	0.76	$XFe^{tot} = 0.30$	$XFe^{tot} = 0.34$					

b.d. below detection limit. * – Fe^{tot}

1.1.2 Intermediate granulites

Matrix of intermediate granulites is orthopyroxene-bearing, fine to medium-grained, quartzofeldspathic with antiperthite and rarely also with perthite (sample DS153/20A). Samples contains variable amounts of biotite depending on the degree of retrogression. In the matrix occur porphyroblasts of garnet and in some cases elongated fine-grained symplectites of corundum, spinel, epidote and K-feldspar, when corundum and spinel are partly replaced by Al-hydroxides. These symplectites are in some cases surrounded by thin corona of garnet followed by plagioclase. Common inclusions in garnet are quartz, and plagioclase, and less common are rutile partly replaced by ilmenite, clinopyroxene, and rarely kyanite. Common accessories are zircon, pyrite, pyrrhotite, graphite, and apatite.

Representative mineral analysis of intermediate granulites are available in Table III. 2. Antiperthite analyses are available in Table S. 6.

Sample DS071B (Figure III. 3) contains up to 2.7 mm large garnet porphyroblasts with rutile, quartz and clinopyroxene inclusions (Figure III. 3a, b). Sample is fresh with only small amount of biotite.

Plagioclase (andesine) in the matrix shows no systematic zoning ($An_{33.8–37.9}Ab_{58.9–63.5}Or_{2.7–3.3}$; see Table). The albite component in the K-feldspar varies from 5.7 to 7.8 %. Integrated anylysis of antiperthite from the matrix has composition: $An_{33.8–26.6}Ab_{40.0–52.1}Or_{14.2–33.4}$. Orthopyroxene is Mg-rich (XFe^{2+} = 0.38–0.44).

Garnet is rich in almandine component and its composition is defined by a rim-ward increase of Fe and Mg and decrease of Ca: $Prp_{24.0→27.0}Alm_{45.5→57.8}Grs_{29.7→13.9}Sps_{0.9→1.4}$; XFe^{2+} = 0.66→0.68 (Figure III. 3d). Biotite has XFe^{tot} = 0.33–0.37 and Ti ~0.3 p.f.u.

Clinopyroxene inclusions in garnet show no distinctive composition zonality from the core towards the rim: $CaTs_{9.0→6.6}Jd_{5.7→4.2}$, XFe^{2+} = 0.31→0.28.

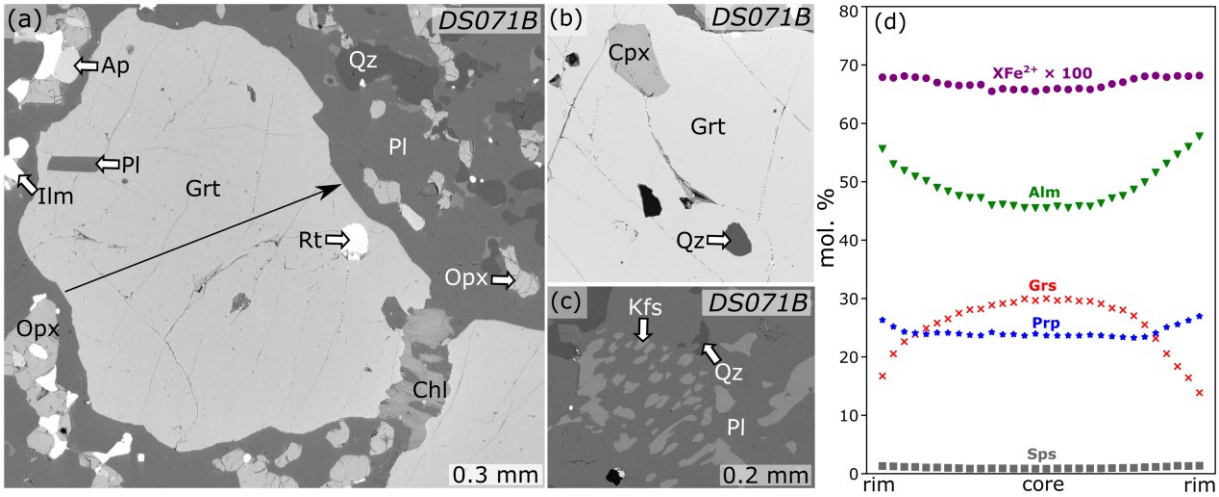

Figure III. 3: a–c) Backscattered electron images of intermediate granulite, and d) Composition profile of garnet from the subfigure a.

Sample DS153/20A (Figure III. 4) is fine-grained and contains garnet up to 0.4 mm in size with clinopyroxene inclusions (Figure III. 4a). Abundant accessory phase in the matrix is ilmenite, which is also present in relatively rare elongated garnet clusters (Figure III. 4b). In the matrix coexist perthite and antiperthite feldspars (Figure III. 4c), which is unique among the studied samples. Biotite was not observed.

Plagioclase (andesine to oligoclase) in the matrix shows no systematic zoning ($An_{26.8–29.5}Ab_{68.4–70.6}Or_{1.7–2.6}$). The albite component in the K-feldspar varies from 7.8 to 8.9 %. Orthopyroxene is Fe-rich (XFe^{2+} = 0.60–0.61).

Garnet is rich in almandine component and its composition is defined by a rim-ward increase of Fe and decrease of Ca, Mg remains similar: $Prp_{13.4→13.8}Alm_{64.0→68.5}Grs_{20.8→15.7}Sps_{1.8→2.1}$; XFe^{2+} = 0.83→0.83 (Figure III. 4d). Garnet forming clusters around Ilm aggregates show no systematic zoning with composition range: $Prp_{14.7–15.6}Alm_{66.6–67.1}Grs_{15.5–16.5}Sps_{1.8–2.1}$; XFe^{2+} = 0.81–0.82.

Documented clinopyroxene inclusion in garnet shows slight Na and Al decrease and Ca increase from the core towards the rim: $CaTs_{2.9–2.0}Jd_{4.7→4.4}$, XFe^{2+} = 0.44→0.44.

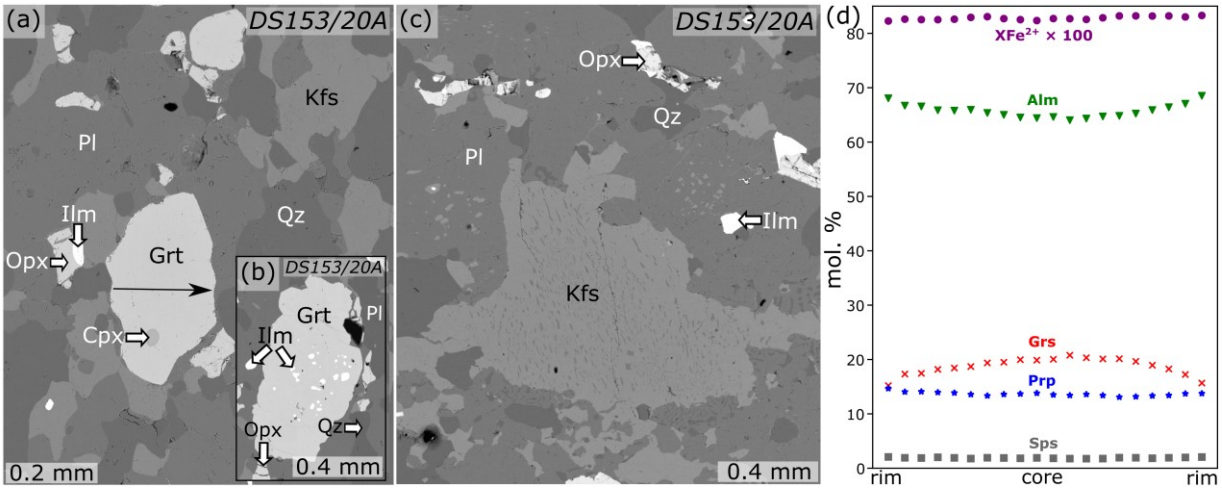

Figure III. 4: a–c) Backscattered electron images of intermediate granulite (DS153/20A), and d) Composition profile of garnet from the subfigure a.

Sample DS155/20A (Figure III. 5) contains up to 0.6 mm garnet porphyroblasts and large amount of elongated garnet clusters up to 1.3 mm surrounding spinel grains together with Al-oxide/hydroxide in epidote-clinozoisite-muscovite mass (Figure III. 5c). Matrix is rich in biotite. Ilmenite is rich accessory phase present in the entire sample volume.

Plagioclase grains in the matrix (andesine) have no systematic zoning ($An_{27.9–35.3}Ab_{63.3–69.1}Or_{1.5–3.0}$). Plagioclase forming rim around garnet surrounding spinel with oxide/hydroxide Al in Ms-Ep-Czo mass shows Ca decrease and Na increase from garnet towards the surrounding matrix: $An_{40.0→31.2}Ab_{58.1→66.2}Or_{1.9→2.7}$. The albite component in the K-feldspar varies from 6.4 to 7.6 %. Orthopyroxene is Fe-rich (XFe^{2+} = 0.54–0.55).

Garnet porphyroblasts are rich in almandine component and their chemical zonality is characterized by the rimward decrease of Ca and increase of Mg and Fe ($Prp_{18.4→21.5}Alm_{51.7→62.1}Grs_{28.8→14.7}Sps_{1.1→1.6}$; XFe^{2+} = 0.74→0.74; Figure III. 5e). Garnet grains forming rim around spinel, oxide/hydroxide Al in Ms-Ep-Czo mass shows the same trend in the chemical zonality with Ca decrease and Fe and Mg increase from the core to the rim with a slightly higher difference in Ca at the contact towards the Ms-Ep-Czo mass (from core to the contact with matrix: $Prp_{18.5→22.4}Alm_{55.5→60.7}Grs_{24.6→15.1}Sps_{1.4→1.8}$, XFe^{2+} = 0.75→0.73; from core to the contact with Ms-Ep-Czo mass: $Prp_{18.5→21.3}Alm_{55.5→60.0}Grs_{24.6→16.9}Sps_{1.4→1.8}$, XFe^{2+} = 0.75→0.74).

Spinel is rich in Al-endmembers: XFe^{2+} = 0.71–0.72, Al ~1.9 p.f.u., Cr ~0.0 p.f.u.

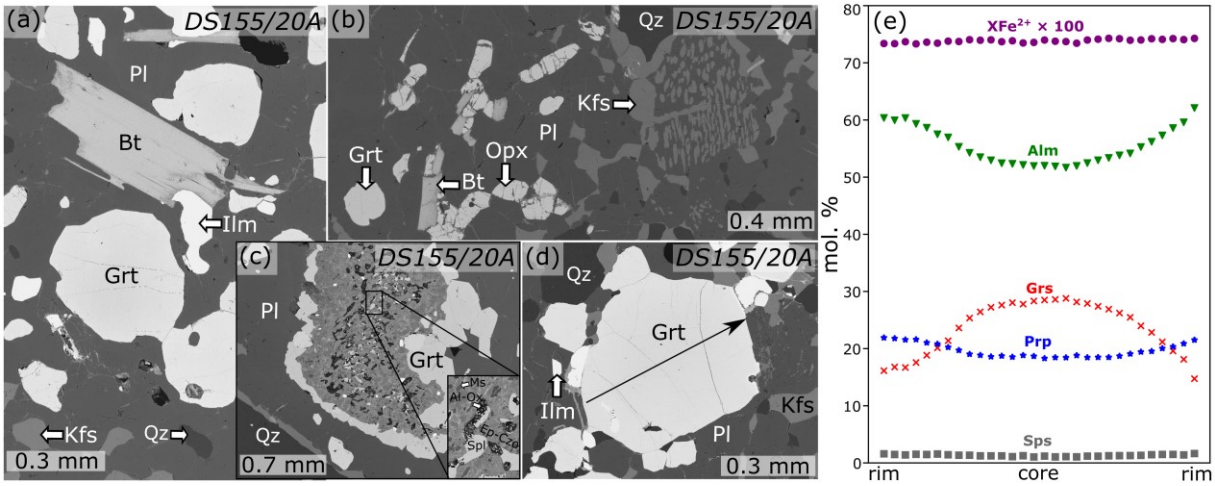

Figure III. 5: a–d) Backscattered electron images of intermediate granulite (DS155/20A), and e) Composition profile of garnet from the subfigure d.

Table III. 2: Representative mineral analyses of intermediate granulites in wt. %.

Lithology	Intermediate granulite												
Thin-section	DS071B	DS071B	DS153/20A	DS153/20A	DS155/20A	DS155/20A	DS153/20A	DS155/20A	DS155/20A	DS155/20A	DS071B	DS071B	DS153/20A
Mineral	Grt	Grt	Grt	Grt	Grt	Grt	Grt	Grt	Grt	Grt	Cpx	Cpx	Cpx
Analysis	Grt-line 15	Grt-line 30	Grt-line 12	Grt-line 20	Grt-line 18	Grt-line 30	Grt-02	Grt-1	Grt-2	Grt-3	Cpx-line 14	Cpx-line 11	Cpx-17
Position	Matrix, core	Matrix, rim	Matrix, core	Matrix, rim	Matrix, core	Matrix, rim	Grt around Spl aggregates	Grt around Spl, oxide/hydroxide Al, rim close to matrix	Grt around Spl, oxide/hydroxide Al, core	Grt around Spl, oxide/hydroxide Al, rim close to Spl, oxide/hydroxide Al	inclusion in Grt, core	inclusion in Grt, rim	inclusion in Grt, core
SiO_2	39.06	38.88	38.11	37.74	38.42	38.34	37.56	38.38	38.57	38.64	51.00	52.31	50.74
TiO_2	0.22	0.04	0.04	0.01	0.16	0.06	0.05	b.d.	0.11	0.06	1.34	0.94	0.27
Cr_2O_3	0.01	0.11	b.d.	b.d.	b.d.	0.02	0.03	0.01	b.d.	b.d.	0.01	b.d.	b.d.
Al_2O_3	21.99	21.72	20.67	20.63	21.41	21.15	20.71	21.05	21.32	21.09	5.36	3.80	1.96
FeO	21.72	26.78	29.09	30.35	23.20	27.56	30.37	27.94	25.51	27.20	9.33	8.79	15.01
MnO	0.40	0.63	0.80	0.90	0.49	0.72	0.81	0.80	0.63	0.79	0.07	0.03	0.18
MgO	6.29	7.01	3.42	3.42	4.64	5.36	3.77	5.75	4.77	5.41	11.70	12.94	10.23
BaO	b.d.	b.d.	b.d.	b.d.	b.d.	b.d.	b.d.	b.d.	b.d.	b.d.	b.d.	b.d.	b.d.
CaO	10.84	5.02	7.37	5.42	10.09	5.10	5.75	5.40	8.81	5.99	20.99	21.87	19.80
Na_2O	0.02	0.01	0.01	b.d.	0.02	0.02	0.06	0.03	0.03	b.d.	0.70	0.53	0.55
K_2O	b.d.	b.d.	b.d.	0.01	b.d.	b.d.	b.d.	b.d.	b.d.	b.d.	b.d.	b.d.	b.d.
ZnO	b.d.	b.d.	b.d.	b.d.	b.d.	b.d.	b.d.	b.d.	b.d.	b.d.	b.d.	b.d.	b.d.
Cl	b.d.	b.d.	b.d.	b.d.	b.d.	b.d.	b.d.	b.d.	b.d.	b.d.	b.d.	b.d.	b.d.
F	b.d.	b.d.	b.d.	b.d.	b.d.	b.d.	b.d.	b.d.	b.d.	b.d.	b.d.	b.d.	b.d.
Total	100.56	100.20	99.50	98.46	98.43	98.32	99.11	99.36	99.74	99.18	100.49	101.22	98.73
Cations/ Charges	8/24	8/24	8/24	8/24	8/24	8/24	8/24	8/24	8/24	8/24	4/12	4/12	4/12
Si	2.99	3.01	3.03	3.05	3.03	3.05	3.00	3.02	3.02	3.05	1.90	1.93	1.96
Ti	0.01	0.00	0.00	0.00	0.01	0.00	0.00	–	0.01	0.00	0.04	0.03	0.01
Cr	0.00	0.01	–	–	–	0.00	0.00	0.00	–	–	0.00	–	–
Al	1.98	1.98	1.94	1.96	1.99	1.99	1.95	1.95	1.97	1.96	0.24	0.16	0.09
Fe^{2+}	1.36	1.73	1.94	2.05	1.53	1.83	1.99	1.83	1.67	1.79	0.29	0.27	0.47
Fe^{3+}	0.03	0.00	0.00	0.00	0.00	0.00	0.04	0.01	0.00	0.00	0.00	0.00	0.01
Mn	0.03	0.04	0.05	0.06	0.03	0.05	0.05	0.05	0.04	0.05	0.00	0.00	0.01
Mg	0.72	0.81	0.41	0.41	0.55	0.64	0.45	0.67	0.56	0.64	0.65	0.71	0.59
Ba	–	–	–	–	–	–	–	–	–	–	–	–	–
Ca	0.89	0.42	0.63	0.47	0.85	0.44	0.49	0.46	0.74	0.51	0.84	0.86	0.82
Na	0.00	0.00	0.00	–	0.00	0.00	0.01	0.00	0.00	0.00	0.05	0.04	0.04
K	–	–	–	–	–	–	–	–	–	–	–	–	–
Zn	–	–	–	–	–	–	–	–	–	–	–	–	–
Cl	–	–	–	–	–	–	–	–	–	–	–	–	–
F	–	–	–	–	–	–	–	–	–	–	–	–	–
XFe^{2+}	0.66	0.68	0.83	0.83	0.74	0.74	0.82	0.73	0.75	0.74	0.31	0.28	0.44

b.d. below detection limit. * – Fe^{tot}

Table III.2 (continued): Representative mineral analyses of intermediate granulites in wt. %.

Lithology	Intermediate granulite														
Thin-section	DS153/20A	DS071B	DS153/20A	DS155/20A	DS071B	DS155/20A	DS071B	DS153/20A	DS155/20A	DS155/20A	DS155/20A	DS071B	DS153/20A	DS155/20A	DS155/20A
Mineral	Cpx	Opx	Opx	Opx	Bt	Bt	Pl	Pl	Pl	Pl	Pl	Kfs	Kfs	Kfs	Spl
Analysis	Cpx-18	Opx-01	Opx-09	Opx-24	Bt-01	Bt-11	Pl-04	Pl-15	Pl-16	Pl-04	Pl-06	Kfs-03	Kfs-14	Kfs-25	Spl-09
Position	inclusion in Grt, rim	Matrix	Matrix	Matrix	Matrix	Matrix	Matrix	Matrix	Matrix	Pl rim around Spl-oxide/hydroxide Al, next to Grt rim	Pl rim around Spl-oxidy/hydroxide Al, next to matrix	Matrix	Matrix	Matrix	Matrix, with oxide/hydroxide Al
SiO_2	51.41	51.39	49.38	50.63	37.09	35.52	59.24	62.09	62.59	58.86	61.41	64.47	65.05	64.90	0.03
TiO_2	0.24	0.03	0.11	0.07	5.50	5.37	0.01	0.01	0.03	0.02	b.d.	0.01	0.01	0.02	0.06
Cr_2O_3	b.d.	b.d	0.03	b.d.	0.12	0.03	0.01	0.02	0.01	b.d.	b.d.	b.d.	b.d.	b.d.	b.d.
Al_2O_3	1.69	1.44	1.18	1.12	14.17	14.71	25.44	23.91	23.95	25.70	24.29	18.59	18.61	18.88	56.10
FeO	14.45	23.74	34.01	31.34	13.23	20.80	0.07	0.07	b.d.	0.10	0.08	0.01	0.01	0.02	35.15
MnO	0.15	0.17	0.32	0.33	0.02	0.03	0.01	0.03	b.d.	b.d.	0.03	0.03	0.02	b.d.	0.04
MgO	10.52	21.03	12.92	14.80	14.31	9.29	0.02	b.d.	b.d.	0.01	b.d.	0.03	b.d.	0.01	6.50
BaO	b.d.	b.d.	b.d.	b.d.	b.d.	0.29	b.d.	b.d.	b.d.	b.d.	b.d.	b.d.	b.d.	b.d.	b.d.
CaO	20.15	0.33	0.58	0.61	0.05	0.05	6.96	5.42	5.76	8.26	6.25	0.11	0.04	0.27	0.06
Na_2O	0.52	b.d	0.02	0.05	0.02	0.10	7.23	7.89	7.66	6.63	7.34	0.86	0.86	0.82	b.d.
K_2O	b.d.	0.02	b.d.	0.03	9.59	9.38	0.47	0.45	0.52	0.32	0.45	15.32	15.43	14.88	0.01
ZnO	b.d.	b.d.	b.d.	b.d.	b.d.	b.d.	b.d.	b.d.	b.d.	b.d.	b.d.	b.d.	b.d.	b.d.	0.25
Cl	b.d.	b.d.	b.d.	b.d.	0.03	0.11	b.d.	b.d.	b.d.	b.d.	b.d.		b.d.	b.d.	b.d.
F	b.d.	b.d.	b.d.	b.d.	0.69	0.26	b.d.	b.d.	b.d.	b.d.	b.d.		b.d.	b.d.	b.d.
Total	99.12	98.14	98.55	98.96	94.08	95.56	99.45	99.88	100.51	99.90	99.85	99.42	100.03	99.79	98.20
Cations/ Charges	4/12	4/12	5/12	5/12	8/22	8/22	5/16	5/16	5/16	5/16	5/16	5/16	5/16	5/16	3/8
Si	1.98	1.96	1.99	2.00	2.68	2.63	2.66	2.77	2.78	2.64	2.75	2.99	3.00	3.00	0.00
Ti	0.01	0.00	0.00	0.00	0.30	0.30	0.00	0.00	0.00	0.00	–	0.00	0.00	0.00	0.00
Cr	–	–	0.00	–	0.01	0.00	0.00	0.00	0.00	–	–	–	–	–	–
Al	0.08	0.06	0.06	0.05	1.21	1.28	1.35	1.26	1.25	1.36	1.28	1.02	1.01	1.03	1.88
Fe^{2+}	0.46	0.74	1.14	1.03	0.80*	1.29*	0.00	0.00	–	0.00	0.00	0.00	0.00	0.00	0.72
Fe^{3+}	0.00	0.01	0.00	0.00	–	–	–	–	–	–	–	–	–	–	0.12
Mn	0.00	0.01	0.01	0.01	0.00	0.00	0.00	0.00	–	–	0.00	0.00	0.00	–	0.00
Mg	0.60	1.20	0.77	0.87	1.54	1.03	0.00	–	–	0.00	–	0.00	–	0.00	0.28
Ba	–	–	–	–	b.d.	0.01	–	–	–	–	–	b.d.	–	–	–
Ca	0.83	0.01	0.02	0.03	0.00	0.00	0.33	0.26	0.27	0.40	0.30	0.01	0.00	0.01	0.00
Na	0.04	–	0.00	0.00	0.00	0.01	0.63	0.68	0.66	0.58	0.64	0.08	0.08	0.07	–
K	–	0.00	–	0.00	0.88	0.89	0.03	0.03	0.03	0.02	0.03	0.91	0.91	0.88	0.00
Zn	–	–	–	–	–	–	–	–	–	–	–	–	–	–	0.01
Cl	–	–	–	–	0.00	0.01	–	–	–	–	–	–	–	–	–
F	–	–	–	–	0.16	0.06	–	–	–	–	–	–	–	–	–
XFe^{2+}	0.44	0.38	0.60	0.54	XFe^{tot} = 0.34	XFe^{tot} = 0.56									0.72

b.d. below detection limit. * – Fe^{tot}

1.1.3 Mafic granulites

In the study area occur mafic granulites, which have the same mineral association but differ in their texture, which may be either granoblastic (M-Gr(G)) or symplectitic (M-Gr(S)) or form a transition between these two textures.

Both types have a fine-grained Cpx-Pl (±Opx, Amp) matrix hosting up to ~2 mm large garnet porphyroblasts.

In the symplectite type, plagioclase forms rim around garnet and "worm-like" intergrows at its rim. Matrix is dominated by coarse-grained Cpx-Pl symplectites, whereas larger clinopyroxene grains with exsolutions of Opx are quite rare in the matrix.

In the granoblastic type are no plagioclase intergrows at the garnet rims and larger Cpx with Opx exsolutions are more common. This granoblastic type resembles more garnet clinopyroxenite (see below), but differs in the considerably higher amount of plagioclase. In the matrix of studied samples occurs spinel as small aggregates surrounded by plagioclase, or fine-grained Pl–Spl ± Amp symplectites replacing garnet. Garnet hosts idiomorphic inclusions of clinopyroxene, kyanite – in some cases in the association with sapphirine.

Representative mineral analysis of mafic granulites are available in Table III. 3.

Sample DS025E (Figure III. 6) contains up to 2.5 mm large garnet porphyroblast surrounded by thin plagioclase rim forming also worm-like intergrowths in the garnet especially on its rim (Figure III. 6a). Garnet contains kyanite, sapphirine, and clinopyroxene inclusions (Figure III. 6b, e). Matrix is formed by coarse-grained clinopyroxene-plagioclase symplectites with small amount of amphibole and orthopyroxene. Larger clinopyroxene grains contain orthopyroxene exsolution lamellae (Figure III. 6c)

Plagioclase forming coarse grained symplectites with Cpx in the matrix has composition range: $An_{42.9–54.9}Ab_{56.3–44.8}Or_{0.3–0.8}$. The composition map of K shows that the rims of the plagioclase in the matrix are enriched by K (Figure III. 6g). Plagioclase surrounding Spl aggregates shows higher Ca content with the composition range: $An_{76.8–82.6}Ab_{17.2–23.1}Or_{0.1–0.1}$. Plagioclase forming intergrowths in garnet has composition range: $An_{57.9–74.2}Ab_{25.7–41.6}Or_{0.1–0.8}$. Plagioclase at the contact with the garnet has composition range: $An_{52.3–52.7}Ab_{46.8–46.8}Or_{0.5–0.9.}$

Orthopyroxene has XFe^{2+} = 0.16–0.18. The larger clinopyroxene grains with Opx lamellae present in the matrix are characterized by a decrease in Na, Al, and XFe^{2+} and a slight increase in Ca from the core to the rim: $CaTs_{18.9→8.2}Jd_{10.9→6.1}$, XFe^{2+} = 0.15→0.13. Clinopyroxene

inclusions in Grt are characterized by a decrease in Na, Al, and Fe^{2+} and increase in Ca from core to rim: $CaTs_{13.8\rightarrow32.6}Jd_{26.3\rightarrow8.4}$, $XFe^{2+} = 0.11\rightarrow0.01$.

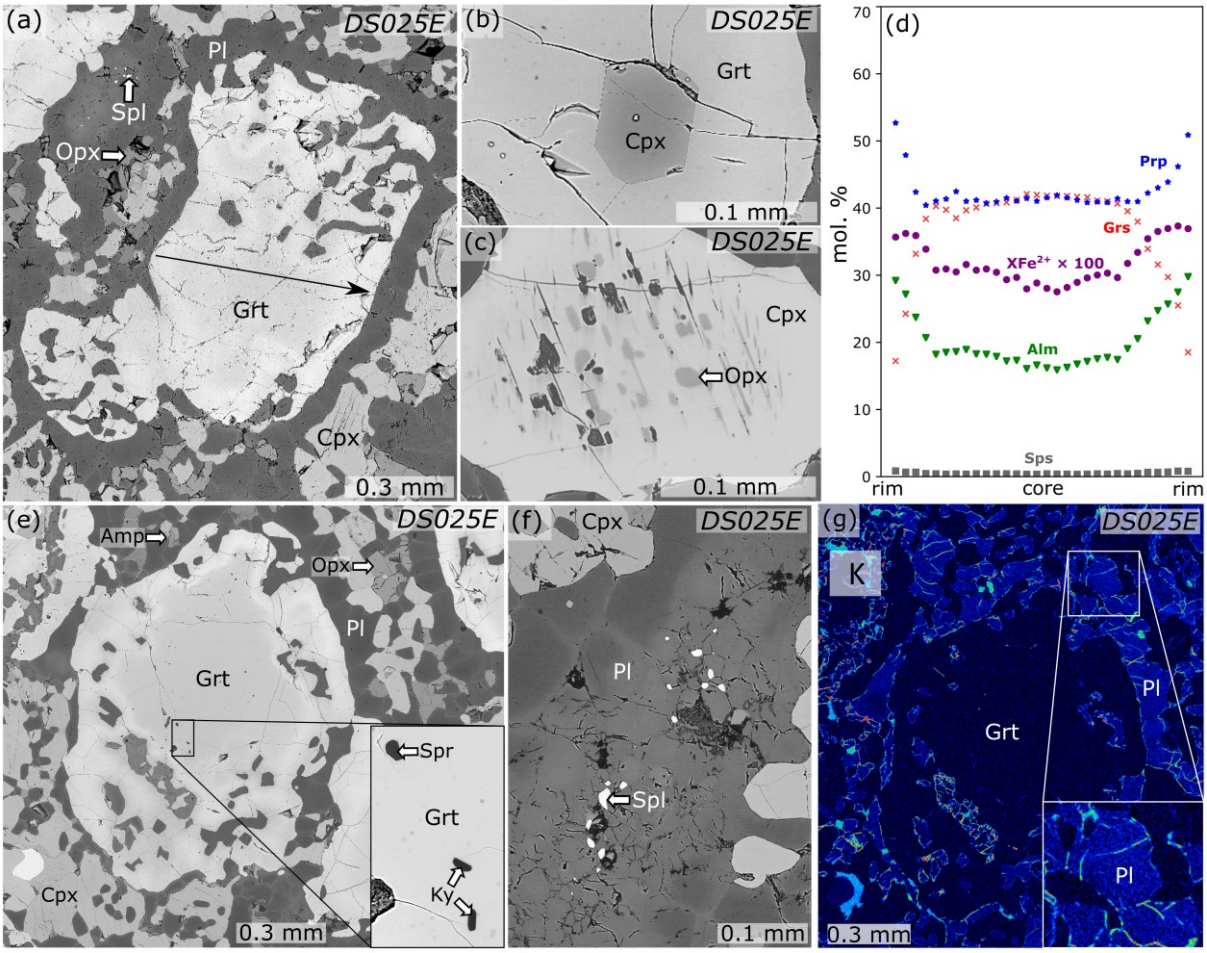

Figure III. 6: Back-scattered electron images, composition profile of garnet, and composition map of K from mafic granulite DS025E with symplectite texture. a) Garnet with plagioclase rim and abundant plagioclase intergrowths. b) Clinopyroxene inclusion in garnet. c) Clinopyroxene in matrix with orthopyroxene exsolutions. d) Composition profile of garnet from the subfigure a. e) Garnet with sapphirine and kyanite inclusions. f) Spinel aggregates in plagioclase. g) Composition map of K in the matrix.

Chemical zoning of garnet is characterized by the compositional plateau followed by Ca decrease and Fe and Mg increase at the rim, whereby the contents of the grossular and pyrope components in the core are approximately equal ($Prp_{41.5\rightarrow52.7}Alm_{16.1\rightarrow29.2}Grs_{42.1\rightarrow17.2}Sps_{0.4\rightarrow0.9}$, $XFe^{2+} = 0.28\rightarrow0.36$; Figure III. 6d).

Spinel forming aggregates in Pl in the matrix has composition range: $XFe^{2+} = 0.44–0.47$, Al 1.4–1.7 p.f.u., Cr 0.3–0.5 p.f.u. (with 0.96–0.99 wt. % ZnO).

Amphibole (pargasite) has the composition range: XFe^{2+} = 0.13–0.16, Ti = 0.1–0.3, Si = 6.1–6.2 p.f.u.

Sample DS025/20B (Figure III. 7) contains up to 1.9 mm large garnet porphyroblasts surrounded by plagioclase rim with Pl worm-like intergrowths and rare kyanite inclusions (Figure III. 7a). Matrix is formed by Cpx-Pl (Opx) symplectites, where larger clinopyroxene grains contain orthopyroxene exsolution lamellae (Figure III. 7b). Matrix also contains Spl aggregates in Pl (Figure III. 7c). Amphibole was not documented.

Plagioclase forming coarse grained symplectites in the matrix has composition range: $An_{40.0–41.4}Ab_{57.7–59.0}Or_{0.9–1.0}$. Large plagioclase grains in the matrix show Ca increase and Na decrease from the core towards the rim: $An_{57.2→60.7}Ab_{42.3→39.0}Or_{0.5→0.3}$ .Plagioclase hosting Spl aggregates shows high Ca content: $An_{71.9}Ab_{27.9}Or_{0.3}$. Plagioclase forming worm-like intergrowths in garnet has composition of $An_{58.8–60.1}Ab_{40.7–39.5}Or_{0.5–0.4}$. Plagioclase at the contact with the garnet shows a slight increase in Ca close to the contact with garnet rim: $An_{47.2→52.9}Ab_{52.0→46.6}Or_{0.8→0.5}$.

Orthopyroxene has XFe^{2+}=0.17–0.18. The larger clinopyroxene grains with Opx lamellae present in the matrix are characterized by a decrease in Na, Al, and XFe^{2+} and a slight increase in Ca from the core to the rim: $CaTs_{20.6→8.8}Jd_{8.6→5.4}$, XFe^{2+} = 0.14→0.12. Clinopyroxene forming coarse-grained symplectites with plagioclase has the composition range: $CaTs_{3.5–12.5}Jd_{5.9–7.3}$, XFe^{2+} = 0.13–0.14.

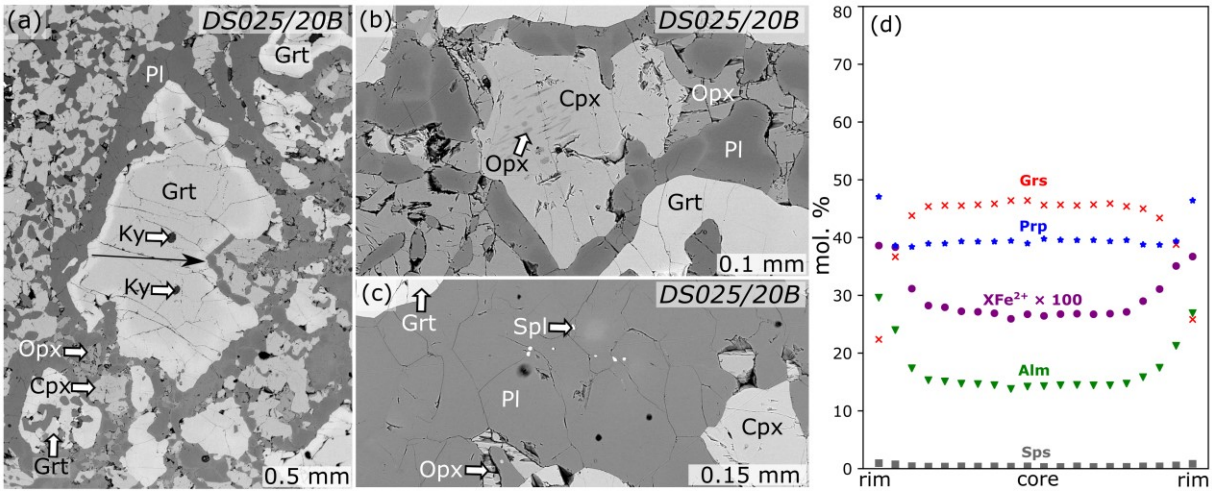

Figure III. 7: a–c) Backscattered electron images of mafic granulite DS025/20B with symplectite texture, and d) Composition profile of garnet from the subfigure a.

Garnet porphyroblasts are rich in grossular component with the chemical zonality characterized by the Ca decrease and Mg and Fe increase at the rim ($Prp_{39.8\rightarrow46.4}Alm_{14.3\rightarrow26.9}Grs_{45.6\rightarrow25.8}Sps_{0.3\rightarrow0.8}$, XFe^{2+} = 0.26→0.38; Figure III. 7d).

Sample DS025/20C (Figure III. 8) contains up to 3 mm large garnet porphyroblasts with rare idiomorphic inclusions of clinopyroxene, kyanite, and rutile. One documented kyanite inclusion hosts small clinopyroxene (Figure III. 8c). Plagioclase forms a rim around the garnet only in some cases and intergrows through it only slightly. Matrix is dominantly formed by Cpx-Pl coarse-grained symplectites. The sample is rich in amphibole, which often forms a rim around abundant accessory phase, ilmenite. Orthopyroxene was not observed. Another common accessory phase in the matrix is up to 1.5 mm large apatite (Figure III. 8b). Another accessory phase is pyrrhotite.

Plagioclase has the following composition ranges: coarse-grained symplectites: $An_{34.0–41.6}Ab_{58.0–65.3}Or_{0.4–0.7}$; intergrowth with garnet: $An_{41.3–52.7}Ab_{47.0–58.4}Or_{0.2–0.3}$. Plagioclase rim around garnet shows a slight Ca increase from the core towards the garnet: $An_{36.9\rightarrow42.6}Ab_{62.8\rightarrow57.1}Or_{0.2\rightarrow0.3}$.

The larger clinopyroxene grains present in the matrix are characterized by a decrease in Na, Al, and XFe^{2+} and a slight increase in Ca from the core to the rim: $CaTs_{21.0\rightarrow17.6}Jd_{12.7\rightarrow10.9}$, XFe^{2+} = 0.20→0.19. Clinopyroxene forming coarse-grained symplectites with plagioclase has the composition range: $CaTs_{14.1–17.1}Jd_{11.4–16.4}$, XFe^{2+} = 0.18–0.21. Clinopyroxene inclusion in garnet is characterized by a large decrease of Na and increase of Al and Ca from the core towards the rim: $CaTs_{13.3–21.2}Jd_{31.3–16.8}$, XFe^{2+} = 0.19–0.18. Small Cpx inclusion in kyanite shows no composition zoning: $CaTs_{7.5}Jd_{41.5}$, XFe^{2+} = 0.13.

Garnet is rich in grossular component and its chemical zonality is characterized by the Ca decrease and Fe and Mg increase from the core towards the rim ($Prp_{35.0\rightarrow42.2}Alm_{26.1\rightarrow37.0}Grs_{38.3\rightarrow19.7}Sps_{0.6\rightarrow1.1}$, XFe^{2+} = 0.43→0.47; Figure III. 8d).

Amphibole (pargasite to sanagaite) has the composition range: XFe^{2+} = 0.19–0.26, Ti = 0.0–0.4, Si = 5.8–6.2 p.f.u.

Apatite composition was not analysed, but according to EDS they are F-rich and contain only negligible amounts of Cl.

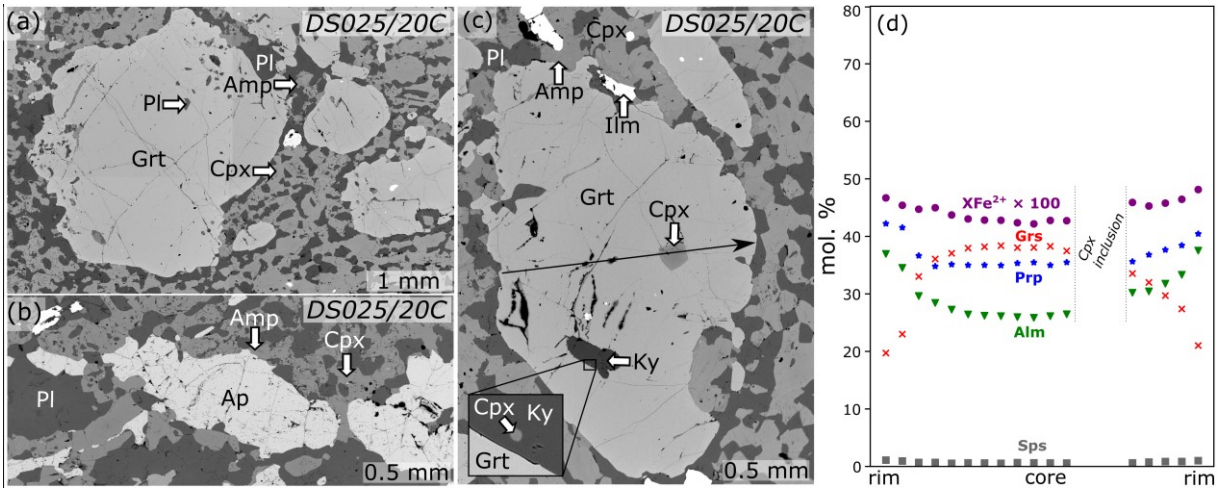

Figure III. 8: a–c) Backscattered electron images of mafic granulite DS025/20C with symplectite texture, and d) Composition profile of garnet from the subfigure a.

Sample DS157/20G (Figure III. 9) contains up to 2.6 mm large garnet porphyroblasts with idiomorphic inclusions of clinopyroxene and plagioclase (Figure III. 9a–c). Preserved garnet grains do not contain distinctive plagioclase rim around and are almost free of plagioclase intergrowths, but the sample also contains garnet relicts significantly replaced by plagioclase and amphibole in places. This sample contains the same type of multiphase solid inclusions (Figure III. 9e) described in detail in the Part I of this thesis.

The texture of the matrix is Cpx–Pl(Amp) granoblastic with transitions to Cpx–Pl(Amp) symplectites. Orthopyroxene was not observed. In the sample occur fine-grained Spl–Pl symplectites that occur in Pl in the matrix or are present at the rim of garnet and are connected with the matrix (Figure III. 9g, h). The matrix also hosts up to 2 mm large spinel grains replaced by corundum and calcite–muscovite–anorthite fine-grained mass (Figure III. 9i).

Common accessory phase are pyrrhotite and graphite.

Plagioclase forming coarse-grained symplectites with Cpx in the matrix has the composition range: $An_{54.5–79.7}Ab_{20.3–45.2}Or_{0.0–0.4}$. Plagioclase grains in granoblastic matrix show Ca increase from the core towards the rim: $An_{49.0–55.0}Ab_{50.6–44.8}Or_{0.4–0.2}$. Plagioclase inclusion in garnet show Ca increase from the core towards the rim: $An_{39.8→46.0}Ab_{59.0→52.9}Or_{0.1→1.1}$. Plagioclase associate with Spl in the matrix has high Ca content: $An_{69.6–73.1}Ab_{26.7–30.0}Or_{0.2–0.4}$.

Large clinopyroxene grains in the matrix and Cpx inclusion in Grt are characterized by the Ca increase and Al, Na, and Fe decrease from the core towards the rim (Cpx in matrix $CaTs_{22.3→9.8}Jd_{6.9→4.7}$, $XFe^{2+} = 0.16→0.16$; inclusion in Grt: $CaTs_{31.6→25.2}Jd_{10.1→6.6}$, $XFe^{2+} = 0.17→0.10$).

Clinopyroxene forming coarse-grained symplectites with Pl and Amp has composition of $CaTs_{23.2–24.0}Jd_{8.1–8.7}$, $XFe^{2+} = 0.13–0.14$.

Preserved garnet grains are rich in grossular component and their composition zoning is characterized by the Ca decrease and Fe increase from the core towards the rim ($Prp_{45.1→44.0}Alm_{20.7→28.3}Grs_{33.8→27.0}Sps_{0.5→0.6}$, $XFe^{2+} = 0.31→0.39$; Figure III. 9d).

Spinel has the composition range: $XFe^{2+} = 0.34–0.38$, Al ~2 p.f.u., $Cr_2O_3 = 0.27–0.67$ wt. %.

Amphibole (pargasite) has the composition range: $XFe^{2+} = 0.17–0.20$, Ti = 0.0–0.1 pf.u., Si = 5.9–6.1 p.f.u.

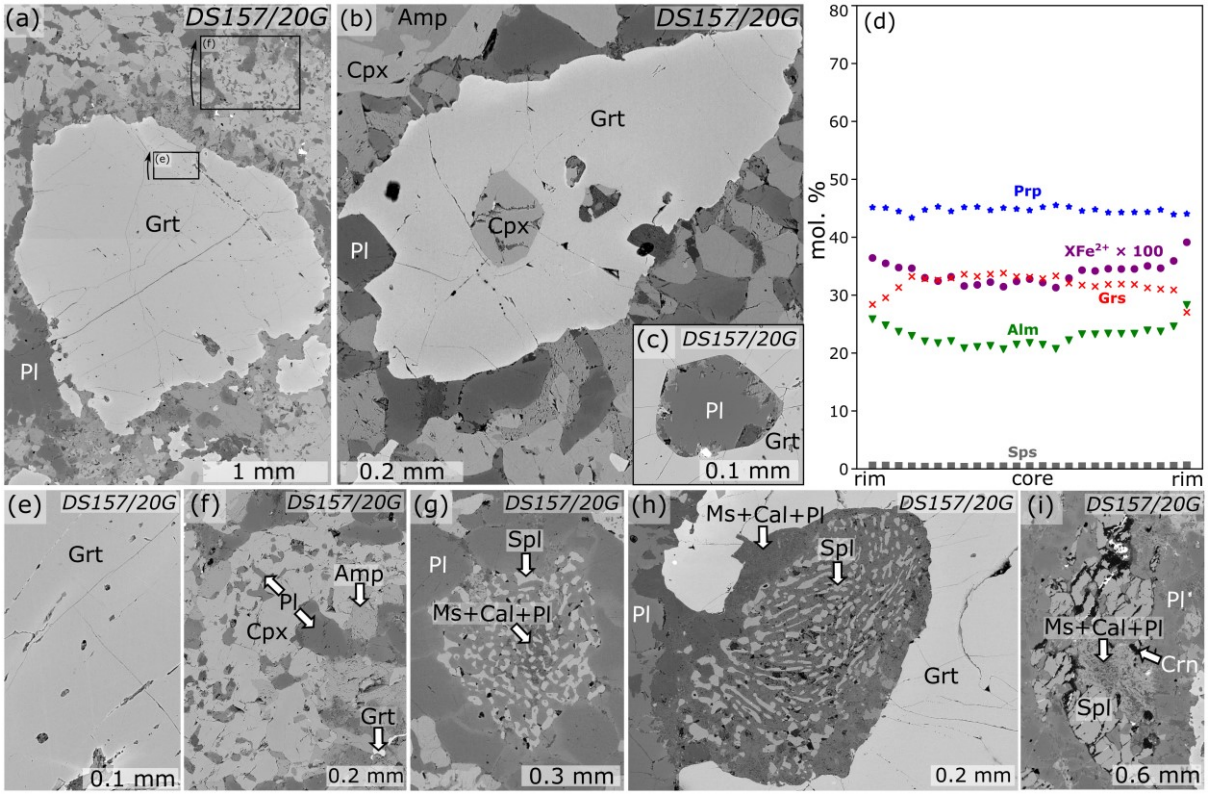

Figure III. 9: Back-scattered electron images and composition profile of garnet from mafic granulite DS157/20G with transitions of granoblastic tu symplectite matrix in places. a) Garnet porphyroblast in clinopyroxene-plagioclase rich matrix. b) Clinopyroxene inclusion in garnet. c) Plagioclase inclusion in garnet. d) Composition profile of garnet from the subfigure a. e) Multiphase solid inclusions in garnet. f) Detail of the clinopyroxene-plagioclase matrix with amphibole. g) Fine-grained spinel-plagioclase symplectites accompanied by muscovite and calcite in the matrix and h) in garnet at the contact with the matrix. i) Spinel in the matrix.

Sample DS027/20B (Figure III. 10) is formed by up to 2.5 mm large garnet porphyroblasts with idiomorphic inclusions of clinopyroxene (Figure III. 10a). These porphyroblasts are partly surrounded by plagioclase rim and do not contain plagioclase intergrowths. Matrix has Cpx-Pl granoblastic texture accompanied in small amount by amphibole and orthopyroxene (Figure III. 10b).

Plagioclase (labradorite to andesine) show no systematic zoning with the composition range: $An_{44.9–57.1}Ab_{42.9–54.8}Or_{0.0–0.3}$.

Orthopyroxene has $XFe^{2+} = 0.20–0.22$. Clinopyroxene grains in the matrix show no systematic zoning with the composition range: $CaTs_{9.4–11.6}Jd_{8.1–9.2}$, $XFe^{2+} = 0.13–0.14$. Clinopyroxene inclusions in garnet are characterized by the decrease of Na and increase of Al and Ca from the core towards the rim: $CaTs_{16.7→32.5}Jd_{16.4→8.3}$, $XFe^{2+} = 0.13$.

Garnet is rich in pyrope component and its chemical zonality is characterized by the Ca decrease and Fe and Mg increase from the core towards the rim ($Prp_{42.9→52.1}Alm_{20.2→31.5}Grs_{36.5→15.5}Sps_{0.4→0.8}$, $XFe^{2+} = 0.32→0.38$; Figure III. 10c.)

Amphibole (pargasite) with the composition range: $XFe^{2+} = 0.12–0.17$, Ti = 0.1–0.2, Si = 6.0–6.2 p.f.u.

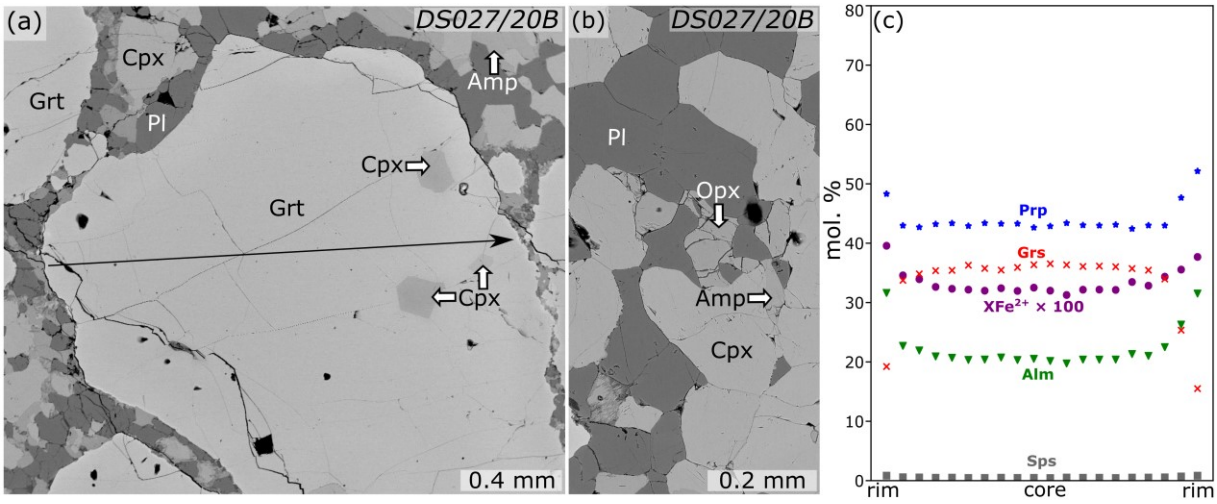

Figure III. 10: a–b) Backscattered electron images of mafic granulite DS027/20B with granoblastic texture, and d) Composition profile of garnet from the subfigure a.

.

Table III. 3: Representative mineral analyses of mafic granulites in wt. %.

Lithology	Mafic granulites														
Thin-section	DS025E	DS025E	DS025/20 B	DS025/20 B	DS025/20 C	DS025/20 C	DS157/20 G	DS157/20 G	DS027/20 B	DS027/20 B	DS025E	DS025E	DS025/20 B	DS025/20 B	DS025/20 C
Mineral	Grt	Grt	Grt	Grt	Grt	Grt	Grt	Grt	Grt	Grt	Cpx	Cpx	Cpx	Cpx	Cpx
Analysis	Grt05-line 17	Grt05-line 01	Grt01-line 11	Grt01-line 01	Grt01-line 11	Grt01-line 01	Grt01-line 25	Grt01-line 11	Grt02-line 11	Grt02-line20	Cpx-line 16	Cpx-line 25	Cpx-02	Cpx-04	Cpx-20
Position	Matrix, core	Matrix, rim	Matrix, core	Matrix, rim	Matrix, core	Matrix, rim	Matrix, rim	Matrix, core	Matrix, core	Matrix, rim	Matrix, core	Matrix, rim	Matrix, core	Matrix, rim	Matrix, core
SiO_2	40.94	40.90	41.40	40.52	40.55	40.30	41.01	40.85	41.18	41.01	49.44	52.60	48.28	52.41	47.85
TiO_2	0.17	0.09	0.24	0.11	0.22	0.05	0.12	0.18	0.18	0.08	0.30	0.56	0.32	0.80	0.71
Cr_2O_3	0.08	0.11	0.05	0.12	0.02	0.06	0.05	0.07	0.03	0.09	0.10	0.06	0.08	0.20	0.01
Al_2O_3	22.71	22.94	23.16	22.94	22.52	22.38	22.72	23.03	23.04	22.87	11.50	4.88	12.04	5.09	12.31
FeO	8.28	14.28	6.98	14.31	12.61	17.52	13.88	10.60	9.88	15.39	4.08	3.81	3.56	3.51	4.97
MnO	0.19	0.41	0.15	0.45	0.29	0.52	0.30	0.22	0.21	0.40	0.10	0.07	0.05	0.06	0.06
MgO	11.54	14.45	10.89	12.77	9.46	11.23	12.11	12.39	11.77	14.28	12.06	14.86	12.09	14.99	10.73
CaO	16.04	6.57	17.38	8.44	14.41	7.30	10.34	12.93	13.96	5.91	21.33	22.61	21.32	22.56	20.43
Na_2O	b.d.	0.02	0.02	0.02	0.06	0.04	0.01	b.d.	0.03	b.d.	1.44	0.81	1.12	0.71	1.65
K_2O	b.d.	0.00	b.d.	b.d.	b.d.	0.01	0.01	0.01	b.d.	b.d.	b.d.	b.d.	b.d.	0.02	b.d.
ZnO	b.d.	b.d.	b.d.	b.d.	b.d.	b.d.	b.d.	b.d.	b.d.	b.d.	b.d.	b.d.	b.d.	b.d.	b.d.
Total	99.95	99.77	100.25	99.68	100.14	99.40	100.55	100.27	100.29	100.02	100.36	100.25	98.85	100.33	98.72
Cations/ Charges	8/24	8/24	8/24	8/24	8/24	8/24	8/24	8/24	8/24	8/24	4/12	4/12	4/12	4/12	4/12
Si	2.99	3.00	3.02	3.00	3.01	3.03	3.01	2.98	3.01	3.01	1.79	1.91	1.77	1.90	1.77
Ti	0.01	0.00	0.01	0.01	0.01	0.00	0.01	0.01	0.01	0.00	0.01	0.02	0.01	0.02	0.02
Cr	0.00	0.01	0.00	0.01	0.00	0.00	0.00	0.00	0.00	0.01	0.00	0.00	0.00	0.01	0.00
Al	1.96	1.99	1.99	2.00	1.97	1.98	1.97	1.98	1.98	1.98	0.49	0.21	0.52	0.22	0.54
Fe^{2+}	0.48	0.88	0.43	0.89	0.78	1.10	0.85	0.62	0.60	0.95	0.11	0.12	0.11	0.11	0.15
Fe^{3+}	0.03	0.00	0.00	0.00	0.00	0.00	0.00	0.03	0.00	0.00	0.01	0.00	0.00	0.00	0.00
Mn	0.01	0.03	0.01	0.03	0.02	0.03	0.02	0.01	0.01	0.02	0.00	0.00	0.00	0.00	0.00
Mg	1.26	1.58	1.18	1.41	1.05	1.26	1.33	1.35	1.28	1.56	0.65	0.81	0.66	0.81	0.59
Ca	1.26	0.52	1.36	0.67	1.15	0.59	0.81	1.01	1.09	0.46	0.83	0.88	0.84	0.88	0.81
Na	–	0.00	0.00	0.00	0.01	0.01	0.00	–	0.00	–	0.10	0.06	0.08	0.05	0.12
K	–	–	–	–	–	0.00	0.00	0.00	–	–	–	–	–	0.00	–
Zn	–	–	–	–	–	–	–	–	–	–	–	–	–	–	–
XFe^{2+}	0.28	0.36	38.61	26.44	42.77	46.69	39.13	31.46	32.00	37.69	0.15	0.13	0.14	0.12	0.20

b.d. below detection limit

Table III. 4 (continued): Representative mineral analyses of mafic granulites in wt. %.

Lithology	Mafic granulites														
Thin-section	DS025/20C	DS157/20G	DS157/20G	DS027/20B	DS027/20B	DS025E	DS025/20B	DS025/20C	DS157/20G	DS027/20B	DS025E	DS025E	DS025/20C	DS025/20C	DS025/20C
Mineral	Cpx	Cpx	Cpx	Cpx	Cpx	Cpx	Cpx	Cpx	Cpx	Cpx	Cpx	Cpx	Cpx	Cpx	Cpx
Analysis	Cpx-21	Cpx-19	Cpx-20	Cpx-13	Cpx-14	Cpx-03	Cpx-13	Cpx-10	Cpx-14	Cpx-21	Cpx-line 08	Cpx-line 11	Cpx-14	Cpx-01	Cpx in Ky
Position	Matrix, rim	Matrix, core	Matrix, rim	Matrix, core	Matrix, rim	Matrix, symplectite with Pl	Matrix, symplectite with Pl	Matrix, symplectite with Pl	Matrix, symplectite with Pl	Matrix, symplectite with Pl	inclusion in Grt, core Cpx	inclusion in Grt, rim Cpx	Inclusion in Grt, core	Inclusion in Grt, rim	Inclusion in Ky in Grt
SiO_2	48.99	47.20	51.48	50.64	51.36	48.72	53.65	50.08	47.48	51.51	51.84	45.94	51.91	48.48	54.08
TiO_2	0.86	0.77	0.38	0.73	0.72	1.05	0.21	0.84	0.67	0.67	0.30	0.88	0.40	0.55	0.43
Cr_2O_3	0.04	0.07	0.08	0.14	0.13	0.11	0.06	0.10	0.04	0.14	0.09	0.13	0.03	0.05	0.10
Al_2O_3	10.11	11.76	5.46	6.87	6.86	8.97	3.36	8.74	12.90	6.38	13.13	16.46	13.72	13.99	14.09
FeO	5.16	4.90	4.69	4.11	4.13	3.70	4.35	5.58	3.82	4.04	2.31	2.15	3.87	3.91	2.25
MnO	0.05	0.07	0.08	0.09	0.05	0.06	0.10	0.08	0.01	0.10	0.03	0.02	0.05	0.04	0.01
MgO	11.91	12.07	14.19	14.12	14.28	13.24	15.64	12.18	11.61	13.97	11.02	10.55	9.54	10.00	8.82
CaO	20.77	21.41	22.51	20.71	20.47	22.66	21.53	20.44	21.91	21.50	17.99	23.02	16.76	20.00	14.56
Na_2O	1.41	0.88	0.62	1.16	1.07	0.94	0.77	1.46	1.16	1.14	3.56	1.17	4.22	2.24	5.71
K_2O	0.01	0.01	b.d.	0.02	b.d.	0.00	b.d.	b.d.	b.d.	b.d.	0.01	b.d.	b.d.	b.d.	b.d.
ZnO	b.d.	b.d.	b.d.	b.d.	b.d.	b.d.	b.d.	b.d.	b.d.	b.d.	b.d.	b.d.	b.d.	b.d.	b.d.
Total	99.32	99.14	99.48	98.58	99.05	99.45	99.67	99.49	99.60	99.45	100.27	100.31	100.48	99.26	100.03
Cations/ Charges	4/12	4/12	4/12	4/12	4/12	4/12	4/12	4/12	4/12	4/12	4/12	4/12	4/12	4/12	4/12
Si	1.80	1.74	1.89	1.87	1.89	1.79	1.96	1.84	1.73	1.89	1.85	1.66	1.85	1.77	1.92
Ti	0.02	0.02	0.01	0.02	0.02	0.03	0.01	0.02	0.02	0.02	0.01	0.02	0.01	0.02	0.01
Cr	0.00	0.00	0.00	0.00	0.00	0.00	0.00	0.00	0.00	0.00	0.00	0.00	0.00	0.00	0.00
Al	0.44	0.51	0.24	0.30	0.30	0.39	0.14	0.38	0.56	0.28	0.55	0.70	0.58	0.60	0.59
Fe^{2+}	0.15	0.12	0.14	0.12	0.13	0.07	0.13	0.17	0.10	0.12	0.07	0.06	0.12	0.12	0.07
Fe^{3+}	0.01	0.03	0.00	0.00	0.00	0.05	0.00	0.00	0.02	0.00	0.00	0.00	0.00	0.00	0.00
Mn	0.00	0.00	0.00	0.00	0.00	0.00	0.00	0.00	0.00	0.00	0.00	0.00	0.00	0.00	0.00
Mg	0.65	0.66	0.78	0.78	0.78	0.72	0.85	0.67	0.63	0.76	0.59	0.57	0.51	0.54	0.47
Ca	0.82	0.85	0.89	0.82	0.81	0.89	0.84	0.81	0.86	0.84	0.69	0.89	0.64	0.78	0.55
Na	0.10	0.06	0.04	0.08	0.08	0.07	0.05	0.10	0.08	0.08	0.25	0.08	0.29	0.16	0.39
K	0.00	0.00	–	0.00	–	0.00	–	–	–	–	0.00	0.00	–	0.00	0.00
Zn	–	–	–	–	–	–	–	–	–	–	–	–	–	–	–
XFe^{2+}	0.19	0.16	0.16	0.14	0.14	0.08	0.13	0.20	0.13	0.14	0.11	0.10	0.19	0.18	0.13

b.d. below detection limit

Table III. 4 (continued): Representative mineral analyses of mafic granulites in wt. %.

Lithology	Mafic granulites														
Thin-section	DS157/20G	DS157/20G	DS027/20B	DS027/20B	DS025E	DS025E	DS025/20B	DS027/20B	DS025E	DS025E	DS025E	DS025E	DS025/20B	DS025/20B	DS025/20B
Mineral	Cpx	Cpx	Cpx	Cpx	Opx	Opx	Opx	Opx	Pl	Pl	Pl	Pl	Pl	Pl	Pl
Analysis	Cpx-36	Cpx-37	Cpx-01	Cpx-02	Opx-01	Opx-04	Opx-08	Opx-17	Pl-03	Pl-02	Pl-01	Pl-11	Pl-20	Pl-05	Pl-06
Position	Inclusion in Grt, core	Inclusion in Grt, rim	Inclusion in Grt, core	Inclusion in Grt, rim	Matrix	Matrix	Matrix	Matrix	Matrix, symplectite with Cpx	intergrowth in Grt	Rim around Grt	Matrix, next to Spl aggregates	Matrix, symplectite with Cpx	Matrix, core	intergrowth in Grt
SiO_2	45.65	47.22	50.39	45.57	53.95	52.95	54.03	53.74	56.78	52.95	54.58	47.53	58.38	53.74	52.25
TiO_2	0.59	1.04	0.33	1.26	0.11	0.10	0.11	0.08	b.d.	0.01	0.02	0.01	b.d.	0.02	b.d.
Cr_2O_3	0.09	0.07	0.10	0.09	0.03	0.25	0.18	0.09	b.d.	b.d.	b.d.	0.03	b.d.	b.d.	0.03
Al_2O_3	17.65	12.50	12.68	16.56	2.79	4.54	4.39	3.76	26.97	29.70	28.66	33.89	26.69	29.67	30.65
FeO	3.52	3.42	3.00	2.86	12.03	11.19	10.89	13.01	0.15	0.26	0.04	0.11	0.03	0.11	0.16
MnO	0.04	0.06	0.06	0.02	0.13	0.06	0.13	0.11	b.d.	b.d.	b.d.	0.03	b.d.	0.02	0.02
MgO	9.59	12.12	11.39	10.41	29.32	29.54	29.59	27.84	0.18	0.01	b.d.	b.d.	0.01	0.03	b.d.
CaO	21.58	22.76	20.05	22.32	0.48	0.38	0.37	0.35	8.66	11.83	10.55	16.52	8.12	11.62	12.13
Na_2O	1.34	0.89	2.18	1.11	0.01	0.00	0.01	b.d.	6.29	4.70	5.22	1.91	6.63	4.74	4.31
K_2O	0.01	b.d.	b.d.	b.d.	0.00	0.02	b.d.	b.d.	0.14	0.08	0.15	0.02	0.17	0.08	0.06
ZnO	b.d.	b.d.	b.d.	b.d.	b.d.	b.d.	b.d.	b.d.	b.d.	b.d.	b.d.	b.d.	b.d.	b.d.	b.d.
Total	100.07	100.08	100.16	100.20	98.84	99.04	99.70	98.98	99.18	99.53	99.21	100.04	100.03	100.02	99.60
Cations/ Charges	4/12	4/12	4/12	4/12	4/12	4/12	4/12	4/12	5/16	5/16	5/16	5/16	5/16	5/16	5/16
Si	1.66	1.72	1.82	1.66	1.93	1.88	1.91	1.93	2.57	2.41	2.48	2.18	2.61	2.43	2.38
Ti	0.02	0.03	0.01	0.03	0.00	0.00	0.00	0.00	–	0.00	0.00	0.00	–	0.00	–
Cr	0.00	0.00	0.00	0.00	0.00	0.01	0.01	0.00	–	–	–	0.00	–	–	0.00
Al	0.76	0.54	0.54	0.71	0.12	0.19	0.18	0.16	1.44	1.59	1.54	1.83	1.41	1.58	1.64
Fe^{2+}	0.11	0.07	0.09	0.09	0.35	0.30	0.32	0.39	0.01	0.01	0.00	0.00	0.00	0.00	0.01
Fe^{3+}	0.00	0.03	0.00	0.00	0.01	0.03	0.00	0.00	–	–	–	–	–	–	–
Mn	0.00	0.00	0.00	0.00	0.00	0.00	0.00	0.00	–	–	–	–	b.d.	0.00	0.00
Mg	0.52	0.66	0.61	0.56	1.56	1.57	1.56	1.49	0.01	0.00	–	0.00	0.00	0.00	–
Ca	0.84	0.89	0.77	0.87	0.02	0.01	0.01	0.01	0.42	0.58	0.51	0.81	0.39	0.56	0.59
Na	0.09	0.06	0.15	0.08	0.00	0.00	0.00	–	0.55	0.41	0.46	0.17	0.58	0.42	0.38
K	0.00	–	–	–	0.00	0.00	–	–	0.01	0.00	0.01	0.00	0.01	0.00	0.00
Zn	–	–	–	–	–	–	–	–	–	–	–	–	–	–	–
XFe^{2+}	0.17	0.10	0.13	0.13	0.18	0.16	0.17	0.21							

b.d. below detection limit

Table III. 4 (continued): Representative mineral analyses of mafic granulites in wt. %.

Lithology	Mafic granulites									
Thin-section	DS025/20B	DS025/20B	DS025/20C	DS025/20C	DS025/20C	DS157/20G	DS157/20G	DS157/20G	DS157/20G	DS157/20G
Mineral	Pl	Pl	Pl	Pl	Pl	Pl	Pl	Pl	Pl	Pl
Analysis	Pl-10	Pl-21	Pl-05	Pl-18	Pl-32	Pl-26	Pl-17	Pl-18	Pl-49	Pl-50
Position	Rim around Grt	Matrix, next to Spl aggregates	Matrix, symplectite with Cpx	intergrowth in Grt	Rim around Grt	Matrix, symplectite with Cpx	Matrix, core	Matrix, rim	Inclusion in Grt, core	Inclusion in Grt, rim
SiO_2	56.47	50.24	59.07	57.55	58.01	52.83	55.60	54.44	57.87	56.62
TiO_2	0.03	b.d.	b.d.	0.02	0.04	0.01	0.00	0.00	b.d.	0.05
Cr_2O_3	0.01	b.d.	b.d.	b.d.	0.02	b.d.	0.01	0.00	b.d.	0.01
Al_2O_3	27.82	32.14	26.00	26.85	26.77	30.07	27.47	28.40	26.43	27.23
FeO	0.03	0.05	0.14	0.23	0.18	0.06	0.02	0.06	0.11	0.19
MnO	b.d.	b.d.	b.d.	0.01	b.d.	0.01	0.02	0.01	b.d.	0.01
MgO	0.01	0.01	0.01	b.d.	0.01	0.02	0.02	0.00	0.02	0.04
CaO	9.53	14.58	7.78	8.51	8.71	12.50	9.99	11.10	8.07	9.23
Na_2O	5.81	3.12	6.95	6.56	6.44	4.19	5.70	4.99	6.61	5.87
K_2O	0.13	0.04	0.09	0.04	0.05	0.04	0.07	0.03	0.21	0.19
ZnO	b.d.	b.d.	b.d.	b.d.	b.d.	b.d.	b.d.	b.d.	b.d.	b.d.
Total	99.84	100.19	100.03	99.77	100.23	99.73	98.88	99.03	99.32	99.43
Cations/Charges	5/16	5/16	5/16	5/16	5/16	5/16	5/16	5/16	5/16	5/16
Si	2.54	2.29	2.64	2.59	2.60	2.40	2.53	2.48	2.61	2.56
Ti	0.00	–	–	0.00	0.00	0.00	0.00	0.00	–	0.00
Cr	0.00	–	–	–	0.00	–	0.00	0.00	–	0.00
Al	1.48	1.72	1.37	1.42	1.41	1.61	1.47	1.53	1.40	1.45
Fe^{2+}	0.00	0.00	0.01	0.01	0.01	0.00	0.00	0.00	0.00	0.01
Fe^{3+}	–	–	–	–	–	–	–	–	–	–
Mn	–	–	–	0.00	–	0.00	0.00	0.00	–	0.00
Mg	0.00	0.00	0.00	–	0.00	0.00	0.00	0.00	0.00	0.00
Ca	0.46	0.71	0.37	0.41	0.42	0.61	0.49	0.54	0.39	0.45
Na	0.51	0.28	0.60	0.57	0.56	0.37	0.50	0.44	0.58	0.51
K	0.01	0.00	0.01	0.00	0.00	0.00	0.00	0.00	0.01	0.01
Zn	–	–	–	–	–	–	–	–	–	–
XFe^{2+}										

b.d. below detection limit

Table III. 4 (continued): Representative mineral analyses of mafic granulites in wt. %.

Lithology						Mafic granulites					
Thin-section	DS157/20G	DS027/20B	DS027/20B	DS025E	DS157/20G	DS157/20G	DS025E	DS025/20C	DS025/20C	DS157/20G	DS027/20B
Mineral	Pl	Pl	Pl	Spl	Spl	Spl	Am	Am	Am	Am	Am
Analysis	Pl-33	Pl-05	Pl-19	Spl-03	Spl-29	Spl-45	Am-01	Am-23	Am-28	Am-10	Am-06
Position	Matrix, symplectite with Spl	Matrix, rim around Grt	Matrix	Matrix, Spl aggregates	Matrix, symplectite with Pl	Matrix, large grain	Matrix	Matrix	Matrix, around Ilm	Matrix	Matrix
SiO_2	49.93	54.04	55.85	0.39	0.09	0.05	42.80	42.46	39.50	40.96	42.373
TiO_2	b.d.	0.02	0.03	0.09	0.03	0.03	2.54	1.46	3.41	1.02	1.006
Cr_2O_3	b.d.	0.02	0.03	12.61	0.65	0.27	0.35	0.09	0.11	0.06	0.113
Al_2O_3	32.05	29.34	27.34	50.94	63.58	63.63	14.56	15.07	16.52	17.83	17.816
FeO	0.10	0.09	0.04	18.99	17.53	17.91	0.04	8.12	7.98	6.87	5.608
MnO	b.d.	0.02	0.01	0.05	0.04	0.09	5.71	0.08	0.06	0.05	0.044
MgO	0.02	0.03	b.d.	12.67	15.56	15.62	15.63	14.50	13.86	14.55	15.627
CaO	14.40	11.48	9.07	0.29	0.11	0.01	11.99	11.33	11.15	11.70	11.267
Na_2O	3.12	4.76	6.12	b.d.	0.01	b.d.	2.64	2.83	3.09	2.57	2.996
K_2O	0.04	0.01	0.05	0.01	b.d.	0.01	0.53	0.49	0.43	1.06	0.214
ZnO	b.d.	b.d.	b.d.	1.09	0.29	0.09	b.d.	0.05	b.d.	b.d.	0.024
Total	99.66	99.80	98.53	97.13	97.88	97.70	96.79	96.47	96.11	96.67	97.09
Cations/Charges	5/16	5/16	5/16	3/8	3/8	3/8	23 O eq.	23 O eq.	23 O eq.	23 O eq.	23 O eq.
Si	2.28	2.45	2.54	0.01	0.00	0.00	6.17	6.18	5.80	5.93	6.02
Ti	–	0.00	0.00	0.00	0.00	0.00	0.28	0.16	0.38	0.11	0.11
Cr	–	0.00	0.00	0.28	0.01	0.01	0.04	0.01	0.01	0.01	0.01
Al	1.73	1.57	1.47	1.69	1.97	1.98	2.47	2.59	2.86	3.04	2.99
Fe^{2+}	0.00	0.00	0.00	0.45	0.38	0.38	0.66	0.85	0.84	0.69	0.46
Fe^{3+}	–	–	–	0.00	0.01	0.01	0.03	0.14	0.14	0.15	0.20
Mn	–	0.00	0.00	0.00	0.00	0.00	0.00	0.01	0.01	0.01	0.01
Mg	0.00	0.00	–	0.53	0.61	0.61	3.36	3.14	3.03	3.14	3.31
Ca	0.71	0.56	0.44	0.01	0.00	0.00	1.85	1.77	1.76	1.82	1.72
Na	0.28	0.42	0.54	–	0.00	–	0.74	0.80	0.88	0.72	0.83
K	0.00	0.00	0.00	0.00	–	0.00	0.10	0.09	0.08	0.20	0.04
Zn	–	–	–	0.02	0.01	0.00	–	0.01	–	–	0.00
XFe^{2+}				0.46	0.38	0.38	0.16	0.21	0.22	0.18	0.12

b.d. below detection limit

1.1.4 Garnet clinopyroxenites

In the Dunkelsteiner Wald granulite massif, garnet clinopyroxenites are quite variable due to the different degree of retrogression. A shared feature is a clinopyroxene-rich fine to medium-grained granoblastic matrix hosting garnet porphyroblasts with inclusions of Cpx, Rt, and Ky (sometimes in association with sapphirine). Clinopyroxene in the matrix contain Opx exsolution lamellae. Retrogression of the samples caused the formation of variable amounts of Pl–Cpx–Opx–Amp coarse-grained and sometimes also fine-grained symplectites accompanied by spinel and rarely by sapphirine. Common accessories are sulphides (mainly pyrrhotite, chalcopyrite, and pentlandite) and rutile partly replaced by ilmenite. In the studied samples occur also as an accessory Ba- and Cl-rich silicates including micas and phosphate minerals. These Ba–Cl-rich mineral assemblage and its significance is described in detail in Part I.

Representative mineral analysis are available in Table III. 4.

Sample DS072C (Figure III. 11) has the best preserved primary mineral assemblage, where up to 2.8 mm garnet porphyroblast with Cpx inclusions are surrounded by ~0.2 mm wide rim formed by a fine-grained symplectite of plagioclase, clinopyroxene, orthopyroxene, spinel, and amphibole (Figure III. 11b–e). The majority of the matrix is formed by clinopyroxene with orthopyroxene exsolutions (Figure III. 11a). Barium-rich micas occur around garnets associated with the symplectites as an accessory phase (see Part I or Zelinková *et al.*, 2023).

Mineral phases from symplectites around garnet have the following composition ranges: Pl: $An_{34.2–43.3}$, Opx: XFe^{2+} ~0.16, Amp (pargasite): XFe^{2+} = 0.16–0.18, Ti ~0.2 Si = 5.9–6.1 p.f.u., Spl: XFe^{2+} ~0.29, Al ~2 p.f.u., Cr ~0.0 p.f.u., Cpx: $CaTs_{9.4–10.5}Jd_{11.6–12.9}$, XFe^{2+} ~0.12.

Orthopyroxene in granoblastic matrix has XFe^{2+}~0.18.

The chemical zoning of clinopyroxene from the matrix and also from the inclusion in garnet is characterized by Na and Fe decrease and Ca and Al increase from the core towards the rim $CaTs_{5.0→11.0}Jd_{20.4→11.1}$, XFe^{2+} = 0.12→0.11 (Cpx in matrix); $CaTs_{4.0→10.4}Jd_{20.1→19.4}$, XFe^{2+} ~0.12 (Cpx inclusion in Grt).

In this sample exist zones defined by a gradual changes in the chemical composition of garnet across the sample. These variations are characterized by the alternation of areas with Mg-rich and Ca-poor garnet and areas with Ca-rich and Mg poor garnet. Garnets from both zones are characterized by similar trends in the chemical composition but with different absolute values,

which is defined by the compositional plateau in the core region followed by Mg and Ca decrease and Fe increase at the rim. Composition of Ca-rich garnet: $Prp_{58.7\rightarrow56.1}Alm_{21.0\rightarrow31.3}Grs_{19.9\rightarrow11.4}Sps_{0.5\rightarrow1.2}$, $XFe^{2+} = 0.26\rightarrow0.36$ (Figure III. 11f); and Mg-rich garnet: $Prp_{63.8\rightarrow61.0}Alm_{21.6\rightarrow26.5}Grs_{14.1\rightarrow11.8}Sps_{0.4\rightarrow0.7}$, $XFe^{2+} = 0.25\rightarrow0.30$ (Figure III. 11g).

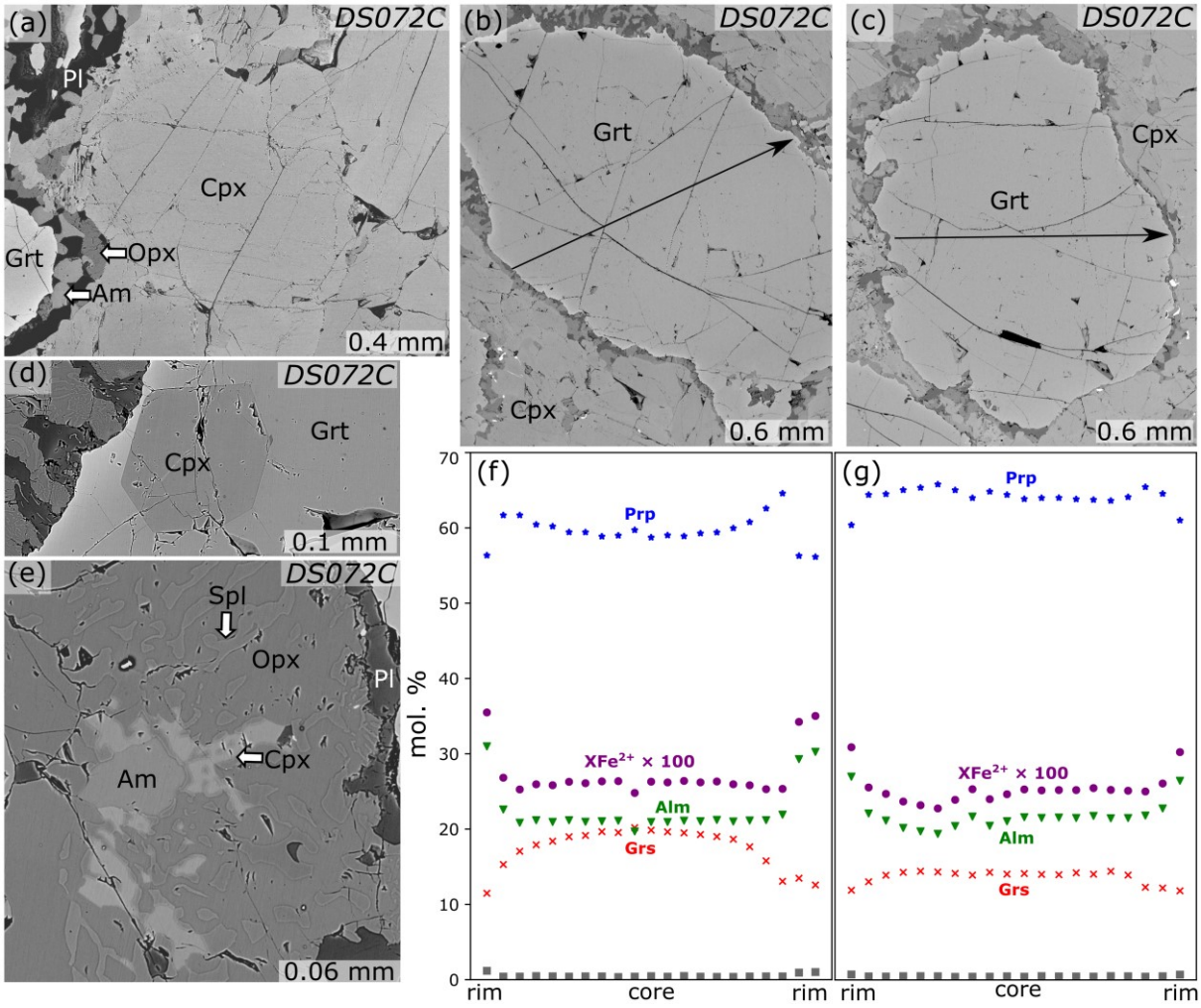

Figure III. 11: Back-scattered electron images (a–e) and composition profiles across garnet (f, g) from garnet clinopyroxenite DS072C. a) Clinopyroxene in the matrix at the contact with garnet. b–c) garnet porphyroblasts. d) Clinopyroxene inclusion in garnet. e) Fine-grained symplectite of amphibole, clinopyroxene, orthopyroxene, and plagioclase at the contact with garnet. g) Composition profile of garnet from the subfigure b. h) Composition profile of garnet from the subfigure c.

Sample DS151/20A (Figure III. 12) contains up to 2.7 mm large garnet porphyroblasts enclosing idiomorphic inclusions of clinopyroxene and rarely fine-grained Spl–Pl symplectites (Figure III. 12a, d, e). Garnet is replaced by fine-grained Spl-Cpx symplectites in some cases (Figure III. 12e).

In this sample, the granoblastic Cpx-rich matrix (Figure III. 12b) accompanied by the smaller amount of Pl, Amp, and Opx transitions into the coarse grained Cpx–Pl (Amp, Opx) in places. Larger clinopyroxene grains contains Opx exsolution lamellae.

Plagioclase (labradorite-andesine) in the matrix show no systematic zoning and no diferrence in the composition between Pl in granoblastic or symplectite texture: $An_{39.1–47.7}Ab_{52.2–60.7}Or_{0.0–0.2.}$ Plagioclase forming fine-grained symplectites with Spl in Grt shows slightly higher Ca content compared to Pl from the matrix: $An_{\sim53.0}Ab_{\sim46.9}Or_{\sim0.1}$.

Orthopyroxene has: XFe^{2+} = 0.13–0.15. Large clinopyroxene grains in Cpx-rich granoblastic matrix show the Na, Al and Fe decrease and Ca increase from the core towards the rim: $CaTs_{13.7→12.2}Jd_{25.2→8.7}$, XFe^{2+} = 0.15→0.11. Clinopyroxene has $CaTs_{14.2–20.2}Jd_{10.2–12.7}$, XFe^{2+} = 0.11–0.13 in coarse-grained Cpx–Pl symplectite, and $CaTs_{16.6–18.1}Jd_{8.6–9.7}$, XFe^{2+} = 0.11–0.14 in Spl-Cpx fine-grained symplectites in/around Grt. Clinopyroxene inclusions show Na decrease and Al and Ca increase from the core towards the rim, whereby some Cpx inclusions show significantly high Na content ($CaTs_{6.1→22.2}Jd_{36.2→22.4}$, XFe^{2+} = 0.11→0.13) compared to other Cpx inclusions ($CaTs_{6.9→12.0}Jd_{16.2→13.8}$, XFe^{2+} = 0.12→0.11).

Garnet is rich in Mg component. The chemical zoning of the garnet from the symplectite texture is characterised by the Ca decrease and Mg with Fe increase from the core towards the rim ($Prp_{51.1→62.6}Alm_{18.0→22.5}Grs_{30.5→14.3}Sps_{0.4→0.6}$, XFe^{2+} = 0.26→0.26; Figure III. 12c). Garnet from the granoblastic texture has less distinct zonality and its composition corresponds to the garnet rims from the symplectite texture ($Prp_{62.4→63.6}Alm_{20.9→22.2}Grs_{16.4→13.9}Sps_{0.4→0.4}$, XFe^{2+} = 0.25→0.26; Figure III. 12f).

Spinel has the composition range: XFe^{2+} = 0.28–0.30, Al ~2.0 p.f.u., Cr_2O_3 = 0.46–2.05 wt. %.

Amphibole (pargasite) has the composition range: XFe^{2+} = 0.07–0.13; Ti = 0.1–0.2, Si = 6.0–6.2 p.f.u.

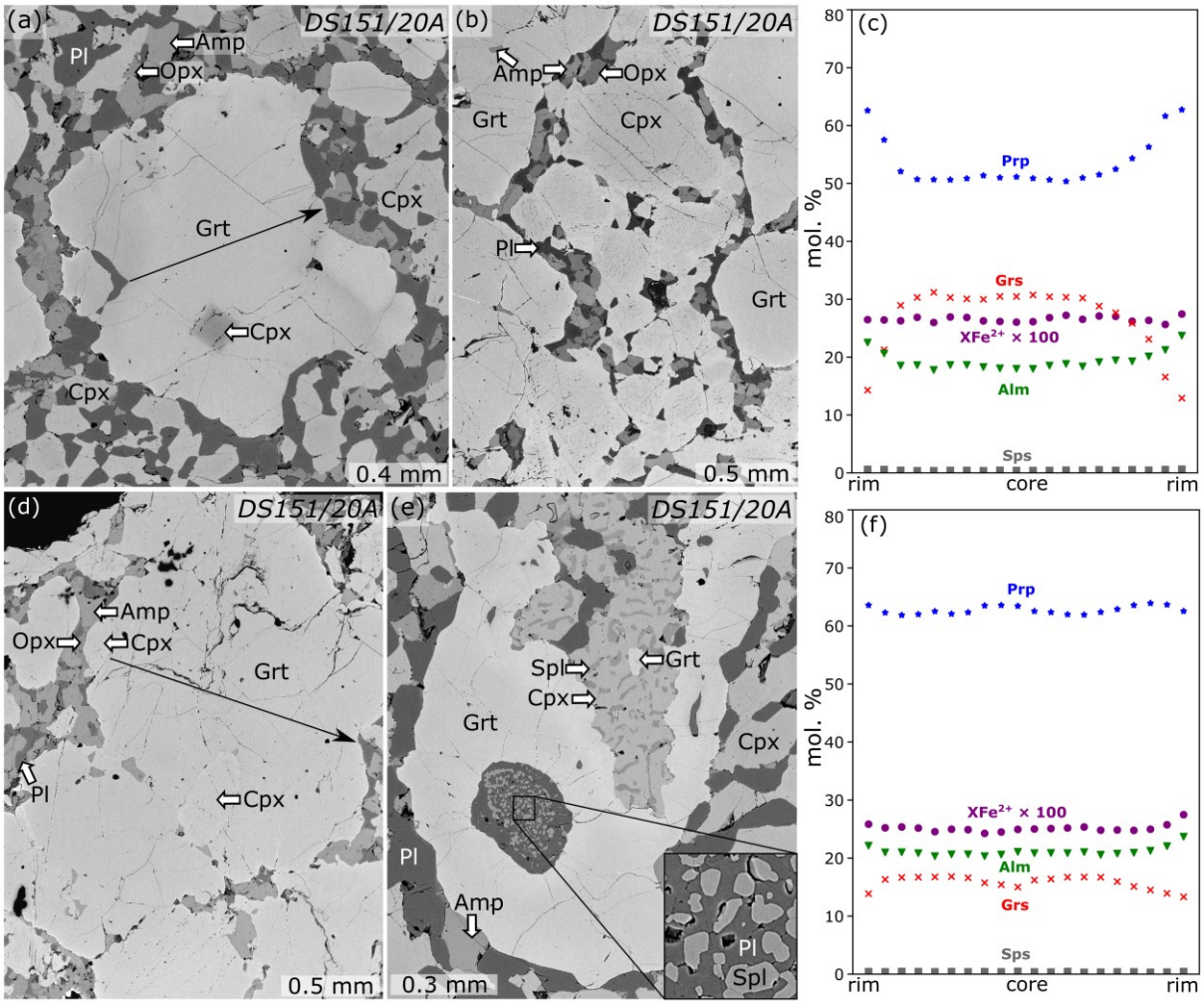

Figure III. 12: Back-scattered electron images and composition profiles across garnet from garnet clinopyroxenite DS151/20A with granoblastic matrix with transitions to sympectite matrix in places. a) Garnet porphyroblast with clinopyroxene inclusion. b) Detail of the matrix dominated by clinopyroxene. c) Composition profile of garnet from the subfigure a). d) Garnet porphyroblast with clinopyroxene inclusion. e) Garnet with spinel-plagioclase fine-grained symplectite in the core and significant replacement by clinopyroxene-spinel fine-grained symplectite. f) Composition profile of garnet from the subfigure d).

Sample DS157/20D (Figure III. 13) is characterized by up to 5.2 mm large garnet porphyroblasts with idiomorphic inclusions of clinopyroxene, plagioclase, and orthopyroxene (Figure III. 13a, c). The matrix is granoblastic and is dominantly formed by clinopyroxene with Opx exsolution lamellae. In smaller amounts, the matrix also consists of amphibole, orthopyroxene, and plagioclase occurring primarily in the vicinity of garnet.

The sample is rich in only few μm large multiphase solid inclusions (Cl-Ap, Pl, Amp, Opx, Spl; this type of inclusions is described in detail in Part I), which creates chains passing the entire garnet grains. In some garnet grains are also small cracks filled by Spl, Pl, Amp, Opx, and Chl (Figure III. 13c, d).

Plagioclase (labradorite to andesine) in the matrix show no systematic zoning and has the composition range: $An_{47.3–59.3}Ab_{39.8–51.6}Or_{0.6–1.1}$. Plagioclase inclusion in garnet is characterized by the Ca increase and Na decrease from the core towards the rim: $An_{41.7–48.1}Ab_{56.8–50.7}Or_{1.5–1.2}$.

Orthopyroxene has XFe^{2+} = 0.17–0.20 in the matrix and XFe^{2+} = 0.17 as the inclusion in garnet. Clinopyroxene in the matrix shows no significant zoning, the composition range is: $CaTs_{6.3–8.3}Jd_{4.2–9.4}$, XFe^{2+} = 0.11–0.14. Clinopyroxene inclusions in garnet are characterized by Na decrease and Ca and Al increase from the core towards the rim $CaTs_{7.2→9.5}Jd_{10.9→8.4}$, XFe^{2+} = 0.12→0.12.

Garnet is rich in Mg and its composition zoning is characterized by almost the composition plateau with Ca decrease and Mg and Fe increase at the rim ($Prp_{56.3→53.0}Alm_{24.8→30.7}Grs_{18.2→15.2}Sps_{0.8→1.1}$, XFe^{2+} = 0.31→0.37; Figure III. 13b).

Amphibole (pargasite) hast the composition range: XFe^{2+} = 0.13–0.14, Ti = 0.1–0.2 p.f.u. Si = 6.1–6.4 p.f.u.

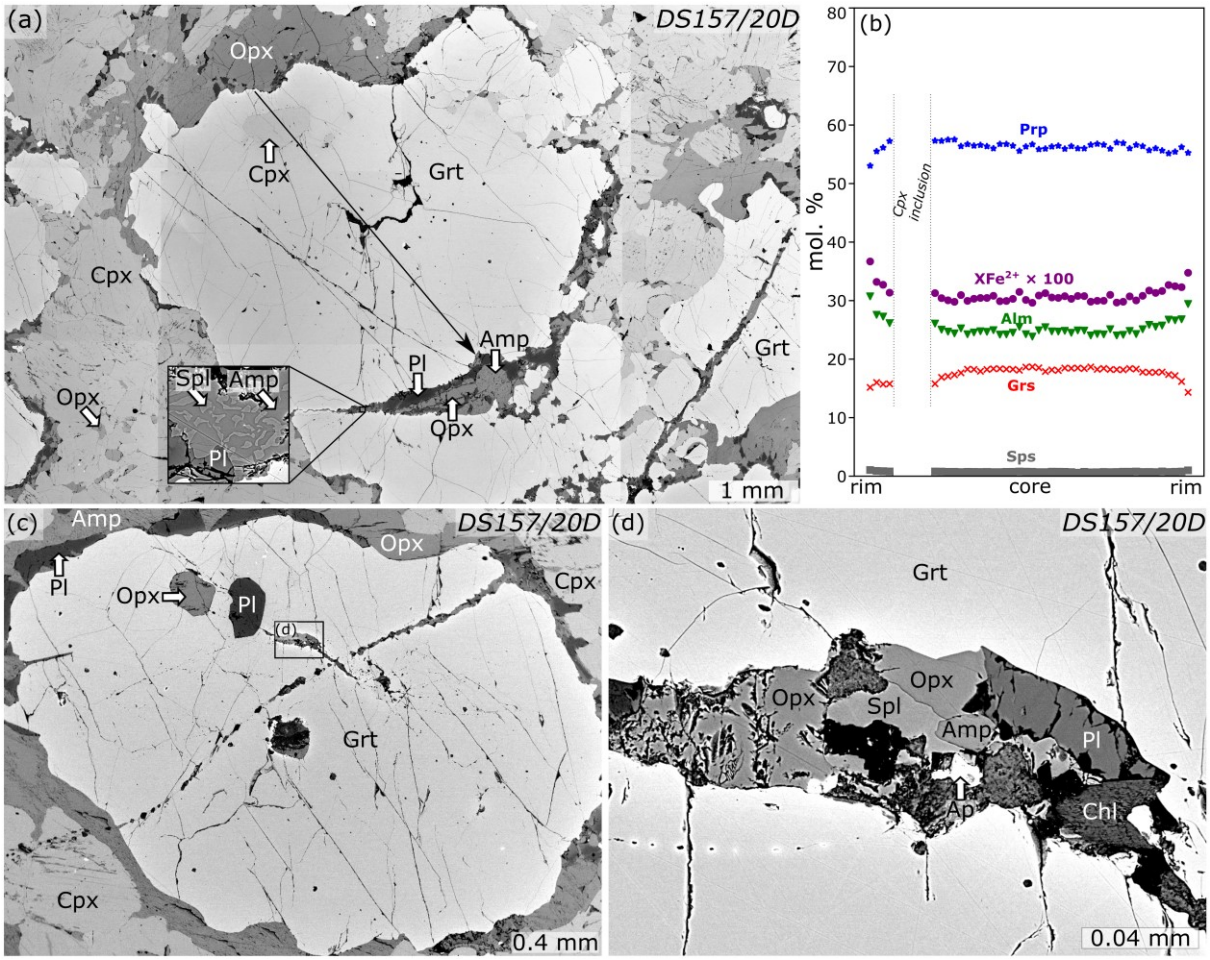

Figure III. 13: Back-scattered electron images and composition profile across garnet from garnet clinopyroxenite DS157/20D with granoblastic matrix. a) Garnet porphyroblast with clinopyroxene inclusion. b) Composition profile of garnet from the subfigure a. c) Garnet with orthopyroxene and plagioclase inclusions, and traces of multiphase solid inclusions. d) Detail of the crack from garnet in the subfigure c).

Table III. 4: Representative mineral analyses of garnet clinopyroxenites in wt. %.

Lithology	Garnet clinopyroxenites										
Thin-section	DS072C	DS072C	DS072C	DS072C	DS151/20A	DS151/20A	DS151/20A	DS151/20A	DS157/20D	DS157/20D	DS072C
Mineral	Grt	Grt	Grt	Grt	Grt	Grt	Grt	Grt	Grt	Grt	Cpx
Analysis	Grt15-line 11	Grt15-line 20	Grt14-line 11	Grt14-line 01	Grt2-line 10	Grt2-line 01	Grt-10	Grt-01	Grt01-line 29	Grt01-line 01	Cpx-line 11
Position	Matrix, core	Matrix, rim	Matrix, core	Matrix, rim	Matrix, core	Matrix, rim	Matrix, core	Matrix, rim	Matrix, core	Matrix, rim	Matrix, core
SiO_2	42.03	41.52	41.82	41.16	41.55	41.97	41.96	42.11	41.52	41.07	53.23
TiO_2	0.12	0.11	0.15	0.06	0.17	0.03	0.10	0.10	0.09	0.04	0.46
Cr_2O_3	0.09	0.16	0.18	0.21	0.15	0.18	0.13	0.13	0.08	0.10	0.17
Al_2O_3	24.35	23.80	23.83	23.69	23.21	23.40	23.82	23.34	22.99	22.66	5.85
FeO	10.84	12.97	10.40	15.47	9.11	11.70	10.56	10.95	12.52	15.55	3.59
MnO	0.21	0.34	0.23	0.57	0.20	0.30	0.24	0.20	0.38	0.51	0.02
MgO	17.96	16.78	16.36	15.56	14.28	17.64	17.82	17.63	15.71	14.62	14.43
CaO	5.53	4.53	7.69	4.41	11.84	5.60	5.87	5.35	7.05	5.82	18.66
Na_2O	0.02	b.d.	0.02	b.d.	0.01	0.00	0.02	0.02	0.00	0.00	2.54
K_2O	b.d.	b.d.	0.01	0.01	0.00	0.00	0.00	0.00	0.00	0.01	b.d.
ZnO	b.d.	b.d.	b.d.	b.d.	b.d.	b.d.	b.d.	b.d.	b.d.	b.d.	b.d.
Cl	b.d.	b.d.	b.d.	b.d.	b.d.	b.d.	b.d.	b.d.	b.d.	b.d.	b.d.
Total	101.16	100.20	100.68	101.14	100.53	100.81	100.51	99.83	100.35	100.37	98.95
Cations/Charges	8/24	8/24	8/24	8/24	8/24	8/24	8/24	8/24	8/24	8/24	4/12
Si	2.98	3.00	2.99	2.98	3.00	3.00	2.99	3.03	3.01	3.00	1.93
Ti	0.01	0.01	0.01	0.00	0.01	0.00	0.01	0.01	0.01	0.00	0.01
Cr	0.01	0.01	0.01	0.01	0.01	0.01	0.01	0.01	0.00	0.01	0.00
Al	2.03	2.03	2.01	2.02	1.97	1.97	2.00	1.98	1.96	1.95	0.25
Fe^{2+}	0.64	0.78	0.62	0.92	0.54	0.68	0.63	0.66	0.74	0.92	0.08
Fe^{3+}	0.00	0.00	0.00	0.01	0.01	0.02	0.00	0.00	0.01	0.03	0.03
Mn	0.01	0.02	0.01	0.04	0.01	0.02	0.01	0.01	0.02	0.03	0.00
Mg	1.90	1.81	1.75	1.68	1.54	1.88	1.89	1.89	1.69	1.59	0.78
Ca	0.42	0.35	0.59	0.34	0.91	0.43	0.45	0.41	0.55	0.46	0.73
Na	0.00	–	0.00	–	0.00	0.00	0.00	0.00	0.00	0.00	0.18
K	–	–	0.00	0.00	0.00	0.00	0.00	0.00	0.00	0.00	–
Zn	–	–	–	–	–	–	–	–	–	–	–
Cl	–	–	–	–	–	–	–	–	–	–	–
XFe^{2+}	0.25	0.30	0.26	0.35	0.26	0.26	0.25	0.26	0.31	0.37	0.09

b.d. below detection limit

Table III. 5 (continued): Representative mineral analyses of garnet clinopyroxenites in wt. %.

Lithology	Garnet clinopyroxenites										
Thin-section	DS072C	DS072C	DS072C	DS151/20A	DS151/20A	DS151/20A	DS151/20A	DS151/20A	DS151/20A	DS151/20A	DS151/20A
Mineral	Cpx	Cpx	Cpx	Cpx	Cpx	Cpx	Cpx	Cpx	Cpx	Cpx	Cpx
Analysis	Cpx-line 01	Cpx-02	Cpx-03	Cpx-35	Cpx-36	Cpx-58	Cpx-37	Cpx-21	Cpx-22	Cpx-01	Cpx-02
Position	Matrix, rim	inclusion in Grt, core	inclusion in Grt, rim	Matrix, core	Matrix, rim	Matrix, symplectite with Pl	Symplectite with Spl in Grt	Inclusion in Grt, core	Inclusion in Grt, rim	Inclusion in Grt, core	Inclusion in Grt, rim
SiO_2	51.53	54.04	51.16	51.07	51.35	48.57	49.73	54.08	48.88	53.06	51.71
TiO_2	0.46	0.26	0.52	0.27	0.44	0.35	0.54	0.23	0.65	0.35	0.52
Cr_2O_3	0.18	0.16	0.15	0.14	0.45	0.11	0.08	0.16	0.16	0.10	0.12
Al_2O_3	7.06	5.96	8.36	12.84	7.46	12.51	10.65	11.99	16.49	7.67	8.77
FeO	3.08	3.44	3.33	3.83	3.03	3.85	3.58	2.37	2.52	3.60	3.15
MnO	0.06	0.06	0.06	0.06	0.06	0.03	0.05	0.03	0.02	0.02	0.05
MgO	14.25	14.24	13.52	11.94	14.26	12.10	12.68	10.51	9.78	14.24	13.82
CaO	21.65	18.69	18.88	16.70	21.61	20.53	21.57	15.40	18.68	18.71	20.16
Na_2O	1.49	2.59	2.52	3.10	1.14	1.66	1.27	4.83	2.98	2.01	1.79
K_2O	b.d.	0.04	0.03	0.01	b.d.	b.d.	b.d.	b.d.	b.d.	b.d.	b.d.
ZnO	b.d.	b.d.	b.d.	b.d.	b.d.	b.d.	b.d.	b.d.	b.d.	b.d.	b.d.
Cl	b.d.	b.d.	b.d.	b.d.	b.d.	b.d.	b.d.	b.d.	b.d.	b.d.	b.d.
Total	99.76	99.46	98.52	99.94	99.79	99.69	100.14	99.61	100.17	99.76	100.08
Cations/Charges	4/12	4/12	4/12	4/12	4/12	4/12	4/12	4/12	4/12	4/12	4/12
Si	1.87	1.95	1.87	1.83	1.87	1.76	1.80	1.93	1.75	1.92	1.87
Ti	0.01	0.01	0.01	0.01	0.01	0.01	0.01	0.01	0.02	0.01	0.01
Cr	0.01	0.00	0.00	0.00	0.01	0.00	0.00	0.00	0.00	0.00	0.00
Al	0.30	0.25	0.36	0.54	0.32	0.54	0.46	0.50	0.70	0.33	0.37
Fe^{2+}	0.06	0.10	0.05	0.11	0.09	0.09	0.11	0.07	0.08	0.11	0.09
Fe^{3+}	0.04	0.00	0.05	0.00	0.00	0.03	0.00	0.00	0.00	0.00	0.00
Mn	0.00	0.00	0.00	0.00	0.00	0.00	0.00	0.00	0.00	0.00	0.00
Mg	0.77	0.77	0.74	0.64	0.77	0.66	0.69	0.56	0.52	0.77	0.74
Ca	0.84	0.72	0.74	0.64	0.84	0.80	0.84	0.59	0.72	0.72	0.78
Na	0.10	0.18	0.18	0.22	0.08	0.12	0.09	0.33	0.21	0.14	0.13
K	–	0.00	0.00	0.00	–	–	–	–	–	–	–
Zn	–	–	–	–	–	–	–	–	–	–	–
Cl	–	–	–	–	–	–	–	–	–	–	–
XFe^{2+}	0.07	0.12	0.06	0.15	0.11	0.12	0.14	0.11	0.13	0.12	0.11

b.d. below detection limit

Table III. 5 (continued): Representative mineral analyses of garnet clinopyroxenites in wt. %.

Lithology	Garnet clinopyroxenites										
Thin-section	DS157/20D	DS157/20D	DS157/20D	DS157/20D	DS072C	DS072C	DS151/20A	DS157/20D	DS157/20D	DS072C	DS151/20A
Mineral	Cpx	Cpx	Cpx	Cpx	Opx	Opx	Opx	Opx	Opx	Pl	Pl
Analysis	Cpx-01	Cpx-02	Cpx-line 07	Cpx-line 10	Opx-05	Opx-02	Opx-15	Opx-11	Opx-34	Pl-01	Pl-04
Position	Matrix, core	Matrix, rim	Inclusion in Grt, core	Inclusion in Grt, rim	Matrix	Matrix, symplectite with Spl, Pl, Cpx, Am	Matrix	Matrix	Inclusion in Grt	Matrix, symplectite with Spl, Opx, Cpx	Matrix
SiO_2	52.60	52.87	52.98	52.22	53.95	53.25	54.17	54.24	54.13	59.13	56.37
TiO_2	0.20	0.18	0.26	0.42	0.05	0.08	0.04	0.03	0.06	b.d.	0.02
Cr_2O_3	0.09	0.10	0.05	0.06	0.09	0.02	0.12	0.05	b.d.	b.d.	b.d.
Al_2O_3	5.65	4.76	5.76	6.14	3.30	4.29	5.56	3.84	4.12	25.45	27.67
FeO	4.25	3.81	4.37	3.70	11.52	10.08	8.49	11.43	11.00	0.26	0.14
MnO	0.09	0.06	0.05	0.06	0.10	0.13	0.06	0.15	0.12	b.d.	b.d.
MgO	14.44	15.20	15.59	15.09	29.32	29.93	30.98	29.52	29.98	0.01	b.d.
CaO	21.09	22.15	19.97	21.33	0.40	0.36	0.38	0.33	0.40	7.52	9.33
Na_2O	1.21	0.79	1.35	1.08	0.03	0.01	0.04	0.01	0.02	7.11	6.08
K_2O	b.d.	b.d.	b.d.	b.d.	b.d.	b.d.	b.d.	b.d.	b.d.	0.03	0.01
ZnO	b.d.	b.d.	b.d.	b.d.	b.d.	b.d.	b.d.	b.d.	b.d.	b.d.	b.d.
Cl	b.d.	b.d.	b.d.	b.d.	b.d.	b.d.	b.d.	b.d.	b.d.	b.d.	b.d.
Total	99.63	99.92	100.39	100.09	98.76	98.15	99.84	99.60	99.82	99.51	99.61
Cations/Charges	4/12	4/12	4/12	4/12	4/12	4/12	4/12	4/12	4/12	5/16	5/16
Si	1.92	1.93	1.91	1.89	3.38	1.90	1.89	1.92	2.38	2.66	2.54
Ti	0.01	0.00	0.01	0.01	0.00	0.00	0.00	0.00	0.00	–	0.00
Cr	0.00	0.00	0.00	0.00	0.00	0.00	0.00	0.00	–	–	–
Al	0.24	0.20	0.24	0.26	0.24	0.18	0.23	0.16	0.21	1.35	1.47
Fe^{2+}	0.13	0.12	0.12	0.11	0.60	0.29	0.25	0.34	0.41	0.01	0.01
Fe^{3+}	0.00	0.00	0.02	0.01	0.00	0.01	0.00	0.00	0.00	–	–
Mn	0.00	0.00	0.00	0.00	0.01	0.00	0.00	0.00	0.00	–	–
Mg	0.79	0.83	0.84	0.82	2.73	1.59	1.61	1.56	1.97	0.00	–
Ca	0.82	0.86	0.77	0.83	0.03	0.01	0.01	0.01	0.02	0.36	0.45
Na	0.09	0.06	0.09	0.08	0.00	0.00	0.00	0.00	0.00	0.62	0.53
K	–	–	–	–	–	–	0.00	–	–	0.00	0.00
Zn	–	–	–	–	–	–	–	–	–	–	–
Cl	–	–	–	–	–	–	–	–	–	–	–
XFe^{2+}	0.14	0.12	0.12	0.12	0.18	0.15	0.13	0.18	0.17		

b.d. below detection limit

Table III. 5 (continued): Representative mineral analyses of garnet clinopyroxenites in wt. %.

Lithology	Garnet clinopyroxenites										
Thin-section	DS151/20A	DS157/20D	DS157/20D	DS157/20D	DS072C	DS151/20A	DS151/20A	DS072C	DS072C	DS151/20A	DS157/20D
Mineral	Pl	Pl	Pl	Pl	Spl	Spl	Spl	Amp	Amp	Amp	Amp
Analysis	Pl-48	Pl-04	Pl-38	Pl-39	Spl-04	Spl-41	Spl-45	Amp-01	Amp-02	Amp-17	Amp-08
Position	Symplectite with Spl in Grt	Matrix	Inclusion in Grt, core	Inclusion in Grt, rim	Matrix, symplectite with Am, Opx, Cpx, Pl	Matrix, symplectite with Cpx	Symplectite with Pl in Grt	Matrix, symplectite with Spl, Opx, Cpx, Pl	Matrix	Matrix	Matrix
SiO_2	53.30	54.28	56.82	55.96	0.07	0.07	0.11	40.09	40.33	43.06	43.897
TiO_2	b.d.	0.01	0.02	0.02	b.d.	b.d.	0.02	2.22	2.07	1.84	0.741
Cr_2O_3	0.02	b.d.	0.01	b.d.	1.06	0.49	0.73	0.24	0.23	0.27	0.088
Al_2O_3	28.91	28.91	26.58	27.32	65.22	64.99	65.10	15.57	15.79	15.97	13.931
FeO	0.56	0.17	0.08	0.27	13.60	13.38	13.62	6.07	5.79	4.85	6.077
MnO	b.d.	b.d.	b.d.	b.d.	0.07	0.04	0.04	0.07	0.05	0.04	0.031
MgO	0.74	0.03	0.04	0.02	18.24	18.60	18.26	15.46	15.61	16.80	16.334
CaO	10.35	11.19	8.36	9.72	0.04	0.13	0.07	11.33	11.26	11.60	11.917
Na_2O	5.07	4.85	6.29	5.67	b.d.	b.d.	b.d.	2.92	2.84	3.15	2.614
K_2O	0.02	0.11	0.25	0.21	0.01	b.d.	b.d.	1.11	1.13	0.07	0.665
ZnO	b.d.	b.d.	b.d.	b.d.	0.22	0.14	0.14	b.d.	b.d.	b.d.	0.058
Cl	b.d.	b.d.	b.d.	b.d.	b.d.	b.d.	b.d.	0.20	0.17	0.03	0.038
Total	98.96	99.53	98.44	99.17	98.52	97.83	98.08	95.07	95.09	97.65	96.35
Cations/Charges	5/16	5/16	5/16	5/16	3/8	3/8	3/8	23 O eq.	23 O eq.	23 O eq.	23 O eq.
Si	2.42	2.47	2.59	2.54	0.00	–	0.00	5.92	5.94	6.09	6.33
Ti	–	0.00	0.00	0.00	–	0.00	0.00	0.25	0.23	0.20	0.08
Cr	0.00	–	0.00	–	0.02	0.01	0.01	0.03	0.03	0.03	0.01
Al	1.55	1.55	1.43	1.46	1.98	1.98	1.98	2.71	2.74	2.66	2.37
Fe^{2+}	0.00	0.01	0.00	0.01	0.29	0.28	0.29	0.56	0.56	0.41	0.62
Fe^{3+}	–	–	–	–	0.00	0.01	0.00	0.09	0.15	0.17	0.12
Mn	–	–	–	–	0.00	0.00	0.00	0.01	0.01	0.01	0.00
Mg	0.05	0.00	0.00	0.00	0.70	0.72	0.70	3.40	3.43	3.54	3.51
Ca	0.50	0.54	0.41	0.47	0.00	0.00	0.00	1.79	1.78	1.76	1.84
Na	0.45	0.43	0.56	0.50	–	–	–	0.84	0.81	0.86	0.73
K	0.00	0.01	0.01	0.01	0.00	–	–	0.21	0.21	0.01	0.12
Zn	–	–	–	–	0.00	0.00	0.00	–	–	–	0.01
Cl	–	–	–	–	–	–	–	0.05	0.04	0.01	0.01
XFe^{2+}					0.29	0.28	0.30	0.14	0.14	0.10	0.15

b.d. below detection limit

1.1.5 Garnet peridotites

Matrix of garnet peridotites is fine-grained, slightly serpentinized and formed by Cpx, Opx, Ol, Amp and small amount of spinel. The matrix host variable up to 5 mm large garnet porphyroblast with Spl–Opx–Cpx–Amp kelyphite rim, which in some cases completely replaced the original garnet. Clinopyroxene and orthopyroxene porphyroblasts occur more rarely in the studied samples.

Common accessories are pentlandite, chalcopyrite, pyrrhotite, and magnetite.

Representative mineral analysis of peridotites are available in Table III. 5.

Sample DS156/20B (Figure III. 14) has a well-preserved mineral assemblage. Matrix is fine-grained and is dominantly formed by olivine and clinopyroxene, and in smaller amount by orthopyroxene and spinel (Figure III. 14a). The matrix host up to 5 mm large garnet porphyroblast with up to ~2 mm wide Spl–Amp–Cpx–Opx kelyphite rim (Figure III. 14b, c). The space between the grains is filled with serpentine group minerals.

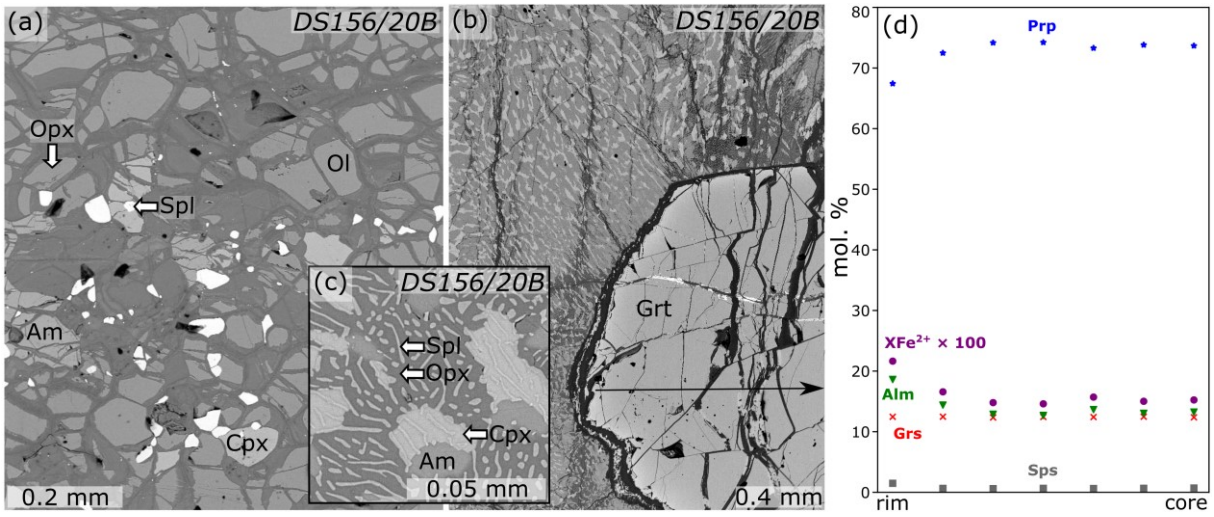

Figure III. 14: Back-scattered electron images (a–c) and composition profile across garnet (d) from garnet peridotite DS156/20B. a) Matrix mineral association formed by olivine, clinopyroxene, orthopyroxene, spinel, and amphibole. b) Part of the garnet porphyroblast and its kelyphite rim. c) Detail of the kelyphite rim. d) Composition profile across the garnet porphyroblast from the subfigure b).

Mineral phases in the matrix have the following composition ranges: Ol: XFe^{2+} = 0.08–0.09, Cpx: $CaTs_{3.5–7.3}Jd_{3.9–11.4}$, XFe^{2+} = 0.05–0.7, Opx: XFe^{2+} = 0.07–0.09, Spl: XFe^{2+} = 0.31–0.33, Al ~ 1.4 p.f.u., Cr ~ 0.6 p.f.u.

Garnet is Mg-rich characterized by the composition plateau with Mg decrease and Fe increase at the rim: $Prp_{73.7\rightarrow67.4}Alm_{13.2\rightarrow18.6}Grs_{12.4\rightarrow12.5}Sps_{0.7\rightarrow1.5}$, XFe^{2+} = 15.24→21.64 (Figure III. 14d).

Sample DS163/20A (Figure III. 15) is formed by Spl–Opx–Ol–Cpx fine-grained matrix with up to 2 mm large clinopyroxene and orthopyroxene porphyroblasts (Figure III. 15a, b). The space between the grains is filled with serpentine group minerals. The matrix hosts up to 2.3 mm large fine-grained Amp–Cpx–Spl–Opx elongated symplectites (Figure III. 15c, d) that probably replaced the garnet, which was not observed in the sample.

Olivine is Mg-rich with XFe^{2+} = 0.09–0.10. The composition range of spinel in the matrix is: XFe^{2+} = 0.27–0.28, Al ~1.7 p.f.u., Cr ~0.3 p.f.u.
Orthopyroxene forming porphyroblasts shows no systematic zoning, the composition range is: XFe^{2+} = 0.09–0.10. Clinopyroxene porphyroblasts are characterized by the Na decrease and Al and Ca increase from the core towards the rim: Cpx: $CaTs_{4.1\rightarrow5.1}Jd_{9.2\rightarrow6.6}$, XFe^{2+} = 0.07→0.07.

Mineral phases forming elongated fine-grained symplectites in the matrix have the following composition ranges: Cpx: $CaTs_{5.8–7.6}Jd_{4.9–7.2}$, XFe^{2+} = 0.05–0.08, Opx: XFe^{2+} = 0.09–0.10, Spl: XFe^{2+} = 0.21–0.22, Al ~1.9 p.f.u., Cr ~0.1 p.f.u., ZnO ~0.11 wt. % (TiO_2 under detection limit); Amp (pargasite): XFe^{2+} ~0.05, Ti ~0.1 p.f.u., Si ~6.2 p.f.u.

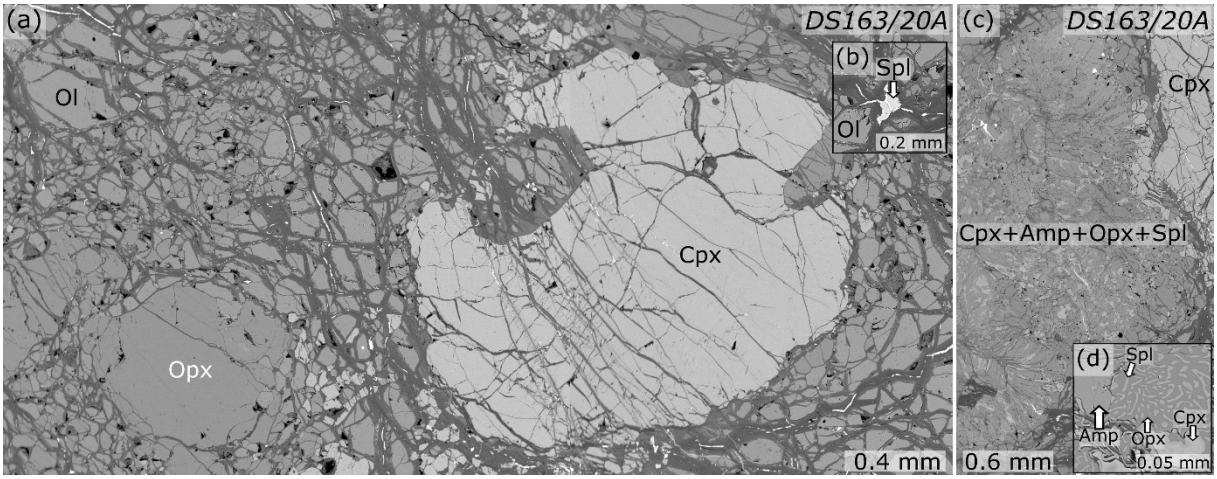

Figure III. 15: Back-scattered electron images (a–d) from garnet peridotite DS163/20A. a) Matrix mineral association with porphyroblasts of clinopyroxene and orthopyroxene. b) Spinel and olivine in the matrix. c) Fine-grained elongated symplectites formed by clinopyroxene, amphibole, orthopyroxene and spinel and d) detail of this symplectite.

Sample DS159/20A (Figure III. 16) contains up to 2.8 mm elongated Amp–Spl–Opx symplectites (Figure III. 16a, b) probably representing products after garnet decay in Spl–Opx–Ol–Cpx fine-grained matrix (Figure III. 16c). Garnet was not observed in the sample. The space between the grains is filled with serpentine group minerals.

Olivine is Mg-rich with XFe^{2+} = 0.07–0.09. Another mineral phases in the matrix has the composition range: Cpx: $CaTs_{2.7–4.6}Jd_{3.4–6.9}$, XFe^{2+} = 0.05–0.06, Opx: XFe^{2+} = 0.07–0.08, Spl: XFe^{2+} = 0.30–0.33, Al = 1.4–1.5 p.f.u., Cr = 0.5–0.6 p.f.u., ZnO = 0.18–0.24 wt. %, TiO_2 = 0.0–0.01 wt. %.

Mineral phases in fine-grained symplectites has the following composition ranges: Opx: XFe^{2+}~0.08; Spl: XFe^{2+} ~0.26, Al ~1.6 p.f.u., Cr ~0.4 p.f.u. ; Amp (pargasite): XFe^{2+} = 0.02–0.04, Si = 6.4–6.5 p.f.u., TiO_2 = 0.07–0.10 wt. %.

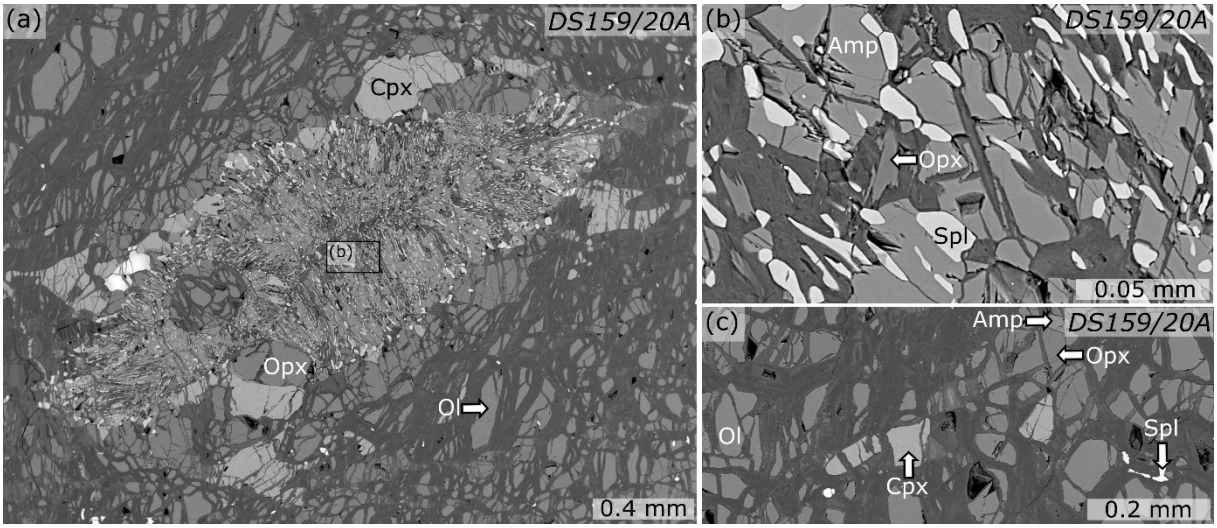

Figure III. 16: Back-scattered electron images (a–c) from garnet peridotite DS159/20A. a) Matrix mineral association with elongated fine-grained symplectites of orthopyroxene, spinel, and amphibole. b) Detail of fine-grained symplectite from the subfigure a. c) Matrix mineral association formed by olivine, orthopyroxene, clinopyroxene, and spinel.

Table III. 5: Representative mineral analyses of peridotites in wt. %.

Lithology	Peridotites										
Thin-section	DS156/20B	DS156/20B	DS156/20B	DS163/20A	DS163/20A	DS163/20A	DS159/20A	DS156/20B	DS163/20A	DS163/20A	DS163/20A
Mineral	Grt	Grt	Cpx	Cpx	Cpx	Cpx	Cpx	Opx	Opx	Opx	Opx
Analysis	Grt-25	Grt-31	Cpx-16	Cpx-01	Cpx-03	Cpx-20	Cpx-10	Opx-12	Opx-04	Opx-06	Opx-17
Position	Matrix, core	Matrix, rim	Matrix	Matrix, core	Matrix, rim	Matrix, symplectite with Amp, Opx, Spl	Matrix	Matrix	Matrix, core	Matrix, rim	Matrix, symplectite with Amp, Cpx, Spl
SiO_2	42.78	41.95	53.44	53.47	53.67	53.33	54.26	56.44	56.50	55.53	54.97
TiO_2	0.26	0.26	0.26	0.22	0.21	0.21	0.02	0.07	0.10	0.08	0.02
Cr_2O_3	1.67	1.68	1.19	0.91	0.65	0.43	1.24	0.44	0.32	0.32	0.18
Al_2O_3	22.46	22.17	4.48	3.06	3.71	5.26	2.88	2.63	2.20	2.55	3.66
FeO	7.39	9.85	1.92	2.85	2.16	2.37	1.78	5.87	6.16	6.63	6.94
MnO	0.36	0.74	0.06	0.10	0.07	0.12	0.10	0.19	0.14	0.17	0.19
NiO	b.d.	b.d.	b.d.	b.d.	b.d.	b.d.	b.d.	b.d.	b.d.	b.d.	b.d.
MgO	21.17	19.02	15.97	16.48	15.98	15.74	16.29	34.46	34.25	33.97	33.13
CaO	4.95	4.89	21.59	20.95	22.60	22.28	22.69	0.42	0.41	0.29	0.32
Na_2O	0.04	0.03	1.28	1.18	0.89	0.95	0.91	b.d.	b.d.	b.d.	0.01
K_2O	b.d.	b.d.	0.01	b.d.	b.d.	b.d.	0.01	b.d.	0.01	b.d.	b.d.
ZnO	b.d.	b.d.	b.d.	b.d.	b.d.	b.d.	b.d.	b.d.	b.d.	b.d.	b.d.
Cl	b.d.	b.d.	b.d.	b.d.	b.d.	b.d.	b.d.	b.d.	b.d.	b.d.	b.d.
Total	101.07	100.58	100.20	99.22	99.94	100.69	100.17	100.52	100.07	99.53	99.43
Cations/Charges	8/24	8/24	4/12	4/12	4/12	4/12	4/12	4/12	4/12	4/12	4/12
Si	3.00	2.99	1.93	1.95	1.95	1.92	1.96	1.93	1.95	1.92	1.91
Ti	0.01	0.01	0.01	0.01	0.01	0.01	0.00	0.00	0.00	0.00	0.00
Cr	0.09	0.09	0.03	0.03	0.02	0.01	0.04	0.01	0.01	0.01	0.00
Al	1.86	1.86	0.19	0.13	0.16	0.22	0.12	0.11	0.09	0.10	0.15
Fe^{2+}	0.40	0.56	0.06	0.07	0.07	0.07	0.05	0.15	0.17	0.16	0.18
Fe^{3+}	0.04	0.03	0.00	0.02	0.00	0.00	0.00	0.01	0.01	0.04	0.03
Mn	0.02	0.04	0.00	0.00	0.00	0.00	0.00	0.01	0.00	0.01	0.01
Ni	–	–	–	–	–	–	–	–	–	–	–
Mg	2.21	2.02	0.86	0.90	0.86	0.84	0.88	1.76	1.76	1.75	1.72
Ca	0.37	0.37	0.83	0.82	0.88	0.86	0.88	0.02	0.02	0.01	0.01
Na	0.00	0.00	0.09	0.08	0.06	0.07	0.06	–	–	–	0.00
K	0.00	0.00	0.00	–	–	–	0.00	–	0.00	–	–
Zn	–	–	–	–	–	–	–	–	–	–	–
Cl	–	–	–	–	–	–	–	–	–	–	–
XFe^{2+}	0.15	0.22	0.06	0.07	0.07	0.08	0.06	0.08	0.09	0.08	0.09

b.d. below detection limit

Table III. 5 (continued): Representative mineral analyses of peridotites in wt. %.

Lithology	Peridotites												
Thin-section	DS159/20A	DS159/20A	DS156/20B	DS163/20A	DS163/20A	DS159/20A	DS159/20A	DS156/20B	DS163/20A	DS159/20A	DS156/20B	DS163/20A	DS159/20A
Mineral	Opx	Opx	Spl	Spl	Spl	Spl	Spl	Amp	Amp	Amp	Ol	Ol	Ol
Analysis	Opx-19	Opx-07	Spl-05	Spl-23	Spl-15	Spl-14	Spl-05	Amp-14	Amp-11	Amp-01	Ol-19	Ol-08	Ol-12
Position	Matrix	Matrix, Symplectite with Amp, Cpx, Spl	Matrix	Matrix	Matrix, Symplectite with Amp, Cpx, Opx	Matrix	Matrix, symplectite with Amp, Opx	Matrix	Matrix, Symplectite with Spl, Cpx, Opx	Matrix, symplectite with Spl, Opx	Matrix	Matrix	Matrix
SiO_2	56.07	58.41	0.06	0.04	0.12	0.03	0.13	42.94	44.04	45.97	41.07	41.30	41.15
TiO_2	0.02	0.01	0.04	0.01	b.d.	0.01	b.d.	1.73	0.50	0.07	b.d.	b.d.	0.01
Cr_2O_3	0.55	0.33	25.76	13.14	5.22	24.57	18.34	1.77	0.53	1.28	b.d.	b.d.	b.d.
Al_2O_3	2.12	1.62	42.01	53.32	62.77	44.32	50.28	13.93	15.40	13.34	b.d.	b.d.	b.d.
FeO	5.60	5.73	14.43	13.22	10.53	12.86	11.13	2.71	3.31	2.40	8.37	9.66	8.15
MnO	0.14	0.13	0.19	0.12	0.08	0.13	0.11	0.02	0.07	0.06	0.16	0.13	0.15
NiO	b.d.	b.d.	b.d.	0.27	0.33	0.25	0.25	0.08	0.03	0.13	0.45	0.39	0.41
MgO	34.46	35.67	15.60	17.58	20.42	16.59	18.09	17.89	17.76	18.83	50.53	48.80	49.58
CaO	0.55	0.18	0.01	b.d.	0.03	b.d.	0.13	11.82	11.96	12.48	0.01	0.01	0.01
Na_2O	0.02	b.d.	0.01	b.d.	b.d.	b.d.	b.d.	2.82	3.12	2.41	b.d.	b.d.	b.d.
K_2O	0.01	b.d.	0.02	b.d.	b.d.	0.01	0.01	0.94	0.08	0.05	0.02	b.d.	b.d.
ZnO	b.d.	b.d.	0.25	0.36	0.11	0.21	0.20	0.04	b.d.	0.02	0.02	b.d.	0.01
Cl	b.d.	b.d.	b.d.	b.d.	b.d.	b.d.	b.d.	0.02	0.01	b.d	b.d.	0.01	b.d.
Total	99.54	102.08	98.37	98.04	99.60	98.98	98.66	96.69	96.81	97.03	100.61	100.27	99.47
Cations/ Charges	4/12	4/12	3/8	3/8	3/8	3/8	3/8	23 O eq.	23 O eq.	23 O eq.	3/8	3/8	3/8
Si	1.94	1.97	0.00	0.00	0.00	0.00	0.00	6.15	6.23	6.46	0.99	1.01	1.01
Ti	0.00	0.00	0.00	0.00	–	0.00	–	0.19	0.05	0.01	–	–	0.00
Cr	0.02	0.01	0.58	0.28	0.10	0.54	0.39	0.20	0.06	0.14	–	–	–
Al	0.09	0.06	1.41	1.70	1.88	1.46	1.61	2.35	2.57	2.21	–	–	–
Fe^{2+}	0.13	0.16	0.33	0.28	0.22	0.30	0.25	0.24	0.19	0.14	0.16	0.20	0.17
Fe^{3+}	0.03	0.00	0.01	0.02	0.01	0.00	0.00	0.09	0.20	0.14	0.01	0.00	0.00
Mn	0.00	0.00	0.00	0.00	0.00	0.00	0.00	0.00	0.01	0.01	0.00	0.00	0.00
Ni	–	–	–	0.00	0.00	0.01	0.01	0.01	0.00	0.01	0.01	0.01	0.01
Mg	1.77	1.79	0.66	0.71	0.77	0.69	0.73	3.82	3.74	3.95	1.82	1.78	1.81
Ca	0.02	0.01	0.00	–	0.00	–	0.00	1.81	1.81	1.88	0.00	0.00	0.00
Na	0.00	–	0.00	–	–	–	–	0.78	0.86	0.66	–	–	–
K	0.00	–	0.00	–	–	0.00	0.00	0.17	0.01	0.01	0.00	–	–
Zn	–	–	0.01	0.01	0.00	0.00	0.00	0.00	–	0.00	0.00	–	0.00
Cl	–	–	–	–	–	–	–	0.01	0.00	–	–	0.00	–
XFe^{2+}	0.07	0.08	0.33	0.28	0.22	0.30	0.26	0.06	0.05	0.03	0.08	0.10	0.08

b.d. below detection limit

2 P–T pseudosection modelling

The P–T pseudosection modelling has been applied to Ky-bearing felsic granulite (sample DS024), intermediate granulite (sample DS071B), mafic granulite with symplectite texture (DS025E), and garnet clinopyroxenite (DS072C) in order to obtain information about their P–T evolution and P–T conditions of possible metasomatic interaction between Ky-bearing felsic granulite with garnet clinopyroxenite.

2.1 Methodology of phase stability modelling

The P–T pseudosection modelling was performed with the software THERMOCALC 3.50 with the internally consistent thermodynamic dataset (Holland & Powell, 2011, dataset version 6.2). The calculated pseudosections were plotted by the pypsbuilder software (Lexa, 2020). The chemical compositions (Table III. 6) of the modelled lithologies were estimated by averaging representative area analyses acquired by SEM–EDS in a scanning mode.

Table III. 6: Chemical compositions in wt. % obtained from averaged SEM–EDS area analyses.

Lithology	Ky-bearing felsic granulite	Intermediate granulite	Mafic granulite with symplectite texture	Garnet clinopyroxenite
Thin-section	DS024	DS071B	DS025E	DS072C
SiO_2	76.29	65.29	49.67	47.31
TiO_2	0.15	0.78	0.29	0.35
Al_2O_3	13.09	16.62	18.51	13.27
Cr_2O_3	0.01	b.d.	0.08	b.d.
NiO	b.d.	b.d.	b.d.	0.06
FeO^{tot}	1.25	5.79	4.44	6.41
MnO	0.03	0.09	0.52	0.11
MgO	0.30	1.89	8.95	15.06
CaO	1.19	4.45	13.79	12.60
Na_2O	3.56	3.73	2.54	1.75
K_2O	4.12	1.87	0.08	0.00
P_2O_5	0.08	0.16	b.d.	0.15
SO_3	0.01	0.33	0.02	0.25
Total	100.08	100.98	98.89	97.32

b.d. below detection limit

The chemical compositions were modified with respect to the content of minerals that cannot be considered for the phase equilibria modelling (apatite for samples DS024, DS071B, and DS072C; pyrrhotite, pentlandite for sample DS072C) but their presence affects the whole rock

analysis. The CaO content was decreased by subtracting of CaO stoichiometrically corresponding to P_2O_5 content reflecting presence of apatite (the contents of other phosphates is negligible). Content of FeO^{tot} was reduced by subtracting of Fe stoichiometrically corresponding to pyrrhotite and pentlandite (S and Ni contents were used for this correction).

The P–T pseudosections for the Ky-bearing felsic granulite (sample DS024) and intermediate granulite (sample DS071B) was undertaken in the system MnO–Na_2O–CaO–K_2O–FeO–MgO–Al_2O_3–SiO_2–H_2O–TiO_2–O_2 (MnNCKFMASHTO) with the following mixing models: garnet, biotite, cordierite, ilmenite, muscovite, and melt models for metapelites (White *et al.*, 2014). Ternary plagioclase/K-feldspar were calculated with models after Holland *et al.,* 2022. In addition, for intermediate granulite were used clinopyroxene model for metabasic rocks (Green *et al.*, 2016), and model of orthopyroxene (White *et al.*, 2014). The amount of H_2O was set to 1 mol. %, a value estimated from phase equilibria calculations of granulites from Lower Austria (e.g. Racek *et al*., 2006, 2008; Schantl *et al.*, 2019).
Calculations for mafic granulite (sample DS025E) and garnet clinopyroxenite (sample DS072C) was undertaken in the system Na_2O–CaO–K_2O–FeO–MgO–Al_2O_3–SiO_2–H_2O–TiO_2–O_2 (NCKFMASHTO) with the mixing models: olivine (Holland & Powell, 2011), clinopyroxene, amphibole, and melt for metabasic rocks (Green *et al.,* 2016), garnet, orthopyroxene, and ilmenite models for metapelites (White *et al.,* 2014). Plagioclase was calculated with the model after Holland *et al.,* 2022. The amount of H_2O was also set to 1 mol. % as in the case of Ky-bearing felsic granulite and intermediate granulite. This value also corresponds to the H_2O content from the whole-rock chemical analyses of garnet clinopyroxenites from the St. Leonhard granulite massif (Becker, 1996a).

2.2 P–T modelling for kyanite-bearing felsic granulite (sample DS024)

The peak mineral assemblage is according to the petrography study garnet, K-feldspar, plagioclase, quartz, kyanite and rutile, which corresponds to the compatibility field Liq–Grt–Kfs–Ky–Pl–Qz–Rt, where composition isopleths of the garnet core $Prp_{25.0}Alm_{56.0}Grs_{17.7}Sps_{1.5}$; XFe^{2+} = 0.69 intersect in a P–T range of 1.9–2.4 GPa and 900–1050 °C (Figure III. 17). The compositional isopleths of the garnet rim $Prp_{31.1}Alm_{64.7}Grs_{2.7}Sps_{1.5}$; XFe^{2+} = 0.68 intersect at 0.8–1.1 GPa and 900–1025 °C within the range of the compatibility fields Liq–Grt–Kfs–Pl–Qz–Rt, Liq–Grt–Ilm–Kfs–Pl–Qz–Rt, Liq–Grt–Ilm–Kfs–Pl–Qz, and Liq–Grt–Pl–Qz–Rt, where the phase change from rutile to ilmenite occurs a kyanite is not stable here.

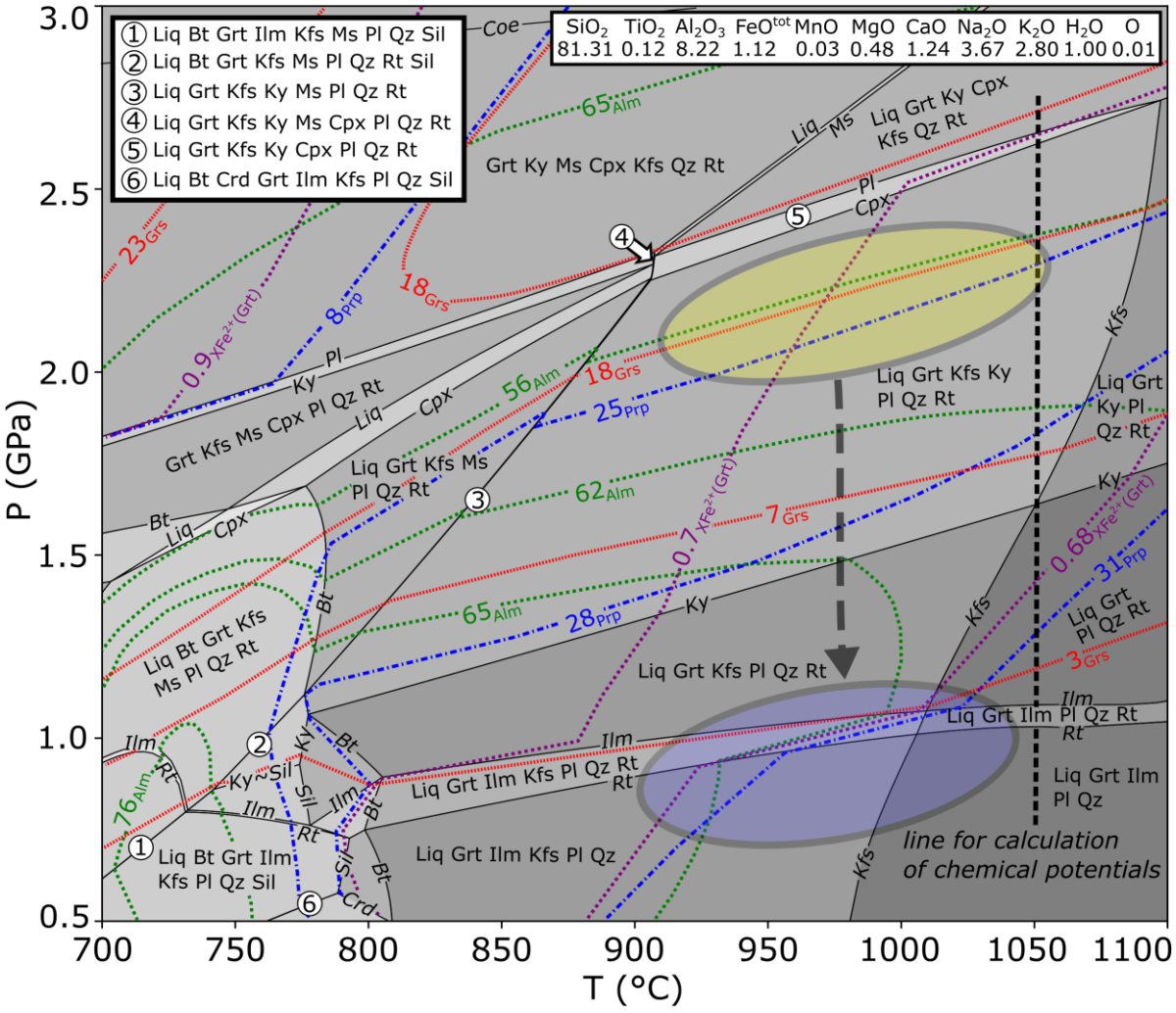

Figure III. 17: P–T pseudosection for the Ky-bearing felsic granulite (DS024) with composition isopleths of garnet. The conditions of formation of the peak assemblage (compatibility field of Liq–Grt–Kfs–Ky–Pl–Qz–Rt) were estimated at 1.9–2.4 GPa and 900–1050 °C (yellow ellipse). The rock has undergone isothermal decompression to 0.8–1.1 GPa and 900–1025 °C, where is no kyanite and ilmenite appears at the expense of rutile (blue ellipse).

2.3 P–T modelling of intermediate granulite (sample DS071B)

The mineral assemblage of the presumed peak metamorphic conditions is garnet, kyanite, K-feldspar, plagioclase, quartz, rutile, and clinopyroxene, which corresponds to the compatibility field Liq–Grt–Kfs–Ky–Cpx–Pl–Qz–Rt at approximately 2.1–2.6 GPa and 900–1100 °C, where, in addition, the composition isopleths of the garnet core $Prp_{24.0}Alm_{45.5}Grs_{29.7}Sps_{0.9}$; XFe^{2+} = 0.66 intersect (Figure III. 18). These garnet isopleths also intersect at 1.4–1.9 GPa and 780–840 °C, where muscovite and biotite appear and where is no kyanite stability.

The compositional isopleths of the garnet rim intersect at 0.8–1.3 GPa and 960–1075 °C in the compatibility field Liq–Grt–Kfs–Opx–Pl–Qz, where the phase changes from rutile to ilmenite and from clinopyroxene to orthopyroxene occur, and kyanite is not stable.

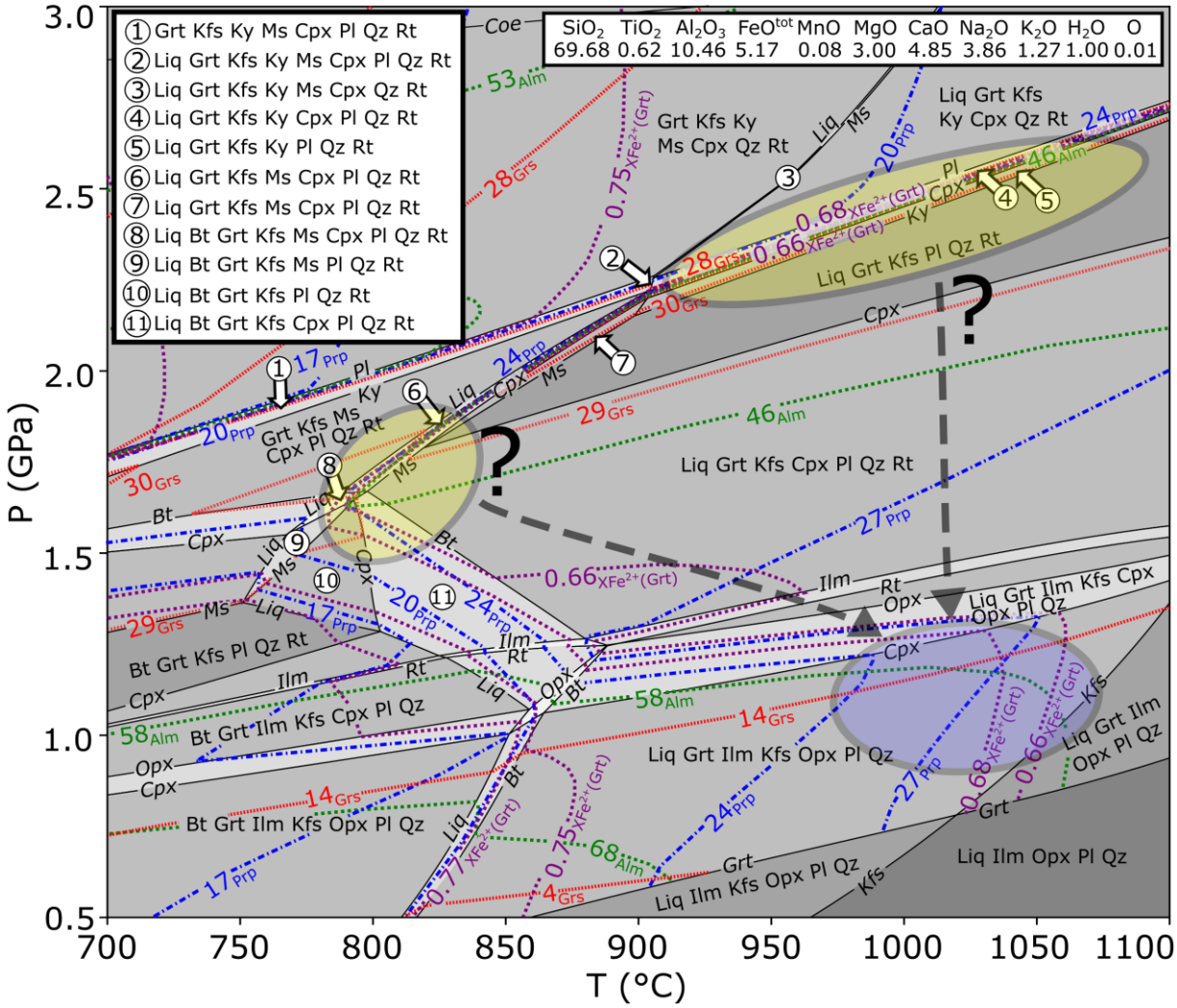

Figure III. 18: P–T pseudosection for the intermediate granulite (DS071B) with composition isopleths of garnet. The conditions of formation of the peak assemblage is uncertain and corresponds to either compatibility field of Liq–Grt–Kfs–Ky–Cpx–Pl–Qz–Rt at 2.1–2.6 GPa and 900–1100 °C or the compatibility fields at approximately 1.4–1.9 GPa and 780–840 °C, where muscovite and biotite appear and where is no kyanite stability (yellow ellipses). The matrix mineral association corresponds to the field Liq–Grt–Ilm–Kfs–Opx–Pl–Qz at 0.8–1.3 GPa and 960–1075 °C, where is no kyanite and ilmenite appears at the expense of rutile (blue ellipse).

2.4 P–T modelling of mafic granulite with symplectite texture (sample DS025E)

The mineral assemblage from peak metamorphic conditions is garnet, clinopyroxene, kyanite, plagioclase, quartz, and rutile, which corresponds to the compatibility field Liq–Cpx–Grt–Ky–Pl–Qz–Rt, where composition isopleths of the garnet core $Prp_{41.9}Alm_{15.9}Grs_{41.8}Sps_{0.4}$; XFe^{2+} = 0.28 intersect in a P–T range 2.3–2.8 GPa and 1050–1240 °C (Figure III. 19). The compositional isopleths of the garnet rim $Prp_{52.7.1}Alm_{29.2}Grs_{17.2}Sps_{0.9}$; XFe^{2+} = 0.36 intersect at 1.0–1.4 GPa and 1030–1150 °C within the range of the compatibility fields Liq–Cpx–Grt–Amp–Pl and Liq–Cpx–Grt–Amp–Opx–Pl.

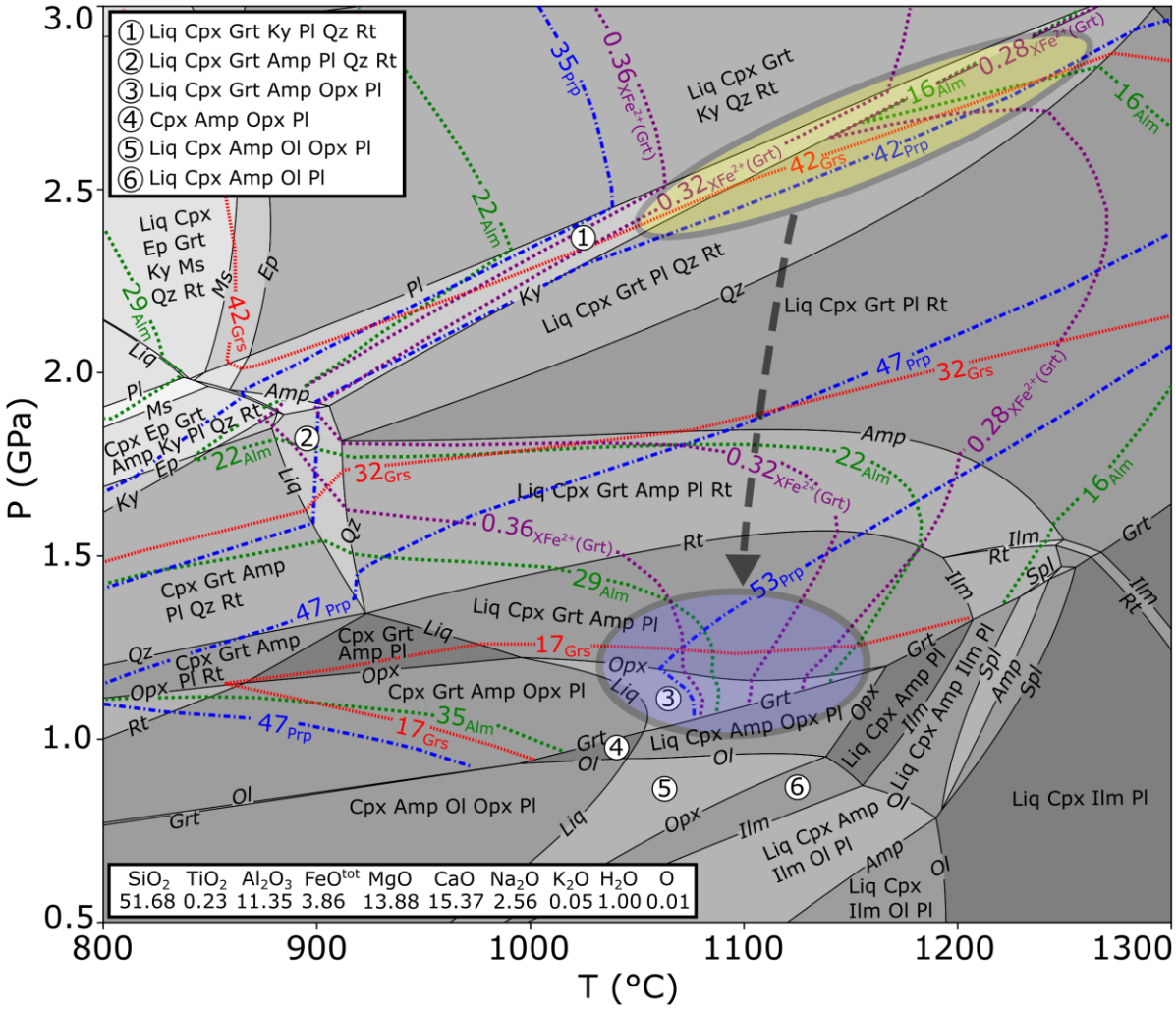

Figure III. 19: P–T pseudosection for the mafic granulite (DS025E) with composition isopleths of garnet. The conditions of formation of the peak assemblage corresponds to compatibility field of Liq–Cpx–Grt–Ky–Pl–Qz–Rt at 2.3–2.8 GPa and 1050–1240 °C. The matrix mineral association corresponds to the fields Liq–Cpx–Grt–Amp–Pl and Liq–Cpx–Grt–Amp–Opx–Pl at 1.0–1.4 GPa and 1030–1150 °C.

2.5 P–T modelling of garnet clinopyroxenite (sample DS072C)

The presumed mineral assemblage from peak metamorphic conditions of the modelled sample DS072C is garnet, clinopyroxene, kyanite, amphibole, and rutile, which corresponds to the compatibility fields Liq–Cpx–Grt–Amp–Rt and Liq–Cpx–Grt–Amp, where composition isopleths of the garnet core $Prp_{58.7}Alm_{21.0}Grs_{19.9}Sps_{0.5}$; XFe^{2+} = 0.26 intersect in a P–T range 1.8–2.6 GPa and 1150–1250 °C (Figure III. 20).

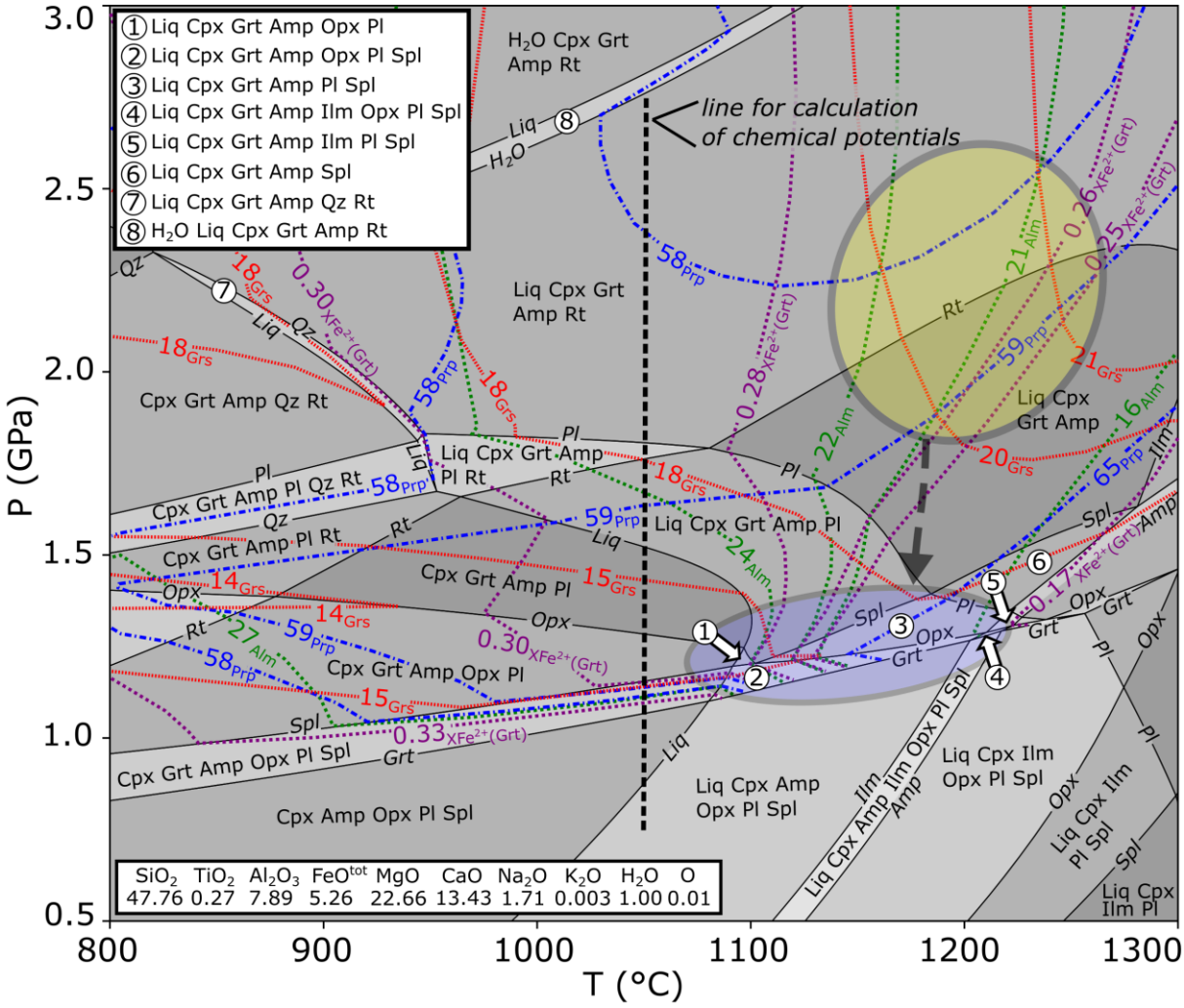

Figure III. 20: P–T pseudosection for the garnet clinopyroxenite (DS072C) with composition isopleths of garnet. The conditions of formation of the peak assemblage corresponds to compatibility fields of Liq–Cpx–Grt–Amp–Rt and Liq–Cpx–Grt–Amp at 1.8–2.6 GPa and 1150–1250 °C. The matrix mineral association corresponds to the fields Liq–Cpx–Grt–Amp–Pl, Liq–Cpx–Grt–Amp–Opx–Pl, Liq–Cpx–Grt–Amp–Opx–Pl–Spl, and Liq–Cpx–Grt–Amp–Pl–Spl at 1.0–1.4 GPa and 1060–1220 °C.

The compositional isopleths of the garnet rim $Prp_{64.6}Alm_{21.9}Grs_{13.1}Sps_{0.4}$; XFe^{2+} = 0.25 approach at 1.0–1.4 GPa and 1060–1220 °C within the range of the compatibility fields Liq–Cpx–Grt–Amp–Pl, Liq–Cpx–Grt–Amp–Opx–Pl, Liq–Cpx–Grt–Amp–Opx–Pl–Spl, and Liq–Cpx–Grt–Amp–Pl–Spl, which corresponds to the observed matrix mineral association additionally containing orthopyroxene, plagioclase, and spinel and which lacks rutile.

2.6 Chemical potentials (μ) across P–T pseudosections of Ky-bearing felsic granulite and garnet clinopyroxenite

As in the Part II, which describes the metasomatic interaction of a few cm large mantle xenoliths with the host granulite, the chemical mass transfer between Ky-bearing felsic granulites and garnet clinopyroxenite bodies also probably took place by diffusion enhanced by the presence of fluid/melt, in accord with the presence of multiphase solid inclusions in garnet clinopyroxenites described in the Part I.

As in the Part II, the chemical potentials of the Ky-bearing felsic granulite (sample DS024) and garnet clinopyroxenite (sample DS072C) mineral assemblages in P–T pseudosections (Figure III. 17, Figure III. 20) were applied to assess the driving force for the possible exchange of chemical components between these lithologies (see Part II for a more detailed explanation).

Chemical potentials (Figure III. 21) were calculated in P–T conditions between the P–T paths estimated for both lithologies, along the 1050 °C isotherm starting at 2.7 GPa with decreasing pressure to 0.75 GPa. The temperature 1050 °C was determined a little closer to the Ky-bearing felsic granulite because it is possible that garnet clinopyroxenite carry the higher temperatures as a record of previous mantle conditions and that the metasomatic interaction took place in P–T conditions closer to Ky-bearing felsic granulite.

For both lithologies, μSiO_2 is almost identical along the whole isotherm, but in granulite there are slightly higher μSiO_2 values (Figure III. 21a). Furthermore, μTiO_2 is almost identical for both lithologies until 1.5 GPa, where it becomes lower in the garnet clinopyroxenite than in the Ky-bearing felsic granulite (Figure III. 21b). The trend of μAl_2O_3 is identical for both lithologies, but μAl_2O_3 is slightly higher for the Ky-bearing felsic granulite than for the garnet clinopyroxenite (Figure III. 21c). The μFeO^{tot} is almost identical at 2.7 GPa and towards 1.7 GPa μFeO^{tot} increases in Ky-bearing felsic granulite compared to garnet clinopyroxenite. From 1.7 GPa the μFeO^{tot} begin to converge again and from 1.25 GPa the μFeO^{tot} for both lithologies are almost identical (Figure III. 21d). Garnet clinopyroxenite has higher μMgO and μCaO along the whole geotherm, but from the 1.5 GPa towards 0.7 GPa, μCaO of both lithologies are more distant (Figure III. 21e, f).

Garnet clinopyroxenite has higher μNa_2O along the whole isotherm compared to Ky-bearing felsic granulite whereby μNa_2O for both lithologies are farther away from 1.5 GPa (Figure III. 21g). Ky-bearing felsic granulite has higher μK_2O along the whole geotherm compared to garnet clinopyroxenite whereby μK_2O of garnet clinopyroxenite approaches μK_2O of Ky-bearing felsic granulites from 1.2 GPa towards lower pressures (Figure III. 21h).

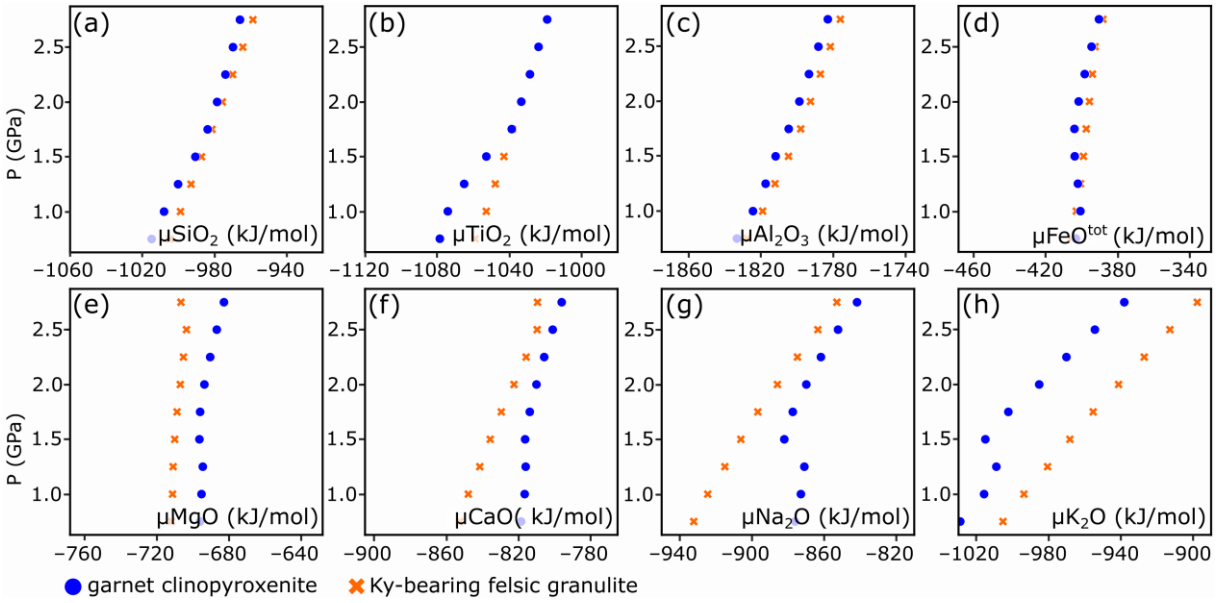

Figure III. 21: Comparison of chemical potentials for garnet clinopyroxenite (DS072C) and Ky-bearing felsic granulite (DS024) calculated from both P–T pseudosections at 1050 °C (Figure III. 17 and Figure III. 20).

Taken together, along the isotherm between the estimated P–T paths along Ky-bearing felsic granulite and garnet clinopyroxenite pseudosections (Figure III. 17, Figure III. 20), the biggest differences in chemical potentials show Mg and Ca, whereby μMgO and μCaO are higher in garnet clinopyroxenite than in Ky-bearing felsic granulite along the whole isotherm. It indicates a tendency for these elements to migrate from garnet clinopyroxenite to granulite. Differences in other chemical potentials are negligible, if any.

3 Zr in rutile thermometry

The Zr content in rutile was used to establish the temperature in felsic and intermediate granulites after the method of Tomkins et al. (2007). This method is usable for lithologies, where rutile coexists with zircon and quartz, which our samples of felsic and intermediate granulites fulfil. The temperatures were calculated using the equation for a β-quartz stability conditions:

$$T\ (°C) = \frac{85.7 + 0.473P(kbar)}{0.1453 - R \times ln\phi} - 273$$

ϕ = Zr content in ppm, R = 0.0083144 kJ K^{-1}.

The zirconium contents in rutile and the calculated temperatures are shown in Figure III. 22. For the peak metamorphic temperatures were used analyses of rutile inclusions in garnet (Figure III. 22a) and for matrix temperature conditions were used rutile analyses from the matrix (Figure III. 22d). From four samples of felsic granulites were measured 21 rutile inclusions in garnet and 36 rutile grains in the matrix. From three samples of intermediate granulites were measured 12 rutile inclusions in garnet and 19 rutile grain in the matrix. All rutile analyses are available in Table S. 7.

Based on the results of the P–T pseudosection modelling (Figure III. 17, Figure III. 18), the peak metamorphic temperatures were calculated at 2.3 GPa for both lithologies, and in addition at 1.7 GPa for intermediate granulites, because the peak P–T conditions of intermediate granulites are still unclear (Figure III. 18). Matrix metamorphic conditions were calculated for both lithologies at 1.2 GPa.

Rutile inclusions in garnet from felsic granulites have 2739.1–4841.6 ppm Zr, which for pressure of 2.3 GPa gives temperatures of 942.0–1019.0 °C with median 974.3 °C. Rutile inclusions in garnet from intermediate granulites have 1295.5–5433.8 ppm Zr, which for pressure of 2.3 GPa gives temperatures of 853.8–1035.8 °C with median 935.0 °C, and for pressure of 1.7 GPa it gives temperatures of 820.7–997.3 °C with median 899.5.

Rutile from matrix have 2480.0–4042.0 ppm Zr in felsic granulites and 3175.9–8335.8 ppm Zr in intermediate granulites. At 1.2 GPa, these values give temperatures of 864.0–925.3 °C with median 891.4 °C for felsic granulites, and temperatures of 894.6–1028.0 °C with median 966.2 °C for the intermediate ones.

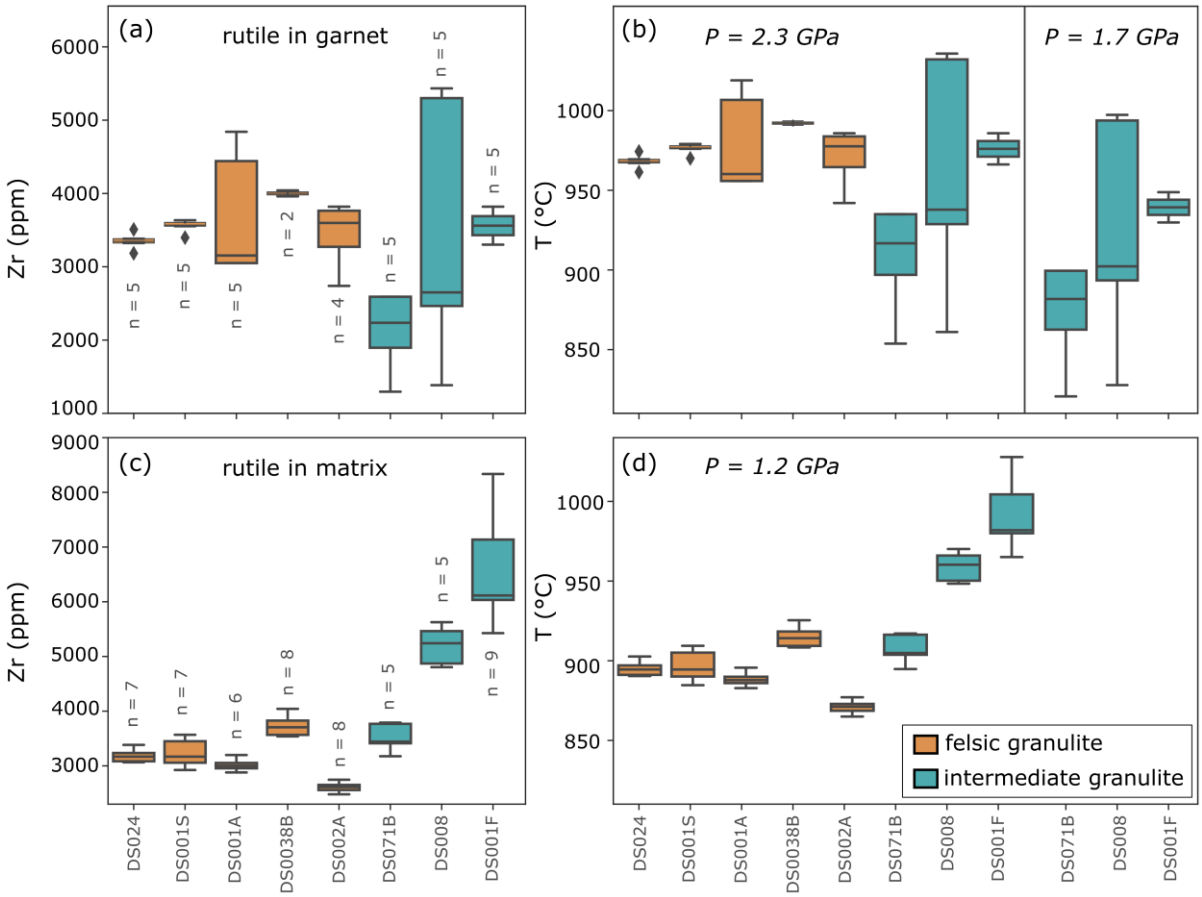

Figure III. 22: Boxplots for Zr in rutile thermometry for Ky-bearing felsic granulites and intermediate granulites after Tomkins et al., 2007. The pressures were determined based on the results of P–T modelling (Figure III. 17, Figure III. 18). a) Zirconium contents in rutile inclusions in garnet from which were calculated b) temperatures for the estimated peak metamorphic pressures. c) Zirconium contents in rutile in the matrix from which were calculated d) temperatures for the estimated matrix metamorphic pressures. All rutile analyses are available in Table S. 7.

4 Ternary feldspar thermometry

The reintegrated compositions of perthite from Ky-bearing felsic granulites and antiperthite from intermediate granulites were used to confirm the estimated matrix metamorphic temperatures obtained from P–T pseudosections (Figure III. 17, Figure III. 18). Most of the analyses are from the matrix except two perthite analyses from garnet that are probably associated with the matrix.

Reintegrated perthite/antiperthite analyses were measured by area SEM scans (Table S. 6 and 7), which covered the representative area of perthite/antiperthite including lamellae and the host

feldspar. The obtained compositions and the representative BSE images of measured areas are shown in Figure III. 23. The temperature isopleths were plotted after Fuhrman & Lindsley (1988) using the program SOLVCALC (Wen & Nekvasil, 1994). According to the estimated pressures from the P–T pseudosections (Figure III. 17, Figure III. 18), temperature isopleths for 1.2 GPa were plotted.

For estimation of the matrix metamorphic temperatures at 1.2 GPa were used 34 reintegrated perthite compositions from four samples of Ky-bearing felsic granulites ($An_{2.1–14.1}Ab_{20.6–49.7}Or_{41.5–76.8}$), and 19 analyses of reintegrated antiperthite compositions from three samples of intermediate granulites ($An_{27.6–40.3}Ab_{35.5–51.7}Or_{15.1–26.5}$). These reintegrated perthite/antiperthite compositions indicate T ≥ 900 °C for Ky-bearing felsic granulites, and T ≥ 1000 °C for intermediate ones.

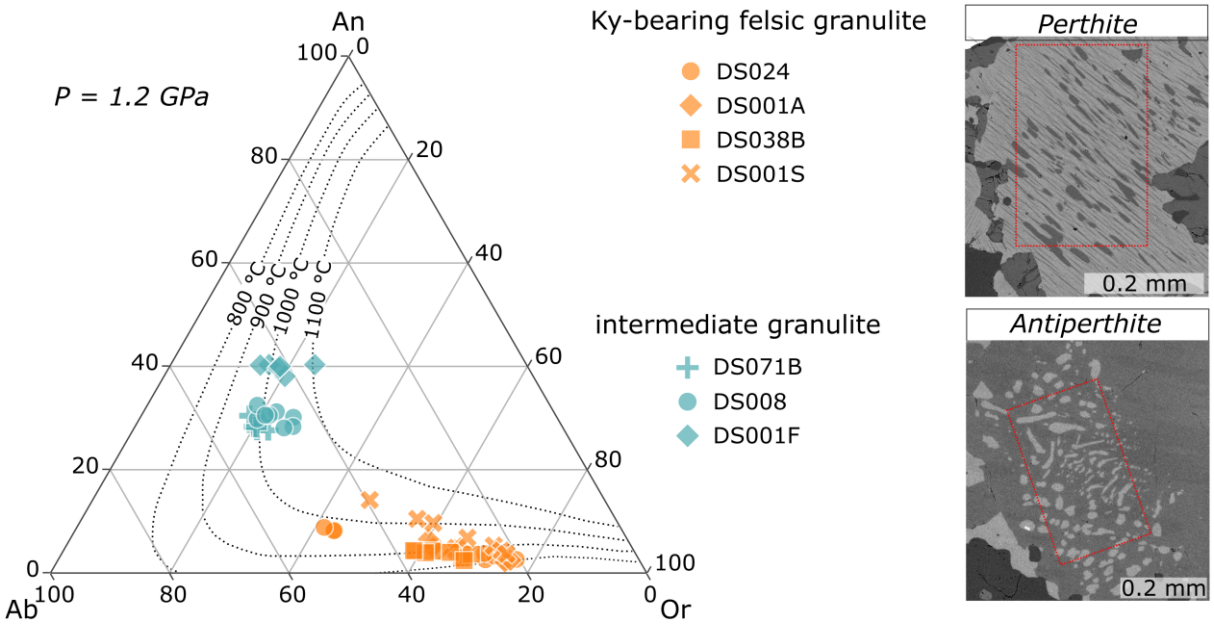

Figure III. 23: Reintegrated perthite compositions from Ky-bearing felsic granulites and reintegrated antiperthite compositions from intermediate granulites measured by area SEM scans (Table S. 6 and 7). Representative measured areas are shown by red rectangles in the BSE images on the right. The temperature isopleths are plotted after Furman & Lindsley (1988) for 1.2 GPa.

5 Discussion

5.1 Possible metasomatic formation of intermediate granulites

In the matrix of intermediate granulites, the elongated fine-grained symplectites of corundum, spinel, epidote and K-feldspar in some cases surrounded by thin corona of garnet followed by

plagioclase probably represent the pseudomorphs after an Al_2SiO_5 phase, probably kyanite (Owen & Dostal, 1996; O'Brien & Rötzler, 2003; Tajčmanová et al., 2007; Štípská et al., 2010; Vrána et al., 2013; Baldwin et al., 2014). These pseudomorphs result from an influx of mainly Ca, which caused the breakdown of kyanite and formation of orthopyroxene as described in detail in the Part II. The surplus Ca probably yielded the nearby clinopyroxenite bodies. The situation was hence similar to the metasomatic interaction described in the Part II, where the likely source of Ca were the garnet clinopyroxenite xenoliths. The petrographic similarity with the Ky-bearing felsic granulites shows that at least some of the intermediate granulites could represent Ky-bearing felsic granulites or their equivalents, in which the Ca supply caused the stabilization of orthopyroxene at the expense of the Al_2SiO_5 phase.

5.2 Possible metasomatic formation of mafic granulites

Studied samples of mafic granulites show the similarity in the peak and also in the matrix mineral association with garnet clinopyroxenites, but differ in the higher Pl (Opx–Amp ± Spl ± Spr) content in the matrix mineral association. Mafic granulites with the symplectite texture in their appearance resemble Opx–Pl symplectite coronae formed at the contact of garnet clinopyroxenite xenoliths with the host granulite described in the Part II. The symplectite textures often reflect the presence of fluid/melt (Spruzeniece *et al.*, 2016; Pistone *et al.*, 2020). The presence of fluid/melt could promoted diffusion as in the case of the metasomatic interaction described in the Part II. Diffusion of chemical components and the presence of fluid/melt are supported by the K-rich net along the grain boundaries in the matrix of mafic granulites with the symplectite texture (Figure III. 6g). The source of K were probably the surrounding granulites. The possible migration of mainly Ca to the surrounding granulites presumably caused the destabilization of clinopyroxene and ensuing growth of Na-rich plagioclase and orthopyroxene. The growth of plagioclase could be also the consequence of the decompression of the garnet clinopyroxenites.

5.3 P–T conditions of the possible metasomatic interaction between Ky-bearing felsic granulites with garnet clinopyroxenites

According to the P–T pseudosections (Figure III. 17–Figure III. 20), almost all lithologies recorded isothermal decompression from ~2.0 to 1.2 GPa at ~1000 °C. The P–T evolution of the intermediate granulite is not unambiguous and featured isothermal decompression from 2.1–2.6 GPa at 900–1100 °C to 0.8–1.3 GPa or decompression with heating from 1.4–1.9 GPa and 780–840 °C to 0.8–1.3 GPa and 960–1075 °C (Figure III. 18). Given the presumed peak

metamorphic association, which is formed by garnet, kyanite, K-feldspar, plagioclase, quartz, rutile, and clinopyroxene, the peak metamorphic conditions at 2.1–2.6 GPa at 900–1100 °C corresponding to the Liq–Grt–Kfs–Ky–Cpx–Pl–Qz–Rt stability field are more probable for the intermediate granulites evolution.

High T around 1000 °C are also confirmed by the conventional thermometry for all modelled lithologies. It is probable that the earlier P–T record for Ky-bearing and intermediate granulites connected with the Variscan subduction has been erased and that the calculated isothermal P–T decompression paths point to the diapiric ascent (e.g. Franěk *et al.,* 2011, Racek *et al*., 2006).

According to the chemical potentials calculated in the P–T pseudosections of Ky-bearing felsic granulite and garnet clinopyroxenite (Figure III. 21), the presumed end-members of the possible metasomatic interaction, along the 1050 °C isotherm from 2.7 GPa to 0.75 GPa, may point to the conditions of mutual metasomatic interaction (the principe is described in detail in the Part II).

The chemical potentials along the isotherms (Figure III. 21) show a very high tendency of Ca migration from garnet clinopyroxenite to Ky-bearing felsic granulite at 1.5 to 0.75 GPa. For other components these differences are not very significant with different pressures along the isotherm. The results are similar to the chemical potentials along the isotherms in the garnet clinopyroxenite xenolith and its host granulite P–T pseudosections in the Part II.

6 Conclusions

The petrographic study indicates possible metasomatic interaction at the contact of garnet clinopyroxenite bodies and their Ky-bearing felsic granulite host. The related component exchange took place by diffusion augmented by the presence of fluid/melt.

Ky-bearing felsic granulites are similar to intermediate granulites, and garnet clinopyroxenites are similar to mafic granulites in the matrix and the presumed peak metamorphic mineral assemblages. The P–T conditions obtained by pseudosection modelling and conventional thermometry for all lithologies show isothermal decompression from ~2.0 to 1.2 GPa at ~1000 °C. This probably reflects a diapiric ascent, which may have erased the previous P–T record. The component exchange between Ky-bearing felsic granulites and garnet clinopyroxenites probably took place at pressures lower than ~1.5 GPa. The Ca input from garnet clinopyroxenites to Ky-bearing felsic granulites may have caused the orthopyroxene growth at the expense of kyanite. The presence of fluid/melt in garnet clinopyroxenites together with the

decompression may have caused the formation of symplectites and the growth of plagioclase (± sapphirine, orthopyroxene, spinel, amphibole). The K supply from surrounding felsic lithologies is proved by the K-rich net observed along the plagioclase grains in the matrix.

This petrographic study shows metasomatic an interaction between garnet clinopyroxenite bodies and the host Ky-bearing felsic granulites. It was analogous to that described in the Part II but on a larger scale.

Part IV: Geochemical characterization of granulites, garnet clinopyroxenites, and peridotites from Lower Austria

In order to assess the degree and mechanism of possible metasomatic interaction between felsic granulites and garnet clinopyroxenites, presumably leading to the formation of intermediate and mafic granulites, a study of the major- and trace-elements whole-rock compositions and Sr–Nd isotopic ratios is necessary.

1 Samples and analytical methods

For the whole-rock geochemical analyses were chosen eleven samples from Dunkelsteiner Wald granulite massif: one felsic granulite (F-Gr; DS152/20A), two intermediate granulites (I-Gr; DS153/20A, DS155/20A), four mafic granulites (M-Gr; DS025/20B, DS025/20C, DS027/20B, DS157/20G), two garnet clinopyroxenites (GPYR; DS157/20D, DS151/20A), and two peridotites (PER; DS156/20B, DS163/20A) complemented by one sample of peridotite from the St. Leonhard granulite massif (DS159/20A). Mafic granulites are further on the basis of their (prevailing) texture divided to the groups with symplectite (M-Gr(S); DS025/20B, DS025/20C) and granoblastic texture (M-Gr(G); DS027/20B, DS157/20G). The detailed petrographical characterization of these samples are in the Part III of this thesis.

The locations of the studied samples is shown in the simplified geological map (Figure 0. 2) and the GPS coordinates are available in the Table S. 1. Mineral assemblages of all studied samples are given in the Table IV.1.

Approximately 6–8 kg of fresh rock was taken directly from the outcrops or from in-situ blocks for each sample. Rock pieces were subsequently crushed and ground to powder under acetone in agate mill at the Czech Geological Survey (CGS) laboratories for the subsequent geochemical analysis.

Major-element whole-rock analyses were performed by wet chemistry at CGS in Prague according to valid laboratory procedures.

Trace-element analyses were obtained by ICP–MS in the Activation Laboratories, Ancaster, Canada using the procedure 4B2-research or 4Lithoresearch (see www.actlabs.com). Trace-elements V, Cr, Co, Ni, Cu, Zn, Ga, Ge, Rb, Sr, Y, Zr, Nb, In, Sb, Cs, Ba, REE (except Sc), Hf, Ta, Bi, Th, U were measured by FUS–MS; As, Mo, Ag, Sn, Li, W, Tl, Pb, Sc, Be, and Cd, were measured by TD–MS.

Whole-rock Sr–Nd analyses were acquired at CGS laboratories. Rock-powders were dissolved with a mixture of HF–HCl–HNO_3. The Sr-Nd isotopic data were obtained by the Thermo Fisher Scientific Triton Plus Thermal-Ionization Mass Spectrometer (TIMS). Complete analytical details of measurement of Sr–Nd analyses used by CGS laboratories are available in Erban Kochergina *et al.,* 2022.

Table IV.1: Overview of information on samples for whole-rock geochemical analyses. The position of the samples within the geological map is shown in Figure 0. 2.

Sample	Locality	Lithology	Modal composition
	Dunkelsteiner Wald granulite massif		
DS152/20A	DS152	felsic granulite (F-Gr)	Qz, Grt, Pl, Kfs *Zrn, Mnz, Ap, Rt, Ilm*
DS153/20A	DS153	Opx-bearing intermediate granulites (I-Gr)	Qz, Grt, Pl, Kfs, Opx (Cpx, Bt) *Zrn, Mnz, Ap, Rt, Ilm, Spl*
DS155/20A	DS155		
DS025/20B DS025/20C	DS025	mafic granulites (M-Gr(S))	Grt, Cpx, Pl, Opx (Amp) *Spl, Ky, Spr, Rt, Ilm*
DS027/20B	DS027	mafic granulites (M-Gr(G))	Grt, Cpx, Pl, Opx (Amp) *Spl, Ky, Spr, Rt, Ilm*
DS157/20G	DS157		
DS157/20D	DS157	garnet clinopyroxenites (GPYR)	Grt, Cpx (Opx, Pl, Amp) *Ky, Spl, Spr, Rt, Ilm, Po, Ccp, Pn*
DS151/20A	DS151		
DS156/20B	DS156	peridotites (PER)	Grt, Ol (Cpx, Opx, Spl, Pl) *Pn, Po, Mag*
DS163/20A	DS163		
	St. Leonhard granulite massif		
DS159/20A	DS159	peridotite (PER)	Grt, Ol (Cpx, Opx, Spl, Pl) *Pn, Po, Mag*

2 Whole-rock geochemistry

Major-element data for all studied samples are given in Table IV. 2 and trace-element analyses in Table IV. 3.

2.1 Felsic and intermediate granulites

Major elements

In the R_1–R_2 classification diagram for plutonic rocks (De la Roche et al. 1980), all samples fall in the granodiorite field, with the felsic granulite plotting near the border between granite and granodiorite (Figure IV. 1a). In the P–Q diagram (Debon & Le Fort 1983, 1988), felsic granulite falls on the border between granodiorite and adamellite (= monzogranite), whereas the intermediate granulites correspond to granodiorite (DS153/20A) or tonalite (DS155/20A)

(Figure IV. 1b). The samples are silicic (F-Gr: SiO_2 = 74.73 wt. %, I-Gr: SiO_2 = 67.68 and 70.12 wt. %, Table IV. 2) and strongly to slightly peraluminous (F-Gr: A/CNK = 1.22, I-Gr: A/CNK ~ 1.12: Figure IV. 1c). In the felsic granulite, both alkalis are present in similar proportions (K_2O/Na_2O = 1.02 by weight), while the intermediate types are sodic (K_2O/Na_2O = 0.45 and 0.93). Iron prevails strongly over Mg (F-Gr: FeOt = 2.09 wt. %, MgO = 0.36 wt. %, mg# = 23.5; I-Gr: FeOt = 4.51 and 4.82 wt. %, MgO = 0.97 and 1.36 wt. %, mg# = 27.7 and 33.5).

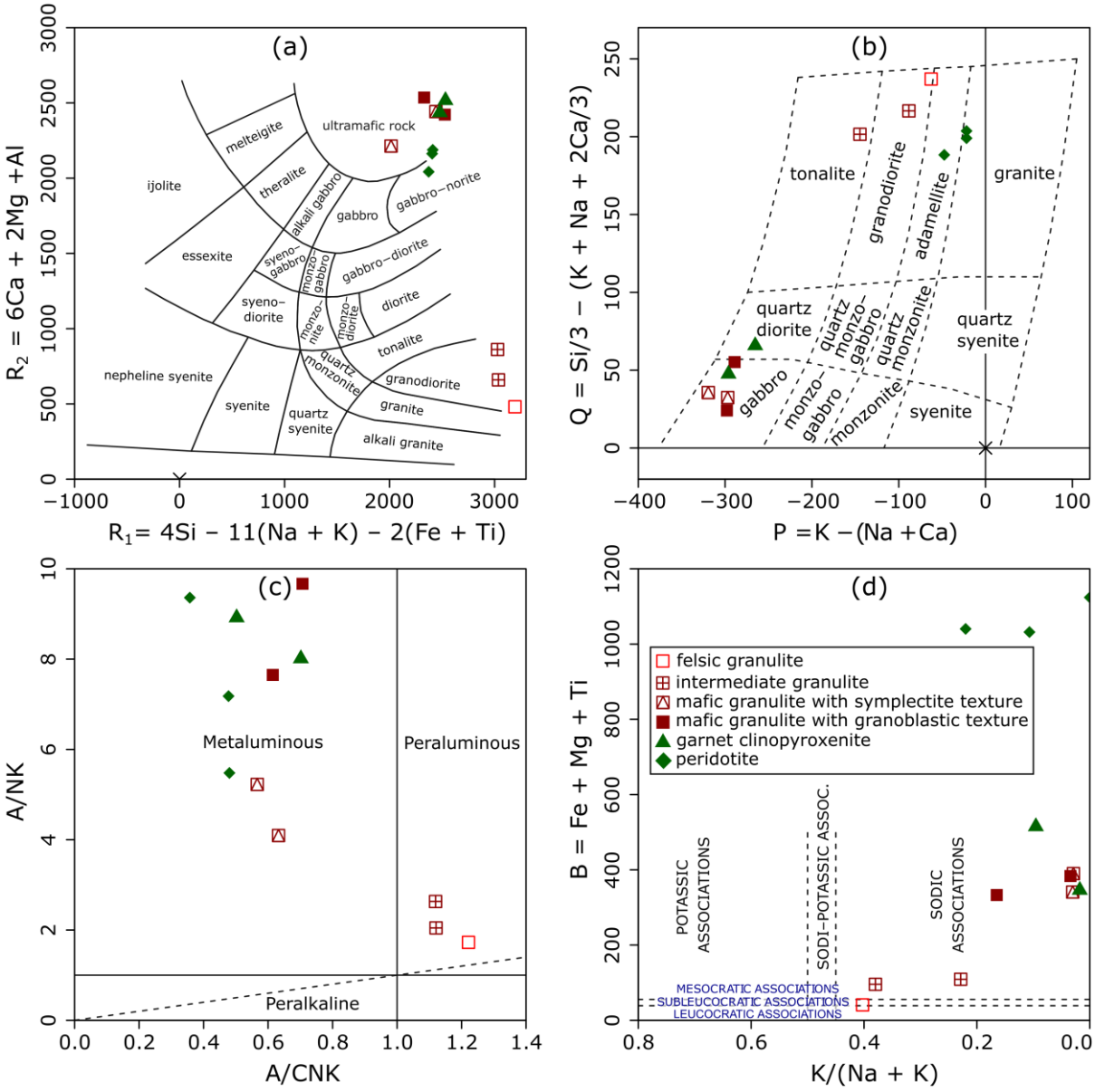

Figure IV. 1: Multicationic classification R1–R2 diagram for plutonic rocks after De la Roche et al. (1980). b) Multicationic P–Q diagram for plutonic rocks after Debon & Le Fort (1983, 1988). c) A/CNK vs. A/NK diagram after Shand (1943). d) Multicationic K/(Na + K) vs. B diagram after Debon & Le Fort (1983, 1988).

According to the maficity (B = Fe + Mg + Ti) versus K/(K + Na) diagram (Figure IV. 1d), both lithologies correspond to sodic associations, whereby the felsic granulite has subleucocratic and intermediate granulites have mesocratic mineral assemblages.

Trace elements

Trace elements for both lithologies were plotted on spider plots normalized to the average bulk continental crust (Taylor & McLennan 1995; Figure IV. 2a, b). In the case of felsic granulite, most normalized contents are lower than unity, except for Rb, Ba, K, Y and HREE (a). Many of the elements even show contents below their respective detection limits. Still it can be inferred that the trace-element pattern is characterised by conspicuous troughs in Cs, Th, U, Nb (and Ta). A similar feature is also visible in Sr and Ti.

Compared to the felsic granulite, intermediate granulites (Figure IV. 2b) are richer in many trace elements, except for HREE and Y, especially in the medium-grained, Bt-rich sample DS155/20A. In this sample is also significant relative depletion in Cs, Th and U, but Cs is at the detection limit. Similar drop is also visible in Nb and Ta. The fine-grained sample with almost no Bt (DS153/20A) shows a strong depletion in Cs, Th, U, Nb, Ta, Sr, and a smaller decrease in Ti. Overall, the Bt-rich granulite (DS155/20A) is poorer at Th, all REE, Zr and Hf than the Bt-poor one (DS153/20A).

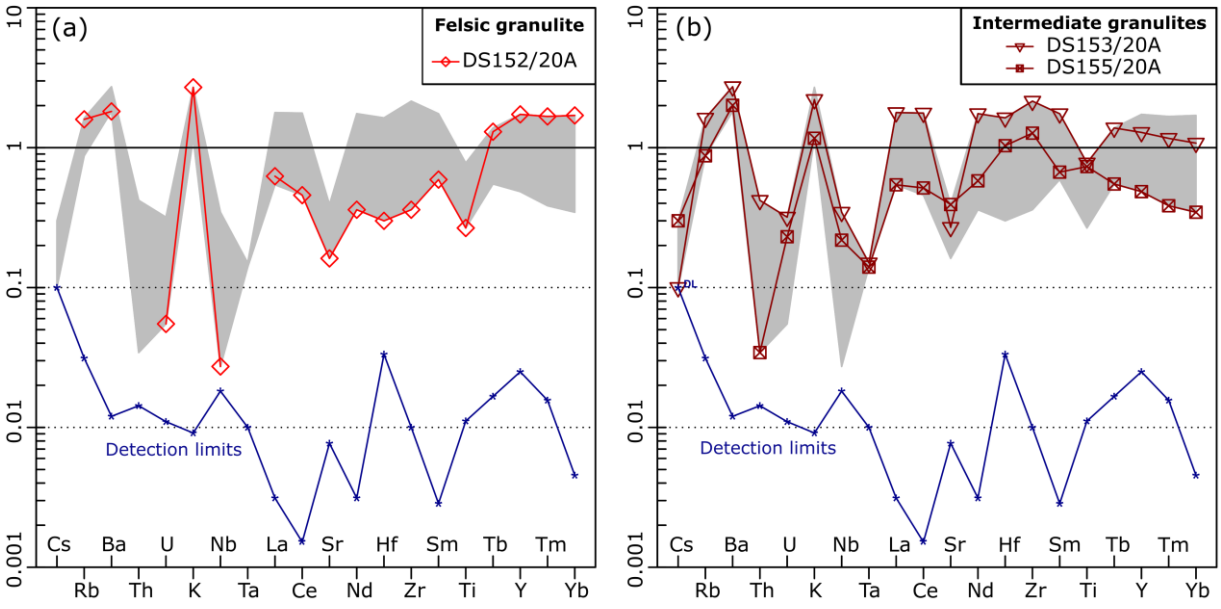

Figure IV. 2: Spider plots normalized to the average bulk continental crust after Taylor & McLennan (1995) for a) felsic granulite and b) intermediate granulites. Gray field corresponds to the total variation in the dataset.

Chondrite-normalized (Boynton 1984) REE pattern for the felsic granulite (Figure IV. 3a) is flat (La_N/Yb_N = 1.80), with a weak enrichment in the lightest REE and strong negative Eu anomaly (Eu/Eu* = 0.42, Eu* = $\sqrt{Sm_N Gd_N}$). The sum of REE is relatively high, 54.4 ppm.

The patterns of the two intermediate granulites (Figure IV. 3b) are mostly mutually comparable, being characterized by moderate LREE/HREE enrichment (La_N/Yb_N = 7.70 and 8.11). Both samples, however, distinctly differ in the character of Eu anomaly, which is negative in the Bt-poor sample (DS153/20A; Eu/Eu* = 0.55), and positive in the Bt-rich sample (DS155/20A; Eu/Eu* = 1.60). The totals of REE are significantly higher in Bt-poor, fine-grained sample (DS153/20A) compared to the Bt-rich, medium-grained sample (DS155/20A; 146.8 vs 47.4 ppm).

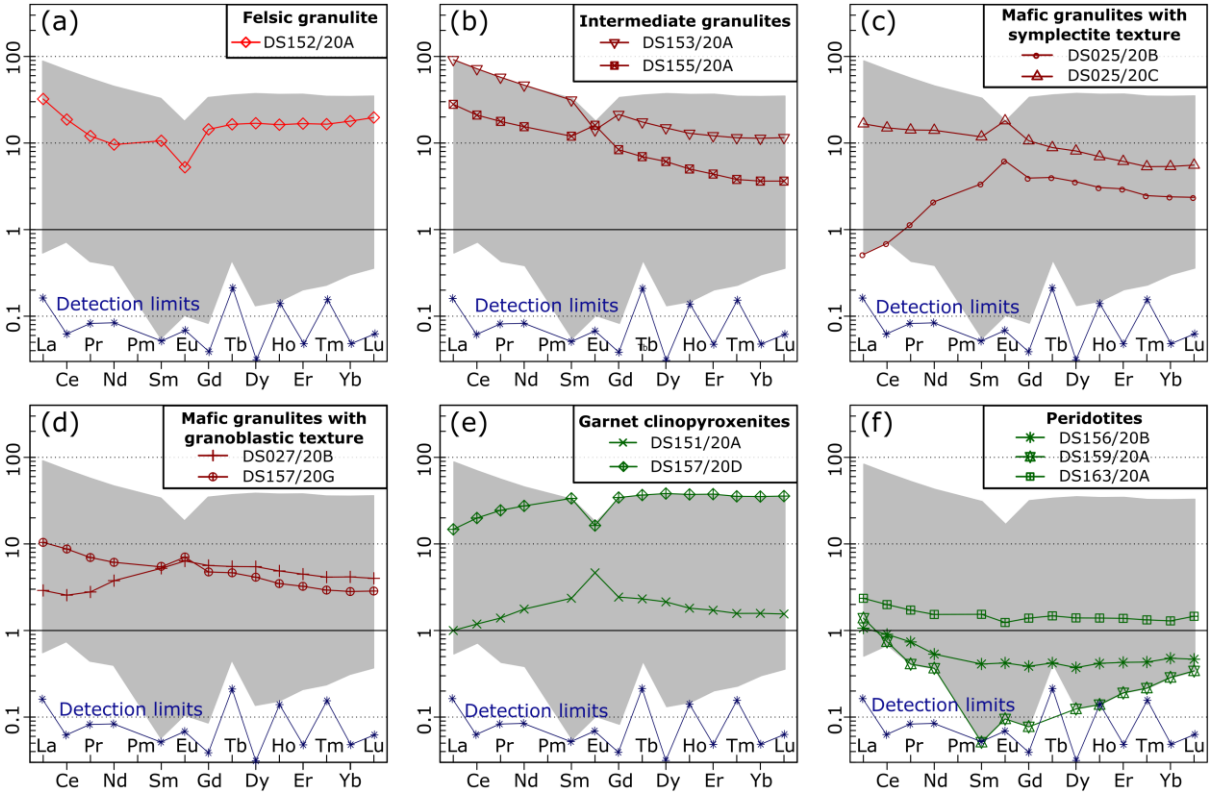

Figure IV. 3: Spider plots normalized to chondrite composition after Boynton (1984) for a) felsic granulite, b) intermediate granulites, c) mafic granulites with symplectite texture, d) mafic granulites with granoblastic texture, e) garnet clinopyroxenites, and f) peridotites.

Table IV. 2: Whole-rock major-element data for studied samples (in wt. %)

Sample	DS152/20A	DS153/20A	DS155/20A	DS025/20B	DS025/20C	DS027/20B	DS157/20G	DS151/20A	DS157/20D	DS156/20B	DS163/20A	DS159/20A
Lithology	F-GR	I-Gr	I-Gr	M-Gr(S)	M-Gr(S)	M-Gr(G)	M-Gr(G)	GPYR	GPYR	PER	PER	PER
SiO_2	74.73	70.12	67.38	49.06	46.94	47.65	44.38	47.24	46.15	38.83	40.34	39.44
TiO_2	0.24	0.70	0.66	0.33	0.99	0.42	0.37	0.26	0.22	0.02	0.13	0.09
Al_2O_3	13.74	14.11	15.94	16.84	16.85	16.94	20.95	19.59	13.14	1.06	2.22	0.77
Fe_2O_3	0.93	1.56	1.43	1.39	2.11	1.73	1.57	2.11	2.73	4.21	3.75	3.31
FeO	1.25	3.11	3.53	3.10	5.21	4.11	3.92	2.85	5.34	2.69	3.43	4.01
MgO	0.36	0.97	1.36	11.13	11.23	12.06	10.24	11.15	16.27	38.28	37.70	41.33
MnO	0.081	0.063	0.071	0.125	0.184	0.157	0.101	0.085	0.230	0.104	0.100	0.117
CaO	1.81	3.13	4.50	14.58	12.39	13.94	15.11	14.01	13.57	1.14	2.32	1.14
SrO	< 0.005	0.006	0.009	0.020	0.019	0.015	0.024	0.013	0.012	<0.005	< 0.005	<0.005
BaO	0.057	0.073	0.060	< 0.005	< 0.005	< 0.005	< 0.005	< 0.005	<0.005	<0.005	< 0.005	<0.005
Li_2O	0.002	0.008	0.006	< 0.001	0.001	0.002	0.006	< 0.001	0.003	<0.001	0.002	0.001
Na_2O	2.89	2.60	2.84	1.90	2.43	1.30	1.10	1.46	0.81	0.07	0.22	0.05
K_2O	2.96	2.42	1.28	0.09	0.11	0.07	0.33	0.04	0.13	0.03	0.04	<0.01
P_2O_5	0.028	0.100	0.185	0.006	0.080	0.017	0.011	0.007	0.040	<0.005	0.012	<0.005
F	0.022	0.036	0.036	0.044	0.040	0.039	0.035	0.029	0.018	0.058	0.022	0.090
CO_2	< 0.01	0.01	0.04	0.04	0.22	0.06	< 0.01	< 0.01	0.03	0.33	0.38	0.22
C	0.015	0.026	0.011	0.064	0.064	0.049	< 0.005	0.039	0.047	0.131	0.021	0.111
S	< 0.010	0.026	0.043	< 0.010	0.032	< 0.010	0.109	0.018	<0.010	<0.010	0.036	<0.010
H_2O^+	< 0.05	0.15	0.43	0.37	0.54	0.49	0.85	0.24	0.56	11.82	8.22	8.48
H_2O^-	< 0.05	< 0.05	0.07	0.05	< 0.05	0.05	0.05	0.06	0.08	0.50	0.20	0.32
F.eq	–0.009	–0.015	–0.015	–0.019	–0.017	–0.016	–0.015	–0.012	–0.008	–0.024	–0.009	–0.038
S.eq	–0.001	–0.007	–0.011	0.000	–0.008	–0.001	–0.027	–0.004	–0.001	0.000	–0.009	–0.001
Total	99.11	99.19	99.84	99.13	99.42	99.08	99.12	99.18	99.37	99.24	99.12	99.45
mg#	23.52	27.70	33.48	82.02	73.80	79.14	77.39	80.72	78.81	91.33	90.81	91.34
A/CNK	1.22	1.12	1.12	0.57	0.63	0.61	0.71	0.70	0.50	0.48	0.48	0.36
K_2O/Na_2O	1.02	0.93	0.45	0.05	0.05	0.05	0.30	0.03	0.16	0.43	0.18	–

Table IV. 3: Whole-rock trace-element data for studied samples (in ppm)

Sample	DS152/20A	DS153/20A	DS155/20A	DS025/20B	DS025/20C	DS027/20B	DS157/20G	DS157/20D	DS151/20A	DS156/20B	DS163/20A	DS159/20A
Lithology	F-GR	I-Gr	I-Gr	M-Gr(S)	M-Gr(S)	M-Gr(G)	M-Gr(G)	GPYR	GPYR	PER	PER	PER
Li	6.7	26.1	27.8	2.3	7.3	15.8	26.6	7.6	1.9	1.8	2.2	1.8
Rb	51	52	28	1	2	1	13	6	1	1	1	< 1
Cs	< 0.1	0.1	0.3	0.1	1.0	0.3	0.5	1.0	< 0.1	0.1	< 0.1	< 0.1
Sr	42	70	102	171	183	143	226	101	146	5	13	2
Ba	454	682	502	17	42	17	27	39	6	14	12	4
Nb	0.3	3.8	2.4	< 0.2	1.8	< 0.2	0.6	0.5	< 0.2	< 0.2	< 0.2	< 0.2
Ta	< 0.01	0.15	0.14	0.01	0.13	0.01	0.16	< 0.01	< 0.01	0.02	0.01	0.04
Zr	36	215	127	6	58	8	19	53	6	2	3	1
Hf	0.9	4.9	3.1	0.3	1.4	0.4	0.6	1.5	0.2	< 0.1	0.1	< 0.1
Ga	16	19	19	13	16	12	15	8	12	1	3	1
In	< 0.1	0.1	< 0.1	< 0.1	0.1	< 0.1	< 0.1	0.1	< 0.1	< 0.1	< 0.1	< 0.1
Tl	0.20	0.19	0.08	< 0.05	< 0.05	< 0.05	< 0.05	< 0.05	< 0.05	< 0.05	< 0.05	< 0.05
Th	< 0.05	1.47	0.12	0.07	0.76	0.27	1.85	1.05	< 0.05	0.08	0.05	0.13
U	0.05	0.29	0.21	0.04	0.39	0.17	0.35	0.39	0.01	0.03	0.04	0.04
Cr	< 20	< 20	20	590	330	490	480	620	690	2330	2220	2740
Mo	< 0.1	< 0.1	0.4	< 0.1	< 0.1	< 0.1	< 0.1	0.3	< 0.1	0.4	< 0.1	0.4
W	< 0.1	< 0.1	< 0.1	< 0.1	< 0.1	0.1	0.1	0.2	< 0.1	0.2	< 0.1	0.1
Ni	< 20	< 20	< 20	110	< 20	160	120	290	300	2120	2230	2490
Co	2	7	8	31	35	39	37	56	44	98	98	115
V	15	59	63	264	297	223	123	189	95	38	66	41
Sc	12.0	16.0	13.0	42.0	39.0	44.0	33.0	< 0.1	20.0	< 0.1	14.0	< 0.1
Pb	0.9	0.2	< 0.1	< 0.1	2.3	1.7	1.4	2.2	0.1	0.4	< 0.1	0.2
Cu	< 10	< 10	< 10	< 10	30	10	130	< 10	60	10	30	< 10

Table IV. 3 (continued): Whole-rock trace-element data for studied samples (in ppm)

Sample	DS152/20A	DS153/20A	DS155/20A	DS025/20B	DS025/20C	DS027/20B	DS157/20G	DS157/20D	DS151/20A	DS156/20B	DS163/20A	DS159/20A
Lithology	F-GR	I-Gr	I-Gr	M-Gr	M-Gr(S)	M-Gr(S)	M-Gr(G)	GPYR	GPYR	PER	PER	PER
Zn	< 30	60	60	< 30	50	< 30	30	110	< 30	40	50	50
Ge	1.5	1.5	1.4	1.5	1.4	1.4	1.2	2.2	1.1	0.9	0.7	0.8
Sn	0.2	< 0.1	0.3	< 0.1	1.3	0.2	0.9	1.4	0.1	< 0.1	0.2	< 0.1
As	< 1	< 1	< 1	< 1	< 1	< 1	< 1	2	< 1	< 1	< 1	< 1
Sb	< 0.2	< 0.2	< 0.2	< 0.2	< 0.2	< 0.2	< 0.2	< 0.2	0.7	< 0.2	< 0.2	< 0.2
La	10.00	28.50	8.68	0.16	5.17	0.90	3.23	4.57	0.31	0.33	0.73	0.43
Ce	15.10	58.30	17.00	0.56	12.10	2.07	7.06	16.10	0.96	0.73	1.61	0.60
Pr	1.47	7.02	2.17	0.14	1.73	0.34	0.85	2.98	0.17	0.09	0.21	0.05
Nd	5.76	28.00	9.27	1.26	8.43	2.26	3.68	16.50	1.06	0.32	0.92	0.22
Sm	2.07	6.12	2.34	0.66	2.30	1.02	1.06	6.55	0.46	0.08	0.30	0.01
Eu	0.386	1.040	1.180	0.458	1.330	0.467	0.517	1.200	0.341	0.031	0.091	0.007
Gd	3.73	5.54	2.17	1.02	2.75	1.46	1.23	8.90	0.63	0.10	0.36	0.02
Tb	0.78	0.83	0.33	0.19	0.42	0.26	0.22	1.74	0.11	0.02	0.07	< 0.01
Dy	5.45	4.82	1.97	1.15	2.61	1.76	1.33	12.30	0.69	0.12	0.45	0.04
Ho	1.17	0.93	0.36	0.22	0.50	0.35	0.25	2.68	0.13	0.03	0.10	0.01
Er	3.52	2.55	0.92	0.62	1.29	0.94	0.68	7.89	0.36	0.09	0.29	0.04
Tm	0.535	0.373	0.123	0.080	0.173	0.134	0.095	1.150	0.051	0.014	0.043	0.007
Yb	3.74	2.37	0.76	0.50	1.12	0.87	0.59	7.38	0.33	0.10	0.27	0.06
Lu	0.635	0.372	0.117	0.076	0.179	0.129	0.092	1.150	0.050	0.015	0.047	0.011
Y	34.6	25.7	9.7	5.9	13.5	9.4	7.1	83.4	3.8	0.8	2.6	< 0.5
Eu/Eu*	0.42	0.55	1.60	1.71	1.62	1.17	1.38	0.48	1.94	1.06	0.85	1.51
La_N/Yb_N	1.80	8.11	7.70	0.22	3.11	0.70	3.69	0.42	0.63	2.22	1.82	4.83
ΣREE	54.35	146.77	47.39	7.09	40.10	12.96	20.88	91.09	5.65	2.07	5.49	1.51

2.2 Mafic granulites and garnet clinopyroxenites

Major elements

In the R_1–R_2 classification diagram, all these samples fit to the field of ultramafic rocks (Figure IV. 1a). In the multicationic P–Q diagram, which, however, does not distinguish ultramafic compositions, nearly all mafic granulite samples correspond to gabbro, except a single mafic granulite with granoblastic texture (DS027/20B) that classifies as quartz diorite (Figure IV. 1b). The range of SiO_2 contents is broad (44.38–49.06 wt. %) for the mafic granulites but is more restricted (46.15–47.24 wt. %) for the garnet clinopyroxenites (Table IV. 2). All samples are metaluminous (M-Gr: A/CNK = 0.57–0.71; GP: 0.50–0.70 – Figure IV. 1c). The K_2O/Na_2O ratios are always much lower than unity (M-Gr: 0.05–0.30; GPYR: 0.03–0.16). The samples are Mg-rich (M-Gr: FeOt = 4.35–7.11 wt. %, MgO = 10.24–12.06 wt. %, mg# = 73.80–82.02; GPYR: FeOt = 4.75–7.80 wt. %, MgO = 11.15–16.27 wt. %, mg# = 78.8–80.7). According to the B (B = Fe + Mg + Ti) versus K/(K + Na) diagram, both lithologies correspond to mesocratic and sodic associations (Figure IV. 1d).

Trace elements

In spider plots normalized to the average primitive mantle (Sun & McDonough 1989), all mafic granulites show similar patterns for the most compatible elements (from Ti to Lu) with a smooth decrease towards Lu (Figure IV. 4a, b). All samples are enriched relative to the primitive mantle, except the one with the symplectite texture (DS025/20B), which shows depletion in Nb and Ta (below and at the detection limit, respectively), LREE, P, and Zr (Figure IV. 4a). Moreover, this sample displays enrichment in alkalis (Cs, Rb, K) and alkali earth elements (Ba and Sr), as well as troughs in Nb, Ta and P. The other symplectite-bearing sample (DS025/20C) has the highest normalized contents of nearly all elements among mafic granulites. It is characterized by relative depletion in Rb, Nb, Ta and P and enrichment in Cs, Th, U, and Pb. Mafic granulite with transition between granoblastic and symplectite texture (DS157/20G) has a pattern with peaks in Cs–Rb, Th–U, K, Pb, Sr and Li, as well as significant troughs in Ba, Nb, and P. The remaining sample with granoblastic texture (DS027/20B) shows strong negative anomaly in Nb–Ta (considering that both elements are close to, or below their respective detection limits) and Zr–Hf, as well as peaks in Cs, U, K, Pb, Sr and Li (Figure IV. 4b).

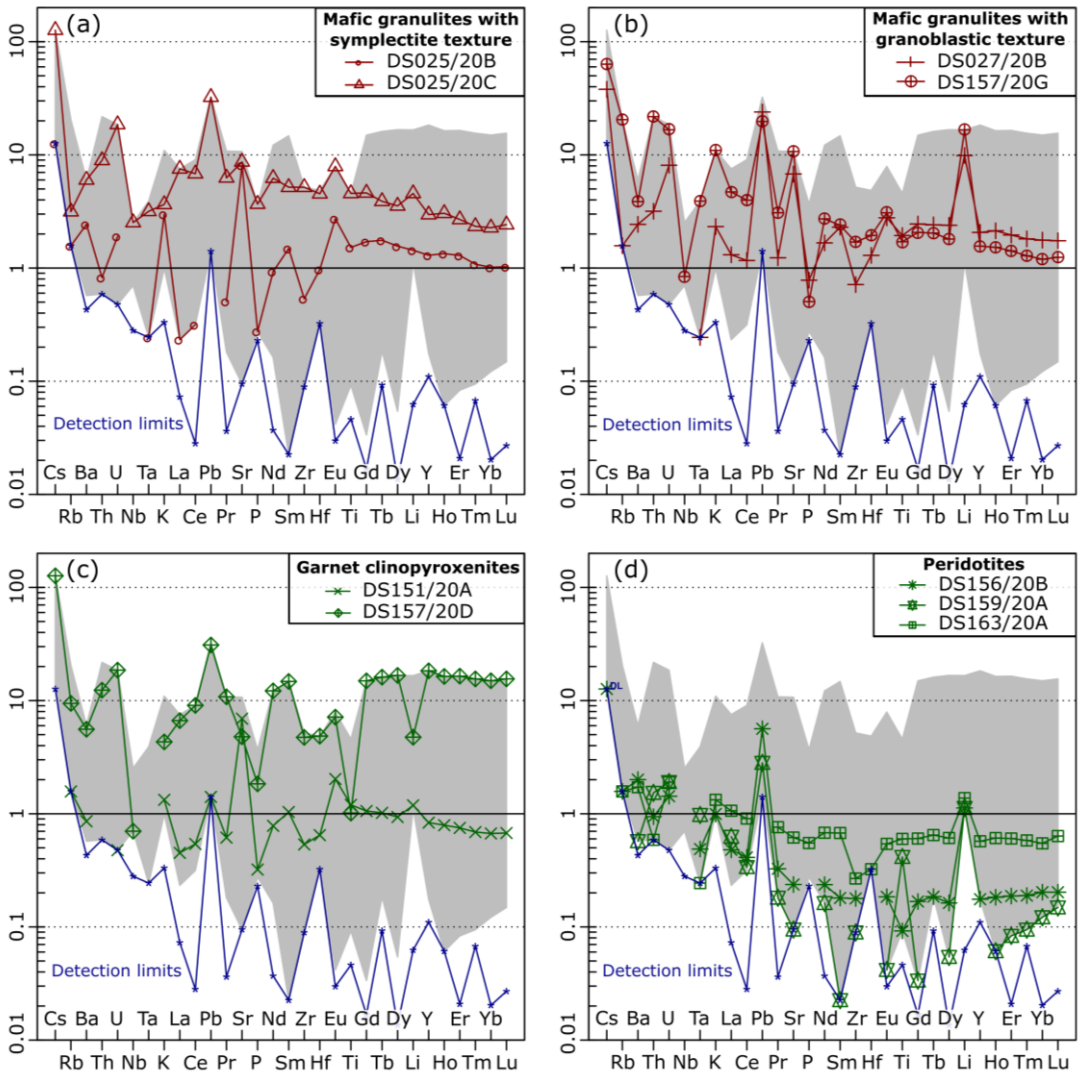

Figure IV. 4: Spider plots normalized to the primitive mantle after Sun & McDonough (1989) for a) mafic granulites with symplectite texture, b) mafic granulites with granoblastic texture, c) garnet clinopyroxenites, and d) peridotites. Gray field portrays the total variation in the dataset.

Chondrite-normalized REE patterns of mafic granulites (Figure IV. 3c, d) are similar to each other, being characterized by low degree of LREE/HREE enrichment (La_N/Yb_N = 0.22–3.69) and variable positive Eu anomalies (Eu/Eu* = 1.17–1.71). Interestingly, the REE patterns of the samples DS025/20B and DS027/20B are convex upward (La_N/Yb_N = 0.22 and 0.70). The pattern of sample with granoblastic texture (DS027/20B) differs in lower LREE contents compared to other mafic granulite samples. The REE sums range 7.09–40.10 ppm.

In primitive-mantle-normalized spiderplot (Figure IV. 4c), both garnet clinopyroxenites show contrasting patterns. The well-preserved garnet clinopyroxenite with granoblastic texture (DS157/20D) displays higher contents of all elements except Sr and Ti, where both patterns

converge. In this sample are significant troughs in Nb–Ta, P, Ti and Li. Some depletion is also seen in Rb, Ba, K, Zr and Hf, while Cs and Pb form peaks compared to the adjacent elements. The sample with local symplectite (DS151/20A) features a significant peak of Sr. Slight decreases are visible for P and Zr with Hf. Many incompatible elements are below their respective detection limits. From Eu to Lu is the pattern characterized by a smooth decrease.

The well-preserved garnet clinopyroxenite (DS157/20D) has much higher total REE contents (91.09 ppm) than the symplectite-bearing sample (DS151/20A: 5.65 ppm; Figure IV. 3e). Still, the overall trend of both samples is similar, being gently upward curved in the central part. The La_N/Yb_N ratios are 0.42 and 0.63. In the better preserved sample (DS157/20D), the HREE segment is subhorizontal, while in the symplectite-bearing sample (DS151/20A), a smooth decrease is seen. However, the character of Eu anomaly is opposite, distinctly negative vs. distinctly positive (Eu/Eu* = 0.42 in DS157/20D vs. 1.94 in DS151/20A).

2.3 Peridotites

In the R_1–R_2 classification diagram, samples DS159/20A (from St. Leonhard massif) and DS163/20 correspond to ultramafic rocks and DS156/20B to gabbro-norite (Figure IV. 1a). All are ultrabasic (SiO_2 = 38.83–40.34 wt. %; Table IV. 2). Magnesium prevails strongly over iron (FeOt = 6.48–6.99 wt. %, MgO = 37.70–41.33 wt. %, mg# = 90.81–91.34). Based on the MgO/SiO_2 vs. Al_2O_3/SiO_2 diagram (Paulick et al., 2006; Figure IV. 5), samples DS159/20A and DS163/20B are more depleted than DS163/20A. All fall onto Mantle Array, explained as reflecting the successive magmatic depletion of an original primitive mantle.

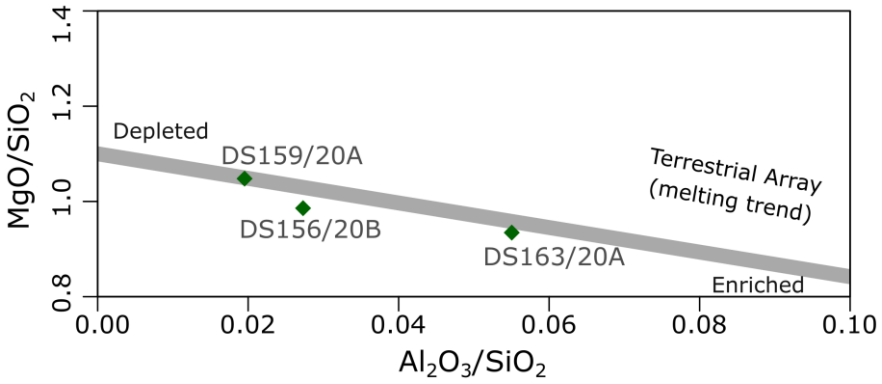

Figure IV. 5: The Al_2O_3/SiO_2 versus MgO/SiO_2 diagram for mantle peridotites of Paulick et al. (2006) assessing the degree of their depletion/enrichment.

Trace elements

Compared to the canonical primitive mantle reservoir, the studied peridotites are mostly variably depleted, except for the most incompatible elements (alkalis, Th, U) and Pb (Figure IV. 4d). Unfortunately, the contents of many trace elements approach, or fall below, their respective detection limits, so their interpretation is difficult. In any case, the patterns of individual peridotite samples do differ. That of the sample DS163/20A is characterized by troughs in Th, (Nb), Ta, Zr and Hf, whereby Th and Ta are near and Nb below the detection limit. The sample DS156/20B shows a significant peaks in Pb and Li, and relatively small troughs in Th, Nb, (Ta) and Ti. The pattern of sample DS159/20A (most pristine peridotite, from St. Leonhard massif) is jagged and discontinuous, as concentrations of many elements approach, or are lower than, the detection limits. With some degree of certainty we can distinguish only conspicuous peaks in Pb, Hf and Ti.

Sample DS163/20A has higher chondrite-normalized REE contents than the other two (Figure IV. 3f), always slightly exceeding unity. The overall shape of REE patterns for Dunkelsteiner Wald peridotites (DS163/20A, DS156/20B) is comparable, flat, being characterized by a slight decrease of LREE and subhorizontal HREE segment (La_N/Yb_N = 1.82 and 4.83, respectively). They show a small negative (DS163/20A; Eu/Eu* = 0.85) to negligible (DS156/20B; Eu/Eu* = 1.06) Eu anomalies. St. Leonhard peridotite (DS159/20A) is characterized by the lowest normalized REE contents except La. The LREE pattern is convex-down, strongly depleted in MREE. The HREE segment is characterized by a steady increase from Gd to Lu. There seems a distinct positive Eu anomaly (Eu/Eu* = 1.51), but this may be an artefact that can be attributed to concentrations approaching detection limits.

2.4 Sr–Nd isotopes

Whole-rock Sr and Nd isotopic data were recalculated to 340 Ma (Table IV. 4), which is the well-established age of high-grade metamorphism in the HP–HT metaigneous lithologies in the Gföhl Unit (Friedl et al., 2011 and references therein). Overall, the data show a broad range of initial Sr isotopic compositions ($^{87}Sr/^{86}Sr_{340}$ = 0.7030–0.7183) as well as of epsilon Nd values (εNd_{340} = +6.83 to –7.54).

Felsic and intermediate granulites have continental crust-like Sr and Nd isotopic compositions ($^{87}Sr/^{86}Sr_{340}$ = 0.70917–0.71827, εNd_{340} = –7.12 to –7.54). Indeed their late Palaeoproterozoic

two-stage Nd model ages (T^{DM}.2stg) of 1.61–1.64 Ga (Figure IV. 6a) point to a long mean crustal residence of their source materials.

Mafic granulites yield rather narrow range of Sr isotopic data ($^{87}Sr/^{86}Sr_{340}$ = 0.70429–0.70638), but differ strikingly in Nd isotopic compositions (εNd_{340} = +6.56 to –2.33). Accordingly, two-stage Nd model ages vary broadly (T^{DM}.2stg = 0.54–1.24 Ga, i.e. Neo- to Mesoproterozoic). However, the Sr isotopic composition of the sample DS025/20B with the most radiogenic Nd could not be measured as the sample was not sufficiently fresh.

The two garnet clinopyroxenites differ both in Sr ($^{87}Sr/^{86}Sr_{340}$ = 0.70296 vs. 0.70836) and Nd (εNd_{340} = +6.83 vs. –5.20) isotopic compositions. The three peridotites have unradiogenic Nd, significantly lower than CHUR (εNd_{340} = –1.74 to –3.95).

Table IV. 4: Sr–Nd isotopic data for studied lithologies

Sample	Lithology	Rb (ppm)	Sr (ppm)	$^{87}Rb/^{86}Sr$	$^{87}Sr/^{86}Sr$	$^{87}Sr/^{86}Sr_{340}$	Sm (ppm)	Nd (ppm)	$^{147}Sm/^{144}Nd$	$^{143}Nd/^{144}Nd$	$^{143}Nd/^{144}Nd_{340}$	εNd_{340}	T^{DM}	T^{DM}.2stg
DS152/20A	F-Gr	51	42	2.68900	0.731283(10)	0.71827	2.07	5.76	0.21725	0.512319(07)	0.51184	–7.12	59.47	1.61
DS153/20A	I-Gr	52	70	1.70789	0.720688(09)	0.71242	6.12	28.00	0.13213	0.512108(08)	0.51181	–7.54	1.83	1.64
DS155/20A	I-Gr	28	102	0.69979	0.712558(09)	0.70917	2.34	9.27	0.15259	0.512168(11)	0.51183	–7.26	2.25	1.62
DS025/20B	M-Gr(S)	–	–	–	–	–	0.66	1.26	0.31673	0.513241(10)	0.51254	+6.56	0.14	0.54
DS025/20C	M-Gr(S)	2	183	0.03508	0.706551(08)	0.70638	2.30	8.43	0.16494	0.512448(06)	0.51208	–2.33	1.98	1.24
DS027/20B	M-Gr(G)	1	143	0.02079	0.704392(08)	0.70429	1.02	2.26	0.27288	0.512902(06)	0.51230	+1.84	-0.71	0.91
DS157/20G	M-Gr(G)	13	226	0.15518	0.705355(08)	0.70460	1.06	3.68	0.17414	0.512590(07)	0.51220	+0.04	1.90	1.05
DS157/20D	GPYR	6	101	0.18394	0.709249(08)	0.70836	6.55	16.5	0.23999	0.512468(08)	0.51193	–5.20	–	–
DS151/20A	GPYR	1	146	0.01205	0.703017(04)	0.70296	0.46	1.06	0.26239	0.513134(08)	0.51255	+6.83	–	–
DS156/20B	PER	–	–	–	–	–	0.08	0.32	0.15113	0.512346(18)	0.51201	–3.72	–	–
DS163/20A	PER	–	–	–	–	–	0.30	0.92	0.19714	0.512550(11)	0.51211	–1.74	–	–
DS159/20A	PER	–	–	–	–	–	0.01	0.22	0.02748	0.512059(28)	0.51200	–3.95	–	–

Lithologies: F-Gr: felsic granulite, I-Gr: intermediate granulite, M-Gr(S): mafic granulite with symplectite texture, M-Gr(G): mafic granulite with granoblastic texture, GPYR: garnet clinopyroxenite, PER: peridotite.

T^{DM}: single-stage Nd model ages (Ga), using the Depleted Mantle parameters of Liew and Hofmann (1988). T^{DM}.2stg: two-stage Depleted Mantle Nd model ages (Ga) calculated after Liew and Hofmann (1988). –: not analysed. Subscripts '340' indicate age-corrected isotopic ratios/epsilon Nd values. In brackets after the measured radiogenic isotope ratios are 2 s.e. on the last decimal place.

3 Discussion

3.1 Sr–Nd isotopic evidence for open-system behaviour

The Sr–Nd isotopic compositions were investigated in order to characterize the likely sources for the studied lithologies and to assess the potential role of open-system processes (e.g., assimilation or hybridization) in their genesis. In particular, we were interested in testing whether mafic and intermediate granulites could represent variable mixtures of continental crust- and mantle-derived material.

In this respect, the $^{87}Sr/^{86}Sr_{340}$ vs. εNd_{340} diagram represents the most powerful tool; this projection is resistant to any subsequent modification by fractional crystallization or crystal accumulation processes (Faure & Mensing, 2004; Janoušek et al., 2016). In our case (Figure IV. 6b), the three analyses of felsic and intermediate granulites clearly correspond to mature crustal rocks (e.g. Faure & Mensing, 2004; Dickin, 2005), even though intermediate granulites show lower $^{87}Sr/^{86}Sr_{340}$. Mafic granulites form a sequence, whereby the samples with granoblastic matrix require a slightly depleted (DS027/20B) or CHUR-like mantle source (DS157/20G). The sample of symplectite-bearing mafic granulite with high amounts of Amp and Ti-oxides (DS025/20C) has the most radiogenic Sr and unradiogenic Nd, pointing to a substantial crustal involvement.

The symplectite-bearing garnet clinopyroxenite DS151/20A clearly requires a derivation from a depleted-mantle source, but, again, the sample with well-preserved granoblastic texture and rich in melt/fluid inclusions (DS157/20D) apparently contains a high proportion of the crustal component, resembling already the intermediate granulites. Unfortunately, our peridotites were too serpentinized to obtain reliable Sr isotopic analyses.

Taken together, all the lithologies studied define approximately a hyperbolic trend in the $^{87}Sr/^{86}Sr_{340}$ vs. εNd_{340} space connecting the crustally-derived felsic granulite DS152/20A with mantle-derived symplectite-bearing garnet clinopyroxenite DS151/20A (Figure IV. 6b). Such a hyperbola, however, does not differ much from an alternative one assuming a garnet lherzolite DW241 (Becker, 1996b) as a mafic end-member (Figure IV. 6b). Still, the latter hyperbola is less curved and the model seems significantly more sensitive to even small degrees of crustal contamination.

Additional petrogenetic insight could provide plots of an independent geochemical parameter vs. Sr or Nd isotopic signatures. In the current case, selected binary plots can not only distinguish between the mixing trends involving garnet clinopyroxenite or peridotite, but

also suggest what could have been the mechanism of their interaction with the crustal component. For instance, mantle metasomatism by continental crust-derived fluids should lead to an increase in $^{87}Sr/^{86}Sr_{340}$ and decrease in εNd_{340} but without any substantial change in CaO or MgO due to generally low CaO and MgO contents in the felsic continental crust and melts/fluids derived therefrom (Becker, 1996a). On the other hand, the mixing of two lithologies (or their melts) with non-negligible elemental concentrations would lead to a strongly curved hyperbolic rather than nearly linear trend.

In Figure IV. 6c–d are shown correlations of $^{87}Sr/^{86}Sr_{340}$ and εNd_{340} with mg#. In these plots, the compositions of felsic granulite (DS152/20A) and garnet clinopyroxenite with local symplectite (DS151/20A) again form two end-members of a mixing hyperbola in the vicinity of which the compositions of intermediate and mafic granulites are plotted (mafic granulites closer to the garnet clinopyroxenite and intermediate granulites closer to the felsic granulite). Garnet clinopyroxenite with granoblastic texture and abundant inclusions (DS157/20D) shows Sr that is more evolved, Nd that is less radiogenic and mg# similar to the other mafic samples (Figure IV. 6c, d). In fact, this sample plots closer to the hyperbola linking the felsic granulite with garnet lherzolite DW241, as do the other peridotites (Figure IV. 6d).

Crucial information bring the CaO vs. $^{87}Sr/^{86}Sr_{340}$ and εNd_{340} plots (Figure IV. 6e–f) where the modelled trends linking garnet lherzolite DW241 with felsic granulite DS152/20A are nearly linear (due to very small contents of CaO in both endmembers). Consequently, all samples except the other peridotites fall far from this modelled trend, and therefore mixing of felsic granulite with peridotite seems unlikely. Much more relevant seems the modelled interaction between the symplectite-bearing garnet clinopyroxenite and the felsic granulite.

Assuming that the mantle and crustal end-members mixed to yield the intermediate and mafic granulites, the $^{87}Sr/^{86}Sr_{340}$ vs. εNd_{340} diagram (Figure IV. 6b) can be used to estimate the proportions of the putative end-members in the mixture. If garnet clinopyroxenite DS151/20A and felsic granulite DS152/20A are taken as end-members, the intermediate granulites would need to contain c. 15 and 30 wt. % of the mantle component and mafic granulites c. 10–30 wt. % of the crustal one, whereby the mafic granulite with symplectite texture (DS025/20C) requires the highest crustal proportion.

Based on the mg# vs. εNd_{340} and CaO vs. εNd_{340} diagrams (Figure IV. 6d, f), intermediate granulites require c. 5–15 wt. % of the mantle component, whereas mafic granulites should include up to 23 wt. % of the crustal one. According to the mg# vs. $^{87}Sr/^{86}Sr_{340}$ and CaO vs.

$^{87}Sr/^{86}Sr_{340}$ diagrams (Figure IV. 6c, e), the intermediate granulites should contain c. 13–25 wt. % of the mantle component, and mafic granulites c. 5–25 wt. % of the crustal material.

Lastly, the low εNd_{340} at practically unchanged mg# and CaO of the garnet peridotites (compared to the garnet clinopyroxenite DS151/20A and garnet lherzolite DW241) supports a late metasomatic influence by continental crust-derived melt/fluid, further evidenced by high amount of melt/fluid inclusions in our garnet clinopyroxenite DS157/20D (Figure IV. 6c–f).

Indeed, the metasomatism in the Variscan lithospheric mantle left a direct evidence in the form of phlogopite-rich veins, interpreted as a product of the reaction between mantle peridotites and granulite-derived ultrapotassic fluids (Becker et al., 1999) as well as highly potassic melt inclusions found in various mantle lithologies (Naemura et al. 2018; Borghini et al. 2020; and part I of this thesis). The Variscan metasomatized mantle domains yielded voluminous (ultra-) potassic (durbachitic) plutons scattered throughout the Moldanubian domain (Janoušek et al., 2022 and references therein).

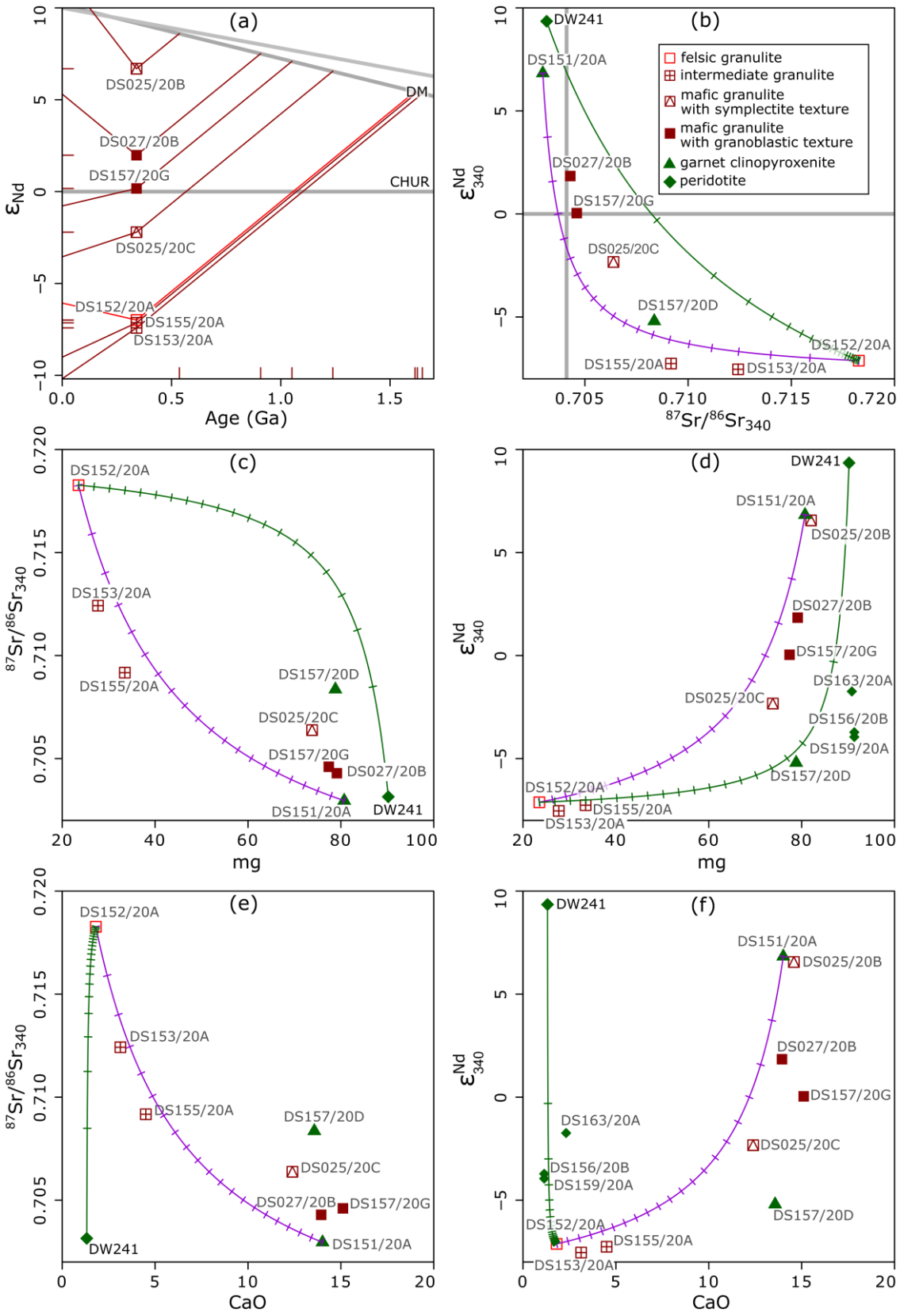

Figure IV. 6: Diagrams for Sr–Nd isotopic data: a) two-stage Nd model ages, b) $^{87}Sr/^{86}Sr_{340}$ vs. εNd_{340}, c) mg vs. $^{87}Sr/^{86}Sr_{340}$, d) mg vs. εNd_{340}, e) CaO vs. $^{87}Sr/^{86}Sr_{340}$, f) CaO vs. εNd_{340}.

3.2 Major-element mixing test

The major-element mixing test (Fourcade & Allègre, 1981) is used to test whether the rock *M* could represent a binary mixture of the two given end-members, 1 and 2. This test is based on the mass-balance equation:

$$C_M = f_1 C_1 + (1 - f_1) C_2$$

where f_1 = proportion of the end-member 1 in the mixture, C_1 = concentration of the element/oxide in the end-member 1, C_2 = concentration of the element/oxide in the end-member 2, and C_M = concentration of the element/oxide in the putative mixture.

This equation can be re-arranged to:

$$(C_M - C_2) = f_1 (C_1 - C_2)$$

Therefore, in $C_1 - C_2$ *vs.* $C_M - C_2$ diagram, the points corresponding to the individual elements/oxides should plot along a straight line of slope f_1, passing through the origin.

We have used the major-element mixing test to check whether the major-element composition of the intermediate and mafic granulite samples can represent binary mixtures between the felsic granulite and the garnet clinopyroxenite and, if so, to estimate proportions of both end-members in the individual intermediate and mafic granulite samples. In here, felsic granulite DS152/20A and garnet clinopyroxenite DS151/20A were selected as end-members based on Sr–Nd isotopic variation (Figure IV. 6). In major-element mixing tests (Figure IV. 7), all points define regression lines with intercepts close to zero and high R^2 values. This confirms that intermediate and mafic granulites could have indeed formed by the interaction of felsic granulites with garnet clinopyroxenites. Based on the mixing test, the two intermediate granulites would contain 15 and 25 wt. % of the garnet clinopyroxenite (Figure IV. 7a, b); mafic granulites are contaminated by up to c. 6 wt. % of the felsic granulite (Figure IV. 7c–e). Mafic granulite DS157/20G corresponds by its composition to the garnet clinopyroxenite (Figure IV. 7f).

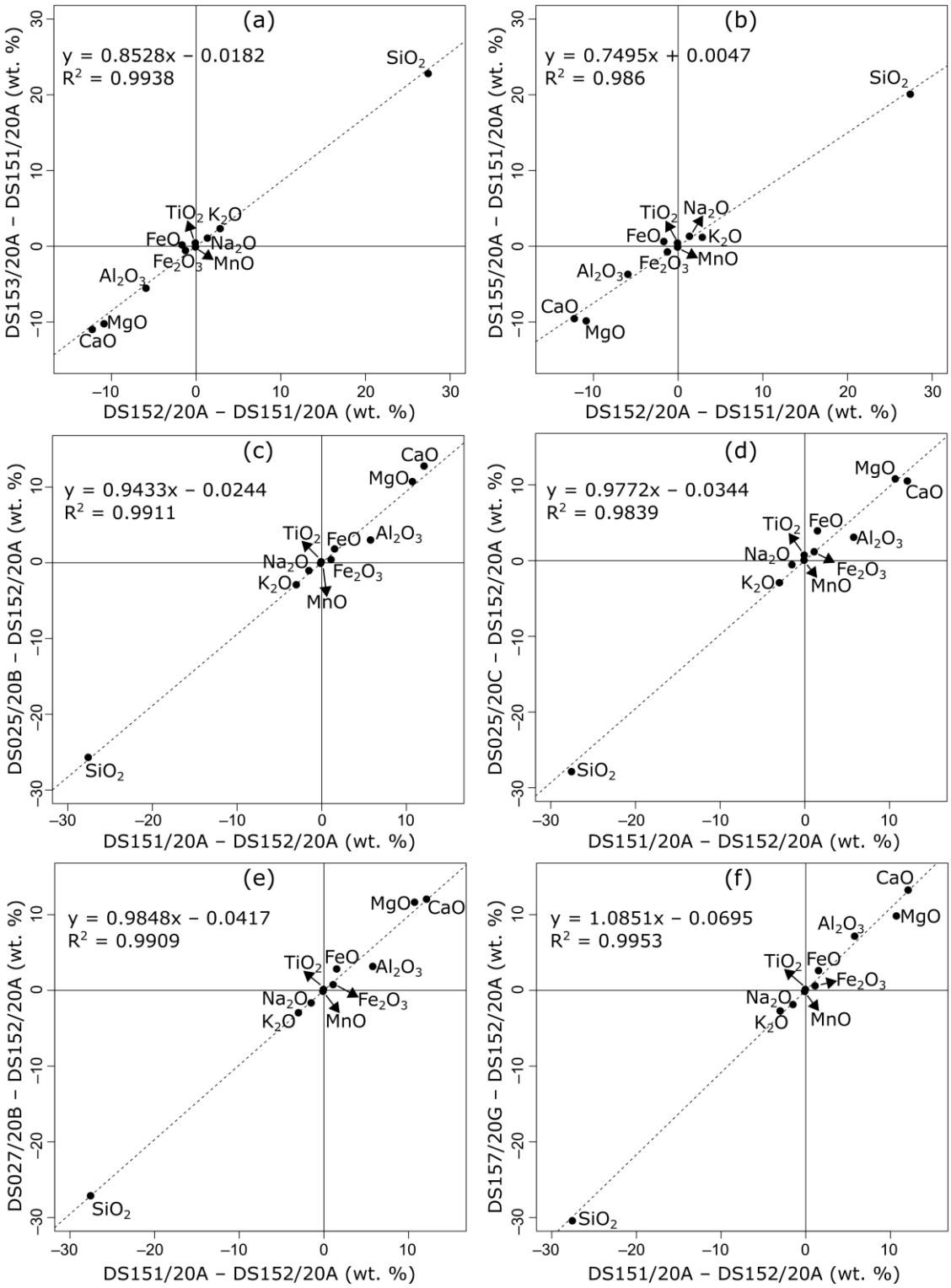

Figure IV. 7: Major-element binary mixing test (after Fourcade & Allègre, 1981) for a–b) intermediate granulites and c–f) mafic granulites.

Compared to the results obtained from Sr–Nd isotopic data (see above), the modelled proportion of garnet clinopyroxenite endmember in intermediate granulites is almost equal. On the other hand, the proportion of felsic granulite end-member in mafic granulites is lower in

relation to Sr–Nd isotopic data. This may indicate that the isotopic composition of mafic granulites has been metasomatically overprinted more than the major elements were. However, it must be taken into account that the data are not accurate enough to decipher the contamination degrees approaching zero and that the end-members could also have shown certain geochemical variability. Nevertheless, Sr–Nd isotopic variation (Figure IV. 6) and major-element-based mixing tests (Figure IV. 7) support the theory of possible metasomatic interaction of felsic granulites with adjacent garnet clinopyroxenites (and vice versa) leading to the formation of intermediate and mafic granulites.

3.3 Geochemical linkage to the geodynamic environment

The above Sr–Nd isotopic data (Figure IV. 6) can also give information about the geodynamic environment(s) of the studied lithologies – especially the link to the possible Saxothuringian subduction under the Moldanubian Domain (see Chapter Geological setting at the beginning of the Thesis).

The Sr–Nd isotopic composition of the felsic and intermediate granulites corresponds to the crustally derived material, very likely represented by felsic, only partly anatectic metaigneous rocks (Fiala et al. 1987; Janoušek et al., 2004, Kotková & Harley, 2010). Their source has been sought in the Saxothuringian plate subducted beneath the Moldanubian Domain as described in the other studies of similar rocks of the Gföhl Unit (Janoušek et al., 2004; Janoušek & Holub, 2007; Schulmann et al., 2014; Maierová et al., 2012, 2021).

The Sr–Nd isotopic data indicate the possible metasomatic interaction of mantle peridotites by ocean-derived fluids from the oceanic part of the subducting Saxothuringian plate that led to the formation of the garnet clinopyroxenites. The progressive subduction of the Saxothuringian slab probably caused an additional metasomatism of garnet clinopyroxenites by fluids and/or melts derived from the subducting continental crust leading to the formation of mafic granulites. Almost identical double metasomatism related to the Saxothuringian subduction beneath the Moldanubian Domain was described from the Mg–K-rich plutons of the Vosges Mts. (E France; Hora et al., 2021). Clearly, our results support the importance of mantle metasomatism by the components coming from the continental crust. Soon thereafter, these metasoms melted to produce analogous Mg–K-rich plutonic rocks in the Moldanubian Zone of the Bohemian Massif (Becker et al., 1999; Janoušek & Holub, 2007; Krmíček et al., 2020; Janoušek et al., 2022 and references therein).

4 Conclusions

Based on the whole-rock geochemistry and Sr–Nd isotopic data, the studied intermediate and mafic granulites of Dunkelsteiner Wald can represent variable mixtures between crustally-derived felsic granulites and mantle-derived garnet clinopyroxenites, and therefore the theory of metasomatic origin of at least some of these transitional lithologies should be considered as a relevant genetic model.

The similarity in the whole-rock geochemical and Sr–Nd isotopic compositions – in combination with the presence of analogous mineral associations (see Part III) – between intermediate and felsic granulites on the one hand, and between mafic granulites and garnet clinopyroxenites on the other, suggests that intermediate granulites could have formed from felsic granulites and mafic granulites from garnet clinopyroxenites by a mutual open-system interaction. The results indicate that a transfer of surplus CaO and MgO from garnet clinopyroxenites into the felsic granulite is required to form intermediate granulites.

Based on the whole-rock and isotopic compositions, garnet clinopyroxenites show signs of derivation from mantle peridotites due to metasomatism by fluids derived from the oceanic part of the subducting Saxothuringian plate. Subsequently, they were variably overprinted by fluids and/or melts derived from the Saxothuringian felsic metaigneous crust – the presumed protolith of the felsic granulites. This later metasomatism could have caused the transformation some of the garnet clinopyroxenites to mafic granulites.

However, on the scale of large garnet clinopyroxenite bodies (tens of metres to first kilometres) – such as those in the Dunkelsteiner Wald massif, where we do not see a direct contact with the host granulite – this theory is difficult to prove. So far we have to rely on small-scale observations, such as of the interaction between felsic granulite and mantle xenoliths described in Part II of this Thesis. Our results are thus preliminary and future research would require more geochemical data for more accurate conclusions.

CONCLUSIONS OF THE THESIS

The current research confirms the possibility of metasomatic origin of at least some of the intermediate and mafic granulites by mutual chemical component exchange between garnet clinopyroxenites and host kyanite-bearing felsic granulites. In the studied lithologies, evidence for operation of two metasomatic processes has been documented.

The first is the occurrence of Ba–Cl-rich mineral phases in garnet clinopyroxenites indicating the metasomatic interaction with Ba–Cl-rich silicocarbonatitic fluids/melts with crustal affinity. This process may also be related to the mantle metasomatism that caused the formation of garnet clinopyroxenites from peridotites.

The second is the metasomatic interaction of Ky-bearing felsic granulites with garnet clinopyroxenites at the lower crustal conditions. This interaction presumably caused the changes in the mineral assemblages and the formation of the reaction textures at contact of those contrasting lithologies. This interaction has been described on a small scale from the St. Leonhard granulite massif and on a likely larger scale from the Dunkelsteiner Wald granulite massif.

In the St. Leonhard granulite massif, the formation of the reaction coronae around mantle xenoliths (at their expense) provides an evidence of the direct metasomatic interaction between the ultramafic xenoliths and their felsic host. Movement of Ca (± small amounts of Mg and Al) from garnet clinopyroxenite xenolith to the surrounding granulite, accompanied by migration of alkalis in the opposite direction, caused the formation of the orthopyroxene–plagioclase symplectite corona at the expense of clinopyroxene. In the case of the peridotite xenolith, the breakdown of olivine and the formation of orthopyroxene corona was the consequence of the movement of Si from the host granulite. The movement of K from the felsic host caused the formation of amphibole and biotite in the entire volume of the xenoliths and the K-feldspar-poor zones around the xenoliths. The Ca supply from garnet clinopyroxenites to the felsic host caused the stabilization of orthopyroxene at the expense of an Al_2SiO_5 phase (probably kyanite). The coronae formation took place in 900–1000 °C and 1.0–1.2 GPa and took 13–532 ka, which is extremely fast in comparison with Variscan orogenic process.

In the Dunkelsteiner Wald granulite massif occur mantle bodies up to several km in size and their direct contact with the host granulite is not visible due to the poor field exposure. In the vicinity of their presumed contacts, transition granulites systematically occur. The extent of the metasomatic interaction between kyanite-bearing felsic granulites and garnet clinopyroxenites

is estimated to be in order of X–X0 metres. The similarity in the mineral assemblages of Ky-bearing felsic granulites with intermediate granulites and garnet clinopyroxenites with mafic granulites indicates that at least some of the intermediate and mafic granulites may have formed due to the mutual metasomatic interaction between garnet clinopyroxenites and their felsic host. We assume that the biggest influence during the metasomatic interaction had the migration of Ca from garnet clinopyroxenites to surrounding kyanite-bearing felsic granulites, which in the kyanite-bearing felsic granulites caused the breakdown of the Al_2SiO_5 phase and the stabilization of orthopyroxene. In garnet clinopyroxenites, the depletion of Ca caused in some cases the growth of Na-rich plagioclase and orthopyroxene at the expense of clinopyroxene. Formation of symplectite texture in some mafic granulites indicates the presence of fluid/melt, which could have accelerated the diffusion of chemical components. The presence of fluid/melt is proven by the K-rich net along plagioclase in the matrix of mafic granulites. Lithologies were isothermally decompressed from ~2.0 to 1.2 GPa at ~1000 °C and the chemical component exchange probably commenced under ~1.5 GPa.

The whole-rock geochemistry and Sr–Nd isotopic data confirm that intermediate granulites could have formed from felsic granulites and mafic granulites from garnet clinopyroxenites by a mutual open-system interaction. An input of CaO and MgO into the felsic granulite is required to form intermediate granulites. Garnet clinopyroxenites show signs of double metasomatism: 1) derivation from mantle peridotites due to metasomatism by fluids derived from the oceanic part of the subducting Saxothuringian plate, and 2) overprint by fluids and/or melts derived from the Saxothuringian felsic metaigneous crust, which could have caused the transformation some of the garnet clinopyroxenites to mafic granulites.

The observed metasomatic origin of transitional granulites implies that the deep crustal chemical exchange between mantle- and crust-derived material may have important consequences for composition, thermal structure and geodynamic evolution of orogenic lower crust. This would be valid especially in hot collisional orogens, exemplified here by the European Variscides.

REFERENCES

Abart, R. & Sperb, R. (2001). Metasomatic coronas around hornblendite xenoliths in granulite facies marble, Ivrea zone, N Italy. II: Oxygen isotope patterns. *Contributions to Mineralogy and Petrology* **141**, 494–504.

Abart, R., Schmud, R. & Harlov, D. (2001). Metasomatic coronas around hornblendite xenoliths in granulite facies marble, Ivrea zone, N Italy, I: constraints on component mobility. *Contributions to Mineralogy and Petrology* **141**, 473–493.

Abuamarah, B. A., Alshehri, F., Azer, M. K., & Asimow, P. D. (2023). Geological and tectonic significance of rodingite in the Ess ophiolite, Arabian Shield, Saudi Arabia. *Lithos* **448–449**, 107168.

Ague, J. J. (1994). Mass transfer during Barrovian metamorphism of pelites, South-Central Connecticut. I. Evidence for changes in composition and volume. *American Journal of Science* **294**, 989–1057.

Ague, J. J. (2003). Fluid infiltration and transport of major, minor, and trace elements during regional metamorphism of carbonate rocks, Wepawaug Schist, Connecticut, USA. *American Journal of Science* **303**, 753–816.

Ague, J. J. & Van Haren, J. L. M. (1996). Assessing metasomatic mass and volume changes using the bootstrap, with application to deep crustal hydrothermal alteration of marble. *Economic Geology* **91**, 1169–1182.

Ankinovich, S.G., Ankinovich, Y. A., Rozhdestvenskaya, I. V. & Frank-Kamenetskiy, V. A. (1973). Chernykhite, a new barium-vanadium mica from northwestern Karatau. *International Geology Review* **15**, 641–647.

Arai, S. & Ishimaru, S. (2008). Insights into petrological characteristics of the lithosphere of mantle wedge beneath arcs through peridotite xenoliths: a review. *Journal of Petrology* **49**, 665–695.

Baldwin, J. A., Powell, R., White, R. & Štípská, P. (2014). Using calculated chemical potential relationships to account for replacement of kyanite by symplectite in high pressure granulites. *Journal of Metamorphic Geology* **33**, 311–330.

Becker, H. (1996a). Crustal trace element and isotopic signatures in garnet pyroxenites from garnet peridotite massifs from lower Austria. *Journal of Petrology* **37**, 785–810.

Becker, H. (1996b). Geochemistry of garnet peridotite massifs from Lower Austria and the composition of deep lithosphere beneath a Palaeozoic convergent plate margin. *Chemical Geology* **134**, 49–65.

Becker, H. (1997). Petrological constraints on the cooling history of high-temperature garnet peridotite massifs in Lower Austria. *Contributions to Mineralogy and Petrology* **128**, 272–286.

Becker, H., Wenzel, T. & Volker, F. (1999). Geochemistry of glimmerite veins in peridotites from Lower Austria – implications for the origin of K-rich magmas in collision zones. *Journal of Petrology* **40**, 315–338.

Bell, D. R. & Rossman, G. R. (1992). Water in Earth's mantle: the role of nominally anhydrous minerals. *Science* **255**, 1391–1396.

Blanco-Quintero, I. F., Lázaro, C., García-Casco, A., Proenza, J. A., & Rojas-Agramonte, Y. (2011). Barium-rich fluids and melts in a subduction environment (La Corea and Sierra del Convento mélanges, eastern Cuba*). Contributions to Mineralogy and Petrology* **162**, 395–413.

Bol, L. C. G. M., Bos, A., Sauter, P. C. C., & Jansen, J. B. H. (1989). Barium-titanium-rich phlogopites in marbles from Rogaland, Southwest Norway. *American Mineralogist* **74**, 439–447.

Borghini, A., Ferrero, S., Wunder, B., Laurent, O., O'Brien, P. J. & Ziemann, M. A. (2018). Granitoid melt inclusions in orogenic peridotite and the origin of garnet clinopyroxenite. *Geology* **46**, 1007–1010.

Borghini, A., Ferrero, S., O'Brien, P. J., Laurent, O., Günter, C. & Ziemann, M. A. (2020). Cryptic metasomatic

agent measured in situ in Variscan mantle rocks: melt inclusions in garnet of eclogite, Granulitgebirge, Germany. *Journal of Metamorphic Geology* **38**, 207–234.

Borghini, A., Nicoli, G., Ferrero, S., O'Brien, P. J., Laurent, O., Remusat, L., Borghini, G. & Milani, S. (2023). The role of continental subduction in mantle metasomatism and carbon recycling revealed by melt inclusions in UHP eclogites. *Science Advances* **9**, eabp9482.

Borinski, S. A., Hoppe, U., Chakraborty, S., Ganguly, J. & Bhowmik, S. K. (2012). Multicomponent diffusion in garnets I: general theoretical considerations and experimental data for Fe–Mg systems. *Contributions to Mineralogy and Petrology* **164**, 571–586.

Boynton W. V. (1984). Cosmochemistry of the rare earth elements: meteorite studies. In: Henderson P. (ed) *Rare Earth Element Geochemistry*, *Elsevier, Amsterdam*, 63–114.

Bucholz, C. & Ague, J. J. (2010). Fluid flow and Al transport during quartz–kyanite vein formation, Unst, Shetland Islands, Scotland. *Journal of Metamorphic Geology* **28**, 19–39.

Carlson, W. D. (2002). Scales of disequilibrium and rates of equilibration during metamorphism. *American Mineralogist* **87**, 185–204.

Carmichael, D. M. (1969). On the mechanism of prograde metamorphic reactions in quartz-bearing pelitic rocks. *Contributions to Mineralogy and Petrology* **20**, 244–267.

Carswell, D. A. (1991). Variscan high P–T metamorphism and uplift history in the Moldanubian Zone of the Bohemian Massif in Lower Austria. *European Journal of Mineralogy* **3**, 323–342.

Carswell, D. A. & O'Brien, P. J. (1993). Thermobarometry and geotectonic significance of high-pressure granulites: examples from the Moldanubian Zone of the Bohemian Massif in Lower Austria. *Journal of Petrology* **34**, 427–459.

Cesare, B., Acosta-Vigil, A., Ferrero, S., & Bartoli, O. (2011). Melt inclusions in migmatites and granulites. *Journal of the Virtual Explorer* **38**, 1–21.

Chakhmouradian, A. R., Reguir, E. P., & Mitchell, R. H. (2002). Strontium-apatite: New occurrences, and the extent of Sr-FOR-Ca substitution in apatite-group minerals. *Canadian Mineralogist* **40**, 121–136.

Cooke, R. A. (1999). The petrology of high-pressure granulites from the St. Leonhard Granulite Massif, Gföhl Unit, Lower Austria. Unpublished PhD Thesis, University of Sheffield.

Cooke, R. A. (2000). High-pressure/temperature metamorphism in the St. Leonhard Granulite Massif, Austria: evidence from intermediate pyroxene-bearing granulites. *International Journal of Earth Sciences* **89**, 631–651.

Cooke, R. A. & O'Brien, P. J. (2001). Resolving the relationship between high P–T rocks and gneisses in collisional terranes: an example from the Gföhl gneiss–granulite association in the Moldanubian Zone, Austria. *Lithos* **58**, 33–54.

Crank, J. (1975) The Mathematics of Diffusion. 2nd Edition, *Oxford University Press*, London, 69-88.

Cruz-Uribe, A. M., Marschall, H. R., Gaetani, G. A. & Le Roux, V. (2018). Generation of alkaline magmas in subduction zones by partial melting of mélange diapirs – an experimental study. *Geology* **46**, 343–346.

Čopjaková, R. & Kotková, J. (2018). Composition of barian mica in multiphase solid inclusions from orogenic garnet peridotites as evidence of mantle metasomatism in a subduction zone setting. *Contributions to Mineralogy and Petrology* **173**, 106.

De La Roche, H., Leterrier, J., Grandclaude, P. & Marchal, M. (1980). A classification of volcanic and plutonic

rocks using R1–R2 diagrams and major element analyses – its relationships with current nomenclature. *Chemical Geology* **29**, 183–210.

Debon, F. & Le Fort, P. (1983). A chemical–mineralogical classification of common plutonic rocks and associations. *Transactions of the Royal Society of Edinburgh, Earth Sciences* **73**, 135–149.

Debon, F. & Le Fort, P. (1988). A cationic classification of common plutonic rocks and their magmatic associations: principles, method, applications. *Bulletin de Minéralogie* **111**, 493–510.

Dickin, A. P. (2005). Radiogenic Isotope Geology. 2nd Edition. *Cambridge University Press, Cambridge*, 509.

Dodson, M. H. (1973). Closure temperature in cooling geochronological and petrological systems. *Contributions to Mineralogy and Petrology* **40**, 259–274.

Dymek, R. F. (1983). Titanium, aluminum and interlayer cation substitutions in biotite from high-grade gneisses, West Greenland. *American Mineralogist* **68**, 880–899.

Chu, X. & Ague, J. J. (2015). Analysis of experimental data on divalent cation diffusion kinetics in aluminosilicate garnets with application to timescales of peak Barrovian metamorphism, Scotland. *Contributions to Mineralogy and Petrology* **170**, 1–27.

Elphick, S. C., Ganguly, J. & Loomis, T. P. (1985). Experimental determination of cation diffusivities in aluminosilicate garnets. *Contributions to Mineralogy and Petrology* **90**, 36–44.

Engvik, A. K., Mezger, K., Wortelkamp, S., Bast, R., Corfu, F., Korneliussen, A., Ihlen, P., Bingen, B. & Austrheim, H. (2011). Metasomatism of gabbro – mineral replacement and element mobilization during the Sveconorwegian metamorphic event. *Journal of Metamorphic Geology* **29**, 399–423.

Erban Kochergina, Y. V., Erban, V., Hora, J. M., 2022. Sample preparation and chromatographic separation for Sr, Nd, and Pb isotope analysis in geological, environmental, and archaeological samples. J. Geosci. **67**, 273–285.

Faryad, S. W., Dolejš, D. & Machek, M. (2009). Garnet exsolution in pyroxene from clinopyroxenites in the Moldanubian Zone: constraining the early pre-convergence history of ultramafic rocks in the Variscan Orogen. . *Journal of Metamorphic Geology,* **27,** 655–671.

Faryad, S. W., Nahodilová, R., & Dolejš, D. (2010) Incipient eclogite facies metamorphism in the Moldanubian granulites revealed by mineral inclusions in garnet. *Lithos* **114**, 54–69.

Faryad, S. W., Jedlička, R., & Ettinger, K. (2013) Subduction of lithospheric upper mantle recorded by solid phase inclusions and compositional zoning in garnet: Example from the Bohemian Massif. *Gondwana Research* **23**, 944–955.

Faure, G. & Mensing, T. M. (2004). Isotopes: Principles and Applications. Third Edition. *Wiley, New Jersey.*

Ferrero, S., Ziemann, M. A., Angel, R. J., O'Brien, P. J., and Wunder, B. (2015a). Kumdykolite, kokchetavite, and cristobalite crystallized in nanogranites from felsic granulites, Orlica-Snieznik Dome (Bohemian Massif): Not evidence for ultrahigh-pressure conditions. *Contributions to Mineralogy and Petrology* **171**, 1–12.

Ferrero, S., Wunder, B., Walczak, K., O'Brien, P.J., and Ziemann, M.A. (2015b). Preserved near ultrahigh-pressure melt from continental crust subducted to mantle depths. *Geology* **43**, 447–450.

Ferrero, S., O'Brien, P. J., Borghini, A., Wunder, B., Wälle, M., Günter, C. & Ziemann, M. A. (2018). A treasure chest full of nanogranitoids: an archive to investigate crustal melting in the Bohemian Massif. In: Ferrero, S., Lanari, P., Goncalves, P. & Grosch, E. G. (eds) Metamorphic Geology: Microscale to Mountain Belts. *Geological Society, London, Special Publications* **478,** 13–38.

Fiala, J., Matějovská, O. & Vaňková, V. (1987). Moldanubian granulites: source material and petrogenetic considerations. *Neues Jahrbuch für Mineralogie, Abhandlungen* **157**, 133–165.

Filut, M. A., Rule, A. C. & Bailey, S. W. (1985). Crystal structure refinement of anandite-2Or, a barium- and sulphur-bearing trioctahedral mica. *American Mineralogist* **70**, 1298–1308.

Fourcade, S. & Allegre, C. J. (1981). Trace elements behavior in granite genesis: A case study The calc-alkaline plutonic association from the Querigut complex (Pyrénées, France). Contr. Mineral. and Petrol. **76**, 177–195.

Franěk, J., Schulmann, K., Lexa, O., Tomek, C. & Edel, J. B. (2011). Model of syn-convergent extrusion of orogenic lower crust in the core of the Variscan Belt; implications for exhumation of high-pressure rocks in large hot orogens. *Journal of Metamorphic Geology* **29**, 53–78.

Franke, W. (2000). The mid-European segment of the Variscides: tectonostratigraphic units, terrane boundaries and plate tectonic evolution. In: Franke, W., Haak, V., Oncken, O. & Tanner, D. (eds) Orogenic Processes: Quantification and Modelling in the Variscan Belt. *Geological Society, London, Special Publications* **179**, 35–61.

Frezzotti, M.-L. & Ferrando, S. (2015). The chemical behavior of fluids released during deep subduction based on fluid inclusions. *American Mineralogist* **100**, 352–377.

Frezzotti, M.-L. & Touret, J. L. R. (2014). CO_2, carbonate-rich melts, and brines in the mantle. *Geoscience Frontiers* **5**, 697–710.

Friedl, G., Cooke, R. A., Finger, F., McNaughton, N. J. & Fletcher, I. R. (2011). Timing of Variscan HP–HT metamorphism in the Moldanubian Zone of the Bohemian Massif: U–Pb SHRIMP dating on multiply zoned zircons from a granulite from the Dunkelsteiner Wald Massif, Lower Austria. *Mineralogy and Petrology* **102**, 63–75.

Fuchs, G. (1986). Zur Diskussion um den Deckenbau der Böhmischen Masse. Jahrbuch der Geologischen Bundesanstalt, **129**, 41–49.

Fuchs, W. & Grill, R. (1984). Geologische Karte der Republik Österreich 1:50.000 Blatt 38 Krems. – Geologische Bundesanstalt, Wien.

Fuchs, G., Kupka, E., Höck, V. & Steininger, F. (1984). Geologische Karte der Republik Österreich 1:50.000 Blatt 20 Gföhl. – Geologische Bundesanstalt, Wien.

Fuhrman, M. L. & Lindsley, D. H. (1988). Ternary feldspar modeling and thermometry. *American Mineralogist* **73**, 201–215.

Gaidies, F., Milke, R., Heinrich, W. & Abart, R. (2017). Metamorphic mineral reactions: porphyroblast, corona and symplectite growth. In: Heinrich, W. & Abart, R. (eds) Mineral reaction kinetics: microstructures, textures, chemical and isotopic signatures. *EMU Notes in Mineralogy* **16**, 469–540.

Gayk, T. & Kleinschrodt, R. (2000). Hot contacts of garnet peridotites in middle/upper crustal levels: new constraints on the nature of the late Variscan high-T/low-P event in the Moldanubian (Central Vosges/NE France). *Journal of Metamorphic Geology* **18**, 293–305.

Gayk, T., Kleinschrodt, R., Langosch, A., & Seidel, E. (1995). Quartz exsolution in clinopyroxene of high-pressure granulite from the Münchberg Massif. *European Journal of Mineralogy* **7**, 1217–1220.

Gnos, E. and Armbruster, T. (2000). Kinoshitalite, $Ba(Mg)_3(Al_2Si_2)O_{10}(OH,F)_2$, a brittle mica from a manganese deposit in Oman: Paragenesis and crystal chemistry. *American Mineralogist* **85**, 242–250.

Grant, J. A. (1986). The isocon diagram; a simple solution to Gresens' equation for metasomatic alteration. *Economic Geology* **81**, 1976–1982.

Grapes, R. H. (1993). Barian mica and distribution of barium in metacherts and quartzofeldspathic schists, Southern Alps, New Zealand. *Mineralogical Magazine* **57**, 265–272.

Green, E. C. R., White, R. W., Diener, J. F. A., Powell, R., Holland, T. J. B. & Palin, R. M. (2016). Activity–composition relations for the calculation of partial melting equilibria in metabasic rocks. *Journal of Metamorphic Geology* **34,** 845–869.

Guggenheim, S. and Frimmel, H. E. (1999). Ferrokinoshitalite, a new species of brittle mica from the Broken Hill mine, South Africa: Structural and mineralogical characterization. *Canadian Mineralogist* **37**, 1445–1452.

Guy, A., Edel, J. B., Schulmann, K., Tomek, C. & Lexa, O. (2011). A geophysical model of the Variscan orogenic root (Bohemian Massif): implications for modern collisional orogens. *Lithos* **124**, 144–157.

Hacker, B. R., Kelemen, P. B. & Behn, M. D. (2011). Differentiation of the continental crust by relamination. *Earth and Planetary Science Letters* **307**, 501–516.

Harlov, D. E., & Austrheim, H. (2013). Metasomatism and the chemical transformation of rock: The role of fluids in terrestrial and extraterrestrial processes. In: Harlov, D. E., & Austrheim, H. (eds) Metasomatism and the Chemical Transformation of Rock. *Springer-Verlag, Berlin*, 805 pp.

Hasalová, P., Janousek, V., Schulmann, K., Štípská, P. & Erban, V. (2008). From orthogneiss to migmatite: geochemical assessment of the melt infiltration model in the Gföhl Unit (Moldanubian Zone, Bohemian Massif). *Lithos* **102**, 508–537.

Hawthorne, F. C., Oberti, R., Zanetti, A., & Czamanske, G. K. (1998). The role of Ti in hydrogen-deficient amphiboles; sodic-calcic and sodic amphiboles from Coyote Peak, California. *Canadian Mineralogist* **36**, 1253–1265.

Hawthorne, F., Oberti, R., Harlow, G., Maresch, W., Martin, R. F., Schumacher, J. & Welch, M. (2012). IMA report: nomenclature of the amphibole supergroup. *American Mineralogist* **97**, 2031–2048.

Henry, D. J. & Daigle, N. M. (2018). Chlorine incorporation into amphibole and biotite in high-grade iron-formations: Interplay between crystallography and metamorphic fluids. *American Mineralogist* **103**, 55–68.

Henry, D. J. & Guidotti, C. V. (2002). Titanium in biotite from metapelitic rocks: Temperature effects, crystal-chemical controls, and petrologic applications. *American Mineralogist* **87**, 375–382.

Henry, D. J., Guidotti, C. V., & Thomson, J. (2005). The Ti-saturation surface for low-to-medium pressure metapelitic biotites: Implications for geothermometry and Ti-substitution mechanisms. *American Mineralogist* **90**, 316–328.

Holland, T. J. B. & Powell, R. (2003). Activity–compositions relations for phases in petrological calculations: an asymmetric multicomponent formulation. *Contributions to Mineralogy and Petrology* **145**, 492–501.

Holland, T. J. B. & Powell, R. (2011). An improved and extended internally consistent thermodynamic dataset for phases of petrological interest, involving a new equation of state for solids. *Journal of Metamorphic Geology* **29**, 333–383.

Holland, T. J. B., Green, E. C. R. & Powell, R. (2022). A thermodynamic model for feldspars in $KAlSi_3O_8$–$NaAlSi_3O_8$–$CaAl_2Si_2O_8$ for mineral equilibrium calculations. *Journal of Metamorphic Geology* **40**, 587–600.

Hora, J. M., Tabaud, A. S., Janoušek, V. & Erban Kochergina, Y.V. (2021). Potassic magmas of the Vosges Mts.

(NE France) delimit the areal extent and nature of long-gone Variscan orogenic mantle domains. *Lithos* **402–403,** 106304.

Hughes, J. M., Cameron, M., & Crowley, K. D. (1991). Ordering of divalent cations in the apatite structure: Crystal structure refinements of natural Mn- and Sr-bearing apatite. *American Mineralogist* **76**, 1857–1862.

Ishimaru, S., Arai, S., Ishida, Y., Shirasaka, M. & Okrugin, V. (2007). Melting and multi-stage metasomatism in the mantle wedge beneath a frontal arc inferred from highly depleted peridotite xenoliths from the Avacha volcano, southern Kamchatka. *Journal of Petrology* **48**, 395–433.

Ivanyuk, G. Y., Yakovenchuk, V. N., Pakhomovsky, Y. A., Panikorovskii, T. L., Konoplyova, N. G., Bazai, A. V., Bocharov, V. N., Antonov, A. A., & Selivanova, E. A. (2017). Goryainovite, Ca_2PO_4Cl, a new mineral from the Stora Sahavaara iron ore deposit (Norrbotten, Sweden). *GFF* **139**, 75–82.

Janoušek, V. & Holub, F. V. (2007). The causal link between HP–HT metamorphism and ultrapotassic magmatism in collisional orogens: case study from the Moldanubian Zone of the Bohemian Massif. *Proceedings of the Geologists' Association* **118**, 75–86.

Janoušek, V., Finger, F., Roberts, M., Frýda, J., Pin, C. & Dolejš, D. (2004). Deciphering the petrogenesis of deeply buried granites: whole-rock geochemical constraints on the origin of largely undepleted felsic granulites from the Moldanubian Zone of the Bohemian Massif. *Transactions of the Royal Society of Edinburgh: Earth Sciences* **95**, 141–159.

Janoušek, V., Farrow, C. M. & Erban, V. (2006). Interpretation of whole-rock geochemical data in igneous geochemistry: introducing Geochemical Data Toolkit (GCDkit). *Journal of Petrology* **47**, 1255–1259.

Janoušek, V., Krenn, E., Finger, F., Míková, J. & Frýda, J. (2007). Hyperpotassic granulites from the Blanský les Massif (Moldanubian Zone, Bohemian Massif) revisited. *Journal of Geosciences* **52**, 73–112.

Janoušek, V., Moyen, J.-F., Martin, H., Erban, V., Farrow, C. M. (2016). Geochemical modelling of igneous processes – Principles and recipes in R Language. In: Bringing the Power of R to a Geochemical Community. 1st Edition. *Springer Geochemistry, Berlin, Heidelberg*, 346 pp.

Janoušek, V., Erban Kochergina, Y. V, Andronikov, A. V & Kusbach, V. K. (2022). Decoupling of Mg from Sr–Nd isotopic compositions in Variscan subduction-related plutonic rocks from the Bohemian Massif; implications for mantle enrichment processes and genesis of orogenic ultrapotassic magmatic rocks. *International Journal of Earth Sciences* **111**, 1491–1518.

Jiang, S.-Y., Palmer, M. R., Li, Y.-H., & Xue, C.-J. (1996). Ba-rich micas from the Yindongzi-Daxigou Pb-Zn-Ag and Fe deposits, Qinling, northwestern China. *Mineralogical Magazine* **60**, 433–445.

Joesten, R. (1977). Evolution of mineral assemblage zoning in diffusion metamorphism. *Geochimica et Cosmochimica Acta* **41**, 649–670.

Joesten, R. (1986). The role of magmatic reaction, diffusion and annealing in the evolution of coronitic microstructures in troctolitic gabbros from Risor, Norway. *Mineralogical Magazine* **50**, 441–467.

Kamineni, D. C., Bonardi, M., & Rao, A. T. (1982) Halogen-bearing minerals from Airport Hill, Visakhapatnam, India. *American Mineralogist* **67**, 1001–1004.

Kenneth, A. J. (2004). Segregation. In: Kenneth, A. J. (2004) (ed) Kinetic Processes: Crystal Growth, Diffusion, and Phase Transitions in Materials, Second Edition. WILEY-VCH. 453.

Kogarko, L. N., Uvarova, Y. A., Sokolova, E., Hawthorne, F. C., Ottolini, L., & Grice, J. D. (2005). Oxykinoshitalite, a new species of mica from Fernando de Noronha Island, Pernambuco, Brazil: Occurrence

and crystal structure. *Canadian Mineralogist* **43**, 1501–1510.

Kogarko, L.N., Lebedev, V.A., and Levskii, L.K. (2007) Heterogeneity of isotope sources of alkaline magmatism in the hot spot of the southwestern Atlantic: Fernando de Noronha Islands. Doklady Earth Sciences, 412, 85–88.

Kotková, J. & Harley, S. L. (2010). Anatexis during high-pressure crustal metamorphism: evidence from garnet–whole-rock REE relationships and zircon–rutile Ti–Zr thermometry in leucogranulites from the Bohemian Massif. *Journal of Petrology* **51**, 1967–2001.

Kotková, J., O'Brien, P. J. & Ziemann, M. A. (2011). Diamond and coesite discovered in Saxony-type granulite: Solution to the Variscan garnet peridotite enigma. *Geology* **39**, 667–670.

Kotková, J., Čopjaková, R. & Škoda, R. (2021a). Multiphase solid inclusions reveal the origin and fate of carbonate-silicate melts in metasomatised peridotite. *Lithos* **398**–**399,** 106309.

Kotková, J., Fedortchouk, Y., Wirth, R. & Whitehouse, M. J. (2021b). Metamorphic microdiamond formation is controlled by water activity, phase transitions and temperature. *Scientific Reports* **11**, 7694.

Krmíček, L., Romer, R. L., Timmerman, M. J., Ulrych, J., Glodny, J., Přichystal, A. & Sudo, M. (2020). Long-lasting (65 Ma) regionally contrasting late- to post-orogenic Variscan mantle-derived potassic magmatism in the Bohemian Massif. *Journal of Petrology* **61**, egaa072.

Kröner, A., O'Brien, P. J., Nemchin, A. A. & Pidgeon, R. T. (2000). Zircon ages for high pressure granulites from South Bohemia, Czech Republic, and their connection to Carboniferous high temperature processes. *Contributions to Mineralogy and Petrology* **138,** 127–142.

Kullerud, K. (1995). Chlorine, titanium and barium-rich biotites: Factors controlling biotite composition and the implications for garnet–biotite geothermometry. *Contributions to Mineralogy and Petrology* **120**, 42–59.

Kusbach, V., Janoušek, V., Hasalová, P., Schulmann, K., Fanning, C. M., Erban, V. & Ulrich, S. (2015). Importance of crustal relamination in origin of the orogenic mantle peridotite – high-pressure granulite association : example from the Náměšť Granulite Massif (Bohemian Massif, Czech Republic). *Journal of the Geological Society* **172,** 479–490.

Lasaga, A. C. (1998). Kinetic Theory in the Earth Sciences. Princeton University Press, **402**, 802.

Lexa, O. (2020). Pypsbuilder © (version 2.2.1) [Software]. THERMOCALC front-end for constructing pseudosections. Available from https://github.com/ondrolexa/pypsbuilder.

Lexa, O., Schulmann, K., Janoušek, V., Štípská, P., Guy, A. & Racek, M. (2011). Heat sources and trigger mechanisms of exhumation of HP granulites in Variscan orogenic root. *Journal of Metamorphic Geology* **29**, 79–102.

Léger, A., Rebbert, C., & Webster, J. (1996). Cl-rich biotite and amphibole from Black Rock Forest, Cornwall, New York. *American Mineralogist* **81**, 495–504.

Li, H., Chen, R., Zheng, Y. & Hu, Z. (2018). Water in garnet pyroxenite from the Sulu orogen: implications for crust-mantle interaction in continental subduction zone. *Chemical Geology* **478**, 18–38.

Liew T. C. & Hofmann A. W. (1988) Precambrian crustal components, plutonic associations, plate environment of the Hercynian Fold Belt of Central Europe: indications from a Nd and Sr isotopic study. *Contributions to Mineralogy and Petrology* **98**, 129–138.

Locock, A. J. (2014). An Excel spreadsheet to classify chemical analyses of amphiboles following the IMA 2012 recommendations. *Computers and Geosciences* **62**, 1–11.

Lopes, R. P. & Ulbrich, M. N. C. (2015). Geochemistry of the alkaline volcanic-subvolcanic rocks of the Fernando de Noronha Archipelago, Southern Atlantic Ocean. Brazilian *Journal of Geology* **45**, 307–333.

Maierová, P., Čadek, O., Lexa, O. & Schulmann, K. (2012). A numerical model of exhumation of the orogenic lower crust in the Bohemian Massif during the Variscan orogeny. *Studia Geophysica et Geodaetica* **56**, 595–619.

Maierová, P., Lexa, O., Schulmann, K. & Štípská, P. (2014). Contrasting tectono-metamorphic evolution of orogenic lower crust in the Bohemian Massif: a numerical model. *Gondwana Research* **25,** 509–521.

Maierová, P., Schulmann, K. & Gerya, T. (2018). Relamination styles in collisional orogens. *Tectonics* **37**, 224–250.

Maierová, P., Schulmann, K., Štípská, P., Gerya, T. & Lexa, O. (2021). Trans-lithospheric diapirism explains the presence of ultra-high pressure rocks in the European Variscides. *Communications Earth & Environment* **2**, 56.

Malaspina, N., Hermann, J., Scambelluri, M. & Compagnoni, R. (2006). Polyphase inclusions in garnet–orthopyroxenite (Dabie Shan, China) as monitors for metasomatism and fluid-related trace element transfer in subduction zone peridotite. *Earth and Planetary Science Letters* **249**, 173–187.

Manuella, F. C., Carbone, S., Ottolini, L., & Gibilisco, S. (2012) Micro-Raman spectroscopy and SIMS characterization of oxykinoshitalite in an olivine nephelinite from the Hyblean Plateau (Sicily, Italy). *European Journal of Mineralogy* **24**, 527–533.

Matura, A. (1983). Geologische Karte der Republik Österreich 1:50.000 Blatt 37 Mautern. – Geologische Bundesanstalt, Wien.

Medaris, L. G., Beard, B. L., Johnson, C. M., Valley, J. W., Spicuzza, M. J., Jelínek, E. & Mísař, Z. (1995). Garnet pyroxenite and eclogite in the Bohemian Massif: geochemical evidence for Variscan recycling of subducted lithosphere. *Geologische Rundschau* **84**, 489–505.

Medaris, G., Wang, H., Jelínek, E., Mihaljevič, M. & Jakeš, P. (2005). Characteristics and origins of diverse Variscan peridotites in the Gföhl Nappe, Bohemian Massif, Czech Republic. *Lithos* **82**, 1–23.

Medaris, L. G., Beard, B. L. & Jelínek, E. (2006a). Mantle-derived, UHP garnet pyroxenite and eclogite in the Moldanubian Gföhl Nappe, Bohemian Massif: a geochemical review, new P–T determinations, and tectonic interpretation. *International Geology Review* **48**, 765–777.

Medaris, L. G., Ghent, E. D., Wang, H. F., Fournelle, J. H. & Jelínek, E. (2006b). The Spačice eclogite: constraints on the P–T–t history of the Gföhl granulite terrane, Moldanubian Zone, Bohemian Massif. *Mineralogy and Petrology* **86**, 203–220.

Medaris, L. G., Jelínek, E., Beard, B. L., Valley, J. W., Spicuzza, M. J. & Strnad, L. (2013). Garnet pyroxenite in the Biskupice peridotite, Bohemian Massif: anatomy of a Variscan high-pressure cumulate. *Journal of Geosciences* **58**, 3–19.Milke, R., Abart, R., Kunze, K., Koch-Müller, M., Schmid, D. & Ulmer, P. (2009). Matrix rheology effects on reaction rim growth I: evidence from orthopyroxene rim growth experiments. *Journal of Metamorphic Geology* **27**, 71–82.

Mongkoltip, P. & Ashworth, J. R. (1983). Quantitative estimation of an open-system symplectite-forming reaction: restricted diffusion of Al and Si in coronas around olivine. *Journal of Petrology* **24**, 635–661.

Müller, T., Massonne, H.-J. & Willner, A. P. (2015). Timescales of exhumation and cooling inferred by kinetic modeling: an example using a lamellar garnet pyroxenite from the Variscan Granulitgebirge, Germany.

*American Mineralogist **100***, 747–759.

Naemura, K., Hirajima, T., & Svojtka, M. (2009). The pressure–temperature path and the origin of phlogopite in spinel–garnet peridotites from the Blanský les Massif of the Moldanubian Zone, Czech Republic. *Journal of Petrology* **50**, 1795–1827.

Naemura, K., Hirajima, T., Svojtka, M., Shimizu, I. & Iizuka, T. (2018). Fossilized melts in mantle wedge peridotites. *Scientific Reports* **8**, 10116.

Nahodilová, R., Hasalová, P., Štípská, P., Schulmann, K., Závada, P., Míková, J., Kylander-Clark, A., Maierová, P. (2020). Exhumation of subducted continental crust along the arc region. *Gondwana research* **80**, 157–187.

Oberti, R., Ungaretti, L., Cannillo, E., & Hawthorne, F. C. (1992). The behaviour of Ti in amphiboles; I, Four- and six-coordinate Ti in richterite. *European Journal of Mineralogy* **4**, 425–440.

Oberti, R., Ungaretti, L., Cannillo, E., & Hawthorne, F. C. (1993). The mechanism of Cl incorporation in amphibole. *American Mineralogist* **78**, 746–752.

O'Brien, P. J. & Rötzler, J. (2003). High-pressure granulites: formation, recovery of peak conditions and implications for tectonics. *Journal of Metamorphic Geology* **21**, 3–20.

Oen, I. S. & Lustenhouwer, W. J. (1992). Cl-rich biotite, Cl–K hornblende, and Cl-rich scapolite in meta-exhalites: Nora, Bergslagen, Sweden. *Economic Geology and the Bulletin of the Society of Economic Geologists* **87**, 1638–1648.

Owen, J. V. & Dostal, J. (1996). Contrasting corona structures in mafic granulite from the Blanský Les complex, Bohemian Massif, Czech Republic. *Canadian Mineralogist* **34**, 959–966.

Pattiaratchi, D. B., Saari, E., & Sahama, T. G. (1967). Anandite, a new barium iron silicate from Wilagedera, North Western Province, Ceylon. *Mineralogical Magazine and Journal of the Mineralogical Society* **36**, 1–4.

Paulick, H, Bach, W., Godard, M., De Hoog, J. C. M., Suhr, G., Harvey, J. (2006). Geochemistry of abyssal peridotites (Mid-Atlantic Ridge, 15o20'N, ODP Leg 209): implications for fluid/rock interaction in slow spreading environments. *Chemical Geology* **234**, 179–210.

Perraki, M. & Faryad, S. W. (2014). First finding of microdiamond, coesite and other UHP phases in felsic granulites in the Moldanubian Zone: implications for deep subduction and a revised geodynamic model for Variscan Orogeny in the Bohemian Massif. *Lithos* **202**–**203**, 157–166.

Petrakakis, K. (1997). Evolution of Moldanubian rocks in Austria: review and synthesis. *Journal of Metamorphic Geology* **15,** 203–222.

Petrakakis, K., Schuster-Bourgin, N., Habler, G. & Abart, R. (2018). Ca-rich garnets and associated symplectites in mafic peraluminous granulites from the Gföhl Nappe System, Austria. *Solid Earth* **9**, 797–819.

Petrishcheva, E., & Abart, R. (2017). Diffusion: Some mathematical foundations and applications in mineralogy. In: Heinrich, W., & Abart, R. (eds) Mineral Reaction Kinetics: Microstructures, Textures, Chemical and Isotopic Signatures. Mineralogical Society Notes in Mineralogy, **16**, 255–294.

Piccardo, G. B., Müntener, O., Zanetti, A., Romairone, A., Bruzzone, S., Poggi, E., & Spagnolo, G. (2004). The Lanzo South peridotite: melt/peridotite interaction in the mantle lithosphere of the Jurassic Ligurian Tethys. *Ofioliti* **29**, 37–62.

Piccoli, F., Lanari, P., Hermann, J., & Pettke, T. (2022). Deep subduction, melting, and fast cooling of metapelites from the Cima Lunga Unit, Central Alps. *Journal of Metamorphic Geology* **40**, 121–143

Pistone, M., Racek, M. & Štípská, P. (2020). Effects of diffusion of water and migration of melts in crustal rocks: an experimental study. *Chemical Geology* **540**, 119548.

Pouchou, J. & Pichoir, F. (1985). "PAP" (φρZ) procedure for improved quantitative microanalysis. In: Armstrong, J. T. (ed) Microbeam Analysis. *San Francisco Press* 104–106.

Racek, M., Štípská, P., Pitra, P., Schulmann, K. & Lexa, O. (2006). Metamorphic record of burial and exhumation of orogenic lower and middle crust: a new tectonothermal model for the Drosendorf window (Bohemian Massif, Austria). *Mineralogy and Petrology* **86**, 221–251.

Racek, M., Štípská, P. & Powell, R. (2008). Garnet–clinopyroxene intermediate granulites in the St. Leonhard massif of the Bohemian Massif: ultrahigh-temperature metamorphism at high pressure or not? *Journal of Metamorphic Geology* **26**, 253–271.

Remmert, P., Heinrich, W., Wunder, B., Morales, L., Wirth, R., Rhede, D. & Abart, R. (2017). Synthesis of monticellite–forsterite and merwinite–forsterite symplectites in the $CaO–MgO–SiO_2$ model system: influence of temperature and water content on microstructure evolution. *Contributions to Mineralogy and Petrology* **173**, 5.

Rieder, M., Cavazzini, G., D'yakonov, Y. S., Frank-Kamenetskii, V. A., Gottardi, G., Guggenheim, S., Koval', P. V., Müller, G., Neiva, A. M. R., Radoslovich, E. W., & others. (1999). Nomenclature of the micas. *Mineralogical Magazine* **63**, 267–279.

Rudnick, R. L. & Gao, S. (2014). Composition of the continental crust. In: Holland, H. D. & Turekian, K. K. (eds) Treatise on Geochemistry. Second Edition. Elsevier, Oxford, **4**, 1–51.

Schantl, P., Hauzenberger, C., Finger, F., Müller, T. & Linner, M. (2019). New evidence for the prograde and retrograde PT-path of high-pressure granulites, Moldanubian Zone, Lower Austria, by Zr-in-rutile thermometry and garnet diffusion modelling. *Lithos* **342–343**, 420–439.

Schmädicke, E., Gose, J. & Will, T. M. (2010). The P–T evolution of ultra high temperature garnet-bearing ultramafic rocks from the Saxonian Granulitgebirge Core Complex, Bohemian Massif. *Journal of Metamorphic Geology* **28**, 489–508.

Schnabel, W. (2002). Geologische Karte von Niederösterreich 1:200.000. – 2 Teile + Legendentafel, Computerplot (Farbe), Verlag der Geologischen Bundesanstalt, Wien.

Schorn, S. (2022). Self-induced incipient 'eclogitization' of metagranitoids at closed-system conditions. *Journal of Metamorphic Geology* **40**, 1271–1290.

Schorn, S. & Diener, J.F.A. (2017). Details of the gabbro-to-eclogite transition determined from microtextures and calculated chemical potential relationships. *Journal of Metamorphic Geology* **35**, 55–75.

Schulmann, K., Konopásek, J., Janoušek, V., Lexa, O., Lardeaux, J. M., Edel, J. B., Štípská, P. & Ulrich, S. (2009). An Andean type Palaeozoic convergence in the Bohemian Massif. *Comptes Rendus – Geoscience* **341**, 266–286.

Schulmann, K., Lexa, O., Janoušek, V., Lardeaux, J. M. & Edel, J. B. (2014). Anatomy of a diffuse cryptic suture zone: an example from the Bohemian Massif, European Variscides. *Geology* **42**, 275–278.

Selverstone, J., Franz, G., Thomas, S., & Getty, S. (1992). Fluid variability in 2 GPa eclogites as an indicator of fluid behavior during subduction. *Contributions to Mineralogy and Petrology* **112**, 341–357.

Shand, S. J. (1943). Eruptive Rocks: Their Genesis, Composition, Classification, and Their Relation to Ore-Deposits with a Chapter on Meteorite, John Wiley & Sons, New York, **552.1**, S43.

Sharygin, V., Kryvdik, S. G., Karmanov, N., & Nigmatulina, E. N. (2014). Chlorine-bearing annite from Khlebodarovka enderbites, Azov Sea region, Ukrainian shield. *Mineralogical Journal* **36**, 77–94.

Siivola, J., & Schmid, R. (2007). List of mineral abbreviations. *IUGS Subcommission on the Systematics of Metamorphic Rocks*, 1–14.

Siron, G., Baumgartner, L., & Bouvier, A.-S. (2018). Significance of OH, F and Cl content in biotite during metamorphism of the Western Adamello contact aureole. *Contributions to Mineralogy and Petrology* **173**, 63.

Spruzeniece, L., Piazolo, S., Daczko, N., Kilburn, M. & Putnis, A. (2016). Symplectite formation in the presence of a reactive fluid: insights from hydrothermal experiments. *Journal of Metamorphic Geology* **35**, 281–299.

Stuart, C., A., Piazolo, S. & Daczko, N., R. (2018). The recognition of former melt flux through high-strain zones. *Journal of Metamorphic Geology* **36**, 1049–1069.

Suhr, G., E. Hellebrand, J. E. Snow, H. A. Seck, & A. W. Hofmann (2003). Significance of large, refractory dunite bodies in the upper mantle of the Bay of Islands Ophiolite. *Geochemistry Geophysics Geosystems* **4**, 8605.

Sun, W. & McDonough, W. (1989). Chemical and isotopic systematics of oceanic basalts: implications for mantle composition and processes. In: Saunders, A. D. & Norry, M. J. (eds) Magmatism in Ocean Basins. *Geological Society of London, London, Special Publications* **42**, 313–345.

Svojtka, M., Ackerman, L., Medaris, L. G., Hegner, E., Valley, J. W., Hirajima, T., Jelínek, E. & Hrstka, T. (2016). Petrological, geochemical and Sr–Nd–O isotopic constraints on the origin of garnet and spinel pyroxenites from the Moldanubian zone of the Bohemian Massif. *Journal of Petrology* **57**, 897–920.

Štípská, P., Schulmann, K. & Kröner, A. (2004). Vertical extrusion and middle crustal spreading of omphacite granulite: a model of syn-convergent exhumation (Bohemian Massif, Czech Republic). *Journal of Metamorphic Geology* **22**, 179–198.

Štípská, P., Powell, R., White, R. W. & Baldwin, J. A. (2010). Using calculated chemical potential relationships to account for coronas around kyanite: an example from the Bohemian Massif. *Journal of Metamorphic Geology* **28**, 97–116.

Štípská, P., Powell, R. & Racek, M. (2014a). Rare eclogite–mafic granulite in felsic granulite in Blanský les: precursor of intermediate granulite in the Bohemian Massif? *Journal of Metamorphic Geology* **32**, 325–345.

Štípská, P., Powell, R., Racek, M. & Lexa, O. (2014b). Intermediate granulite produced by transformation of eclogite at a felsic granulite contact, in Blanský les, Bohemian Massif. *Journal of Metamorphic Geology* **32**, 347–370.

Tajčmanová, L., Konopásek, J. & Connolly, J. A. D. (2007). Diffusion-controlled development of silica-undersaturated domains in felsic granulites of the Bohemian Massif (Variscan belt of Central Europe). *Contributions to Mineralogy and Petrology* **153**, 237–250.

Taylor, S. R., McLennan, S. M. (1995). The geochemical evolution of the continental crust. *Reviews in Geophysics* **33**, 241–265.

Teertstra, D. K. & Sherriff, B. L. (1997). Substitutional mechanisms, compositional trends and the end-member formulae of scapolite. *Chemical Geology* **136**, 233–260.

Tischendorf, G., Förster, H.-J., Gottesmann, B., & Rieder, M. (2007). True and brittle micas: Composition and solid-solution series. *Mineralogical Magazine* **71**, 285–320.

Tomkins, H. S., Powell, R. & Ellis, D. J. (2007). The pressure dependence of the zirconium-in-rutile thermometer.

Journal of Metamorphic Geology **25**, 703–713.

Tracy, R. J. (1991). Ba-rich micas from the Franklin Marble, Lime Crest and Sterling Hill, New Jersey. *American Mineralogist* **76**, 1683–1693.

Tsikouras, B., Karipi, S., Rigopoulos, I., Perraki, M., Pomonis, P. & Hatzipanagiotou, K. (2009). Geochemical processes and petrogenetic evolution of rodingite dykes in the ophiolite complex of Othrys (Central Greece). *Lithos **113***, 540–554.

Tumiati, S., Godard, G., Martin, S., Klötzli, U., & Monticelli, D. (2007). Fluid-controlled crustal metasomatism within a high-pressure subducted mélange (Mt. Hochwart, Eastern Italian Alps). *Lithos* **94**, 148–167.

Vellmer, C. (1992). Stoffbestand und Petrogenese von Granuliten und granitischen Gesteinen der südlichen Böhmischen Masse in Niederösterreich. Unpublished Ph.D. Thesis, Göttingen, Georg-August-Universität.

Vrána, S., Janoušek, V. & Franěk, J. (2013). Contrasting mafic to felsic HP–HT granulites of the Blanský les Massif (Moldanubian Zone of southern Bohemia): complexity of mineral assemblages and metamorphic reactions. *Journal of Geosciences* **58**, 347–378.

Wen, S. & Nekvasil, H. (1994). SOLVCALC: An interactive graphics program package for calculating the ternary feldspar solvus and for two-feldspar geothermometry. *Computers & Geosciences* **20**, 1025–1040.

White, A. J. R., Smith, R. E, Nadoll, P. & Legras, M. (2014). Regional-scale Metasomatism in the Fortescue Group Volcanics, Hamersley Basin, Western Australia: implications for hydrothermal ore systems. *Journal of Petrology* **55**, 977–1009.

White, R. W., Powell, R. & Baldvin, J.A. (2008). Calculated phase equilibria involving chemical potentials to investigate the textural evolution of metamorphic rocks. *Journal of Metamorphic Geology* **26**, 181–198.

White, R. W., Powell, R., Holland, T. J. B., Johnson, T. E. & Green, E. C. R. (2014). New mineral activity–composition relations for thermodynamic calculations in metapelitic systems. *Journal of Metamorphic Geology* **32,** 261–286.

Whitney, D. & Evans, B. (2010). Abbreviations for names of rock-forming minerals. *American Mineralogist* **95**, 185–187.

Willner, A. P., Sebazungu, E., Gerya, T. V., Maresch, W. V., & Krohe, A. (2002). Numerical modelling of PT-paths related to rapid exhumation of high-pressure rocks from the crustal root in the Variscan Erzgebirge Dome (Saxony/Germany). *Journal of Geodynamics* **33**, 281–314.

Zaccarini, F., Stumpfl, E.F., & Garuti, G. (2004). Zirconolite and Zr-Th-U minerals in chromitites of the Finero Complex, Western Alps, Italy: Evidence for carbonatite-type metasomatism in a subcontinental mantle plume. *Canadian Mineralogist* **42**, 1825–1845.

Zelinková, T., Racek, M. & Abart, R. (2023). Compositional trends in Ba-, Ti-, and Cl-rich micas from metasomatized mantle rocks of the Gföhl Unit, Bohemian Massif, Austria. *American Mineralogist* **108**, 1840–1851.

Zelinková, T., Racek, M., Janoušek, V., Štípská, P., Abart, R. & Asenbaum, R. (2024). Metasomatic interaction of ultramafic mantle xenoliths with their felsic HP–UHT granulite host (Moldanubian Domain, Bohemian Massif in Lower Austria). *Journal of Petrology,* **65,** egae075.

SUPPLEMENTARY MATERIAL

Table S. 1: coordinates for all localities. Their positions in the simplified geological map is shown in Figure 0. 2 in chapter Geological setting.

Locality	N, E coordinates (WGS 84)	
D441	48.600580	15.53042
D458	48.634938	15.54129
D461	48.631527	15.54989
D554	48.630559	15.51513
DS001	48.345019	15.62593
DS002	48.343758	15.62454
DS008	48.319433	15.54841
DS024	48.329541	15.50360
DS025	48.333606	15.50580
DS027	48.340066	15.49517
DS038	48.369402	15.59302
DS071	48.333068	15.50801
DS072	48.334431	15.50828
DS140	48.334086	15.51244
DS142	48.335810	15.50617
DS148	48.338589	15.61386
DS149	48.334383	15.51095
DS152	48.331880	15.50495
DS153	48.329320	15.52595
DS155	48.287280	15.42408
DS156	48.344570	15.62618
DS157	48.293210	15.45675
DS158	48.629733	15.54138
DS159	48.629350	15.54103
DS160	48.623162	15.56504
DS163	48.240780	15.51218
SL	48.629049	15.54085

Table S. 2: All chemical analyses all of Ba-, Ti-, and Cl-rich micas in wt. % recalculated to 8 cations.

Sample	DS025	DS025	DS025	DS025	DS025-17A	DS025-17A	DS025-17A	DS025-17A	DS025-17A	DS025-17A	DS025-17A	DS025-17A	DS025-17A	DS025-17A	DS025-17A	DS025-17A	DS025-17A
Analysis	Mca-03	Mca-29	Mca-04	Mca-02	Mca-59	Mca-30	Mca-21	Mca-13	Mca-06	Mca-27	Mca-07	Mca-07b	Mca-12	Mca-08	Mca-60	Mca-01	Mca-02
Position	in Grt	in Grt	in Grt	Matrix	in Grt	in Grt	in Grt	in Grt	in Grt	in Grt	in Grt	in Grt	in Grt	in Grt	in Grt	in Grt	in Grt
P_2O_5	0.03	b.d.	b.d.	b.d.	b.d.	b.d.	b.d.	b.d.	b.d.	b.d.	b.d.	b.d.	b.d.	b.d.	b.d.	b.d.	b.d.
SiO_2	30.61	38.65	20.19	34.90	21.76	22.98	21.99	23.00	23.28	23.41	22.58	24.65	22.38	25.68	21.67	22.31	22.69
TiO_2	6.31	1.76	0.82	4.68	6.86	8.05	8.37	7.97	7.27	5.86	5.16	6.52	6.54	6.03	6.70	6.09	4.90
Al_2O_3	17.63	21.37	15.53	17.42	17.78	17.54	17.16	17.41	17.56	16.55	18.69	17.05	17.26	16.61	16.90	17.14	17.60
V_2O_3	b.d.	0.13	b.d.	0.02	b.d.	b.d.	b.d.	b.d.	b.d.	b.d.	b.d.	b.d.	b.d.	b.d.	b.d.	b.d.	b.d.
Cr_2O_3	0.09	0.01	0.27	0.03	0.03	0.25	0.21	0.01	0.36	0.11	0.21	b.d.	b.d.	0.02	b.d.	0.05	0.03
MgO	18.18	22.42	1.16	17.26	6.73	10.26	9.47	9.99	11.16	4.77	5.05	11.02	8.90	11.68	8.48	7.69	8.86
CaO	0.23	0.10	0.26	0.04	0.23	0.27	0.30	0.24	0.24	0.12	0.18	0.12	0.15	0.17	0.15	0.19	0.30
MnO	b.d.	b.d.	b.d.	b.d.	b.d.	b.d.	b.d.	b.d.	b.d.	b.d.	b.d.	b.d.	b.d.	b.d.	b.d.	0.03	b.d.
FeO	5.58	3.31	30.14	6.11	16.71	11.77	12.70	12.65	11.32	21.84	22.11	12.71	15.06	12.23	16.16	17.91	16.12
SrO	0.17	b.d.	0.08	0.20	0.11	0.13	0.16	0.09	0.18	0.19	0.14	0.19	0.10	0.14	0.07	0.14	0.17
BaO	9.83	2.95	21.77	5.04	23.75	23.69	24.48	23.60	22.20	19.86	21.57	20.08	23.10	18.12	24.24	22.72	23.15
Na_2O	0.68	0.69	0.05	0.28	0.25	0.52	0.39	0.45	0.46	0.10	0.26	0.13	0.22	0.12	0.26	0.22	0.28
K_2O	4.97	4.65	0.62	5.96	0.16	0.03	0.05	0.49	0.56	1.76	0.64	2.28	0.65	2.76	0.17	0.57	0.34
F	b.d.	b.d.	b.d.	b.d.	b.d.	b.d.	b.d.	b.d.	b.d.	b.d.	b.d.	b.d.	b.d.	b.d.	b.d.	b.d.	b.d.
Cl	0.36	0.26	10.34	1.09	3.51	2.89	3.13	2.23	2.98	3.86	3.63	3.34	3.96	3.10	3.81	4.18	4.22
Total	94.63	96.03	90.88	91.94	94.36	95.49	95.27	95.90	94.59	94.58	96.60	94.75	94.35	93.55	94.79	95.05	94.40
P	0.00	–	–	–	–	–	–	–	–	–	–	–	–	–	–	–	–
Si	2.45	2.81	2.13	2.79	2.12	2.14	2.09	2.14	2.15	2.25	2.13	2.24	2.13	2.32	2.08	2.13	2.15
Ti	0.38	0.10	0.07	0.28	0.50	0.56	0.60	0.56	0.51	0.42	0.37	0.45	0.47	0.41	0.48	0.44	0.35
Al^{tot}	1.66	1.83	1.93	1.64	2.04	1.93	1.92	1.91	1.91	1.87	2.08	1.83	1.94	1.77	1.92	1.92	1.97
IAl	0.12	0.64	0.05	0.43	0.16	0.07	0.01	0.05	0.07	0.12	0.21	0.07	0.07	0.09	0.00	0.05	0.12
TAl	1.55	1.19	1.87	1.21	1.88	1.86	1.91	1.86	1.85	1.75	1.87	1.76	1.87	1.68	1.92	1.87	1.85
V	–	0.01	–	0.00	–	–	–	–	–	–	–	–	–	–	–	–	–
Cr	0.01	0.00	0.02	0.00	0.00	0.02	0.02	0.00	0.03	0.01	0.02	–	–	0.00	–	0.00	0.00
Mg	2.17	2.43	0.18	2.06	0.98	1.43	1.34	1.39	1.54	0.68	0.71	1.49	1.26	1.57	1.22	1.09	1.25
Ca	0.02	0.01	0.03	0.00	0.02	0.03	0.03	0.02	0.02	0.01	0.02	0.01	0.01	0.02	0.02	0.02	0.03
Mn	–	–	–	–	–	–	–	–	–	–	–	–	–	–	–	0.00	–
Fe^{tot}	0.37	0.20	2.65	0.41	1.36	0.92	1.01	0.98	0.88	1.76	1.75	0.97	1.20	0.92	1.30	1.43	1.28
Sr	0.01	–	0.00	0.01	0.01	0.01	0.01	0.00	0.01	0.01	0.01	0.01	0.01	0.01	0.00	0.01	0.01
Ba	0.31	0.08	0.90	0.16	0.91	0.87	0.91	0.86	0.80	0.75	0.80	0.72	0.86	0.64	0.91	0.85	0.86
Na	0.11	0.10	0.01	0.04	0.05	0.09	0.07	0.08	0.08	0.02	0.05	0.02	0.04	0.02	0.05	0.04	0.05
K	0.51	0.43	0.08	0.61	0.02	0.00	0.01	0.06	0.07	0.22	0.08	0.26	0.08	0.32	0.02	0.07	0.04
F	–	–	–	–	–	–	–	–	–	–	–	–	–	–	–	–	–
Cl	0.05	0.03	1.85	0.15	0.58	0.46	0.50	0.35	0.47	0.63	0.58	0.52	0.64	0.47	0.62	0.68	0.68
O	0.76	0.19	0.13	0.56	1.00	1.13	1.20	1.11	1.01	0.85	0.73	0.89	0.94	0.82	0.97	0.87	0.70
OH	1.19	1.78	0.02	1.29	0.42	0.41	0.30	0.53	0.52	0.52	0.69	0.59	0.42	0.71	0.41	0.45	0.62
XFe^{tot}	0.15	0.08	0.94	0.17	0.58	0.39	0.43	0.42	0.36	0.72	0.71	0.39	0.49	0.37	0.52	0.57	0.51
$Mg+Fe^{tot}$	2.55	2.63	2.83	2.46	2.34	2.35	2.35	2.37	2.41	2.44	2.46	2.46	2.46	2.50	2.51	2.52	2.53

b.d. below detection limit

Table S. 2 (continued): All chemical analyses all of Ba-, Ti-, and Cl-rich micas in wt. % recalculated to 8 cations.

Sample	DS025-17A	DS025-17A	DS025-17A	DS025-17A	DS025-17A	DS025-17A	DS025-17A	DS072C	DS072C	DS072C	DS072C	DS072C	DS072C	DS072C	DS072C	DS072C	DS072C
Analysis Position	Mca-63 in Grt	Mca-09 in Grt	Mca-15 in Grt	Mca-25 in Grt	Mca-84 in Grt	Mca-14 in Grt	Mca-64 in Grt	Mca-11 Matrix	Mca-15 Matrix	Mca-06 Matrix	Mca-07 Matrix	Mca-09 Matrix	Mca-03 Matrix	Mca-12 Matrix	Mca-08 Matrix	Mca-04 Matrix	Mca-10 Matrix
P_2O_5	0.06	0.05	b.d.	b.d.	0.05	b.d.	b.d.	b.d.	b.d.	b.d.	b.d.	b.d.	b.d.	b.d.	b.d.	b.d.	b.d.
SiO_2	25.17	23.33	22.18	21.17	21.81	20.06	20.62	32.04	31.93	32.66	33.05	32.17	34.11	36.58	35.66	34.07	30.94
TiO_2	5.85	5.04	5.56	4.00	3.38	0.72	0.54	7.10	5.45	5.89	5.89	6.54	5.28	4.82	4.94	4.99	5.69
Al_2O_3	16.17	16.78	17.27	17.13	17.45	16.51	16.46	17.52	18.11	17.64	17.70	17.21	17.40	17.09	17.12	17.14	16.72
V_2O_3	b.d.	b.d.	b.d.	b.d.	b.d.	b.d.	b.d.	b.d.	b.d.	b.d.	b.d.	b.d.	b.d.	0.04	0.04	b.d.	b.d.
Cr_2O_3	0.02	0.02	0.02	0.10	b.d.	b.d.	b.d.	0.25	0.97	0.33	0.25	0.27	0.28	0.15	0.23	0.22	0.24
MgO	11.45	9.71	6.57	7.34	7.90	3.79	5.56	15.79	17.25	17.11	17.37	16.79	17.52	19.15	18.98	18.33	17.47
CaO	0.29	0.07	0.25	0.23	0.31	0.44	0.51	0.09	0.16	0.10	0.13	0.02	0.04	0.04	0.04	0.02	0.04
MnO	0.02	b.d.	b.d.	b.d.	b.d.	0.05	b.d.	b.d.	b.d.	b.d.	b.d.	b.d.	b.d.	b.d.	b.d.	b.d.	b.d.
FeO	13.13	14.99	20.28	18.92	18.92	26.41	26.02	7.28	5.77	7.03	6.97	7.31	6.91	5.92	5.95	6.63	6.23
SrO	0.17	0.17	0.08	0.16	b.d.	0.11	0.10	0.15	0.14	0.17	0.20	0.15	0.21	0.19	0.17	0.18	0.15
BaO	18.88	21.89	22.86	23.62	22.38	23.50	23.78	10.35	9.81	8.57	8.00	9.54	6.97	3.17	4.17	5.19	6.60
Na_2O	0.18	0.31	0.38	0.14	0.12	0.08	0.06	0.64	0.49	0.87	0.87	0.57	0.70	0.94	0.81	0.77	0.68
K_2O	2.47	0.97	0.17	0.49	0.91	0.05	0.04	5.37	5.63	5.60	5.94	5.74	6.48	7.74	7.49	7.22	6.57
F	b.d.	b.d.	b.d.	b.d.	b.d.	b.d.	b.d.	b.d.	b.d.	b.d.	b.d.	b.d.	b.d.	b.d.	b.d.	b.d.	b.d.
Cl	3.15	4.46	3.28	4.95	6.02	9.25	9.59	0.23	0.19	0.18	0.16	0.18	0.19	0.14	0.13	0.18	0.15
Total	93.86	93.32	95.60	93.27	93.23	91.71	93.68	96.57	95.71	95.97	96.37	96.30	95.91	95.83	95.58	94.75	91.32
P	0.00	0.00	–	–	0.00	–	–	–	–	–	–	–	–	–	–	–	–
Si	2.29	2.21	2.12	2.07	2.10	2.06	2.05	2.56	2.53	2.56	2.57	2.55	2.64	2.73	2.69	2.62	2.51
Ti	0.40	0.36	0.40	0.29	0.24	0.06	0.04	0.43	0.33	0.35	0.34	0.39	0.31	0.27	0.28	0.29	0.35
Al^{tot}	1.73	1.87	1.94	1.98	1.98	2.00	1.93	1.65	1.69	1.63	1.62	1.61	1.59	1.50	1.52	1.55	1.60
IAl	0.02	0.08	0.06	0.05	0.08	0.06	0.00	0.21	0.22	0.19	0.19	0.15	0.23	0.24	0.22	0.18	0.10
TAl	1.71	1.79	1.88	1.93	1.90	1.94	1.93	1.44	1.47	1.44	1.43	1.45	1.36	1.27	1.31	1.38	1.49
V	–	–	–	–	–	–	–	–	–	–	–	–	–	0.00	0.00	–	–
Cr	0.00	0.00	0.00	0.01	–	–	–	0.02	0.06	0.02	0.02	0.02	0.02	0.01	0.01	0.01	0.02
Mg	1.55	1.37	0.94	1.07	1.13	0.58	0.82	1.88	2.04	2.00	2.01	1.98	2.02	2.13	2.14	2.10	2.11
Ca	0.03	0.01	0.03	0.02	0.03	0.05	0.05	0.01	0.01	0.01	0.01	0.00	0.00	0.00	0.00	0.00	0.00
Mn	0.00	–	–	–	–	0.00	–	–	–	–	–	–	–	–	–	–	–
Fe^{tot}	1.00	1.19	1.62	1.55	1.52	2.27	2.16	0.49	0.38	0.46	0.45	0.48	0.45	0.37	0.38	0.43	0.42
Sr	0.01	0.01	0.00	0.01	–	0.01	0.01	0.01	0.01	0.01	0.01	0.01	0.01	0.01	0.01	0.01	0.01
Ba	0.67	0.81	0.86	0.91	0.84	0.95	0.93	0.32	0.30	0.26	0.24	0.30	0.21	0.09	0.12	0.16	0.21
Na	0.03	0.06	0.07	0.03	0.02	0.02	0.01	0.10	0.08	0.13	0.13	0.09	0.11	0.14	0.12	0.11	0.11
K	0.29	0.12	0.02	0.06	0.11	0.01	0.01	0.55	0.57	0.56	0.59	0.58	0.64	0.74	0.72	0.71	0.68
F	–	–	–	–	–	–	–	–	–	–	–	–	–	–	–	–	–
Cl	0.48	0.72	0.53	0.82	0.98	1.61	1.61	0.03	0.02	0.02	0.02	0.02	0.02	0.02	0.02	0.02	0.02
O	0.80	0.72	0.80	0.59	0.49	0.11	0.08	0.85	0.65	0.70	0.69	0.78	0.62	0.54	0.56	0.58	0.69
OH	0.72	0.57	0.67	0.59	0.53	0.28	0.31	1.12	1.32	1.28	1.29	1.20	1.36	1.44	1.42	1.40	1.29
XFe^{tot}	0.39	0.46	0.63	0.59	0.57	0.80	0.72	0.21	0.16	0.19	0.18	0.20	0.18	0.15	0.15	0.17	0.17
$Mg+Fe^{tot}$	2.55	2.56	2.56	2.62	2.66	2.85	2.98	2.37	2.42	2.46	2.47	2.47	2.47	2.50	2.51	2.53	2.53

b.d. below detection limit

Table S. 2 (continued): All chemical analyses all of Ba-, Ti-, and Cl-rich micas in wt. % recalculated to 8 cations.

Sample	DS072C	DS072C	DS142C	DS142C	DS142C	DS142C	DS148A	DS148A	DS148A	DS148A	DS148A	DS148A	DS148A	DS148A	DS148A	DS148A	DS148A
Analysis	Mca-01	Mca-02	Mca-34	Mca-01b	Mca-01	Mca-33	Mca-M39	Mca-M40	Mca-M41	Mca-M36	Mca-M30	Mca-M44	Mca-02	Mca-M48	Mca-M33	Mca-M42	Mca-M45
Position	Matrix	Matrix	in Grt	Matrix	Matrix	Matrix	in Grt	in Grt	in Grt	in Grt	in Grt	in Grt	in Grt	in Grt	in Grt	in Grt	in Grt
P_2O_5	b.d.	b.d.	b.d.	b.d.	b.d.	b.d.	0.06	b.d.	b.d.	b.d.	b.d.	0.03	b.d.	b.d.	b.d.	0.05	b.d.
SiO_2	35.28	35.05	33.43	31.99	31.94	33.12	23.84	23.53	23.22	22.63	24.34	22.28	23.51	24.15	21.20	23.82	21.77
TiO_2	4.72	4.67	2.58	6.03	6.12	3.82	12.52	12.55	11.30	11.17	8.12	11.03	9.83	9.62	7.72	11.05	10.46
Al_2O_3	16.78	16.69	18.73	18.08	17.52	17.62	18.82	18.93	18.44	18.48	19.35	18.50	18.00	18.75	17.83	18.17	18.00
V_2O_3	b.d.	0.02	b.d.	b.d.	b.d.	b.d.	b.d.	b.d.	b.d.	b.d.	b.d.	b.d.	b.d.	b.d.	b.d.	b.d.	b.d.
Cr_2O_3	0.23	0.17	0.19	0.07	0.03	0.09	0.06	0.06	0.11	0.05	0.02	0.03	b.d.	0.06	0.09	0.09	0.08
MgO	19.02	18.63	20.00	17.31	18.44	19.71	9.19	9.16	10.28	9.75	8.79	10.21	9.15	10.82	2.83	11.94	8.85
CaO	0.03	0.04	0.06	0.09	0.11	0.06	0.25	0.24	0.26	0.38	0.49	0.44	0.37	0.29	0.41	0.31	0.40
MnO	b.d.	b.d.	b.d.	b.d.	b.d.	b.d.	b.d.	b.d.	b.d.	b.d.	b.d.	b.d.	b.d.	b.d.	b.d.	b.d.	b.d.
FeO	6.62	7.55	4.87	5.39	5.24	4.72	8.00	8.25	8.92	9.75	11.70	9.21	11.92	9.68	21.13	7.81	12.03
SrO	0.20	0.20	0.27	0.20	0.18	0.28	0.19	0.19	0.14	b.d.	0.30	0.09	0.18	0.20	0.26	0.12	b.d.
BaO	3.75	3.77	7.28	10.09	10.16	7.72	22.33	22.27	22.65	22.57	23.13	24.10	22.44	21.42	23.17	22.13	23.74
Na_2O	0.75	0.69	0.53	0.60	0.72	0.48	0.34	0.28	0.24	0.24	0.20	0.20	0.12	0.68	0.14	0.34	0.27
K_2O	7.03	6.85	6.52	4.88	5.35	6.16	1.13	1.16	0.95	0.91	0.53	0.48	1.30	0.68	0.15	1.02	0.37
F	b.d.	b.d.	b.d.	b.d.	b.d.	b.d.	b.d.	b.d.	b.d.	b.d.	b.d.	b.d.	b.d.	b.d.	b.d.	b.d.	b.d.
Cl	0.16	0.15	1.16	0.36	0.35	0.91	0.75	0.69	0.48	1.14	3.09	0.95	0.96	0.71	3.92	0.36	1.92
Total	94.41	94.35	94.45	94.73	95.80	93.78	96.74	96.61	96.50	95.92	96.99	96.59	96.81	96.33	94.93	96.84	95.95
P	–	–	–	–	–	–	0.00	–	–	–	–	0.00	–	–	–	0.00	–
Si	2.70	2.69	2.57	2.57	2.52	2.59	2.19	2.16	2.13	2.09	2.24	2.06	2.16	2.18	2.12	2.14	2.05
Ti	0.27	0.27	0.15	0.36	0.36	0.22	0.86	0.87	0.78	0.78	0.56	0.77	0.68	0.65	0.58	0.75	0.74
Al^{tot}	1.51	1.51	1.70	1.71	1.63	1.63	2.04	2.05	1.99	2.02	2.10	2.02	1.95	1.99	2.10	1.92	2.00
IAl	0.21	0.20	0.27	0.27	0.14	0.22	0.22	0.21	0.12	0.11	0.33	0.09	0.12	0.17	0.21	0.06	0.05
TAl	1.30	1.31	1.43	1.43	1.48	1.41	1.81	1.84	1.87	1.91	1.76	1.94	1.84	1.82	1.88	1.86	1.95
V	–	0.00	–	–	–	–	–	–	–	–	–	–	–	–	–	–	–
Cr	0.01	0.01	0.01	0.00	0.00	0.01	0.00	0.00	0.01	0.00	0.00	0.00	–	0.00	0.01	0.01	0.01
Mg	2.17	2.13	2.30	2.07	2.17	2.30	1.26	1.26	1.41	1.35	1.21	1.41	1.26	1.45	0.42	1.60	1.24
Ca	0.00	0.00	0.00	0.01	0.01	0.01	0.02	0.02	0.03	0.04	0.05	0.04	0.04	0.03	0.04	0.03	0.04
Mn	–	–	–	–	–	–	–	–	–	–	–	–	–	–	–	–	–
Fe^{tot}	0.42	0.49	0.31	0.36	0.35	0.31	0.61	0.63	0.68	0.75	0.90	0.71	0.92	0.73	1.76	0.59	0.95
Sr	0.01	0.01	0.01	0.01	0.01	0.01	0.01	0.01	0.01	–	0.02	0.01	0.01	0.01	0.01	0.01	–
Ba	0.11	0.11	0.22	0.32	0.31	0.24	0.80	0.80	0.81	0.82	0.83	0.88	0.81	0.76	0.91	0.78	0.88
Na	0.11	0.10	0.08	0.09	0.11	0.07	0.06	0.05	0.04	0.04	0.04	0.04	0.02	0.12	0.03	0.06	0.05
K	0.69	0.67	0.64	0.50	0.54	0.61	0.13	0.14	0.11	0.11	0.06	0.06	0.15	0.08	0.02	0.12	0.04
F	–	–	–	–	–	–	–	–	–	–	–	–	–	–	–	–	–
Cl	0.02	0.02	0.15	0.05	0.05	0.12	0.12	0.11	0.07	0.18	0.48	0.15	0.15	0.11	0.66	0.05	0.31
O	0.54	0.54	0.30	0.73	0.73	0.45	1.73	1.74	1.56	1.56	1.12	1.54	1.36	1.30	1.16	1.49	1.48
OH	1.44	1.44	1.55	1.22	1.23	1.43	0.16	0.16	0.37	0.27	0.40	0.31	0.49	0.59	0.18	0.45	0.21
XFe^{tot}	0.16	0.19	0.12	0.15	0.14	0.12	0.33	0.34	0.33	0.36	0.43	0.34	0.42	0.33	0.81	0.27	0.43
$Mg+Fe^{to}_{t}$	2.59	2.62	2.61	2.43	2.51	2.61	1.87	1.89	2.09	2.10	2.10	2.13	2.17	2.18	2.19	2.19	2.19

b.d. below detection limit

Table S. 2 (continued): All chemical analyses all of Ba-, Ti-, and Cl-rich micas in wt. % recalculated to 8 cations.

Sample	DS148A	DS148A	DS148A	DS148A	DS148A	DS148A	DS148A	DS148A	DS148A	DS148A	DS148A	DS148A	DS148A	DS148A	DS148A	DS148A	DS148C
Analysis	Mca-M01	Mca-M04	Mca-M43	Mca-01	Mca-M17	Mca-M02	Mca-M14	Mca-M27	Mca-M03	Mca-M05	Mca-06	Mca-08	Mca-M28	Mca-M21	Mca-04	Mca-M35	Mca-22
Position	in Grt	in Grt	in Grt	in Grt	in Grt	in Grt	in Grt	in Grt	in Grt	in Grt	in Grt	in Grt	in Grt	in Grt	in Grt	in Grt	in Grt
P_2O_5	b.d.	b.d.	b.d.	b.d.	b.d.	b.d.	b.d.	b.d.	b.d.	b.d.	0.03	0.03	b.d.	b.d.	b.d.	b.d.	0.08
SiO_2	24.60	25.09	25.65	27.75	24.05	23.93	22.25	24.37	24.09	25.25	27.00	29.12	23.81	26.09	29.03	28.75	29.12
TiO_2	10.53	10.68	10.35	9.16	10.27	10.34	11.20	9.28	10.07	10.01	8.68	7.68	9.15	9.43	8.42	8.34	4.90
Al_2O_3	18.22	17.77	17.62	17.08	17.74	17.68	17.87	17.46	17.53	17.05	18.50	18.43	17.20	17.29	16.95	16.96	18.52
V_2O_3	0.19	b.d.	b.d.	b.d.	b.d.	b.d.	b.d.	b.d.	b.d.	b.d.	b.d.	b.d.	b.d.	b.d.	b.d.	b.d.	0.06
Cr_2O_3	0.13	0.07	0.05	0.02	b.d.	0.11	0.08	b.d.	0.06	0.08	0.12	0.05	0.03	0.05	0.07	0.05	0.32
MgO	11.05	12.31	13.24	13.00	12.39	12.18	11.85	11.22	12.13	12.21	14.68	15.56	11.24	13.83	15.44	15.75	16.63
CaO	0.27	0.23	0.31	0.31	0.19	0.22	0.24	0.21	0.54	0.26	0.26	0.27	0.29	0.40	0.51	0.23	0.26
MnO	b.d.	b.d.	b.d.	b.d.	b.d.	b.d.	b.d.	b.d.	b.d.	b.d.	b.d.	b.d.	b.d.	b.d.	b.d.	b.d.	b.d.
FeO	9.90	7.65	7.50	8.38	8.30	8.65	8.77	10.20	8.99	9.44	6.75	5.94	10.64	7.87	6.49	6.46	4.92
SrO	0.27	0.30	0.14	0.23	0.07	0.23	0.24	0.31	0.18	0.20	0.23	0.25	0.31	0.24	0.22	0.12	0.21
BaO	20.24	19.97	19.50	16.16	20.81	20.28	21.04	20.69	20.26	19.20	17.59	14.39	19.96	18.52	14.93	13.62	13.13
Na_2O	0.55	0.32	0.36	0.26	0.42	0.47	0.30	0.20	0.41	0.40	0.44	0.45	0.22	0.45	0.42	0.43	0.31
K_2O	1.23	1.69	2.27	3.44	1.44	1.40	1.12	1.65	1.45	1.89	2.76	3.91	1.72	2.15	3.99	4.13	3.67
F	b.d.	b.d.	b.d.	b.d.	b.d.	b.d.	b.d.	b.d.	b.d.	b.d.	b.d.	b.d.	b.d.	b.d.	b.d.	b.d.	b.d.
Cl	0.27	0.25	0.31	0.57	0.35	0.53	0.24	1.06	0.61	0.14	0.26	0.32	1.05	0.42	0.49	0.32	2.14
Total	97.16	96.08	96.98	95.78	95.68	95.49	94.95	95.58	95.70	95.98	97.03	96.08	94.56	96.33	96.48	94.83	92.11
P	–	–	–	–	–	–	–	–	–	–	0.00	0.00	–	–	–	–	0.01
Si	2.19	2.23	2.23	2.39	2.16	2.15	2.04	2.21	2.16	2.24	2.28	2.41	2.18	2.26	2.41	2.40	2.46
Ti	0.70	0.71	0.68	0.59	0.69	0.70	0.77	0.63	0.68	0.67	0.55	0.48	0.63	0.61	0.53	0.52	0.31
Al^{tot}	1.91	1.86	1.81	1.73	1.88	1.87	1.93	1.87	1.85	1.78	1.84	1.80	1.85	1.77	1.66	1.67	1.84
IAl	0.10	0.10	0.04	0.12	0.04	0.02	0.00	0.08	0.01	0.02	0.12	0.20	0.03	0.03	0.07	0.07	0.30
TAl	1.81	1.77	1.77	1.61	1.84	1.85	1.93	1.79	1.84	1.76	1.72	1.59	1.82	1.74	1.59	1.60	1.54
V	0.01	–	–	–	–	–	–	–	–	–	–	–	–	–	–	–	0.00
Cr	0.01	0.00	0.00	0.00	–	0.01	0.01	–	0.00	0.01	0.01	0.00	0.00	0.00	0.00	0.00	0.02
Mg	1.46	1.63	1.72	1.67	1.66	1.63	1.62	1.52	1.62	1.62	1.85	1.92	1.53	1.79	1.91	1.96	2.09
Ca	0.03	0.02	0.03	0.03	0.02	0.02	0.02	0.02	0.05	0.03	0.02	0.02	0.03	0.04	0.05	0.02	0.02
Mn	–	–	–	–	–	–	–	–	–	–	–	–	–	–	–	–	–
Fe^{tot}	0.74	0.57	0.55	0.60	0.62	0.65	0.67	0.77	0.67	0.70	0.48	0.41	0.81	0.57	0.45	0.45	0.35
Sr	0.01	0.02	0.01	0.01	0.00	0.01	0.01	0.02	0.01	0.01	0.01	0.01	0.02	0.01	0.01	0.01	0.01
Ba	0.71	0.70	0.67	0.55	0.73	0.71	0.75	0.74	0.71	0.67	0.58	0.47	0.71	0.63	0.49	0.45	0.43
Na	0.09	0.06	0.06	0.04	0.07	0.08	0.05	0.03	0.07	0.07	0.07	0.07	0.04	0.08	0.07	0.07	0.05
K	0.14	0.19	0.25	0.38	0.16	0.16	0.13	0.19	0.17	0.21	0.30	0.41	0.20	0.24	0.42	0.44	0.40
F	–	–	–	–	–	–	–	–	–	–	–	–	–	–	–	–	–
Cl	0.04	0.04	0.05	0.08	0.05	0.08	0.04	0.16	0.09	0.02	0.04	0.04	0.16	0.06	0.07	0.05	0.31
O	1.41	1.43	1.36	1.19	1.39	1.40	1.54	1.27	1.36	1.34	1.10	0.95	1.26	1.23	1.05	1.05	0.62
OH	0.55	0.53	0.60	0.73	0.56	0.52	0.42	0.57	0.55	0.64	0.86	1.00	0.58	0.71	0.88	0.90	1.07
XFe^{tot}	0.33	0.26	0.24	0.27	0.27	0.29	0.29	0.34	0.29	0.30	0.21	0.18	0.35	0.24	0.19	0.19	0.14
$Mg+Fe^{tot}$	2.20	2.20	2.26	2.27	2.28	2.28	2.29	2.29	2.30	2.32	2.33	2.33	2.34	2.36	2.36	2.42	2.44

b.d. below detection limit

Table S. 2 (continued): All chemical analyses all of Ba-, Ti-, and Cl-rich micas in wt. % recalculated to 8 cations.

Sample	DS148C	DS148C	DS148C	DS148C	DS148C	DS148C	DS148C	DS148C	SL1-X-3	SL-PX-1-Y	SL-PX-1-Y	SL-PX-1-Y	SL-PX-1-Y	SL-PX-1-Y	SL-PX-1-Y	SL-PX-1-Y	SL-PX-1-Y
Analysis Position	Mca-29 in Grt	Mca-28 in Grt	Mca-13 Matrix	Mca-02 Matrix	Mca-03 Matrix	Mca-10 Matrix	Mca-05 Matrix	Mca-11 Matrix	Mca-02 in Grt	Mca-80 in Grt	Mca-70 in Grt	Mca-08 in Grt	Mca-24 in Grt	Mca-83 in Grt	Mca-75 in Grt	Mca-61 in Grt	Mca-27 in Grt
P_2O_5	0.05	b.d.	b.d.	b.d.	b.d.	b.d.	b.d.	b.d.	b.d.	b.d.	b.d.	b.d.	b.d.	0.05	b.d.	0.25	b.d.
SiO_2	27.62	22.05	33.67	34.82	34.66	34.80	34.90	35.69	30.73	36.75	31.41	34.81	35.75	32.85	30.48	30.98	37.01
TiO_2	5.87	0.34	3.90	4.20	3.80	3.66	3.90	2.73	7.21	1.64	3.05	2.67	6.18	4.37	2.61	3.68	2.97
Al_2O_3	17.65	15.05	18.57	17.84	18.38	17.53	17.77	17.91	15.39	21.20	21.38	20.12	17.29	17.42	18.86	18.60	19.31
V_2O_3	b.d.	b.d.	b.d.	0.07	0.10	0.08	0.07	0.10	b.d.	b.d.	b.d.	b.d.	0.06	b.d.	b.d.	b.d.	0.02
Cr_2O_3	0.29	0.06	0.21	0.26	0.43	0.27	0.24	0.20	0.64	0.22	0.26	0.21	0.10	0.16	0.27	0.28	0.13
MgO	16.00	4.83	20.21	20.89	21.15	20.00	21.16	20.80	12.94	16.61	16.58	18.48	19.92	17.27	14.93	16.90	19.33
CaO	0.15	0.28	0.04	0.03	0.05	0.03	0.01	0.10	0.36	1.08	0.14	0.22	0.11	0.18	0.24	0.18	0.78
MnO	b.d.	0.03	0.02	b.d.	b.d.	b.d.	b.d.	b.d.	b.d.	b.d.	0.02	b.d.	0.02	0.03	b.d.	b.d.	0.06
FeO	7.02	28.50	3.63	2.81	2.76	4.38	3.00	4.04	9.86	5.74	5.48	3.84	3.37	5.53	9.53	6.85	5.64
SrO	0.19	0.15	0.15	0.14	0.12	0.14	0.23	0.16	0.16	0.36	0.45	0.28	0.42	0.35	0.25	b.d.	0.24
BaO	15.48	20.35	8.19	6.49	6.59	6.08	6.80	4.93	11.39	5.22	10.34	11.16	8.76	14.01	11.91	14.23	7.24
Na_2O	0.30	0.09	0.45	0.42	0.42	0.42	0.43	0.47	0.40	0.43	0.31	0.73	0.81	0.50	0.67	0.58	0.61
K_2O	3.12	1.16	6.60	7.26	7.28	7.38	7.33	7.81	4.98	4.62	4.33	2.52	3.91	2.07	2.76	2.55	3.51
F	b.d.	b.d.	b.d.	b.d.	b.d.	b.d.	0.08	b.d.	b.d.	b.d.	b.d.	b.d.	b.d.	b.d.	b.d.	b.d.	b.d.
Cl	2.00	10.76	0.34	0.27	0.36	0.57	0.36	0.58	1.07	0.55	0.84	0.80	0.46	1.24	1.67	2.26	0.90
Total	93.74	92.89	95.63	95.22	95.75	94.78	95.83	94.94	94.06	93.86	93.74	95.03	96.71	94.78	92.50	95.07	96.87
P	0.00	–	–	–	–	–	–	–	–	–	–	–	–	0.00	–	0.02	–
Si	2.36	2.17	2.58	2.64	2.61	2.66	2.63	2.68	2.60	2.86	2.54	2.76	2.76	2.72	2.57	2.55	2.81
Ti	0.38	0.03	0.22	0.24	0.21	0.21	0.22	0.15	0.46	0.10	0.19	0.16	0.36	0.27	0.17	0.23	0.17
Al^{tot}	1.78	1.75	1.68	1.60	1.63	1.58	1.58	1.59	1.54	1.94	2.04	1.88	1.57	1.70	1.87	1.80	1.73
IAl	0.13	0.00	0.25	0.24	0.24	0.24	0.21	0.27	0.14	0.80	0.57	0.64	0.33	0.41	0.44	0.36	0.55
TAl	1.64	1.75	1.42	1.36	1.39	1.34	1.37	1.32	1.40	1.14	1.46	1.24	1.24	1.28	1.43	1.45	1.19
V	–	–	–	0.00	0.01	0.00	0.00	0.01	–	–	–	–	0.00	–	–	–	0.00
Cr	0.02	0.00	0.01	0.02	0.03	0.02	0.01	0.01	0.04	0.01	0.02	0.01	0.01	0.01	0.02	0.02	0.01
Mg	2.04	0.71	2.31	2.36	2.37	2.28	2.38	2.33	1.63	1.93	2.00	2.18	2.29	2.13	1.87	2.07	2.19
Ca	0.01	0.03	0.00	0.00	0.00	0.00	0.00	0.01	0.03	0.09	0.01	0.02	0.01	0.02	0.02	0.02	0.06
Mn	–	0.00	0.00	–	–	–	–	–	–	–	0.00	–	0.00	0.00	–	–	0.00
Fe^{tot}	0.50	2.35	0.23	0.18	0.17	0.28	0.19	0.25	0.70	0.37	0.37	0.25	0.22	0.38	0.67	0.47	0.36
Sr	0.01	0.01	0.01	0.01	0.01	0.01	0.01	0.01	0.01	0.02	0.02	0.01	0.02	0.02	0.01	–	0.01
Ba	0.52	0.79	0.25	0.19	0.19	0.18	0.20	0.15	0.38	0.16	0.33	0.35	0.26	0.45	0.39	0.46	0.22
Na	0.05	0.02	0.07	0.06	0.06	0.06	0.06	0.07	0.07	0.06	0.05	0.11	0.12	0.08	0.11	0.09	0.09
K	0.34	0.15	0.64	0.70	0.70	0.72	0.71	0.75	0.54	0.46	0.45	0.26	0.38	0.22	0.30	0.27	0.34
F	–	–	–	–	–	–	–	–	–	–	–	–	–	–	–	–	–
Cl	0.29	1.80	0.04	0.04	0.05	0.07	0.05	0.07	0.15	0.07	0.12	0.11	0.06	0.17	0.24	0.31	0.12
O	0.75	0.05	0.45	0.48	0.43	0.42	0.44	0.31	0.92	0.19	0.37	0.32	0.72	0.54	0.33	0.46	0.34
OH	0.96	0.15	1.51	1.49	1.52	1.51	1.51	1.62	0.93	1.74	1.51	1.57	1.22	1.28	1.43	1.23	1.54
XFe^{tot}	0.20	0.77	0.09	0.07	0.07	0.11	0.07	0.10	0.30	0.16	0.16	0.10	0.09	0.15	0.26	0.19	0.14
$Mg+Fe^{tot}$	2.54	3.06	2.54	2.54	2.55	2.56	2.57	2.58	2.33	2.30	2.37	2.44	2.51	2.51	2.55	2.55	2.55

b.d. below detection limit

Table S. 2 (continued): All chemical analyses all of Ba-, Ti-, and Cl-rich micas in wt. % recalculated to 8 cations.

Sample	SL-PX-1-Y	SL-PX-1-Y	SL-PX-1-Y	SL-PX-1-Y	SL-PX-1-Y	SL-PX-1-Y	SL-PX-1-Y	SL-PX-1-Y	SL-PX-1-Y	SL-PX-1-Y	SL-PX-A	SL-PX-A	SL-PX-A	SL-PX-A	SL-PX-A
Analysis	Mca-66	Mca-79	Mca-68	Mca-60	Mca-85	Mca-65	Mca-62	Mca-82	Mca-11	Mca-12	Mca-10	Mca-14	Mca-13	Mca-12	Mca-11
Position	in Grt	in Grt	in Grt	in Grt	in Grt	in Grt	in Grt	in Grt	in Cpx	in Cpx	in Grt	in Grt	in Cpx	in Cpx	in Cpx
P_2O_5	0.44	b.d.	0.17	0.11	b.d.	0.11	0.07	b.d.	0.04	0.04	b.d.	b.d.	b.d.	b.d.	b.d.
SiO_2	33.83	25.47	21.57	20.70	21.53	18.93	25.89	27.67	29.83	30.05	32.36	32.89	29.81	30.79	30.37
TiO_2	0.09	1.00	0.80	0.05	0.29	0.07	0.83	0.16	5.30	5.28	6.28	6.61	5.96	5.40	5.76
Al_2O_3	20.31	16.68	15.09	15.43	15.60	15.20	14.47	17.10	16.35	16.28	20.01	17.36	16.53	15.44	15.29
V_2O_3	b.d.	b.d.	b.d.	b.d.	b.d.	b.d.	b.d.	b.d.	b.d.	b.d.	b.d.	0.09	b.d.	0.07	0.06
Cr_2O_3	0.21	0.18	0.27	0.02	0.08	0.02	0.18	0.12	0.35	0.34	0.06	0.18	0.77	0.51	0.56
MgO	20.02	5.90	4.61	5.98	5.54	2.34	9.97	11.98	15.97	16.10	17.27	18.55	14.43	14.05	13.95
CaO	1.16	0.88	0.30	0.75	0.18	0.17	1.01	0.12	0.37	0.39	0.08	0.28	0.21	0.75	0.34
MnO	b.d.	b.d.	0.08	b.d.	0.02	0.03	0.05	0.10	b.d.	b.d.	b.d.	0.02	0.02	b.d.	b.d.
FeO	3.28	25.12	26.22	24.99	26.20	30.15	23.07	20.21	7.73	8.16	3.67	4.81	9.27	10.65	10.79
SrO	b.d.	0.38	b.d.	0.83	0.17	b.d.	0.91	0.19	0.15	0.16	0.20	0.21	0.14	0.18	0.19
BaO	8.97	18.14	19.64	21.57	20.00	22.76	17.68	11.73	13.64	13.87	13.83	11.43	13.35	12.85	12.85
Na_2O	0.65	0.20	0.19	0.13	0.16	0.05	0.20	0.33	0.64	0.66	0.40	0.76	0.70	0.59	0.45
K_2O	3.84	1.13	1.09	0.61	0.99	0.19	1.13	0.47	3.66	3.79	3.42	2.89	3.71	3.85	3.91
F	b.d.	b.d.	b.d.	b.d.	b.d.	b.d.	b.d.	b.d.	b.d.	b.d.	b.d.	b.d.	b.d.	b.d.	b.d.
Cl	0.86	8.00	9.07	10.04	8.97	10.98	7.99	5.28	1.36	1.33	0.57	0.28	1.67	1.67	2.05
Total	92.79	95.08	90.03	91.17	90.76	90.02	95.45	90.18	94.05	95.12	97.58	96.07	94.89	95.12	94.51
P	0.03	–	0.01	0.01	–	0.01	0.01	–	0.00	0.00	–	–	–	–	–
Si	2.66	2.37	2.19	2.08	2.15	2.01	2.34	2.49	2.50	2.49	2.58	2.62	2.50	2.58	2.57
Ti	0.01	0.07	0.06	0.00	0.02	0.01	0.06	0.01	0.33	0.33	0.38	0.40	0.38	0.34	0.37
Al^{tot}	1.88	1.83	1.80	1.83	1.84	1.91	1.54	1.81	1.62	1.59	1.88	1.63	1.63	1.53	1.53
IAl	0.54	0.20	0.00	0.00	0.00	0.00	0.00	0.30	0.12	0.09	0.46	0.26	0.14	0.11	0.10
TAl	1.34	1.63	1.80	1.83	1.84	1.91	1.54	1.51	1.50	1.51	1.42	1.38	1.50	1.42	1.43
V	–	–	–	–	–	–	–	–	–	–	–	0.01	–	0.00	0.00
Cr	0.01	0.01	0.02	0.00	0.01	0.00	0.01	0.01	0.02	0.02	0.00	0.01	0.05	0.03	0.04
Mg	2.34	0.82	0.70	0.90	0.83	0.37	1.35	1.61	2.00	1.99	2.05	2.21	1.81	1.76	1.76
Ca	0.10	0.09	0.03	0.08	0.02	0.02	0.10	0.01	0.03	0.03	0.01	0.02	0.02	0.07	0.03
Mn	–	–	0.01	–	0.00	0.00	0.00	0.01	–	–	–	0.00	0.00	–	–
Fe^{tot}	0.22	1.96	2.22	2.10	2.19	2.68	1.75	1.52	0.54	0.57	0.24	0.32	0.65	0.75	0.77
Sr	–	0.02	–	0.05	0.01	–	0.05	0.01	0.01	0.01	0.01	0.01	0.01	0.01	0.01
Ba	0.28	0.66	0.78	0.85	0.78	0.95	0.63	0.41	0.45	0.45	0.43	0.36	0.44	0.42	0.43
Na	0.10	0.04	0.04	0.02	0.03	0.01	0.03	0.06	0.10	0.11	0.06	0.12	0.11	0.10	0.07
K	0.38	0.13	0.14	0.08	0.13	0.03	0.13	0.05	0.39	0.40	0.35	0.29	0.40	0.41	0.42
F	–	–	–	–	–	–	–	–	–	–	–	–	–	–	–
Cl	0.11	1.26	1.56	1.71	1.52	1.98	1.23	0.81	0.19	0.19	0.08	0.04	0.24	0.24	0.29
O	0.01	0.14	0.12	0.01	0.04	0.01	0.11	0.02	0.67	0.66	0.75	0.79	0.75	0.68	0.73
OH	1.87	0.60	0.32	0.28	0.44	0.01	0.66	1.17	1.14	1.15	1.17	1.17	1.01	1.08	0.97
XFe^{tot}	0.08	0.70	0.76	0.70	0.73	0.88	0.56	0.49	0.21	0.22	0.11	0.13	0.26	0.30	0.30
$Mg+Fe^{tot}$	2.56	2.77	2.92	3.00	3.01	3.05	3.09	3.13	2.54	2.56	2.30	2.53	2.46	2.50	2.53

b.d. below detection limit

Table S. 3: Chemical analyses of silicates and carbonates in multiphase solid inclusions (MSI) in wt. %.

Mineral	Orthopyroxene			Clinopyroxene					Plagioclase	
Position	MSI in Grt		lamella with Mca in Cpx	MSI Grt					MSI in Grt	
Comment	with Mca, Ap, Mnz	with Mca	with Mca	with Mca, Spl	with Mca, Spl, Ap, Am	with Opx, Mca, Py rim	with Opx, Mca, Py core	close to Mca	small automorphic inclusion	with Am, Opx, Mca, Py
Sample	SL-PX-1-Y	DS025	SL-PX-A	DS148A	DS148A	DS025-17A			SL-PX-A	DS025
Analysis	Opx-47	Opx-29	Opx-47	Cpx-01	Cpx-22	Cpx-34	Cpx-35	Cpx-36	Pl-15	Pl-28
P_2O_5	–	–	–	–	–	–	–	–	–	–
SiO_2	55.89	53.79	56.33	49.31	49.82	50.56	51.50	51.05	57.98	52.36
TiO_2	0.13	0.05	0.08	1.53	1.26	0.56	0.21	0.69	0.00	0.00
Al_2O_3	4.66	5.67	2.35	8.60	7.48	7.69	6.47	7.14	27.46	30.56
Cr_2O_3	0.03	0.01	0.13	0.00	0.01	0.41	0.33	0.35	0.01	0.00
MgO	34.62	32.21	31.72	14.06	14.59	13.69	14.30	14.13	0.11	0.00
CaO	0.27	0.32	0.43	23.99	23.06	21.41	21.37	21.48	8.92	12.73
MnO	0.08	0.04	0.17	0.03	0.01	0.07	0.05	0.04	0.03	0.00
FeO	4.85	7.01	9.55	2.86	3.08	2.95	3.25	2.99	0.45	0.22
ZnO	–	–	–	–	–	–	–	–	–	–
SrO	–	–	–	–	–	–	–	–	–	–
BaO	–	–	–	–	–	–	–	–	–	–
Na_2O	0.03	0.08	0.02	0.40	0.48	1.48	1.36	1.37	5.26	4.27
K_2O	0.02	0.19	b.d.	b.d.	b.d.	b.d.	b.d.	b.d.	0.07	0.03
Cl	–	–	–	–	–	–	–	–	–	–
total	100.55	99.36	100.77	100.77	99.81	98.82	98.83	99.24	100.29	100.16
Cations/Charges	4/12	4/12	4/12	4/12	4/12	4/12	4/12	4/12	5/16	5/16
P	–	–	–	–	–	–	–	–	–	–
Si	1.90	1.87	1.96	1.79	1.82	1.85	1.89	1.86	2.62	2.37
Ti	0.00	0.00	0.00	0.04	0.03	0.02	0.01	0.02	0.00	0.00
Al	0.19	0.23	0.10	0.37	0.32	0.33	0.28	0.31	1.46	1.63
Cr	0.00	0.00	0.00	0.00	0.00	0.01	0.01	0.01	0.00	0.00
Mg	1.76	1.67	1.64	0.76	0.79	0.75	0.78	0.77	0.01	0.00
Ca	0.01	0.01	0.02	0.93	0.90	0.84	0.84	0.84	0.43	0.62
Mn	0.00	0.00	0.01	0.00	0.00	0.00	0.00	0.00	0.00	0.00
Fe^{2+}	0.13	0.16	0.28	0.08	0.09	0.07	0.08	0.08	0.02	0.00
Fe^{3+}	0.01	0.04	0.00	0.01	0.01	0.02	0.02	0.01	0.00	0.01
Zn	–	–	–	–	–	–	–	–	–	–
Sr	–	–	–	–	–	–	–	–	–	–
Ba	–	–	–	–	–	–	–	–	–	–
Na	0.00	0.01	0.00	0.03	0.03	0.11	0.10	0.10	0.46	0.37
K	0.00	0.01	0.00	0.00	0.00	0.00	0.00	0.00	0.00	0.00
Cl	–	–	–	–	–	–	–	–	–	–
XFe^{2+}	0.07	0.09	0.14	0.10	0.10	0.08	0.09	0.09		

– not measured, b.d. below detection limit

Table S. 3 (continued): Chemical analyses of silicates and carbonates in multiphase solid inclusions (MSI) in wt. %.

Mineral	Celsian			Spinel			Amphibole				
Position	MSI in Grt			MSI in Grt		MSI in Grt	MSI in Grt				MSI in Cpx
Comment	with Mca, Cpx, Am	with Opx, Mca, Mgs, Am, Py	with Ap, dol, SiO2, Mca	with Mca, Ap, Cpx, Am	with Mca, Ap, Cls, Cpx	with Py, Mca, Mgs, Pl, SiO2	with Ap, Mca, Mnz sadanagaite	pargasite	with Mca, Ap, Mgs, Scp sadanagaite		with Mca, Ap Ti-rich tschermakite
Sample	DS025-17A	DS025	DS148A		DS025-17A	DS025	DS025-17A		DS148A	SL-PX-A	SL-1-X3
Analysis	Cls-83	Cls-28	Spl-08	Spl-24	Spl-41	Spl-06	Am-66	Am-67	Am-34	Am-21	Am-14
P_2O_5	–	–	–	–	–	–	–	–	–	–	–
SiO_2	32.51	37.03	0.08	0.05	0.08	0.10	36.31	41.80	38.24	42.63	44.11
TiO_2	0.00	0.00	0.04	0.03	0.00	b.d.	0.55	0.51	2.64	3.10	1.82
Al_2O_3	26.47	26.33	65.52	66.60	68.18	64.19	20.53	17.50	18.19	17.38	13.70
Cr_2O_3	0.01	0.00	0.49	0.46	0.12	0.34	0.01	0.02	0.03	0.23	0.63
MgO	0.01	0.52	20.01	21.18	20.75	14.30	11.78	14.76	14.22	16.84	15.79
CaO	0.32	0.34	0.13	0.14	0.04	0.07	12.21	12.37	11.75	11.32	11.93
MnO	0.00	0.00	0.02	0.03	0.02	0.05	0.02	0.04	0.01	0.03	0.06
FeO	0.43	0.74	11.91	10.44	10.53	20.08	8.80	5.88	5.56	2.80	5.16
ZnO	–	–	0.21	0.28	0.20	0.09	–	–	–	–	–
SrO	b.d.	b.d.	–	–	–	–	–	–	–	–	–
BaO	38.79	32.28	–	–	–	–	2.71	0.63	2.35	0.26	0.42
Na_2O	0.10	0.49	0.01	0.01	0.01	b.d.	2.02	2.10	2.36	1.84	2.64
K_2O	0.15	2.02	b.d.	b.d.	0.01	0.01	0.04	0.03	0.06	0.28	0.61
Cl	–	–	–	–	–	–	3.10	1.36	1.58	0.39	0.48
total	99	100	98.44	99.21	99.96	99.24	94.73	96.17	93.06	97.45	96.86
Cations/Charges	5/16	5/16	3/8	3/8	3/8	3/8	23 O eq.	23 O eq.	23 O eq.	23 O eq.	23 O eq.
P	–	–	–	–	–	–	–	–	–	–	–
Si	2.03	2.15	0.00	0.00	0.00	0.00	5.42	6.06	5.65	6.00	6.35
Ti	0.00	0.00	0.00	0.00	0.00	–	0.06	0.06	0.29	0.33	0.20
Al	1.95	1.80	1.97	1.97	2.00	1.98	3.61	2.99	3.17	2.88	2.32
Cr	0.00	0.00	0.01	0.01	0.00	0.01	0.00	0.00	0.00	0.03	0.07
Mg	0.00	0.04	0.76	0.79	0.77	0.56	2.62	3.19	3.13	3.53	3.39
Ca	0.02	0.02	0.00	0.00	0.00	0.00	1.95	1.92	1.86	1.71	1.84
Mn	0.00	0.00	0.00	0.00	0.00	0.00	0.00	0.01	0.00	0.00	0.01
Fe^{2+}	0.03	0.00	0.23	0.20	0.22	0.44	0.50	0.49	0.44	0.11	0.62
Fe^{3+}	0.00	0.04	0.02	0.02	0.00	0.00	0.62	0.23	0.24	0.22	0.00
Zn	–	–	0.00	0.01	0.00	0.00	–	–	–	–	–
Sr	–	–	–	–	–	–	–	–	–	–	–
Ba	0.95	0.74	–	–	–	–	0.23	0.05	0.20	0.02	0.0
Na	0.01	0.06	0.00	0.00	0.00	–	0.59	0.59	0.68	0.50	0.74
K	0.01	0.15	0.00	0.00	0.00	0.00	0.01	0.01	0.01	0.05	0.11
Cl	–	–	–	–	–	–	0.78	0.33	0.40	0.09	0.12
XFe^{2+}	0.96	0.00	0.24	0.20	0.22	0.44	0.16	0.13	0.12	0.03	0.15

– not measured, b.d. below detection limit

Table S. 3 (continued): Chemical analyses of silicates and carbonates in multiphase solid inclusions (MSI) in wt. %.

Mineral	Cordierite	Scapolite	Margarite	Dolomite		Magnesite		Calcite	
Position	MSI in Grt	MSI in Grt	MSI in Grt	inclusion in Grt		inclusion in Grt		inclusion in Grt	
Comment	with Fe-dol, SiO_2	higher CaO	with Spl, Mca, gor, sch, Opx	single inclusion	MSI in Grt with Ba-FSpl,	with Dol	with Ba-Mca,	with Ba-FSpl, Dol	
Sample	DS148A	SL-PX-1-Y	SL-PX-1-Y	SL-PX-1-Y	DS148A	SL-PX-1-Y	DS148A	DS148A	DS148A
Analysis	Crd-50	Scp-25c	Mrg-69	Dol-07	Dol-11	Mgs-08	Mgs-41	Cal-10	Cal-13
P_2O_5	0.08	–	1.37	0.17	0.14	0.03	0.03	0.27	0.26
SiO_2	49.36	43.78	31.94	0.09	0.10	0.09	0.24	0.07	0.12
TiO_2	b.d.	–	0.09	–	–	–	–	–	–
Al_2O_3	33.75	28.42	48.16	–	–	–	–	–	–
Cr_2O_3	0.05	–	0.17	–	–	–	–	–	–
MgO	9.66	0.48	0.84	17.61	12.42	38.66	23.66	1.67	1.14
CaO	0.30	18.01	10.50	28.06	29.64	0.84	2.45	50.29	50.53
MnO	0.08	0.05	0.04	0.24	0.11	0.36	0.56	0.09	0.06
FeO	7.11	0.45	0.76	5.59	9.47	5.93	26.38	1.02	0.71
ZnO	–	–	–	–	–	–	–	–	–
SrO	–	0.94	0.10	0.06	0.32	b.d.	b.d.	0.88	0.98
BaO	b.d.	0.16	b.d.	b.d	b.d	b.d	b.d	b.d	b.d
Na_2O	0.03	2.19	1.20	b.d.	b.d.	b.d.	0.01	b.d.	b.d.
K_2O	b.d.	0.06	0.01	b.d.	b.d.	b.d.	b.d.	b.d.	b.d.
Cl	–	0.74	0.04	b.d.	b.d.	b.d.	b.d.	b.d.	b.d.
total	100.45	95.32	95.26	51.56	51.98	45.80	53.09	53.95	53.42
Cations/Charges	11/36	16	7/22	2	2	1	1	1	1
P	0.01	–	0.08	0.00	0.00	0.00	0.00	0.00	0.00
Si	4.95	6.80	2.11	0.00	0.00	0.00	0.00	0.00	0.00
Ti	–	–	0.00	–	–	–	–	–	–
Al	3.99	5.20	3.75	–	–	–	–	–	–
Cr	0.00	–	0.01	–	–	–	–	–	–
Mg	1.45	0.11	0.08	0.85	0.63	0.90	0.58	0.04	0.03
Ca	0.03	3.00	0.74	0.98	1.08	0.01	0.04	0.93	0.94
Mn	0.01	0.01	0.00	0.01	0.00	0.00	0.01	0.00	0.00
Fe^{2+}	0.59	0.06*	0.04*	0.15*	0.27*	0.08*	0.36*	0.01*	0.01*
Fe^{3+}	0.00	0.00	–	–	–	–	–	–	–
Zn	–	–	–	–	–	–	–	–	–
Sr	–	0.08	0.00	0.00	0.01	–	–	0.01	0.01
Ba	–	0.01	–	–	–	–	–	–	–
Na	0.00	0.66	0.15	–	–	–	0.00	–	–
K	0.00	0.01	0.00	0.00	0.00	0.00	0.00	0.00	0.00
Cl	–	0.20	0.00	–	–	–	–	–	–
XFe^{2+}	0.29								

– not measured, b.d. below detection limit

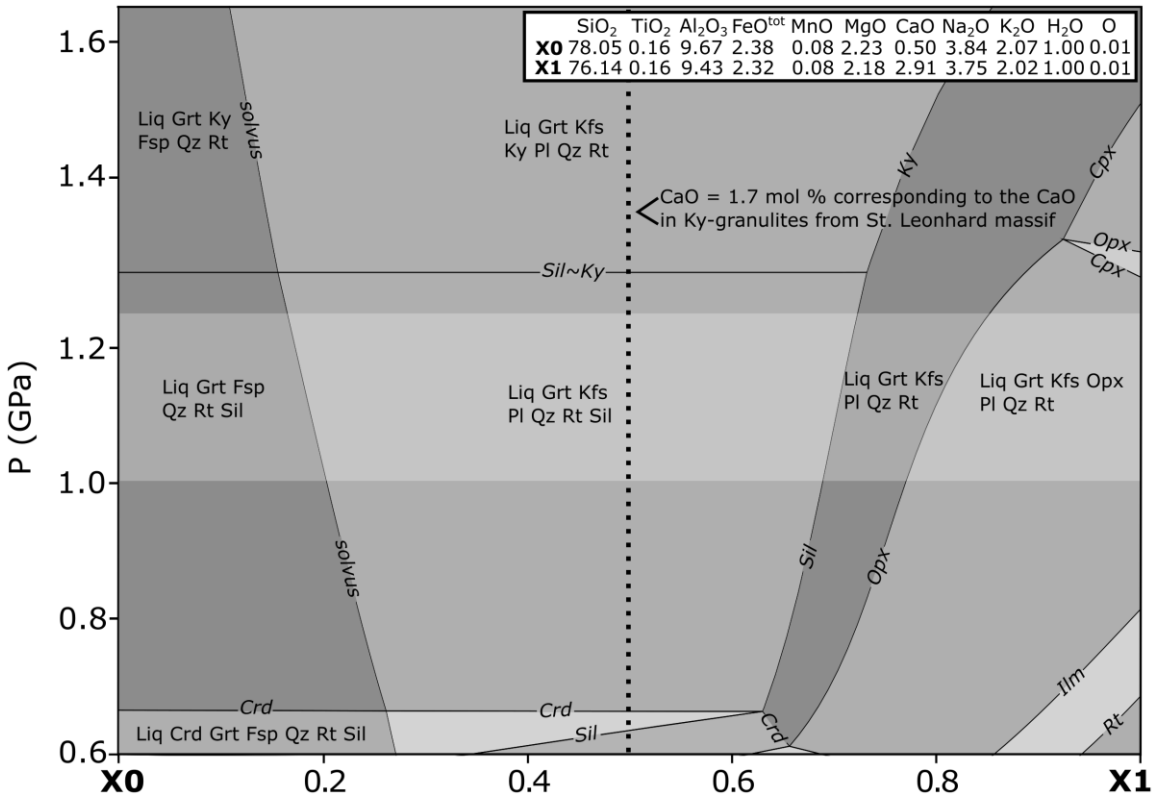

Figure S. 1: P–X diagram for felsic granulites calculated at 950 °C and showing the effect of CaO addition to the original Ky-granulite. The X1 is the current chemical composition of the intermediate granulite; towards the X0 the chemistry approaches the original one, i.e. that before interaction with the garnet clinopyroxenite xenoliths. The highlighted area at 1.0–1.2 GPa corresponds to the estimated pressure conditions of the corona formation. Dotted line at X ~0.5 indicates where the CaO content corresponds to the average of a typical Ky-bearing felsic granulite samples from the St. Leonhard massif (Table II. 5).

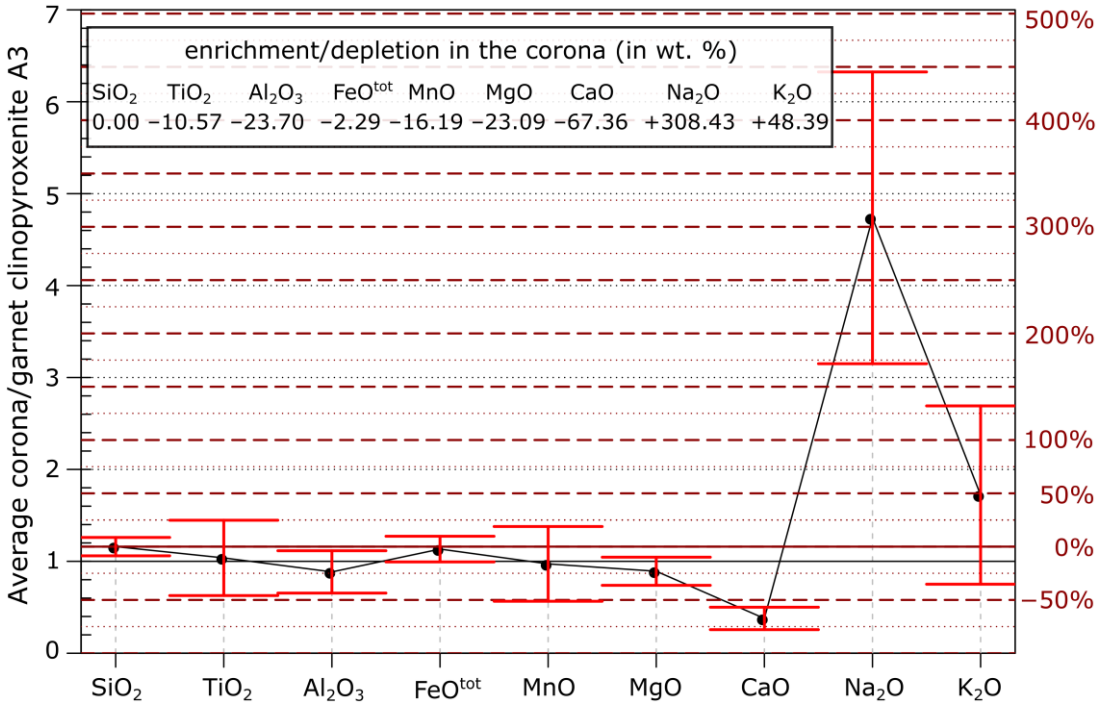

Figure S. 2: Assessment of the major-element mobility in course of the Opx–Pl corona formation around the garnet clinopyroxenite xenolith by means of the concentration ratio diagram (Ague, 2003) with SiO_2 as the immobile oxide. As the "fresh" rock was taken an average of the area analyses of the xenolith A3; the "altered rock" represents averaged analyses from all the three bands distinguished in the corona (Table II. 5). Error bars are ± 1 sigma.

Table S. 4: Restoring the hypothetical composition X0 of the Ky-bearing granulite before its interaction with the garnet clinopyroxenite with SiO2 as an immobile component

	[1] garnet clinopyroxenite (wt. %)	×	[2] wt. % change in corona	/100 =	[3] compositional change vector for garnet clinopyroxenite	[4] compositional change vector for intermediate granulite	+	[5] intermediate granulite (wt. %)	=	[6] hypothetical composition X0 of pristine Ky-granulite (wt. %)
SiO_2	45.91		0.00*		0.00	0.00		71.54		71.54
TiO_2	0.34		–10.57		–0.04	–0.01		0.21		0.20
Al_2O_3	16.78		–23.70		–3.98	–1.07		15.03		13.95
FeO^{tot}	9.24		–2.29		–0.21	–0.06		2.61		2.55
MnO	0.15		–16.19		–0.02	–0.01		0.08		0.08
MgO	15.24		–23.09		–3.52	–0.95		1.37		0.42
CaO	11.27		–67.36		–7.59	–2.05*		2.55		0.50*
Na_2O	0.47		308.43		1.44	0.39		3.63		4.02
K_2O	0.27		48.39		0.13	0.03		2.98		3.02

* assumed. As a basis served the compositional change vector [3] obtained by multiplying the garnet clinopyroxenite composition [1] with wt. % change in its corona [2] (inferred from the concentration ratio diagram; Figure S. 2) and dividing by 100.

These elemental losses/gains had to be compensated by the Opx-bearing felsic granulite host. Considering that the degree of the change is limited by the availability of CaO (a component with the most dramatic depletion that would be exhausted first), the CaO content in composition X0 [6] was set to an arbitrarily low value of 0.5 wt. %. This means that the CaO value changes by –2.05 [4]. The remaining items of the compositional change vector [4] were obtained from [3] multiplied by the factor of 2.05/7.59. Applying the vector [4] to the actual Opx-bearing felsic granulite composition [5], we obtained the hypothetical pristine felsic granulite composition X0 [6].

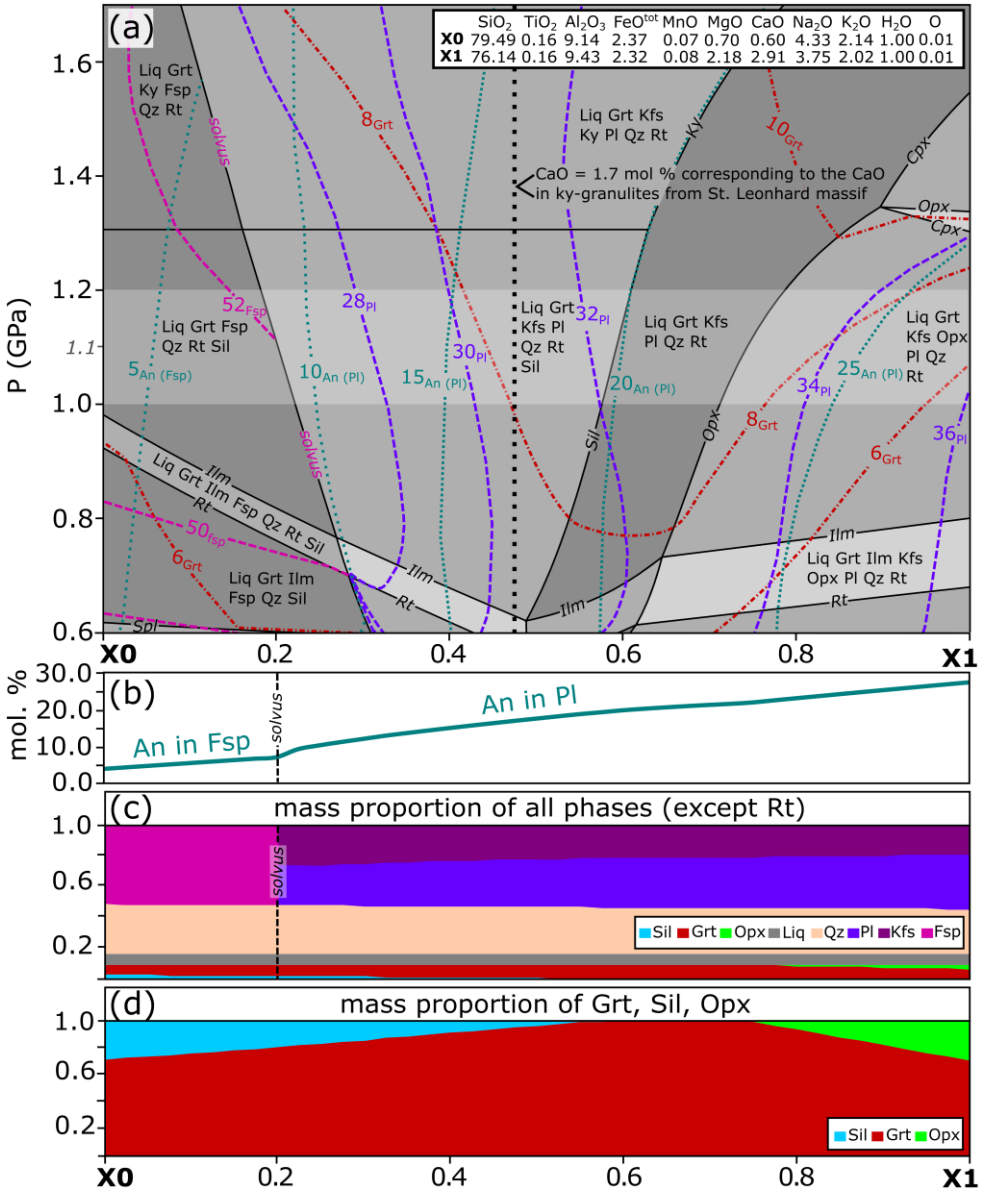

Figure S. 3: P–X diagram with SiO_2 as the immobile component modelling transition between the Opx- and Ky-bearing felsic granulites calculated at 950 °C (a) with sections at 1.1 GPa portraying An in ternary feldspar/plagioclase (b), and mass proportions of individual phases (c, d). The X1 is the measured chemical composition of the Opx-bearing felsic granulite; towards X0 the composition approaches the estimated hypothetical chemistry of a pristine Ky-granulite prior to the interaction with garnet clinopyroxenite. a) The highlighted area at 1.0–1.2 GPa corresponds to the pressure interval estimated for corona formation using the P–T pseudosection (Figure II. 7). The most significant change is the disappearance of Opx and stabilization of an Al_2SiO_5 phase (sillimanite in the diagram) towards the X0. Dotted line at X ~0.46 indicates where the CaO content corresponds to the average of typical Ky-bearing felsic granulite samples from the St. Leonhard massif. b). Molar percentages of anorthite component in plagioclase (or in ternary feldspar if above solvus). c) Mass proportions of all phases, except rutile. d) Mass proportions of garnet, sillimanite, and orthopyroxene.

Supplementary text to the discussion chapter Thermal history of crust-mantle interaction from Fe–Mg diffusion chronometry (Part II)

Garnet from the garnet pyroxenite xenolith is partially replaced by the orthopyroxene-.plagioclase symplectitic corona. Based on theoretical considerations and experiment, symplectite replacement fronts have been inferred to propagate at constant velocity (Remmert et al 2017; Gaidies et al 2017). As indicated by the enrichment of the almandine and depletion of the pyrope component in garnet next to the interface, where it is replaced by the orthopyroxene-plagioclase corona, the orthopyroxene-plagioclase assemblage of the corona was not in equilibrium with the pre-existing garnet. This drove diffusion of Fe from the orthopyroxene-plagioclase corona into the retreating garnet and of Mg into the opposite direction. Given that the symplectite replacement front propagated into the garnet at constant velocity, a stationary diffusion profile is expected to develop in the garnet next to the propagating replacement front. Such a stationary diffusion profile can be described by an exponential function (S Eq. 1). The fit to the observed concentration profile is, however, rather poor, indicating that this model is inappropriate. The profile shape rather corresponds to the characteristics of an error function (erf) (Fig. 13c, main text), which is the solution for diffusion into a half space with constant concentration at the boundary with fixed geometry. It is inferred from these relations that likely the initial diffusion profile that had developed during the partial replacement of the garnet by the orthopyroxene-plagioclase corona further relaxed in a fixed geometry after propagation of the orthopyroxene-plagioclase symlectite had stopped.

The fitting parameter Φ of the erf solution can be interpreted in two different ways. If the secondary diffusion profile was formed at constant temperature, the fitting parameter yields $\Phi = D_{Fe-Mg} \times t$ S-Eq. 2. If it was formed during cooling, then it may be described as $\Phi = D_{Fe-Mg}(t_0) \times \omega_{max}$ S-Eq. 11.

The time scales and cooling rates obtained for initial P-T conditions of 1000 °C/1.0 GPa and 900 °C/1.2 GPa, using S-Eq. 2 and S-Eq. 10 are 12.907 (± 0.273)–531.870 (± 11.253) ka and the cooling rates are 4.656 (±0.099)–0.093 (±0.002) °C/ka, respectively, with the 2σ error in brackets.

Noting that the fitted diffusion profile probably developed from the steady state diffusion profile instead of a step function, the extracted time scales represent maximum estimates. Note that the fitting errors are rather small compared to the errors using different calibrations for Fe-Mg-interdiffusion.

For the corona formation and evolution, we assume an initial steady state stage of the diffusion profile in front of the garnet replacement front that than relaxed over time to the now observed profile shape after the corona formation stopped.

1. Diffusion model for steady state (stationary) diffusion with moving boundary:

Given that stationary diffusion prevailed, i.e. the geometry of the diffusion profile in the precursor phase in front of the symplectite replacement front was time invariant in a coordinate system moving with the symplectite replacement front, the diffusion profile can be described by (e.g. Kenneth, 2004; their eq. 11.17):

$$n(z,t) = n_c + (n_c - n_r) exp\left(-\frac{v}{D_{Fe-Mg}} z\right), \qquad \text{S-Eq. 1}$$

where n_c and n_r are the background composition of the garnet (starting composition) and the composition of the garnet at the symplectite replacement front, respectively, z is the coordinate along the composition

profile with the origin at the replacement front moving with the interface, v is the velocity of the replacement front, and D_{Fe-Mg} is the Fe-Mg interdiffusion coefficient.

Fitting $n(z,t)$ from S-Eq. 1 to the measured almandine profile yields $\frac{v}{D_{Fe-Mg}}$. Multiplying by D_{Fe-Mg} taken from experimental calibrations gives v, and knowing the thickness of the symplectite, the time required for symplectite formation is calculated.

2. Diffusion model for fixed geometry

Inverse modelling based on the assumption of fixed geometry, implies that corona formation occurred first, and the secondary diffusion profiles developed later when propagation of the symplectite replacement front had stopped.

One-dimensional diffusion into a semi-infinite half-space with constant concentration at the boundary, with fixed system geometry and with constant diffusion coefficient is described by (e.g. Crank, 1975; their eq. 2.45):

$$n(x,t) = n_r + (n_c - n_r) erf\left(\frac{x}{2\sqrt{D_{Fe-Mg}t}}\right) \qquad \text{S-Eq. 2}$$

where n_c and n_r are the background composition of the garnet (starting composition) and the composition of the garnet at the symplectite replacement front, respectively, x is the coordinate along the composition profile with the origin at the garnet-symplectite interface, t is time, and D_{Fe-Mg} is the Fe-Mg interdiffusion coefficient calculated for certain P-T conditions.

Fitting S-Eq. 2 to the measured almandine profile $n(x,t)$ yields the parameter $\Phi = D_{Fe-Mg} \times t$. Knowing D_{Fe-Mg}, the time can be calculated.

2.1. Cooling with constant cooling rates

A constant coefficient is used to calculate the cooling rates based on S-Eq. 2 The T-dependence of the interdiffusion coefficient is given by the Arrhenius relation:

$$D_{Fe-Mg}(T) = {D_{Fe-Mg}}^0 \times exp\left(-\frac{\Delta Q}{RT}\right), \qquad \text{S-Eq. 3}$$

where ${D_{Fe-Mg}}^0$ is the pre-exponential factor, ΔQ is the activation energy of diffusion, R the unsiveral gas constant and T is absolute temperature.

The diffusivity decreases exponentially with decreasing T, and at some stage of the cooling history becomes too slow to produce measurable effects. This determines the closure of a geochronological or petrological system, where the compositions of the phases in the system are essentially frozen (Dodson, 1973). In most geological processes, T varies with time and therefore also D_{Fe-Mg}, as:

$$D_{Fe-Mg}(T) = {D_{Fe-Mg}}^0 \times exp\left(-\frac{\Delta Q}{RT(t)}\right) \qquad \text{S-Eq. 4}$$

A simple but realistic cooling history (Lasaga, 1998) could be:

$$T(t) = \frac{T_0}{1 + st/T_0} \qquad \text{S-Eq. 5}$$

where T_0 is the initial temperature of the system, and s the initial cooling rate (°C/s). For the initial stage of cooling, $st/T_0 << T_0$ so that $T \approx T_0 - st$. For the later stages of cooling, $st/T_0 >> T_0$. The approximation $1 + x \approx 1/(1 - x)$ can be applied to satisfy S-Eq. 5.

Using this specific cooling history, the time-dependent diffusivity reads:

$$D_{Fe-Mg}(t) = {D_{Fe-Mg}}^0 \times exp\left(-\frac{\Delta Q}{RT_0} - \frac{s\Delta Q}{RT_0^2}t\right) = D_{Fe-Mg}(t_0) \times exp\left(-\frac{s\Delta Q}{RT_0^2}t\right) \quad \text{S-Eq. 6}$$

where $D_{Fe-Mg}(t_0) = {D_{Fe-Mg}}^0 \times exp\left(-\frac{\Delta Q}{RT_0}\right)$ is the interdiffusion coefficient at the initial temperature T_0.

Let $\gamma = s\Delta Q/RT_0^2$, then S-Eq. 6 becomes:

$$D_{Fe-Mg}(t) = D_{Fe-Mg}(t_0) \times exp(-\gamma t) \quad \text{S-Eq. 7}$$

By introducing a compressed time ω (see Petrishcheva & Abart, 2017), as:

$$\omega = \frac{1}{\gamma}[1 - e^{-\gamma t}]. \quad \text{S-Eq. 8}$$

When $t \to \infty$, the compressed time scale ω approaches the limit:

$$\lim_{t\to\infty}(\omega) = \omega_{max} = \frac{1}{\gamma} = \frac{RT_0^2}{s\Delta Q}. \quad \text{S-Eq. 9}$$

Rearranging and combining S-Eq. 6 and S-Eq. 9 for $t \to \infty$ yields:

$$D_{Fe-Mg}(t) = D_{Fe-Mg}(t_0) \times \omega_{max} \quad \text{S-Eq. 10}$$

Noting that $D_{Fe-Mg}(t_0)$ is the Fe-Mg interdiffusion coefficient at the beginning of the cooling history and the same Fe-Mg interdiffusion coefficient as in equation S-Eq. 2.

Combining S-Eq. 2 and 10 we obtain:

$$n(x, \omega) = n_r + (n_c - n_r)erf\left(\frac{x}{2\sqrt{D_{Fe-Mg}(t_0) \times \omega_{max}}}\right) \quad \text{S-Eq. 11}$$

Fitting S-Eq. 10 to the measured almandine profile $n(x, \omega)$ yields the parameter $\Phi = D_{Fe-Mg}(t_0) \times \omega_{max}$. Knowing $D_{Fe-Mg}(t_0)$, T_0, and ΔQ the cooling rate can be calculated.

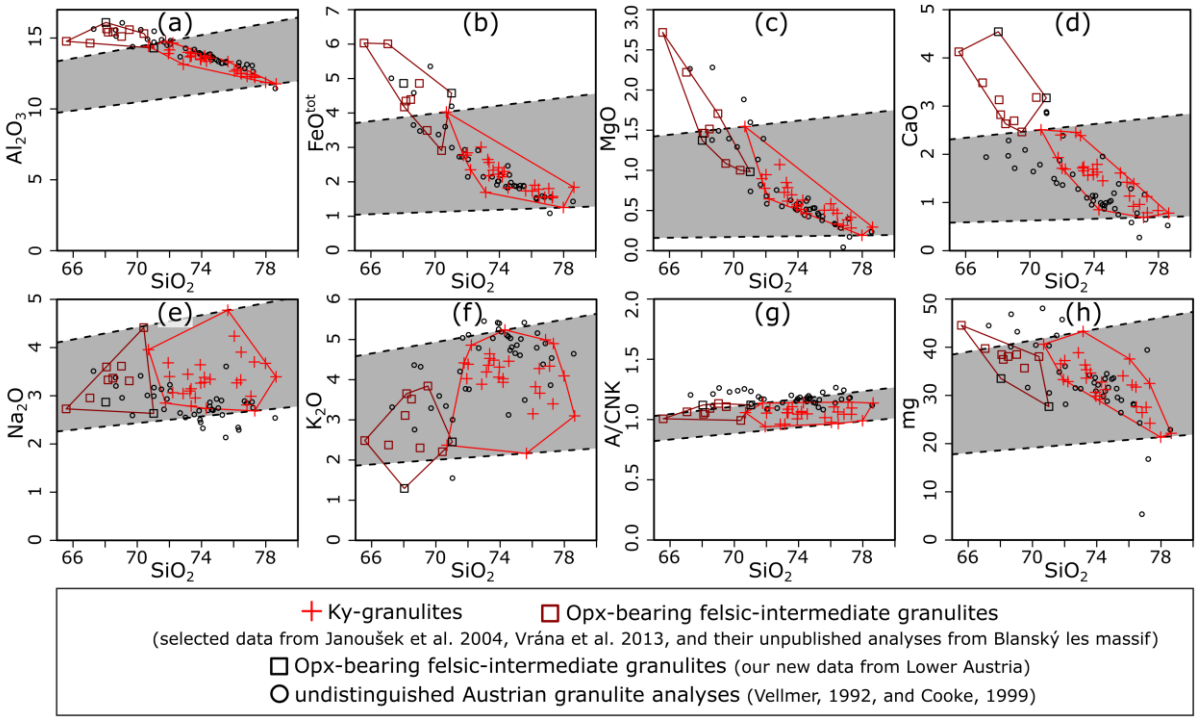

Figure S. 4: a–h) Wedge plots (Ague, 1994; Bucholz and Ague, 2010) with SiO_2 as the reference oxide comparing analyses of pristine felsic Ky-granulites with 'transitional', Opx-bearing felsic–intermediate types (Janoušek et al., 2004; Vrána et al., 2013) and undistinguished Austrian analyses from the Ph.D. theses (Vellmer, 1992; Cooke, 1999). The grey fields ("wedges") denote the protolith variability (and no perceptible gain/loss of components in the altered samples). All data were recalculated to 100 % anhydrous basis.

Table S. 5: Chemical analyses of perthites from Ky-bearing felsic granulites.

Lithology	Ky-bearing felsic granulites																
Thin-section	DS024	DS024	DS024	DS024	DS024	DS024	DS024	DS024	DS024	DS001A	DS001A	DS001A	DS001A	DS001A	DS001A	DS001A	DS001A
Analysis	Spec_1	Spec_2	Spec_3	Spec_4	Spec_5	Spec_7	Spec_8	Spec_9	Spec_10	Spec_1	Spec_ 6	Spec_7	Spec_10	Spec_11	Spec_12	Spec_13	Spec_14
Position	Matrix	Matrix	Matrix	Matrix	Matrix	Matrix	Matrix	Matrix	Matrix	Matrix	Matrix	Matrix	Matrix	Matrix	Matrix	Matrix	Matrix
SiO_2	63.98	63.69	63.49	63.52	63.25	63.59	63.51	63.94	63.77	64.17	63.35	63.90	63.45	63.61	63.63	63.69	63.92
P_2O_5	0.16	0.14	0.16	0.09	0.07	0.13	0.17	0.13	0.10	0.12	0.12	0.10	0.12	0.14	0.14	0.10	0.08
Al_2O_3	19.14	20.35	20.35	18.98	20.41	19.09	19.26	19.02	19.28	19.51	19.26	19.47	19.34	19.62	19.35	19.37	19.02
FeO	0.04	0.08	0.01	0.07	0.01	b.d.	0.08	b.d.	0.01	0.02	b.d.	b.d.	0.01	0.03	0.03	b.d.	0.01
CaO	0.54	1.75	1.71	0.44	1.85	0.68	0.79	0.55	0.72	0.94	0.96	0.93	1.01	1.06	1.00	1.05	0.46
BaO	0.09	0.05	0.06	0.08	0.05	0.07	0.11	0.15	0.07	0.12	0.09	0.09	0.14	0.08	0.11	0.14	0.18
Na_2O	2.98	5.63	5.57	2.55	5.76	2.74	2.94	2.37	3.33	3.47	3.53	3.76	3.33	3.77	3.82	3.86	2.63
K_2O	12.61	7.73	7.61	13.13	7.31	12.75	12.50	13.48	11.90	11.57	11.42	11.07	11.63	10.84	10.82	10.83	13.20
Total	99.54	99.41	98.95	98.87	98.72	99.05	99.36	99.65	99.18	99.92	98.72	99.32	99.02	99.16	98.90	99.04	99.49
Cations/Charges	5 / 16	5 / 16	5 / 16	5 / 16	5 / 16	5 / 16	5 / 16	5 / 16	5 / 16	5 / 16	5 / 16	5 / 16	5 / 16	5 / 16	5 / 16	5 / 16	5 / 16
Si	2.93	2.88	2.89	2.93	2.88	2.93	2.91	2.94	2.92	2.92	2.92	2.92	2.92	2.91	2.92	2.92	2.93
P	0.01	0.01	0.01	0.00	0.00	0.00	0.01	0.01	0.00	0.00	0.00	0.00	0.00	0.01	0.01	0.00	0.00
Al	1.03	1.08	1.09	1.03	1.09	1.04	1.04	1.03	1.04	1.05	1.04	1.05	1.05	1.06	1.05	1.05	1.03
Fe	0.00	0.00	0.00	0.00	0.00	–	0.00	–	0.00	0.00	–	–	0.00	0.00	0.00	–	0.00
Ca	0.03	0.08	0.08	0.02	0.09	0.03	0.04	0.03	0.04	0.05	0.05	0.05	0.05	0.05	0.05	0.05	0.02
Ba	0.00	0.00	0.00	0.00	0.00	0.00	0.00	0.00	0.00	0.00	0.00	0.00	0.00	0.00	0.00	0.00	0.00
Na	0.26	0.49	0.49	0.23	0.51	0.25	0.26	0.21	0.30	0.31	0.32	0.33	0.30	0.33	0.34	0.34	0.23
K	0.74	0.45	0.44	0.77	0.42	0.75	0.73	0.79	0.70	0.67	0.67	0.65	0.68	0.63	0.63	0.63	0.77

b.d. below detection limit

Table S. 5 (continued): Chemical analyses of perthites from Ky-bearing felsic granulites.

Lithology	Ky-bearing felsic granulites																
Thin-section	DS001A	DS001A	DS038B	DS038B	DS038B	DS038B	DS038B	DS038B	DS038B	DS038B	DS001S	DS001S	DS001S	DS001S	DS001S	DS001S	DS001S
Analysis	Spec_15	Spec_16	Spec_1	Spec_2	Spec_3	Spec_4	Spec_8	Spec_9	Spec_10	Spec_11	Spec_1	Spec_3	Spec_7	Spec_8	Spec_9	Spec_12	Spec_13
Position	Matrix	Matrix	Matrix	Matrix	Matrix	Matrix	Matrix	Matrix	Matrix	Matrix	In Grt, assoc. with matrix	In Grt, assoc. with matrix	Matrix	Matrix	Matrix	Matrix	Matrix
SiO_2	63.90	63.65	64.11	64.09	64.27	64.41	63.92	64.46	63.98	64.32	63.03	62.14	63.51	63.79	62.76	64.19	63.04
P_2O_5	0.13	0.10	0.03	0.04	0.07	0.03	0.10	0.12	0.08	0.11	b.d.	b.d.	b.d.	b.d.	b.d.	b.d.	b.d.
Al_2O_3	19.05	19.96	19.54	19.42	19.19	19.33	19.42	19.53	19.38	19.02	20.29	21.44	19.54	19.33	20.48	19.09	19.56
FeO	0.01	0.01	0.04	b.d.	0.02	b.d.	b.d.	0.04	0.01	b.d.	0.08	0.16	0.01	0.05	0.07	b.d.	0.04
CaO	0.52	1.38	0.89	0.89	0.62	0.83	0.83	0.92	0.76	0.51	2.03	2.93	1.10	0.90	2.19	0.77	1.42
BaO	0.11	0.02	0.08	0.11	0.07	0.07	0.10	0.04	0.14	0.05	0.20	0.30	0.31	0.27	0.22	0.26	0.22
Na_2O	2.49	3.90	4.26	3.91	3.42	4.11	3.57	4.31	3.19	3.44	3.59	4.52	2.64	2.57	3.84	2.49	3.07
K_2O	13.28	10.68	10.40	10.92	11.88	10.80	11.42	10.42	12.07	12.11	10.46	8.10	12.52	12.93	9.87	13.03	11.65
Total	99.49	99.70	99.35	99.38	99.54	99.57	99.37	99.84	99.62	99.56	99.68	99.59	99.64	99.85	99.43	99.82	99.01
Cations/Charges	5 / 16	5 / 16	5 / 16	5 / 16	5 / 16	5 / 16	5 / 16	5 / 16	5 / 16	5 / 16	5 / 16	5 / 16	5 / 16	5 / 16	5 / 16	5 / 16	5 / 16
Si	2.94	2.89	2.92	2.93	2.94	2.93	2.92	2.92	2.93	2.94	2.88	2.83	2.91	2.92	2.87	2.94	2.90
P	0.01	0.00	0.00	0.00	0.00	0.00	0.00	0.00	0.00	0.00	–	–	–	–	–	–	–
Al	1.03	1.07	1.05	1.04	1.03	1.04	1.05	1.04	1.04	1.02	1.09	1.15	1.06	1.04	1.10	1.03	1.06
Fe	0.00	0.00	0.00	–	0.00	–	–	0.00	0.00	–	0.00	0.01	0.00	0.00	0.00	–	0.00
Ca	0.03	0.07	0.04	0.04	0.03	0.04	0.04	0.04	0.04	0.02	0.10	0.14	0.05	0.04	0.11	0.04	0.07
Ba	0.00	0.00	0.00	0.00	0.00	0.00	0.00	0.00	0.00	0.00	0.00	0.01	0.01	0.00	0.00	0.00	0.00
Na	0.22	0.34	0.38	0.35	0.30	0.36	0.32	0.38	0.28	0.30	0.32	0.40	0.24	0.23	0.34	0.22	0.27
K	0.78	0.62	0.60	0.64	0.69	0.63	0.67	0.60	0.70	0.71	0.61	0.47	0.73	0.76	0.58	0.76	0.68

b.d. below detection limit

Table S. 6: Chemical analyses of antiperthites from intermediate granulites.

Lithology	Intermediate granulites									
Thin-section	DS071B	DS071B	DS071B	DS071B	DS071B	DS008	DS008	DS008	DS008	DS008
Perthite/Antiperthite	Antiperthite	Antiperthite	Antiperthite	Antiperthite	Antiperthite	Antiperthite	Antiperthite	Antiperthite	Antiperthite	Antiperthite
Analysis	Spec_1	Spec_2	Spec_5	Spec_6	Spec_7	Spec_1	Spec_4	Spec_7	Spec_8	Spec_9
Position	Matrix	Matrix	Matrix	Matrix	Matrix	Matrix	Matrix	Matrix	Matrix	Matrix
SiO_2	59.96	59.84	59.40	59.84	59.80	59.62	58.58	59.06	59.38	59.27
P_2O_5	b.d.	b.d.	b.d.	b.d.	b.d.	b.d.	b.d.	b.d.	b.d.	b.d.
Al_2O_3	23.80	23.98	24.21	23.90	23.90	24.14	24.56	24.27	24.21	24.24
FeO	0.11	0.11	0.16	0.13	0.16	0.04	0.10	0.16	0.07	0.10
CaO	5.78	5.92	6.37	5.79	5.89	6.22	6.72	6.47	6.38	6.41
BaO	0.08	0.12	0.05	0.19	0.10	0.11	0.07	0.08	0.03	0.09
Na_2O	5.94	5.97	5.94	5.75	5.92	5.82	5.61	5.33	5.55	5.65
K_2O	3.64	3.51	3.19	4.00	3.58	3.47	3.21	3.88	3.76	3.66
Total	99.32	99.45	99.32	99.61	99.35	99.42	98.85	99.24	99.39	99.42
Cations/Charges	5 / 16	5 / 16	5 / 16	5 / 16	5 / 16	5 / 16	5 / 16	5 / 16	5 / 16	5 / 16
Si	2.71	2.70	2.69	2.70	2.71	2.70	2.67	2.68	2.69	2.68
P	–	–	–	–	–	–	–	–	–	–
Al	1.27	1.28	1.29	1.27	1.27	1.29	1.32	1.30	1.29	1.29
Fe	0.00	0.00	0.01	0.00	0.01	0.00	0.00	0.01	0.00	0.00
Ca	0.28	0.29	0.31	0.28	0.29	0.30	0.33	0.32	0.31	0.31
Ba	0.00	0.00	0.00	0.00	0.00	0.00	0.00	0.00	0.00	0.00
Na	0.52	0.52	0.52	0.50	0.52	0.51	0.50	0.47	0.49	0.50
K	0.21	0.20	0.18	0.23	0.21	0.20	0.19	0.22	0.22	0.21

b.d. below detection limit

Table S.6 (continued): Chemical analyses of antiperthites from intermediate granulites.

Lithology	Intermediate granulites								
Thin-section	DS008	DS008	DS008	DS001F	DS001F	DS001F	DS001F	DS001F	DS001F
Perthite/Antiperthite	Antiperthite	Antiperthite	Antiperthite	Antiperthite	Antiperthite	Antiperthite	Antiperthite	Antiperthite	Antiperthite
Analysis	Spec_10	Spec_11	Spec_12	Spec_1	Spec_4	Spec_5	Spec_6	Spec_7	Spec_8
Position	Matrix	Matrix	Matrix	Matrix	Matrix	Matrix	Matrix	Matrix	Matrix
SiO_2	59.45	59.50	59.71	57.29	56.79	56.98	57.12	56.69	56.18
P_2O_5	b.d.	b.d.	b.d.	b.d.	b.d.	b.d.	b.d.	b.d.	b.d.
Al_2O_3	24.22	23.73	23.74	25.78	26.20	26.16	25.97	26.02	25.83
FeO	0.14	0.13	0.12	0.10	0.09	0.11	0.03	0.09	0.12
CaO	6.31	5.86	5.87	7.94	8.34	8.33	8.25	8.21	8.30
BaO	0.07	0.13	0.14	0.11	0.06	0.02	0.07	0.09	0.00
Na_2O	5.11	5.16	5.41	4.80	4.93	5.11	4.81	4.71	4.04
K_2O	4.51	4.60	4.41	3.56	2.86	2.62	3.22	3.20	4.18
Total	99.81	99.12	99.40	99.57	99.28	99.33	99.47	99.01	98.64
Cations/Charges	5 / 16	5 / 16	5 / 16	5 / 16	5 / 16	5 / 16	5 / 16	5 / 16	5 / 16
Si	2.69	2.71	2.71	2.60	2.58	2.59	2.60	2.59	2.58
P	–	–	–	–	–	–	–	–	–
Al	1.29	1.27	1.27	1.38	1.40	1.40	1.39	1.40	1.40
Fe	0.01	0.01	0.00	0.00	0.00	0.00	0.00	0.00	0.00
Ca	0.31	0.29	0.29	0.39	0.41	0.41	0.40	0.40	0.41
Ba	0.00	0.00	0.00	0.00	0.00	0.00	0.00	0.00	0.00
Na	0.45	0.46	0.48	0.42	0.43	0.45	0.42	0.42	0.36
K	0.26	0.27	0.26	0.21	0.17	0.15	0.19	0.19	0.24

b.d. below detection limit

Table S. 7: Zirconium content in rutile for Zr in rutile thermometry (see Figure III. 22)

Sample	ZrO_2 (wt. %)	Zr (ppm)	Lithology	Analysis	Position
DS024	0.41	3064.85	(F-Gr)	Rt-03	matrix
DS024	0.41	3064.85	(F-Gr)	Rt-04	matrix
DS024	0.44	3227.72	(F-Gr)	Rt-05	matrix
DS024	0.46	3383.18	(F-Gr)	Rt-06	matrix
DS024	0.43	3168.49	(F-Gr)	Rt-07	matrix
DS024	0.42	3101.86	(F-Gr)	Rt-08	matrix
DS024	0.44	3242.52	(F-Gr)	Rt-10	matrix
DS024	0.46	3383.18	(F-Gr)	Rt-09	Grt
DS024	0.47	3509.03	(F-Gr)	Rt-11	Grt
DS024	0.45	3323.96	(F-Gr)	Rt-12	Grt
DS024	0.45	3346.16	(F-Gr)	Rt-01	Grt
DS024	0.43	3183.30	(F-Gr)	Rt-02	Grt
DS001S	0.48	3531.24	(F-Gr)	Rt-07	matrix
DS001S	0.46	3368.37	(F-Gr)	Rt-08	matrix
DS001S	0.48	3568.26	(F-Gr)	Rt-09	matrix
DS001S	0.40	2924.19	(F-Gr)	Rt-10	matrix
DS001S	0.42	3087.06	(F-Gr)	Rt-11	matrix
DS001S	0.41	3027.83	(F-Gr)	Rt-12	matrix
DS001S	0.43	3168.49	(F-Gr)	Rt-13	matrix
DS001S	0.48	3568.26	(F-Gr)	Rt-01	Grt
DS001S	0.49	3634.88	(F-Gr)	Rt-02	Grt
DS001S	0.49	3605.27	(F-Gr)	Rt-03	Grt
DS001S	0.46	3397.99	(F-Gr)	Rt-04	Grt
DS001S	0.48	3553.45	(F-Gr)	Rt-06	Grt
DS001A	0.40	2961.21	(F-Gr)	Rt-01	matrix
DS001A	0.40	2953.80	(F-Gr)	Rt-02	matrix
DS001A	0.41	3057.45	(F-Gr)	Rt-03	matrix
DS001A	0.39	2879.77	(F-Gr)	Rt-09	matrix
DS001A	0.41	3042.64	(F-Gr)	Rt-10	matrix
DS001A	0.43	3198.10	(F-Gr)	Rt-11	matrix
DS001A	0.65	4841.57	(F-Gr)	Rt-04	Grt
DS001A	0.60	4441.81	(F-Gr)	Rt-05	Grt
DS001A	0.41	3050.04	(F-Gr)	Rt-06	Grt
DS001A	0.43	3153.69	(F-Gr)	Rt-07	Grt
DS001A	0.41	3050.04	(F-Gr)	Rt-08	Grt
DS038B	0.51	3790.35	(F-Gr)	Rt-01	matrix
DS038B	0.55	4042.05	(F-Gr)	Rt-02	matrix
DS038B	0.52	3849.57	(F-Gr)	Rt-03	matrix
DS038B	0.48	3568.26	(F-Gr)	Rt-04	matrix
DS038B	0.49	3620.08	(F-Gr)	Rt-05	matrix
DS038B	0.48	3560.85	(F-Gr)	Rt-06	matrix
DS038B	0.48	3538.64	(F-Gr)	Rt-07	matrix
DS038B	0.52	3819.96	(F-Gr)	Rt-09	matrix
DS038B	0.55	4042.05	(F-Gr)	Rt-08	Grt
DS038B	0.54	3960.62	(F-Gr)	Rt-10	Grt

Table S. 7 (continued): Zirconium content in rutile for Zr in rutile thermometry (Figure III. 22)

Sample	ZrO_2 (wt. %)	Zr (ppm)	Lithology	Analysis	Position
DS002A	0.35	2598.46	(F-Gr)	Rt-03	matrix
DS002A	0.36	2642.88	(F-Gr)	Rt-04	matrix
DS002A	0.37	2746.52	(F-Gr)	Rt-05	matrix
DS002A	0.34	2480.01	(F-Gr)	Rt-06	matrix
DS002A	0.34	2502.22	(F-Gr)	Rt-07	matrix
DS002A	0.35	2576.25	(F-Gr)	Rt-08	matrix
DS002A	0.36	2679.89	(F-Gr)	Rt-09	matrix
DS002A	0.36	2628.07	(F-Gr)	Rt-10	matrix
DS002A	0.37	2739.12	(F-Gr)	Rt-01	Grt
DS002A	0.47	3449.81	(F-Gr)	Rt-02	Grt
DS002A	0.52	3819.96	(F-Gr)	Rt-11	Grt
DS002A	0.51	3745.93	(F-Gr)	Rt-12	Grt
DS071B	0.47	3442.40	(I-Gr)	Rt-01	matrix
DS071B	0.51	3790.35	(I-Gr)	Rt-02	matrix
DS071B	0.43	3175.90	(I-Gr)	Rt-05	matrix
DS071B	0.51	3768.14	(I-Gr)	Rt-09	matrix
DS071B	0.46	3412.79	(I-Gr)	Rt-10	matrix
DS071B	0.35	2591.06	(I-Gr)	Rt-07	Grt
DS071B	0.18	1295.53	(I-Gr)	Rt-08	Grt
DS071B	0.26	1895.17	(I-Gr)	Rt-11	Grt
DS071B	0.30	2235.71	(I-Gr)	Rt-03	Grt
DS071B	0.35	2591.06	(I-Gr)	Rt-04	Grt
DS008	0.76	5626.29	(I-Gr)	Rt-03	matrix
DS008	0.71	5241.34	(I-Gr)	Rt-04	matrix
DS008	0.66	4871.19	(I-Gr)	Rt-05	matrix
DS008	0.65	4804.56	(I-Gr)	Rt-06	matrix
DS008	0.74	5463.43	(I-Gr)	Rt-07	matrix
DS008	0.72	5300.56	(I-Gr)	Rt-01	Grt
DS008	0.73	5433.82	(I-Gr)	Rt-02	Grt
DS008	0.36	2650.28	(I-Gr)	Rt-08	Grt
DS008	0.33	2465.21	(I-Gr)	Rt-09	Grt
DS008	0.19	1384.36	(I-Gr)	Rt-10	Grt
DS001F	0.83	6114.89	(I-Gr)	Rt-02	matrix
DS001F	0.78	5796.56	(I-Gr)	Rt-04	matrix
DS001F	0.96	7136.51	(I-Gr)	Rt-05	matrix
DS001F	0.96	7069.88	(I-Gr)	Rt-06	matrix
DS001F	0.73	5426.41	(I-Gr)	Rt-07	matrix
DS001F	0.83	6114.89	(I-Gr)	Rt-08	matrix
DS001F	0.99	7343.79	(I-Gr)	Rt-09	matrix
DS001F	0.82	6033.46	(I-Gr)	Rt-10	matrix
DS001F	1.13	8335.80	(I-Gr)	Rt-11	matrix
DS001F	0.45	3301.75	(I-Gr)	Rt-01	Grt
DS001F	0.52	3819.96	(I-Gr)	Rt-03	Grt